A Finite Element Investigation of Topographic Variation

at Mid-Ocean Ridges Spreading at the Same Rate

by

' CHRIS EUGENE ZERVAS

A dissertation submitted in partial fulfillment
of the requirements for the degree of

Doctor of Philosophy

University of Washington

1988

Approved by _____
(Chairperson of Supervisory Committee)

Program Authorized
to Offer Degree_____Geophysics_____

Date_____November 28, 1988_____

Doctoral Dissertation

In presenting this dissertation in partial fulfillment of the requirements for the Doctoral degree at the University of Washington, I agree that the Library shall make its copies freely available for inspection. I further agree that extensive copying of this dissertation is allowable only for scholarly purposes, consistent with "fair use" as prescribed in the U. S. Copyright Law. Requests for copying or reproduction of this dissertation may be referred to University Microfilms, 300 North Zeeb Road, Ann Arbor, Michigan 48106, to whom the author has granted "the right to reproduce and sell (a) copies of the manuscript in microform and/or (b) printed copies of the manuscript made from microform."

Signature _Chris E. Jenns_

Date _November 29, 1988_

University of Washington

Abstract

A FINITE ELEMENT INVESTIGATION OF TOPOGRAPHIC VARIATION AT MID-OCEAN RIDGES SPREADING AT THE SAME RATE

by Chris Eugene Zervas

Chairperson of the Supervisory Committee: Professor Brian T.R. Lewis
Geophysics Program

The Juan de Fuca ridge and the Gorda ridge are two spreading centers located off the west coast of North America. Both are spreading at the rate of 3 cm/yr, yet the Gorda ridge has a wide, deep, axial valley and the Juan de Fuca ridge has a large axial peak. A finite element program for two-dimensional, steady state, viscous flow was used to determine the cause of spreading rate independent topography. Viscoplastic rheology was used to represent the behavior of the brittle lithosphere. The yield stress was the shear failure criterion for slip on normal faults.

The asthenospheric viscosity was varied by several orders of magnitude. Both Newtonian and non-Newtonian rheologies were tested. The cold, brittle, hydrothermally cooled layer at the axis was substantially thinned. Partial melting of the upwelling mantle was modeled by lowering viscosities and densities beneath the ridge axis. All models produced deep axial valleys. The results show that ridge crest topography is determined by the state of stress in the

TABLE OF CONTENTS

iii

LIST OF FIGURES

viii

x

LIST OF TABLES

Introduction

Oceanic lithosphere is formed at mid-ocean spreading centers where hot mantle material rises and partially melts through pressure release. A melted fraction separates to form the oceanic crust. The material loses heat to the ocean and contracts as it moves away from the spreading center. The high temperature of the upwelling material elevates the topography of the ocean bottom near the spreading center. It has been observed that the ocean bottom deepens away from the ridge axis as a function of the square root of age where the age is zero at the axis. If the spreading rate is constant over time, the bathymetry increases as the square root of distance from the axis.

However, this rule breaks down in the vicinity of the ridge axis. Generally, slow spreading ridges (less than 2.5 cm/yr half spreading rate) such as the Mid-Atlantic Ridge have a wide (15-20 km), deep (1.5-3.0 km), axial valley (Macdonald, 1982). Fast spreading ridges (greater than 4.5 cm/yr half spreading rate) such as the East Pacific Rise have a distinct axial peak. Intermediate rate spreading centers have a small axial valley (50-200 m deep). However, there are many exceptions. The Reykjanes Ridge, a section of the Mid-Atlantic Ridge near the Icelandic hot spot, is spreading at 1 cm/yr but has a large axial peak. Therefore spreading rate alone does not control ridge crest topography.

Ocean Crustal Structure

The oceanic crust is typically 5 to 6 kilometers thick. Seismically, the ocean crust can be divided into 3 layers (Turcotte and Schubert, 1982). Seismic velocities are low in the top kilometer of the crust known as layer 1. Velocities increase rapidly with depth in layer 2 which is about 1.5 kilometers thick. They increase less rapidly in the lower crust which is known as layer 3. The transition to upper mantle velocities of 7.5 to 8.5 km/sec may be gradual or sharp (Lewis, 1983; Orcutt, 1987).

The study of ophiolites has shed some light on the petrology of the ocean crust. Ophiolites are believed to be sections of ocean crust that have been obducted onto the continents (Gass, 1982). Although there are large variations in the structure of ophiolites (Lewis, 1983), the seismic layers have been associated with specific structural units. The top layer is composed of marine sediments and is associated with layer 1 (Figure 1). The next layer consists of pillow basalts which have been extruded on the ocean floor. Beneath the pillow basalts is the sheeted dike complex composed of vertical basaltic dikes roughly one meter wide. Together, the pillow basalts and the sheeted dikes form layer 2. Layer 3 consists of isotropic gabbros at the top and layered gabbros on the bottom. Gabbroic rocks are of the same composition as basaltic rocks. However, they are coarser grained indicating a slower rate of cooling. The gabbros are believed to have been formed by the cooling of a crustal magma chamber. Accretion to the

roof of the magma chamber is believed to produce the isotropic gabbros and deposition of crystals on the bottom of the magma chamber is believed to produce the layered gabbros. Below the gabbros, across the petrologic Moho, tectonized peridotites are found. These are believed to be mantle rocks depleted of their basaltic fraction. If water was present, these ultramafic rocks may have been serpentinized. Serpentinites have lower densities and seismic velocities than peridotites. Some petrologic studies of ophiolites indicate that the crustal magma chamber is 10-20 kilometers wide and steady-state in time with periodic infusions of fresh magma.

Investigation of the ocean floor at spreading centers and deep-sea drilling confirm that the top of the ocean crust resembles layer 2 of the ophiolite section (Sempere and Macdonald, 1987). The marine sediments are absent at the spreading center where basaltic rocks are exposed at the surface. The deepest drilled hole, has a 570 meter thick layer of pillow basalts and a 250 meter thick transition zone between pillows and dikes before ending in the sheeted dike complex. However, it is unknown if the ophiolite complexes found on land are representative of the crust being produced at mid-ocean spreading centers. It has been argued that they may have originated at back-arc spreading centers or only at fast spreading ridges (Gass, 1982; Lister, 1983).

Seismic Evidence

Numerous seismic experiments have been conducted at mid-ocean ridge axes to determine their crustal structure (Macdonald, 1982; 1983; Orcutt, 1987; Sempere and Macdonald, 1987). There is substantial evidence of crustal magma chambers on some segments of the East Pacific Rise. Seismic refraction experiments using ocean bottom seismometers have been used to find low velocity zones under the ridge axis. A low velocity zone at 2-3 kilometers below the ocean floor has been found at 9° N (Orcutt et al., 1976), 12° N (Lewis and Garmany, 1982), 21° N (Reid et al., 1977), and 22° N (McClain and Lewis, 1980).

Shear waves from microearthquakes or explosions which cross the ridge axis are often attenuated beneath the East Pacific Rise indicating the presence of partial melt. Riedesel et al. (1982) has investigated microearthquakes in a hydrothermal field at 21° N and found a maximum depth of 2-3 kilometers, indicating the thickness of the brittle layer at the axis. Similar microearthquake depths were obtained by McClain and Lewis (1980) at 22° N. The half spreading rate at these locations is 3 cm/yr. However, magma chambers may not be present at all locations. Bratt and Solomon (1984) found no attenuation of shear or compressional waves propagating across the axis at 12° N indicating a narrow or discontinuous magma chamber. Nearby at 13° N, Orcutt et al. (1984) found a low velocity zone 1.5 kilometers deep and McClain et al. (1985) constrained its width to less than 4 kilometers.

Seismic multichannel reflection profiles have also been used to locate magma chambers. Reflections from the top of a rock-liquid interface should be strong and phase shifted by 180°. Herron et al. (1980) found a magma chamber reflection at a depth of 1.5 to 2 kilometers at 9.5° N. The magma chamber is asymmetric, with a width of 4 kilometers (Hale et al., 1982). A reflector at 400 meters has been interpreted as the transition between the pillow basalts and the sheeted dike layer (Herron et al., 1982). A multichannel reflection profile between 9° N to 13° N along the strike of the East Pacific Rise shows a strong, almost continuous reflector (Detrick et al., 1987). Phase reversal suggests that it might be the roof of a magma chamber. The reflector is limited to 2 kilometers from the axis. Another magma chamber has been discovered on the Valu Fa Ridge in the Lau back-arc basin in the South Pacific (Morton and Sleep, 1985). Five profiles were made across the ridge axis. The strong, polarity reversed reflector is 2-3 kilometers wide and 3.5 kilometers deep. The ridge spreads at 3.5 cm/yr.

In contrast, there is no evidence of a seismically detectable crustal magma chamber on the Mid-Atlantic Ridge (Macdonald, 1982, 1983; Orcutt, 1987; Sempere and Macdonald, 1987). No low velocity zones have been discovered by seismic refraction. Shear waves from microearthquakes or explosions are not attenuated and hypocenters are located as deep as 10 kilometers below the ridge axis. Purdy and Detrick (1986) found normal mature oceanic crust along a 120 kilometer section of the Mid-Atlantic Ridge at 23° N using seismic refraction. There was no evidence of a steady-state magma

chamber. Toomey et al. (1985) recorded microearthquakes as deep as 7-8 kilometers below the median valley at 23° N. Focal mechanisms indicate a fault plane dipping at 30°. Huang et al. (1986) determined the focal mechanisms of earthquakes on the Mid-Atlantic Ridge using teleseismically recorded data. The focal mechanisms showed normal faulting on fault planes dipping 45°. The centroid depths were at 1-3 kilometers and the fault planes could extend as deep as 6 kilometers. Huang et al. (1987) obtained similar results for earthquakes in the Indian Ocean.
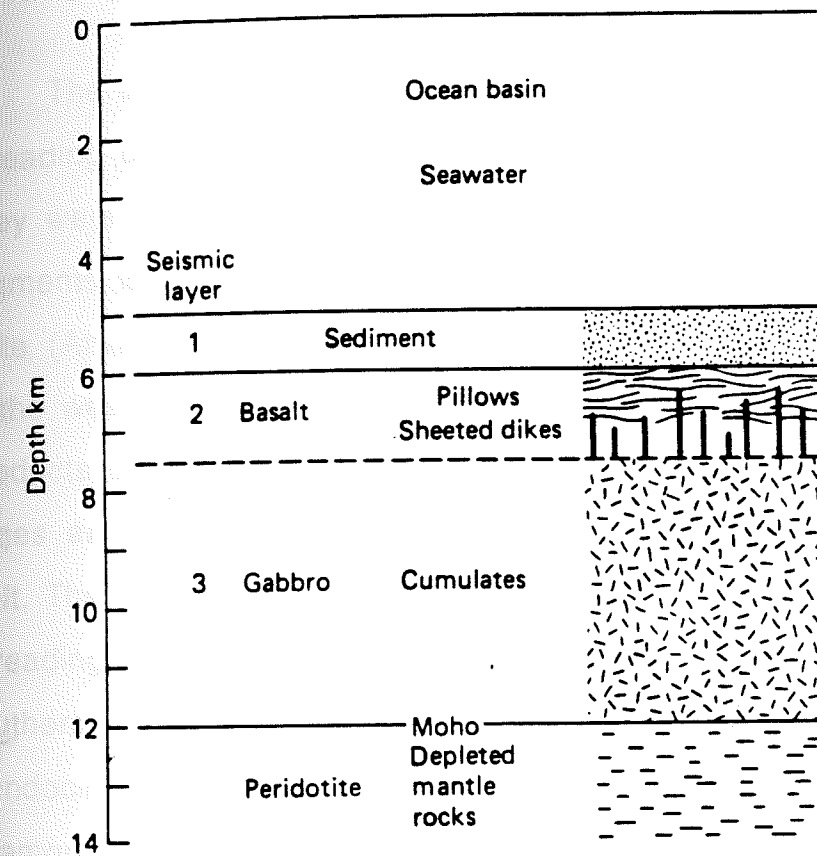
Figure 1. Oceanic crustal model based on ophiolite data and seismic structure (Turcotte and Schubert, 1982).

The Juan de Fuca ridge and the Gorda ridge are two isolated spreading centers off the west coast of North America (Figure 2). They were once part of the East Pacific Rise but the intervening segments to the south were subducted under the North American plate (Atwater, 1970; Riddihough, 1984). The Pacific plate spreads to the west and the Juan de Fuca plate spreads to the east where it subducts beneath the continental North American plate. The two ridges are separated by the 360 kilometer long Blanco transform fault. The Juan de Fuca ridge and the northern Gorda ridge are both spreading at the half rate of 3 cm/yr. The spreading rate of the southern Gorda ridge gradually decreases to 1 cm/yr at the Mendocino transform fault. There is a hot spot, called Axial Seamount, near the mid-point of the Juan de Fuca ridge.

Topographically, the Juan de Fuca has a 0.5 kilometer high axial peak along most of its length. In some places, a small, shallow axial graben (roughly 1 kilometer wide and 100 meters deep) is seen at the peak. The Gorda ridge has a wide, deep, axial valley (about 15 kilometers wide and 1.5 kilometers deep) along its entire length. Bathymetric profiles of the southern Juan de Fuca and the northern Gorda ridges are shown in Figure 3.

A number of seismic experiments have been conducted on both ridges to determine their seismic velocity structures. Seismic

refraction experiments on the northern JDF, southern JDF, and northern Gorda ridges have shown that, at all three locations, the crustal structure is essentially the same (McClain and Lewis, 1982; Johnson, 1987; Jung, 1988). The seismic velocities and crustal thicknesses are similar to those commonly found in oceanic crust. There is no detectable low velocity zone beneath the axis.

Although a crustal magma chamber may be too small to be resolved by a refraction profile, a small amount of molten material will have a strong attenuating effect on seismic shear waves. Seismic waves crossing the East Pacific Rise are often significantly attenuated (Lewis and Garmany, 1982). However, this effect does not occur on the JDF or Gorda ridges (McClain and Lewis, 1982).

Seismic reflection experiments have also been conducted across and along the Juan de Fuca ridge crest in an effort to find crustal magma chambers. Although a narrow magma chamber reflection has been reported on the southern JDF at a depth of 2.5 kilometers (Morton, 1987), the evidence is ambiguous. Other deep tow reflection profiles have failed to show such reflectors (Denny, 1988).

A glance at a map of seismicity for the region off the west coast of North America shows that the Gorda ridge and the Blanco transform fault are very seismically active while the Juan de Fuca ridge is almost aseismic (Figure 4). OBS experiments designed to measure low level microseismicity over a short period of time also indicate a large difference in seismicity levels. No earthquakes were recorded on the northern JDF over the course of a 7 day

deployment. All the events recorded on the southern JDF over an 8 day period were from the nearby Blanco fracture zone. Seismic shear waves crossing the ridge axis were not attenuated, suggesting the absence of a crustal magma chamber. On the northern Gorda ridge, 40 earthquakes were locatable over a 8 day deployment (Johnson, 1987). They were found in the axial valley at all depths in the 6 km thick crust. No attenuation of seismic energy was observed for waves traveling nearly vertically from the lower crust to the receivers, ruling out a crustal magma chamber. Similar results were obtained on the Gorda ridge by other experiments (Solano-Borrego, 1984; Sverdrup, 1985).

Therefore, the crust at both the Juan de Fuca and the Gorda ridge crests are similar to normal ocean crust in thickness and seismic velocity. Since the crust is formed from liquid magma which has solidified, there will be many thermal contraction cracks formed as the rock cools. Seawater will be able to penetrate the crust and will set up a convecting hydrothermal system (Lister, 1974). This convective heat loss will keep the temperature of most of the crust at 0°C (Lewis, 1983). Any magma dike or intrusion is rapidly cooled (Lister, 1983). Therefore, it seems likely that the cause of the topographic variation between the Juan de Fuca and the Gorda ridges may be found in the upper mantle.
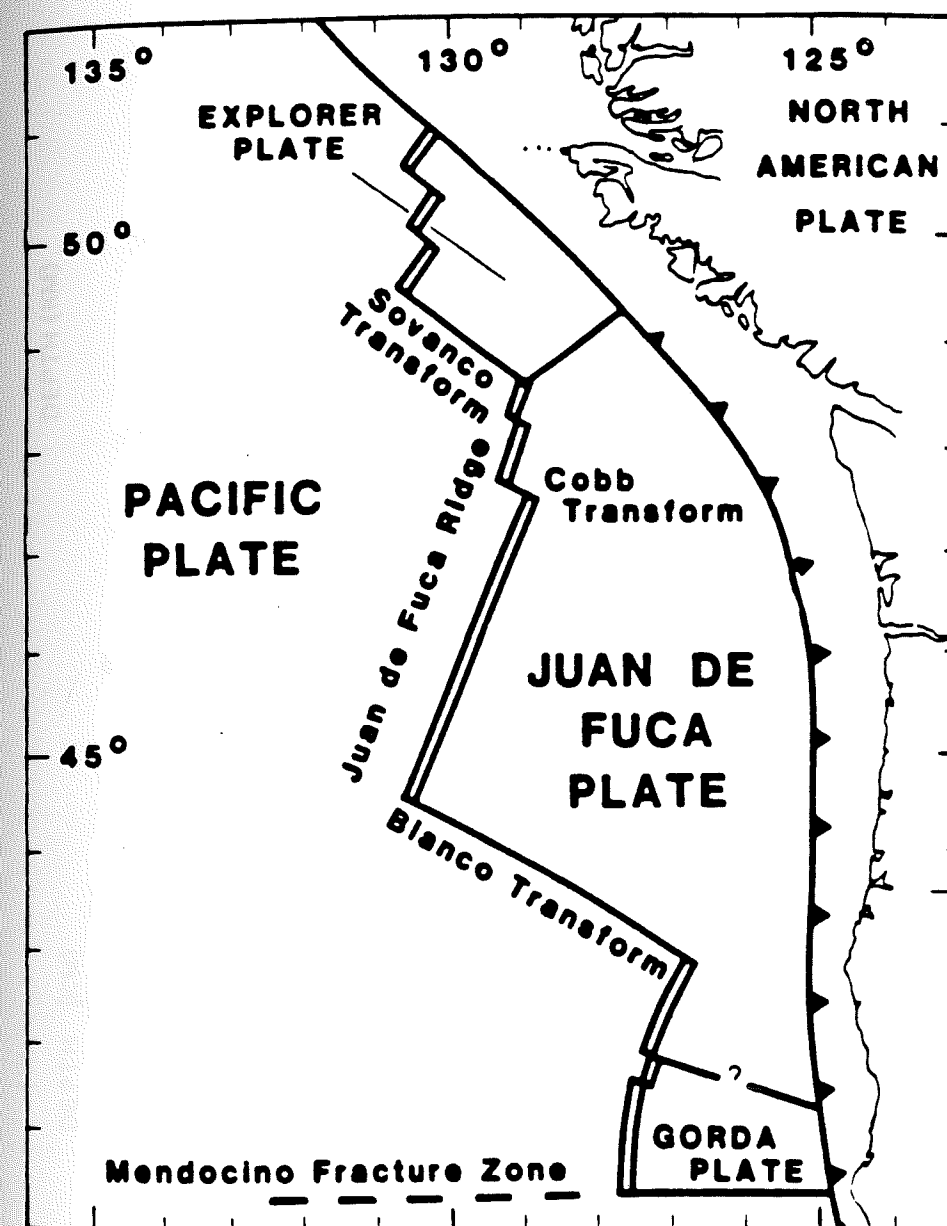
Figure 2. Regional map of spreading ridge system off the west coast of North America (Riddihough, 1984).
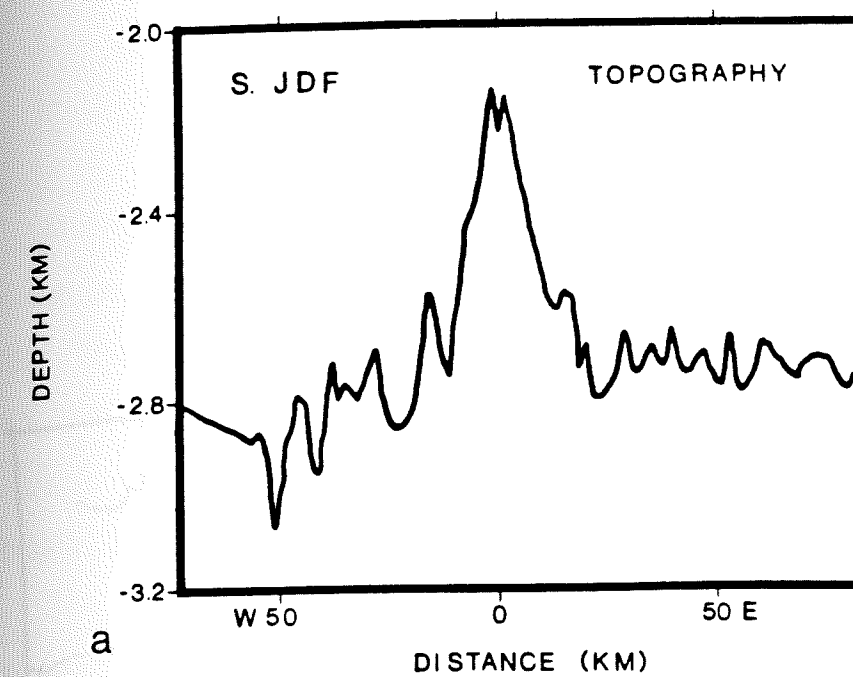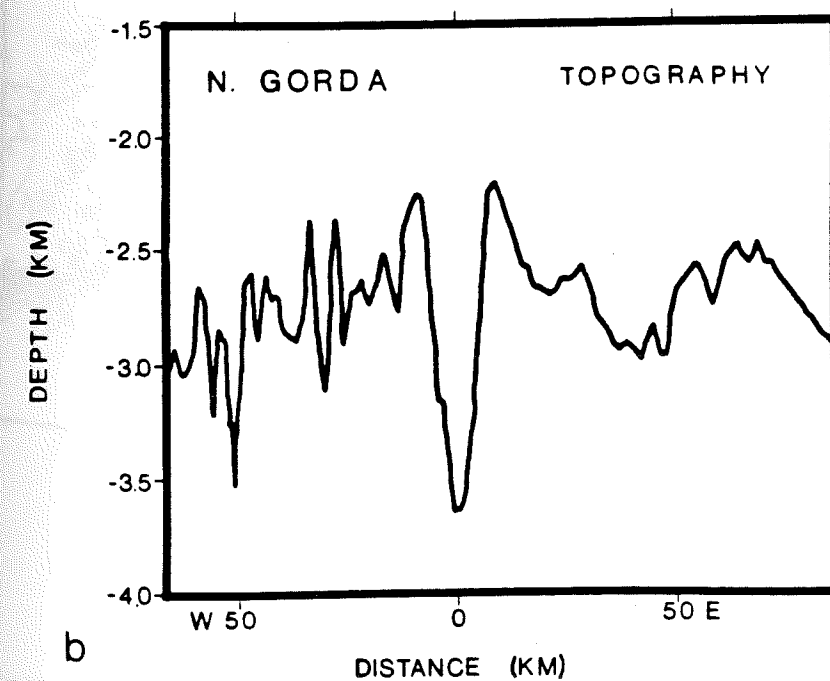
Figure 3. Topographic profiles across a) the Juan de Fuca ridge at 44°50'N and b) the Gorda ridge at 42°30'N.
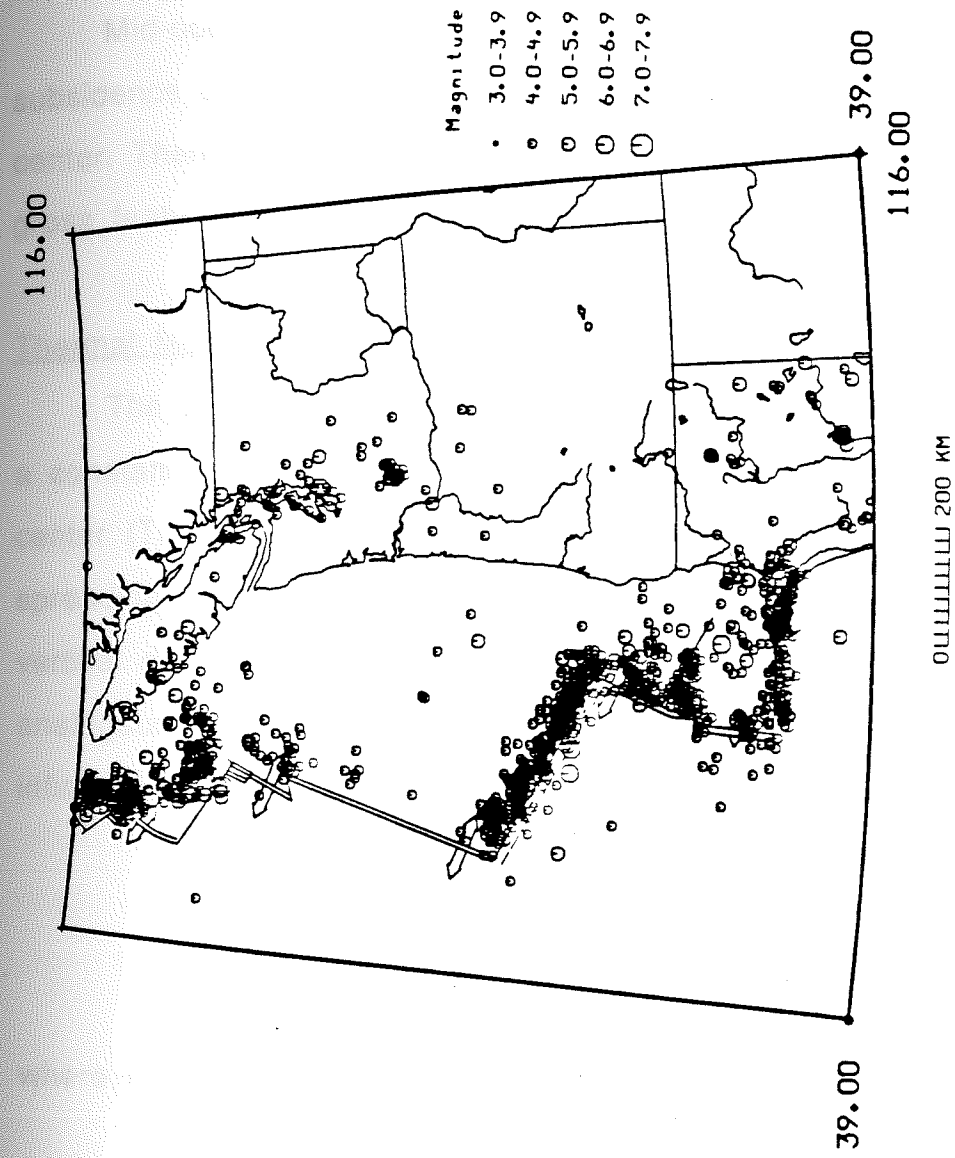
Figure 4.   Pre-1985 seismicity of the spreading ridge system off the west coast of North America (NOAA catalog, magnitudes > 4.0).

Theories about Ridge Crest Topography

Mid-ocean ridges are the result of the thermal contraction and subsidence of the lithosphere as it moves away from the spreading center. There are a number of models put forward to explain the gross features of ocean bottom topography.

Thermal Models

The simplest possible model is that of a column of material at a constant temperature T_m suddenly emplaced at the spreading center (Turcotte and Schubert, 1982). It moves away from the spreading center at a constant velocity u, and loses heat only in the vertical direction. The ocean temperature is 0°C. The solution is analogous to that for the instantaneous heating or cooling of a semi-infinite half-space. The resulting temperature field is

$$T(x,z) = T_m \ \text{erf}\left(\frac{z}{2}\sqrt{\frac{u}{\kappa x}}\right)$$

where the error function is an integral of the Gaussian function,

$$\text{erf}(x) = \frac{2}{\sqrt{\pi}} \int_0^x e^{-x'^2} dx'$$

and κ is the thermal diffusivity. x is the horizontal distance from the ridge axis and z is the depth measured from the ocean bottom. The density field can be calculated from the equation of state

$$\rho(x,z) = \rho_m(1+\alpha(T_m-T(x,z)))$$

where ρ_m is the density of the material at T_m and α is the volumetric coefficient of thermal expansion.

Assuming that the material only contracts vertically, the depth of the ocean floor is

$$h(x) = 2\alpha T_m \sqrt{\frac{\kappa x}{\pi u}}.$$

This is true if there are no oceans, but the deepening of the ocean basins away from the ridge crest means that the water mass load on each column increases with distance from the axis. If T_m is high enough, the material has a viscosity which permits flow at depth. Mass will flow toward the ridge axis in order to establish isostasy. Then the ocean depth becomes

$$h(x) = 2\alpha T_m \frac{\rho_m}{\rho_m-\rho_w} \sqrt{\frac{\kappa x}{\pi u}}$$

where ρ_w is the density of seawater. The ocean floor topography is proportional to the square root of distance or of age, which is distance divided by velocity. This relationship applies over most of

the world's ocean basins. However at about 60 to 80 million years, the ocean floor gets shallower than predicted by the square root of age law (Parsons and Sclater, 1977).

McKenzie (1967) developed a model with a column of material emplaced at the spreading center at a constant temperature T_m but maintaining, by some unspecified means, a constant bottom boundary temperature T_m at some depth L. The material moves away from the ridge axis at a constant velocity u. There is an analytic solution with horizontal as well as vertical heat conduction;

$$T(x,z) = T_m\left[1 - \frac{z}{L} + \sum_n A_n\sin(n\pi z/L)\exp(-\alpha_n x/L)\right]$$

where

$$A_n = \frac{2(-1)^{n+1}}{n\pi}, \quad \alpha_n = R-\sqrt{R^2-n^2\pi^2}, \quad \text{and} \quad R = \frac{uL}{2\kappa}.$$

The density field can now be calculated from the temperatures in the same way as before. Assuming isostasy at depth L, the topography can be calculated by keeping the mass load in each column constant as it moves away from the ridge axis. Now the topography approaches a limiting depth with age. However, near the ridge axis the topography is essentially unchanged.

A major problem with both these models is that heat flow is infinite at the ridge axis where material at $T=T_m$ comes in contact

with seawater at T=0°C. Davis and Lister (1974) modified the McKenzie model by specifying the local thermal balance condition

$$uT(0,z) - \kappa \frac{\partial T(0,z)}{\partial x} = uT_m$$

as the ridge axis boundary condition instead of $T=T_m$. This represents the intermittent propagation of magma through the cold boundary layer at the axis. The only change in the solution is that

$$A_n = \frac{2(-1)^{n+1}}{n\pi(1-\alpha_n/2R)}$$

The isotherms no longer converge at the surface. Although the heat flow is now more realistic, the topography again remains almost unchanged.

A different method uses a solid-liquid phase boundary as the bottom of the lithosphere and takes the latent heat of fusion into account in the heat budget (Parker and Oldenburg, 1973; Oldenburg, 1975). However, the temperature field and the topography are very close to the Davis and Lister model (Pearson and Lister, 1979).

Dynamic Models

The thermal models provide a good explanation for the age-dependent variation in ocean floor depth but they break down within a few kilometers of the ridge axis. As stated earlier, mid-ocean spreading center topography can vary greatly at the ridge axis. A

theory known as steady state necking was presented by Tapponnier and Francheteau (1978) to account for axial valleys on slow spreading ridges. They argued that the thin layer of mechanical strength at the ridge axis is the most important factor controlling axial morphology. This layer undergoes horizontal extension and vertical contraction by normal faulting in the cold brittle part of the layer near the surface and by viscous flow in the warmer, ductile part at depth. If the process is steady-state, the thickness of the layer is maintained by volcanic eruptions at the ocean floor and conductive cooling at depth.

One problem with the previous models is that the material must be flowing vertically not horizontally under the ridge axis. Another possible explanation for the variation in topography at the ridge crest is the response of the surface to the dynamics of fluid flow--i.e. the viscous head loss theory (Sleep, 1969). The upwelling material will have a higher temperature and lower density than the surrounding material. The buoyancy force acting on this material pushing it up will be opposed by a viscous drag force. Lachenbruch (1973) has derived this force balance for a model in which fluid flows up a narrow conduit and accretes to the walls at the same rate as the spreading velocity V. Assuming a uniform and incompressible fluid in the conduit, the horizontal and vertical velocities and the pressures are

$$u(x,z) = \frac{V}{2a^3} \, x(3a^2 - x^2)$$

$$w(x,z) = \frac{3(a^2-x^2)}{2a^3} V(H-z)$$

and

$$P(x,z) = \rho_L gH - \rho gz + \frac{3\mu V}{2a^3}\left[z(z-2H)+a^2-x^2\right]$$

where ρ_L is the density of the lithosphere, H is the thickness of the lithosphere, a is the half-width of the conduit, ρ is the fluid density, and μ is the fluid viscosity. x is the horizontal distance from the center of the conduit and z is the vertical distance from the bottom of the conduit. The pressure at x=a and z=0 is set equal to the lithostatic pressure of the H kilometer thick lithosphere. The total normal stress on the top of the conduit (z=H) is the sum of the deviatoric vertical stress and the pressure.

$$2\mu\frac{\partial w}{\partial z} - P(x,H) = -\frac{9\mu V}{2a^3}(a^2-x^2) - \rho_L gH + \rho gH + \frac{3\mu VH^2}{2a^3}$$

The normal stress can be converted to the pressure of the topography supportable in seawater with

$$2\mu\frac{\partial w}{\partial z} - P(x,H) = -(\rho-\rho_w)gh(x)$$

so that

$$h(x) = \frac{\rho_L - \rho}{\rho - \rho_w} H - \frac{3\mu V}{2a^3(\rho - \rho_w)g}\left[H^2 - 3(a^2 - x^2)\right]$$

The first term is the isostatic level the fluid would rise to without viscous forces. The second term is the drop of the conduit surface due to viscous drag. It is proportional to the fluid viscosity, the spreading velocity, and the dimensions of the conduit. Since faster spreading ridges don't have deeper axial valleys, spreading velocity alone cannot be the controlling factor. It is reasonable to suppose that viscosity variations could be responsible for axial topography. Then, if the other parameters remain the same, the viscous drag of a high viscosity fluid would depress the surface further than that of a low viscosity fluid.

Let us assume that the conduit is 10 kilometers wide and 20 kilometers deep and the spreading rate is 3 cm/yr. Let the density of the lithosphere be 3.45 g/cm^3 and the fluid density be 3.3 g/cm^3. If the fluid has a viscosity of 10^{20} poise, then

$$h(x) = 1.3 - 2.02 + 0.25[1-(x/5)^2]$$

There will be a 10 kilometer wide, 720 meter deep axial valley with a 250 meter bulge in the center. However, if the viscosity is 10^{19} poise, the viscous drag is only one tenth of the amount in the previous case and the buoyancy force dominates. Then

$$h(x) = 1.3 - 0.20 + 0.025[1-(x/5)^2]$$

and there will be a 10 kilometer wide, 1100 meter high axial peak with only a 25 meter bulge in the center.

Although axial valleys and axial peaks can be obtained with the narrow conduit model, some unrealistic simplifying assumptions must be made about the physical properties and the flow field at the ridge axis. The chosen dimensions of the conduit result in unrealistic topographic profiles. The reason is that physical properties such as temperature, density, and viscosity vary continuously with position near the ridge axis. To model sea floor topography more accurately, artificial constraints such as a narrow conduit or arbitrary assumptions of uniform fluid velocity should be avoided. Therefore, numerical rather than analytical solutions should be found.

Numerical Modeling of Viscous Flow

Many attempts have been made to model viscous flow in the mantle using numerical methods. A wide variety of different thermal models, rheologies, driving forces, and boundary conditions have been considered by different investigators. Most modelers have used two-dimensional, rectangular boxes of varying dimensions to model incompressible, steady-state, viscous flow in the mantle. Some model whole mantle convection while others assume layered convection and only model the upper mantle. The conceptually simpler finite difference method has been used more often than the more complex finite element method (Torrance, 1979). However, an important advantage of the finite element method is that the elements can vary in size. This makes it possible to concentrate grid points in areas of interest or areas where parameters change rapidly with position.

Torrance and Turcotte (1971) used a finite difference technique to model Newtonian flow in a 700 kilometer deep, surface driven layer with a temperature of 1420°K at the top and 2100°K at the bottom. They did not include the lithosphere because of its high viscosity. Andrews (1972) studied viscous flow with a 1000 km X 340 km grid. Three layers were specified--an 80 kilometer thick, high viscosity lithosphere, an 80 kilometer thick, low viscosity asthenosphere, and a 180 kilometer thick mesosphere. The mass and

momentum equations were rewritten in terms of a stream function and solved by the finite difference method. McKenzie et al. (1974) performed a similar study on a 700 kilometer thick layer but used a constant viscosity.

Using the same numerical method as Andrews, Houston and De Bremaecker (1975) considered a 2000 kilometer wide, 700 kilometer thick layer with a Newtonian temperature and pressure dependent viscosity and a specified heat flow at the bottom boundary. Later, De Bremaecker (1977) used a variable grid spacing and assumed isostasy at the bottom of the grid to calculate surface topography for Newtonian and non-Newtonian viscosity. He found a 0.7 kilometer deep, 30 kilometer wide median valley at the axis.

Parmentier et al. (1976) used a non-Newtonian strain rate dependent rheology which was independent of temperature and pressure to study convection in a closed cell with rigid isothermal top and bottom boundaries. Using the finite difference method with a stream function formulation, they concluded that the temperature and pressure dependence of viscosity was more important than the strain rate dependence in determining flow structure. Parmentier and Turcotte (1978) studied flow beneath a rigid accreting lithosphere which thickens as the square root of age and moves at a specified velocity. The bottom of the plate is the 1000°C isotherm where the viscosity is 10^{22} poise. They found that the motion of the lithosphere determines the mantle flow pattern. The calculated topography is a function of the thermal contraction of the lithosphere proportional to the square root of age and the flow

induced pressure variations at the base of the lithosphere. A narrow 1.5 kilometer deep depression appears at the ridge axis which deepens with increasing plate velocity.

Kopitzke (1979) used the finite element method with a stream function formulation to model a convection cell heated within and from below. A Newtonian rheology with a maximum viscosity of 4 X 10^{25} poise was specified. Flow in a shallow cell was compared to flow in a deep cell. Zones of weakness had to be introduced by viscosity reductions in the top 100-150 kilometers at the spreading center and at the subduction zone. Schmeling and Jacoby (1981) compared Newtonian and non-Newtonian rheologies with a finite difference stream function formulation in a 700 kilometer deep layer. They also had to introduce zones of weakness at the spreading center and the subduction zone by specifying a yield stress of 500 bars.

All these studies modeled an entire convection cell in order to find viscous flow rates and patterns given various rheological laws and thermal conditions. Sleep and Rosendahl (1979) focused on modeling flow in the vicinity of the spreading center in order to predict axial topography given a spreading rate. They used a finite difference stream function formulation to model a slow spreading ridge (1 cm/yr), a fast spreading ridge (8 cm/yr), and a hot spot ridge (3 cm/yr). The spreading velocity was imposed as a boundary condition.

The viscosity structure was based on a spreading rate dependent thermal model which included the latent heat of fusion of

magma (Sleep, 1975). The effect of hydrothermal circulation is ignored. Four viscosity regions are distinguished: lithosphere, asthenosphere, crustal magma chamber, and axial intrusion zone. The lithosphere is given a temperature and pressure dependent Newtonian viscosity with an upper limit of 10^{23} poise. The asthenosphere is assigned a viscosity of 10^{20} poise. A crustal magma chamber is given a viscosity of 10^{20} poise for the slow spreading ridge and a viscosity of 10^{17} or 10^{18} poise for the fast spreading and hot spot ridges. The magma chamber is at a depth of 4 kilometers and is only 1 kilometer wide at the slow spreading ridge. At the fast spreading ridge, it is only 1 kilometer deep widening to 20 kilometers wide at the Moho. A narrow, 1-2 kilometer wide, axial intrusion zone is introduced above the magma chamber in the lithosphere. On some fast spreading and hot spot ridge models, the axial intrusion zone was assigned the same viscosity as the magma chamber. In other models, a viscoplastic rheology was used. A viscoplastic material behaves as a viscous fluid if the strain rate is such that the shear stress is less than a yield stress. If the strain rate would result in a shear stress higher than the yield stress, the material will yield plastically. On fast spreading ridges, yield stresses of 9 and 30 bars were used while on slow spreading ridges yield stresses of 180 and 240 bars were used. Axial valleys of the right shape and scale were produced for slow spreading ridges but the models for fast spreading ridges had curious side lobes and did not resemble the topographic profiles seen at such ridges.

The Finite Element Method

The momentum equations governing viscous flow are very simple. The only forces are pressure gradients, viscous forces, and gravity. The inertial terms in the momentum equations are dropped because they are negligible when the velocity is small and the viscosity is high. Also, according to the Boussinesq approximation, the compressibility of the fluid can be ignored if it undergoes "small" pressure changes. This will be true if its vertical motion is less than the scale height of the material. For the upper mantle the scale height is about 6500 km, so the conservation of mass equation becomes

$$\frac{\partial u}{\partial x} + \frac{\partial w}{\partial z} = 0$$

where u is velocity in the horizontal (x) direction and w is velocity in the vertical (z) direction. Density is retained in the momentum equations however. The momentum equations are

$$\frac{\partial P}{\partial x} = \frac{\partial \tau_{xx}}{\partial x} + \frac{\partial \tau_{xz}}{\partial z}$$

and

$$\frac{\partial P}{\partial z} = \frac{\partial \tau_{xz}}{\partial x} + \frac{\partial \tau_{zz}}{\partial z} + \rho g$$

where P is pressure, ρ is density, and the τ_{ij}'s are deviatoric stresses. The stresses are given by

$$\tau_{ij} = 2\mu'\varepsilon_{ij}$$

where μ is viscosity and the strain rates are

$$\varepsilon_{ij} = \frac{1}{2}\left(\frac{\partial u_i}{\partial x_j} + \frac{\partial u_j}{\partial x_i}\right)$$

There are three unknowns to be solved for: the pressure and the two components of velocity.

The equations will be solved by the Galerkin finite element method (Juhlin, 1983). The finite elements are triangles consisting of six points, three at the vertices of the triangle and three at the midpoints of each side. The value of a variable u anywhere in the element S is approximated by a number of linearly-independent basis functions $\phi_j(x)$ where

$$u(x) = \sum_1^N u_j\phi_j(x)$$

If the differential equation to be solved is F(u(x))=f(x), and if the basis functions are used to approximate u(x), the error is

$$E_N = F\left(\sum_1^N u_j\phi_j\right) - f(x)$$

If the approximation was perfect the error would be zero. Since the error is the unparameterized part of the solution, the error should be orthogonal to each basis function integrated over the element.

$$\int_S \phi_i E_N da = 0 \qquad \text{for } i=1,2,...,N$$

This is known as the Galerkin method. Using the Galerkin method on the mass and the momentum equations, the final integral equations have no derivatives of the pressure basis functions and only first derivatives of the velocity basis functions. Therefore, the pressure basis functions are linear, there are 3 of them, and the pressure is calculated only at the three vertices of the triangular element. The velocity basis functions are quadratic, there are 6 of them, and the velocities are calculated at all six points of the triangular element.

On each boundary, the normal velocity or the normal stress and the tangential velocity or the shear stress must be fixed. The normal stress, if specified, is the sum of the pressure and the deviatoric normal stress.

The solution of the finite element program consists of a velocity field, a pressure field, a strain rate field, a stress field, and a final viscosity field if the rheology is not Newtonian. The

$$E_N = F\left(\sum_1^N u_j\phi_j\right) - f(x)$$

If the approximation was perfect the error would be zero. Since the error is the unparameterized part of the solution, the error should be orthogonal to each basis function integrated over the element.

$$\int_S \phi_i E_N da = 0 \qquad \text{for } i=1,2,...,N$$

This is known as the Galerkin method. Using the Galerkin method on the mass and the momentum equations, the final integral equations have no derivatives of the pressure basis functions and only first derivatives of the velocity basis functions. Therefore, the pressure basis functions are linear, there are 3 of them, and the pressure is calculated only at the three vertices of the triangular element. The velocity basis functions are quadratic, there are 6 of them, and the velocities are calculated at all six points of the triangular element.

On each boundary, the normal velocity or the normal stress and the tangential velocity or the shear stress must be fixed. The normal stress, if specified, is the sum of the pressure and the deviatoric normal stress.

The solution of the finite element program consists of a velocity field, a pressure field, a strain rate field, a stress field, and a final viscosity field if the rheology is not Newtonian. The

pressure field now reflects the thermal effects of contraction and subsidence and the dynamic forces responsible for the motion of the fluid. The sum of the pressure and the normal stress at the top of the grid can be easily transformed into sea floor topography h(x), using

$$\tau_{zz}(x,L) - P(x,L) = -\rho_w g d - (\rho_m - \rho_w) g h(x)$$

where d is the ocean depth at the ridge axis, ρ_w is the density of seawater, and ρ_m is the mantle density (Parmentier and Forsyth, 1985). The right hand side is simply the hydrostatic pressure of the ocean and the topography on the top of the grid.

As an example, the solution for the narrow conduit model has been obtained numerically. A constant density of 3.3 g/cm^3 and a constant viscosity of 10^{20} poise were specified in the conduit. The density of the lithosphere was chosen to be 3.45 g/cm^3. The conduit was 8 kilometers wide and 16 kilometers deep. Only the right half of the conduit was modeled since symmetric spreading was assumed. The grid points were half a kilometer apart in the horizontal direction and two kilometers apart in the vertical direction. Therefore, there were 81 points and 32 elements (Figure 5a). The velocity boundary conditions were zero normal velocity on the left side (the axis) and the top and 3 cm/yr normal velocity and zero tangential velocity on the right side. The normal stress was specified on the bottom boundary and zero tangential stresses were specified on the top, bottom and left sides.

The numerical results correspond closely to the analytic solution in the appendix to Lachenbruch (1973). Figure 5b shows the velocity field and Figure 6 shows the topography from both the analytic and the numerical solutions. The expected axial valley is 1.5 kilometers deep at the edge of the conduit shallowing to 1.0 kilometers deep at the axis. This shape is a result of using this particular conduit geometry.

The ability of the finite element program to handle a varying viscosity field can be demonstrated with a solution for Couette flow. A viscous fluid is constrained to move only in the horizontal direction by two rigid plates 1 kilometer apart. The bottom boundary is stationary, (u=0,w=0), and the top plate moves horizontally at u=3 cm/yr (w=0). If there are no pressure or density gradients in the fluid, the equation to be solved is

$$\frac{d}{dz}\left(\mu \ \frac{du}{dz}\right) = 0$$

If μ is a constant, u is simply the linear function u=3z. If μ is a function of 1/z, the solution is a quadratic function of z. Since the basis functions for velocity (u,w) are quadratic, the solution should be exact.

Let the viscosity field be described by

$$\mu(z) = \frac{10^{18}}{9z+1}$$

Then the velocity field should be

$$u(z) = \frac{6}{11}\left(\frac{9}{2} z^2 + z\right)$$

A finite element solution was obtained for a 1 kilometer square grid with 32 elements and 81 points. The points were 0.125 kilometers apart in both directions. The accuracy of the results are demonstrated in Table 1.
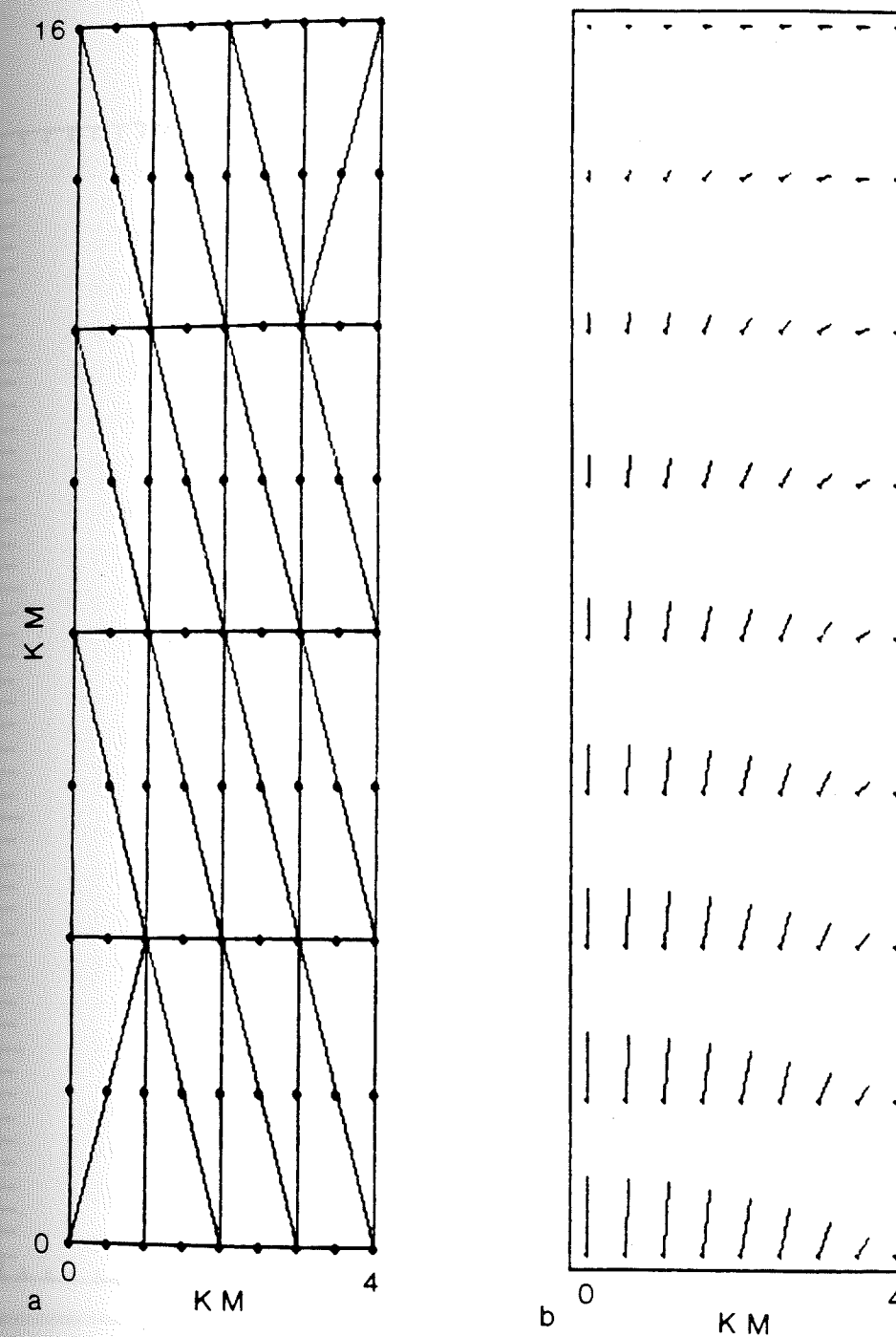
Figure 5. a) Finite element grid for one side of a narrow conduit of dimensions 8 km wide by 16 km deep. b) Velocity field for narrow conduit model spreading at 3 cm/yr with a density of 3.3 g/cm^3 and a viscosity of 10^{20} poise.
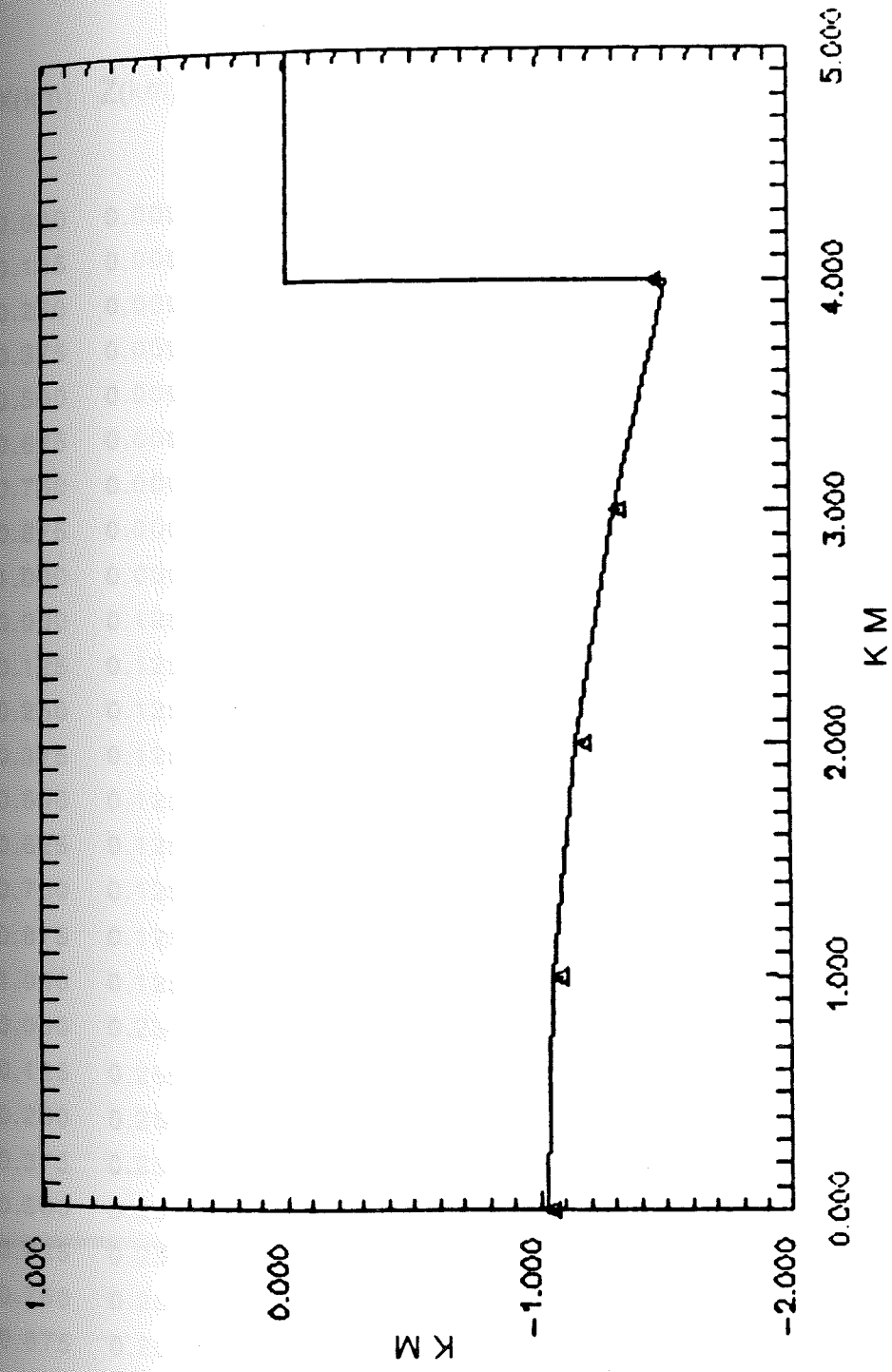
Figure 6. Topography (km) for velocity field in Figure 5 from
analytic equation (solid line) and numerical solution (triangles).

Table 1

Finite Element Solution for Couette Flow with a Viscosity Gradient

X(km)	Z(km)	Viscosity(P)	u(cm/yr)	Finite Element Solution u(cm/yr)	w(cm/yr)
0.000	0.000	1.000E+18	0.000000000	0.000000000	0.000000000
0.125	0.000	1.000E+18	0.000000000	0.000000000	0.000000000
0.250	0.000	1.000E+18	0.000000000	0.000000000	0.000000000
0.375	0.000	1.000E+18	0.000000000	0.000000000	0.000000000
0.500	0.000	1.000E+18	0.000000000	0.000000000	0.000000000
0.625	0.000	1.000E+18	0.000000000	0.000000000	0.000000000
0.750	0.000	1.000E+18	0.000000000	0.000000000	0.000000000
0.875	0.000	1.000E+18	0.000000000	0.000000000	0.000000000
1.000	0.000	1.000E+18	0.000000000	0.000000000	0.000000000
0.000	0.125	4.706E+17	0.106534091	0.106535682	0.000000000
0.125	0.125	4.706E+17	0.106534091	0.106535609	0.000000279
0.250	0.125	4.706E+17	0.106534091	0.106535197	0.000000016
0.375	0.125	4.706E+17	0.106534091	0.106535362	-0.000000064
0.500	0.125	4.706E+17	0.106534091	0.106535391	-0.000000058
0.625	0.125	4.706E+17	0.106534091	0.106535451	-0.000000031
0.750	0.125	4.706E+17	0.106534091	0.106535531	-0.000000035
0.875	0.125	4.706E+17	0.106534091	0.106535608	-0.000000135
1.000	0.125	4.706E+17	0.106534091	0.106535753	0.000000000
0.000	0.250	3.077E+17	0.289772727	0.289775275	0.000000000
0.125	0.250	3.077E+17	0.289772727	0.289775196	0.000000278
0.250	0.250	3.077E+17	0.289772727	0.289775604	0.000000140
0.375	0.250	3.077E+17	0.289772727	0.289775332	-0.000000074
0.500	0.250	3.077E+17	0.289772727	0.289775186	-0.000000079
0.625	0.250	3.077E+17	0.289772727	0.289775279	-0.000000061
0.750	0.250	3.077E+17	0.289772727	0.289775345	-0.000000067
0.875	0.250	3.077E+17	0.289772727	0.289774962	-0.000000230
1.000	0.250	3.077E+17	0.289772727	0.289774027	0.000000000

Table 1 (continued)

Finite Element Solution for Couette Flow with a Viscosity Gradient

X(km)	Z(km)	Viscosity(P)	u(cm/yr)	Finite Element Solution u(cm/yr)	w(cm/yr)
0.000	0.375	2.286E+17	0.549715909	0.549718947	0.000000000
0.125	0.375	2.286E+17	0.549715909	0.549719706	-0.000000251
0.250	0.375	2.286E+17	0.549715909	0.549719997	-0.000000149
0.375	0.375	2.286E+17	0.549715909	0.549720056	-0.000000126
0.500	0.375	2.286E+17	0.549715909	0.549720111	-0.000000087
0.625	0.375	2.286E+17	0.549715909	0.549720175	-0.000000055
0.750	0.375	2.286E+17	0.549715909	0.549720284	-0.000000004
0.875	0.375	2.286E+17	0.549715909	0.549720424	-0.000000058
1.000	0.375	2.286E+17	0.549715909	0.549721164	0.000000000
0.000	0.500	1.818E+17	0.886363636	0.886370559	0.000000000
0.125	0.500	1.818E+17	0.886363636	0.886369540	0.000000138
0.250	0.500	1.818E+17	0.886363636	0.886369333	-0.000000256
0.375	0.500	1.818E+17	0.886363636	0.886369317	-0.000000225
0.500	0.500	1.818E+17	0.886363636	0.886369558	-0.000000176
0.625	0.500	1.818E+17	0.886363636	0.886369486	-0.000000112
0.750	0.500	1.818E+17	0.886363636	0.886369635	-0.000000101
0.875	0.500	1.818E+17	0.886363636	0.886368903	-0.000000201
1.000	0.500	1.818E+17	0.886363636	0.886367753	0.000000000
0.000	0.625	1.509E+17	1.299715909	1.299721570	0.000000000
0.125	0.625	1.509E+17	1.299715909	1.299722270	-0.000000305
0.250	0.625	1.509E+17	1.299715909	1.299722582	-0.000000392
0.375	0.625	1.509E+17	1.299715909	1.299722689	-0.000000425
0.500	0.625	1.509E+17	1.299715909	1.299722848	-0.000000342
0.625	0.625	1.509E+17	1.299715909	1.299722965	-0.000000226
0.750	0.625	1.509E+17	1.299715909	1.299723149	0.000000031
0.875	0.625	1.509E+17	1.299715909	1.299722909	-0.000000041
1.000	0.625	1.509E+17	1.299715909	1.299723447	0.000000000

Table 1 (continued)

Finite Element Solution for Couette Flow with a Viscosity Gradient

X(km)	Z(km)	Viscosity(P)	u(cm/yr)	Finite Element Solution u(cm/yr)	w(cm/yr)
0.000	0.750	1.290E+17	1.789772727	1.789784720	0.000000000
0.125	0.750	1.290E+17	1.789772727	1.789784418	-0.000000596
0.250	0.750	1.290E+17	1.789772727	1.789785171	-0.000000626
0.375	0.750	1.290E+17	1.789772727	1.789784483	-0.000000369
0.500	0.750	1.290E+17	1.789772727	1.789785052	-0.000000577
0.625	0.750	1.290E+17	1.789772727	1.789784808	-0.000000263
0.750	0.750	1.290E+17	1.789772727	1.789786153	-0.000000008
0.875	0.750	1.290E+17	1.789772727	1.789783984	0.000000505
1.000	0.750	1.290E+17	1.789772727	1.789783218	0.000000000
0.000	0.875	1.127E+17	2.356534091	2.356542414	0.000000000
0.125	0.875	1.127E+17	2.356534091	2.356541984	-0.000000523
0.250	0.875	1.127E+17	2.356534091	2.356541725	-0.000000236
0.375	0.875	1.127E+17	2.356534091	2.356541145	-0.000000260
0.500	0.875	1.127E+17	2.356534091	2.356540939	-0.000000392
0.625	0.875	1.127E+17	2.356534091	2.356540626	-0.000000432
0.750	0.875	1.127E+17	2.356534091	2.356539717	-0.000000062
0.875	0.875	1.127E+17	2.356534091	2.356540950	0.000000879
1.000	0.875	1.127E+17	2.356534091	2.356541025	0.000000000
0.000	1.000	1.000E+17	3.000000000	3.000000000	0.000000000
0.125	1.000	1.000E+17	3.000000000	3.000000000	0.000000000
0.250	1.000	1.000E+17	3.000000000	3.000000000	0.000000000
0.375	1.000	1.000E+17	3.000000000	3.000000000	0.000000000
0.500	1.000	1.000E+17	3.000000000	3.000000000	0.000000000
0.625	1.000	1.000E+17	3.000000000	3.000000000	0.000000000
0.750	1.000	1.000E+17	3.000000000	3.000000000	0.000000000
0.875	1.000	1.000E+17	3.000000000	3.000000000	0.000000000
1.000	1.000	1.000E+17	3.000000000	3.000000000	0.000000000

Physical Conditions at the Ridge Axis

A finite element program for 2-dimensional, steady-state, viscous flow will be used to derive the dynamic response of the sea floor (Juhlin, 1983). Time-dependent elastic behavior of the material is not considered. A rectangular mesh of grid points is generated to represent a slab of material of thickness L, on one side of the ridge axis. Symmetric spreading is assumed. The elements are right triangles consisting of six points, three at the vertices of the triangle and three at the midpoints of each side. Figure 7 shows the grid used for a 100 km X 100 km section of the upper mantle below a 5 km thick hydrothermally cooled crust. There are 775 points and 180 elements.

Temperature and Density

The top of the grid represents the ocean floor. Assuming hydrothermal circulation extends to the base of the crust, the temperature is 0°C to a depth of 5 kilometers. A temperature field is specified for the mantle. The Davis and Lister temperature field for a spreading velocity of 3 cm/yr, a diffusivity of 0.0085 cm^2/sec, and a bottom boundary temperature of 1200°C is shown in Figure 8a.

From the temperature field, the density field of the mantle can be calculated as

$$\rho(x,z) = \rho_m(1+\alpha(T_m-T(x,z)))$$

where ρ_m is the density at T_m and α is the coefficient of thermal expansion. Figure 8b shows the density field corresponding to the temperature field in Figure 8a if $\alpha=0.00004$ and $\rho_m=3.3$ g/cm^3. The crust is assumed to have a uniform density of 3.0 g/cm^3.

Isostatic Thermal Topography and Pressure

If it is assumed that all the volume contraction occurs in the vertical direction, a layer of unit thickness at the axis will contract by

$$\frac{\alpha(T(0,z)-T(x,z))}{1+\alpha(T_m-T(x,z))}$$

where $T(0,z)$ is the temperature at the ridge axis. By adding up the contractions of all layers below a point, the subsidence of the point is determined. However, if isostasy is assumed at the bottom boundary, each point must subside further in response to the ocean loading. This additional subsidence is

$$\frac{\rho_w}{\rho_m-\rho_w} h_T(x)$$

where ρ_w is the density of seawater and $h_T(x)$ is the subsidence at the surface due to thermal contraction alone. Total subsidence at the surface is

$$h(x) = \frac{\rho_m}{\rho_m - \rho_w} h_T(x) = \frac{\rho_m}{\rho_m - \rho_w} \int_0^L \frac{\alpha(T(0,z) - T(x,z))}{1 + \alpha(T_m - T(x,z))} dz$$

Now the pressure at each point in the mantle can be calculated as

$$P(x,z) = \rho_w g(d + h(x)) + \rho_c gc + \int_z^L \rho(0,z) g dz$$

where d is the ocean depth at the ridge axis, c is the thickness of the crust and ρ_c is the density of the crust. Figure 9a is a plot of the difference between the pressure at a point and the pressure at the ridge axis at the same level. This horizontal pressure gradient is the ridge push force, one of the tectonic driving forces.

Viscosity

Thermally activated viscous creep processes in solid rock can be linear or non-linear (Turcotte and Schubert, 1982). Diffusion creep is the diffusion of atoms through crystals (Herring-Nabarro creep) or along crystal boundaries (Coble creep). For diffusion creep, strain rate is linearly proportional to stress. The material deforms as a Newtonian fluid and the constant of proportionality is the viscosity. Dislocation creep is the movement of dislocations in a crystal lattice structure. For dislocation creep, the strain rate is

proportional to a power of the stress. The material behaves as a non-Newtonian or power-law fluid. The effective viscosity is stress dependent.

According to experimental results for basalts and peridotites, the strain rate is proportional to the cube of the stress. However, these experiments are performed for strain rates many orders of magnitude higher than strain rates expected in the mantle and the results are extrapolated to lower strain rates. Therefore, it is not known by what mechanism the mantle deforms.

If a stress is imposed on a rock, it will deform according to the flow law that results in the highest strain rate. Alternatively, imposing a strain rate on a rock will cause it to deform according to the flow law resulting in the smallest stress. In Figure 10, Turcotte and Schubert (1982) compare two creep laws for dry olivine, the most common mineral in the mantle.

$$\dot{\varepsilon} = 300\sigma e^{-E/RT} \qquad \dot{\varepsilon} = (4.2 \times 10^5)\, \sigma^3\, e^{-E/RT}$$

where σ is in megapascals (1 MPa=10 bars), $\dot{\varepsilon}$ is in sec^{-1}, E=523 kJ/mole, and R is the ideal gas constant. The first law was obtained from diffusive flow theory with several assumptions made in choosing parameter values. The second law is based on experiments conducted at laboratory strain rates. Power law creep is the preferred process above 0.027 MPa (0.27 bars) while Newtonian flow is preferred below this transition stress. Furthermore, given a

strain rate, a rock will undergo dislocation creep at a low temperature and diffusion creep at a higher temperature.

From theoretical considerations (Turcotte and Schubert, 1982), Newtonian viscosity will be pressure and temperature dependent according to the following equation,

$$\mu = \frac{T}{2B_1} \exp\left(\frac{E^* + PV^*}{RT}\right)$$

where B_1, E^*, V^*, and R are constants (Schubert et al., 1976, 1978). E^* is called the activation energy, V^* is called the activation volume, and R is the ideal gas constant. The values for olivine are B_1=0.0024 cm s °K/g, E^*=95 kcal/mole, and V^*=10 cm^3/mole. As temperature decreases, viscosity increases exponentially. Between 1200°C and 0°C, viscosity increases by over 60 orders of magnitude. The range of viscosities must be limited to prevent matrix singularity problems in the solution algorithm. Therefore all viscosities greater than a cutoff viscosity are set equal to the cutoff viscosity. The cutoff viscosity must be chosen so that regions of high viscosity move as a solid block. Figure 9b is the viscosity field derived from the temperature field in Figure 8a with a cutoff viscosity of 10^{25} poise. The temperature, density, horizontal pressure gradient and Newtonian viscosity fields for T_m=1300°C and T_m=1400°C are displayed in Figures 11-14.

When the rheology is Newtonian (linear), the viscosity depends only on temperature and pressure and the input viscosity field is

used to solve the Galerkin integral equations directly. If the rheology is non-Newtonian (non-linear), the viscosity is also stress dependent

$$\mu = \frac{T}{2B_n} \frac{1}{\Sigma^{n-1}} \exp\left(\frac{E^*+PV^*}{RT}\right)$$

where $\Sigma = \sqrt{\frac{1}{2}\tau_{ij}\tau_{ij}}$ is the stress invariant and n is the power of the power-law fluid (Schubert et al., 1976). For olivine, n=3 and $B_3 = 6.45 \times 10^{-13}$ cm^3 s^5 °K/g^3. The viscosity can be rewritten to be strain rate dependent as

$$\mu = \left[\frac{T}{2B_n} \exp\left(\frac{E^*+PV^*}{RT}\right)\right]^{1/n} \frac{1}{\Pi^{(n-1)/n}}$$

where $\Pi = \sqrt{\frac{1}{2}\dot{\varepsilon}_{ij}\dot{\varepsilon}_{ij}}$ is the strain rate invariant. Now the viscosity is dependent on temperature, pressure, and strain rate. The Newtonian viscosity field is used in the first calculation of the velocity, from which the strain rates are obtained. Then, a new non-Newtonian viscosity field is derived to be used in recalculating the velocity field. The iterations are continued until the viscosity field is stable.

Viscoplasticity, Yield Stress and Shear Failure on Faults

Using a temperature dependent viscosity with the strain rates necessary near the ridge axis can lead to unrealistically high

stresses. This occurs because the temperature is low and the viscosity is large near the surface. A viscoplastic rheology can resolve this problem. A viscoplastic material will behave as a viscous fluid if the stress invariant Σ is less than a yield stress (Sleep and Rosendahl, 1979). Whenever, the strain rate is high enough for Σ to exceed the yield stress, the material undergoes a process which reduces stress. The most likely candidate is brittle fracture at low temperatures and pressures and plastic creep at high temperatures and pressures. This can be incorporated into the algorithm for Newtonian rheology by lowering the viscosity at the positions where Σ exceeds the yield stress. The velocity field is recalculated using the new viscosity field and a new stress field is obtained. If the stress at any position still exceeds the yield stress, the viscosity is again lowered at that point and the process is repeated until all stresses are below the yield stress.

Brace and Kohlstedt (1980) have combined the rheological laws for frictional strength, viscous creep and plastic creep with a continental geotherm to determine which law predominates at any depth. Deviatoric stresses are calculated as a function of depth for each law and the law giving the lowest stress at each depth predominates. Rock which can undergo brittle fracture is assumed to be already faulted, so the Byerlee frictional strength law is presumed to apply.

$$\tau = 0.85 \, \sigma_n \qquad \sigma_n < 2 \text{ kbars}$$

$$\tau = 600 + 0.6\,\sigma_n \qquad \sigma_n > 2 \text{ kbars}$$

where τ is the shear stress and σ_n is the effective normal stress.

$$\sigma_n = s_n - P_P$$

where s_n is the total normal stress and P_P is the pore pressure of water. The equations can be rewritten in terms of the maximum principal effective stress σ_1,

$$\tau = 0.4\,\sigma_1 \qquad \sigma_1 < 5.5 \text{ kbars}$$

$$\tau = 0.34\,\sigma_1 + 340 \qquad \sigma_1 > 5.5 \text{ kbars}$$

If the region is under horizontal deviatoric tension the maximum principal stress is simply the lithostatic pressure. Assuming hydrostatic pore pressure,

$$\sigma_1 = \rho g z - P_P = (\rho - \rho_w) g z$$

If the rock density is 3 g/cm^3, the gradient in σ_1 is 200 bars/km and

$$\tau = 80z \qquad z < 27.5 \text{ km}$$

$$\tau = 68z + 340 \qquad z > 27.5 \text{ km}$$

Brace and Kohlstedt (1980) used a non-Newtonian viscous flow law for olivine at low stresses ($\tau<1$ kbar) and a Dorn plasticity law for olivine at high stresses ($\tau>1$ kbar).

By combining these laws on a stress versus depth plot and choosing the law giving the lowest stress at each depth, one obtains a yield envelope. This method has been used to model continental extension and sedimentary basin formation (Sawyer, 1985; Houseman and England, 1986) and transition depths between brittle and ductile behavior in the Basin and Range region (Smith and Bruhn, 1984).

Since the lithosphere is very thin near the spreading center, only the brittle yield stress for depths of less than 27.5 kilometers will be used. This prevents stresses in the mantle from building up to 1 kilobar, so the Dorn plasticity law is not needed. Therefore, brittle fracture at low temperatures and pressures occurs in the lithosphere and Newtonian or non-Newtonian viscous flow occurs in the asthenosphere. The actual yield stress to be used in the finite element calculations is

$$\tau = 10 \text{ bars} + 80z$$

because, for a yield stress of zero at the ocean bottom, the viscosity would have to be lowered to zero.

The yield stress of the brittle lithosphere cannot be less than 80 bars/km unless the pore pressure of water is greater than hydrostatic pressure or the coefficient of friction in the Byerlee

law is less than 0.85. These possibilities are unlikely to occur at mid-ocean ridges. The pervasive fissuring of the crust near the ridge axis and the existence of hydrothermal circulation make it unlikely that the pore pressure can exceed hydrostatic pressures. The low frictional strength of fault gouge minerals is one of the possible explanations for low shear stresses on the San Andreas fault (Lachenbruch and Sass, 1980). However, the San Andreas fault has been active for several million years and has had several hundred kilometers of cumulative displacement. The normal faults at spreading centers do not have large enough displacements in the short period in which they are active to form a low strength fault zone.

Tectonic Driving Forces and Boundary Conditions

The ridge push force is a gravitational body force due to the horizontal pressure gradient arising from the elevation of the ridge axis relative to older parts of the plate. The horizontal pressure gradient shown in Figure 9a must be opposed by an equal force or else the plate will accelerate. There are a number of locations where the opposing forces can be imposed. Frictional and viscous resistance at transform faults, viscous drag on the bottom of the lithosphere, frictional resistance from the overriding plate at the subduction zone, and viscous drag on the subducting slab can all oppose plate motion.

It is known from intraplate earthquake focal mechanisms, that much of the world's oceanic lithosphere is under deviatoric

horizontal compression (Sykes and Sbar, 1973). Lister (1975) has derived an expression for the buildup of horizontal compressive stress in a cooling and contracting oceanic plate described by

$$T(x,z) = T_m \ erf\left(\frac{z}{2}\sqrt{\frac{u}{\kappa x}}\right).$$

If there are negligible resisting stresses at the transform faults,

$$\frac{\partial F}{\partial x} - \tau \cong \frac{g\rho_m\alpha T_m\kappa}{u}$$

where F is the summed normal force per unit length parallel to the axis on a vertical plane through the lithosphere, and τ is the shear stress on the bottom of the lithosphere. If the shear stress on the bottom of the plate is small, then $\frac{\partial F}{\partial x}$=13.85 bars using T_m=1200°C, ρ_m=3.3 g/cm^3, α=0.00004, κ=0.0085 cm^2/s, and u=3 cm/yr. If the deviatoric stress at the axis is assumed to be zero, $\frac{\partial F}{\partial x}$ can be integrated from the axis to any point on the plate and divided by the thickness of the lithosphere at that point to get the average horizontal compressive stress. At 100 kilometers from the axis the lithosphere is about 15 kilometers thick assuming no hydrothermal cooling, so the horizontal compressive stress will be about 90 bars.

To determine what boundary conditions to use at 100 kilometers, deviatoric stresses were calculated using the finite element program for the T_m=1200°C density field (Figure 8b) and

Newtonian viscosity field (Figure 9b). Shear stresses were set to zero on all boundaries. Horizontal velocity on the left (axis) boundary and vertical velocity on the top boundary were set to zero. The normal stress on the bottom boundary was lithostatic. The normal stress imposed at 100 kilometers was the lithostatic stress in a column under the axis. This stress is enough to oppose the ridge push force and support the ridge. Figure 15a shows the deviatoric tensile stresses at all the points of the grid in Figure 7. The lengths are proportional to the magnitudes. Deviatoric compressive stresses are perpendicular to the tensile stresses. Deviatoric stresses are near zero at the axis building up to about 60 bars of horizontal compressive stress at the right boundary. This is less than the compressive stress derived previously because a 5 kilometer thick, 0°C crust has been added to the top of the mantle.

There is no reason to assume that the stresses at the axis are lithostatic (no deviatoric stresses). Focal mechanisms of earthquakes at ridge crests indicate that horizontal tensile stresses are present (Huang et al., 1986, 1987). If the boundary condition imposed on the right side is changed to the lithostatic stress at 100 kilometers, the tensile stress plot (Figure 15b) shows horizontal deviatoric tension from the axis out to 100 kilometers. Beyond 100 kilometers there would be horizontal deviatoric compression.

There is no reason to suppose that 100 kilometers from the axis is the point where horizontal tensile stresses change to horizontal compressive stresses. There is no way of knowing what normal stresses to impose on the right boundary in the lithosphere.

However, the horizontal velocity of the plate at 100 kilometers from the axis must be the spreading rate and this can be used as a boundary condition.

The boundary conditions to be used can now be stated. Shear stresses are set to zero on the bottom and on the right and left sides. At the left (axis) boundary, the horizontal velocity is set to zero, since symmetric spreading is assumed. Isostasy is assumed at the bottom boundary, so the normal stress is lithostatic. On the right side, lithostatic normal stress can be assumed where the viscosity is low. However, since the state of stress in the lithosphere is unlikely to be lithostatic, a horizontal velocity of 3 cm/yr is imposed where viscosity is high (greater than 10^{25} poise). At the top boundary, the vertical velocity is set to zero. The horizontal velocity is set to 3 cm/yr at first, in order to obtain the strain rates needed to calculate the non-Newtonian and/or viscoplastic viscosity fields. For succeeding iterations, the shear stress at the surface is set to zero. It was observed that after the first iteration, the changes to the viscosity field were negligible, whether a non-Newtonian or a viscoplastic rheology was used. The models presented in the next chapter are the results after the second iteration.
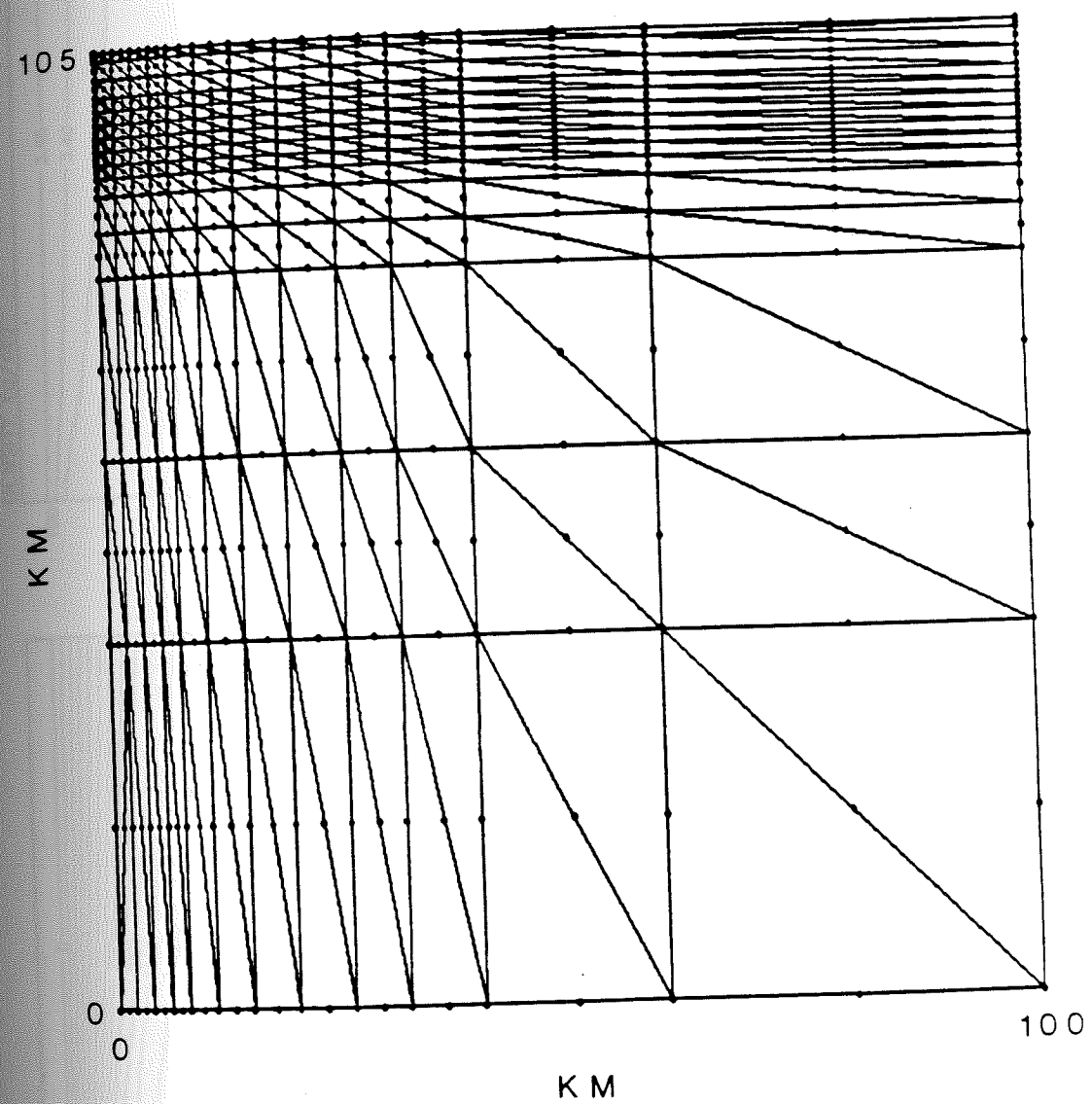
Figure 7. Finite element grid composed of 775 points and 180 elements for a 100 km thick upper mantle and a 5 km thick cooled crustal layer on one side of a ridge axis.
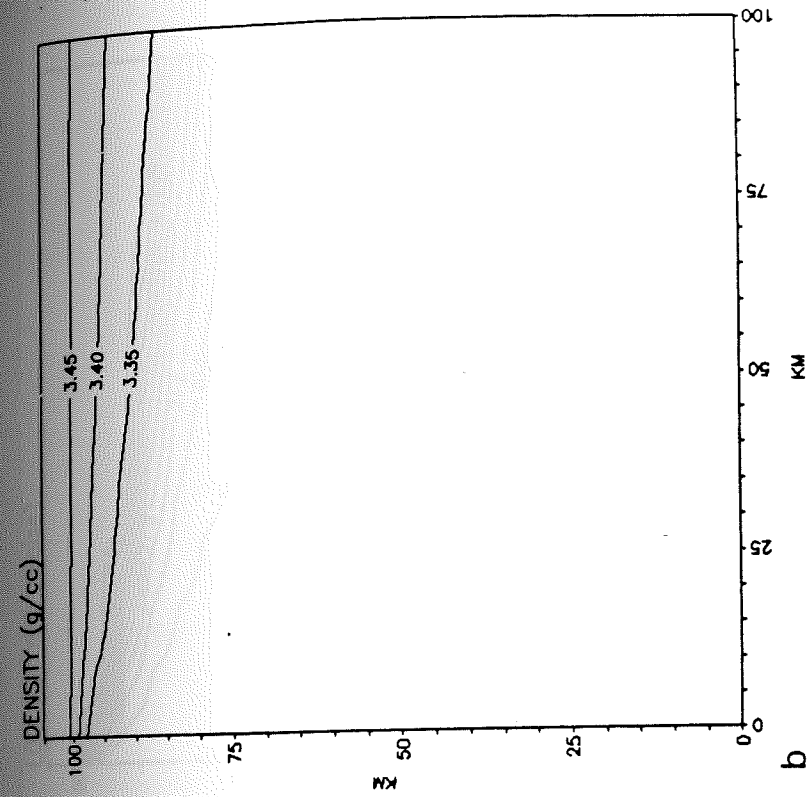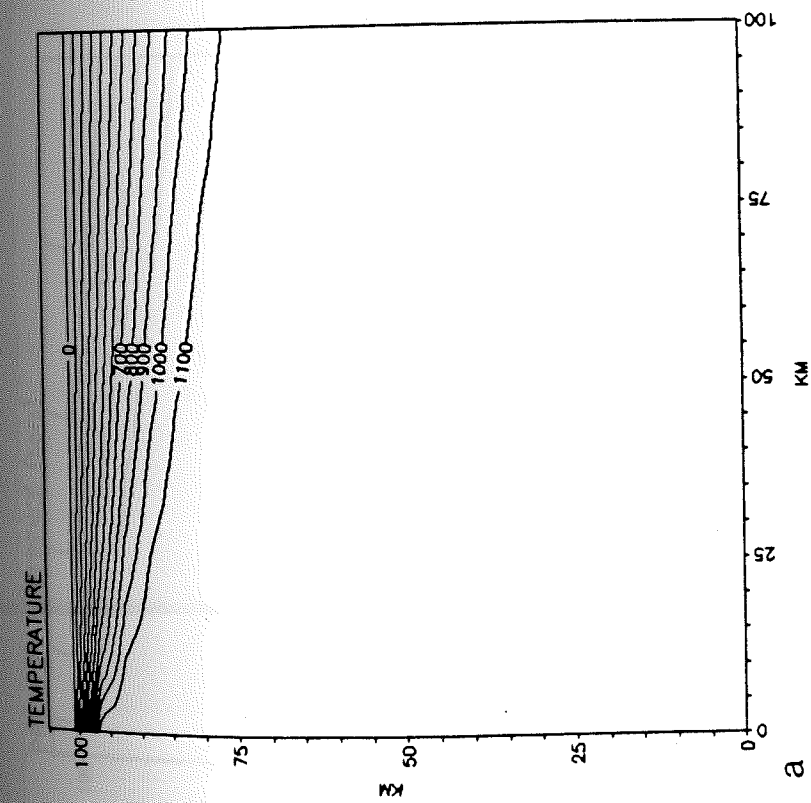
Figure 8. a) Temperature field (°C) for spreading velocity of 3 cm/yr and T_m=1200°C. b) Density field (g/cm³) with coefficient of thermal expansion α=0.00004 and ρ_m=3.3 g/cm³.

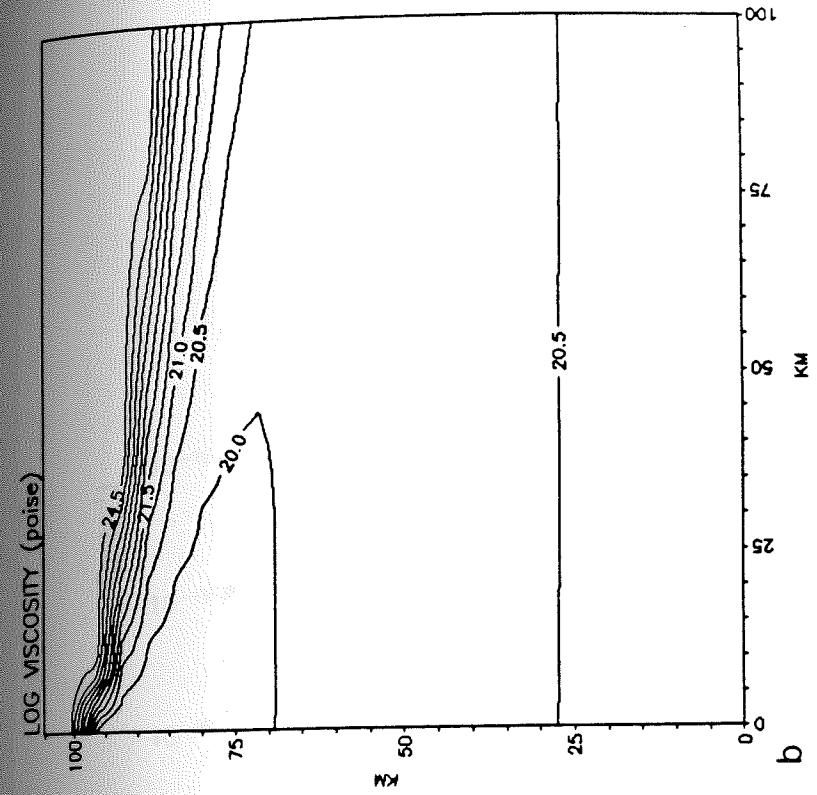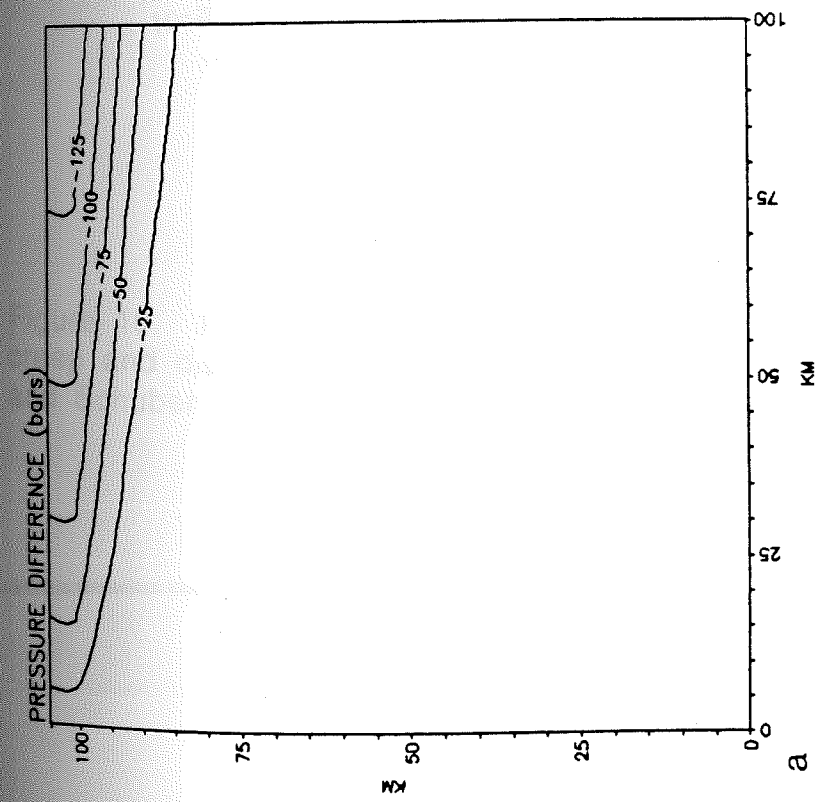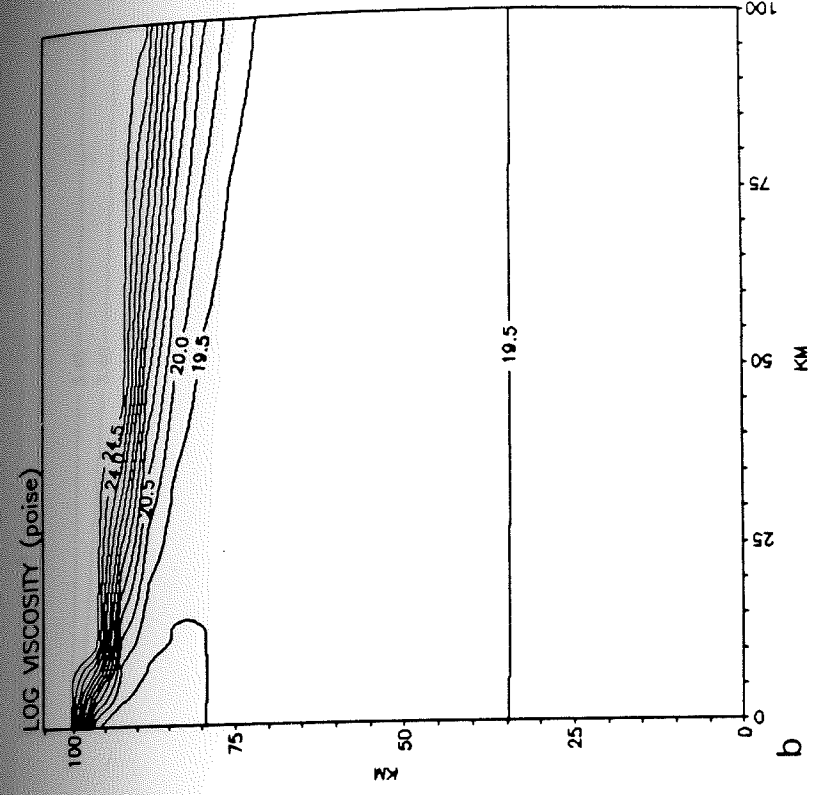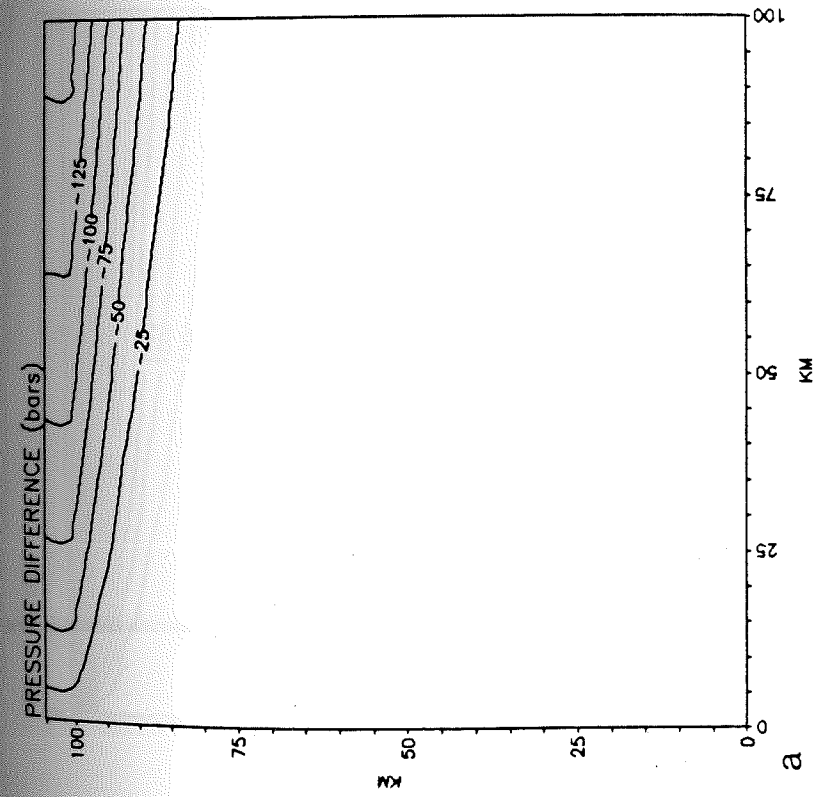Figure 9. a) Horizontal pressure difference (bars) relative to lithostatic pressure at the ridge axis for $T_m = 1200°C$. b) Log of Newtonian viscosity field (poise) with cutoff viscosity of 10^{25} poise.

Figure 10. Relationship between strain rate and stress for diffusion creep and dislocation creep over a range of temperatures (Turcotte and Schubert, 1982).
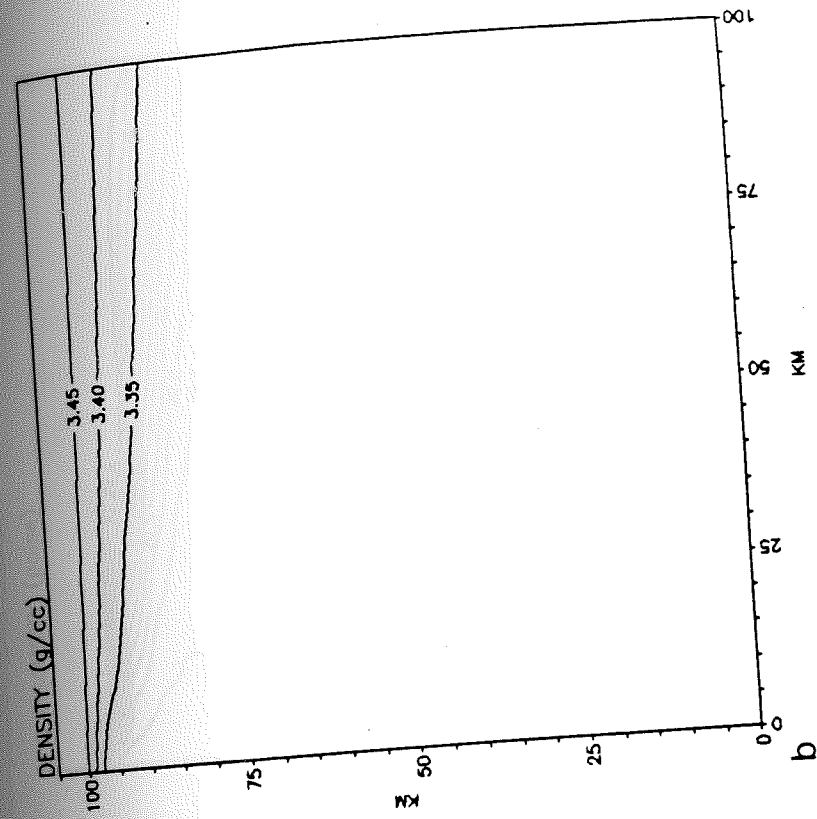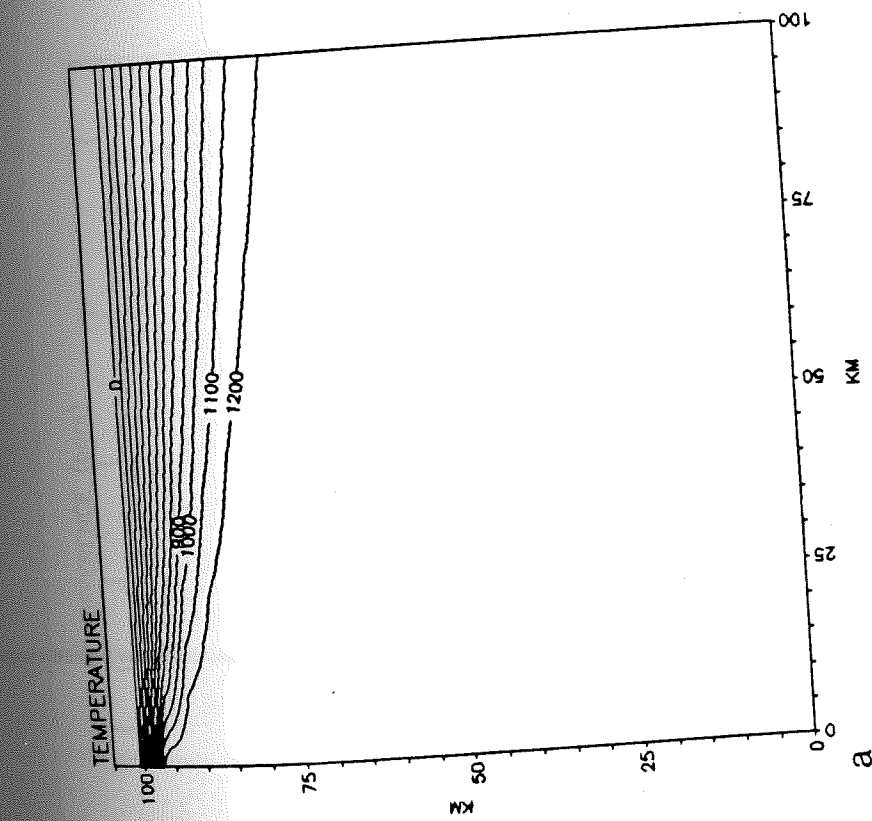
Figure 11. a) Temperature field (°C) for spreading velocity of 3 cm/yr and T_m=1300°C. b) Density field (g/cm³) with coefficient of thermal expansion α=0.00004 and ρ_m=3.3 g/cm³.

Figure 12. a) Horizontal pressure difference (bars) relative to lithostatic pressure at the ridge axis for $T_m = 1300°C$. b) Log of Newtonian viscosity field (poise) with cutoff viscosity of 10^{25} poise.
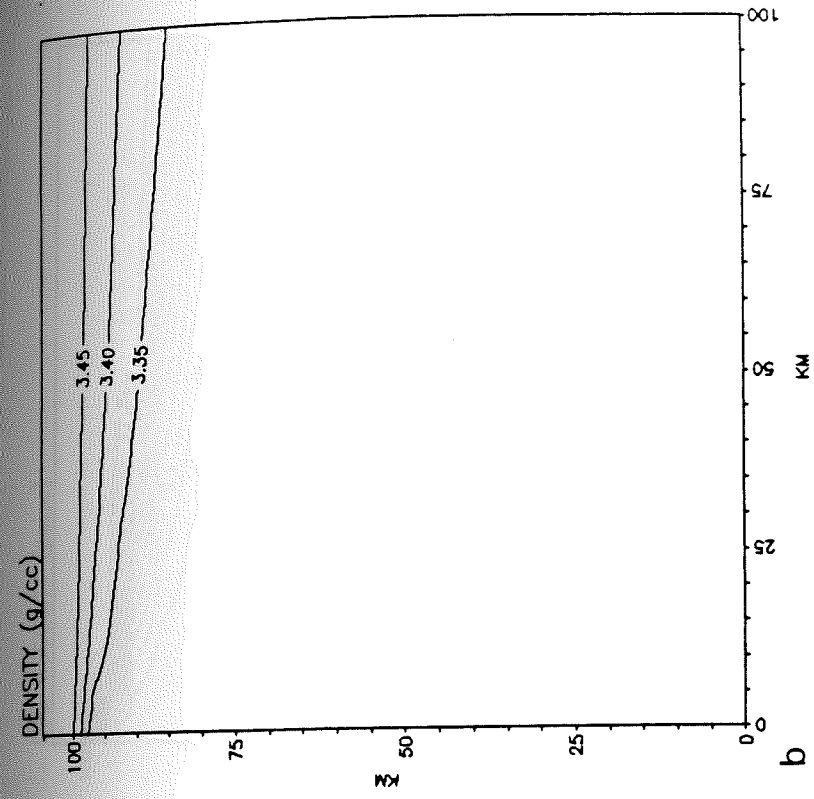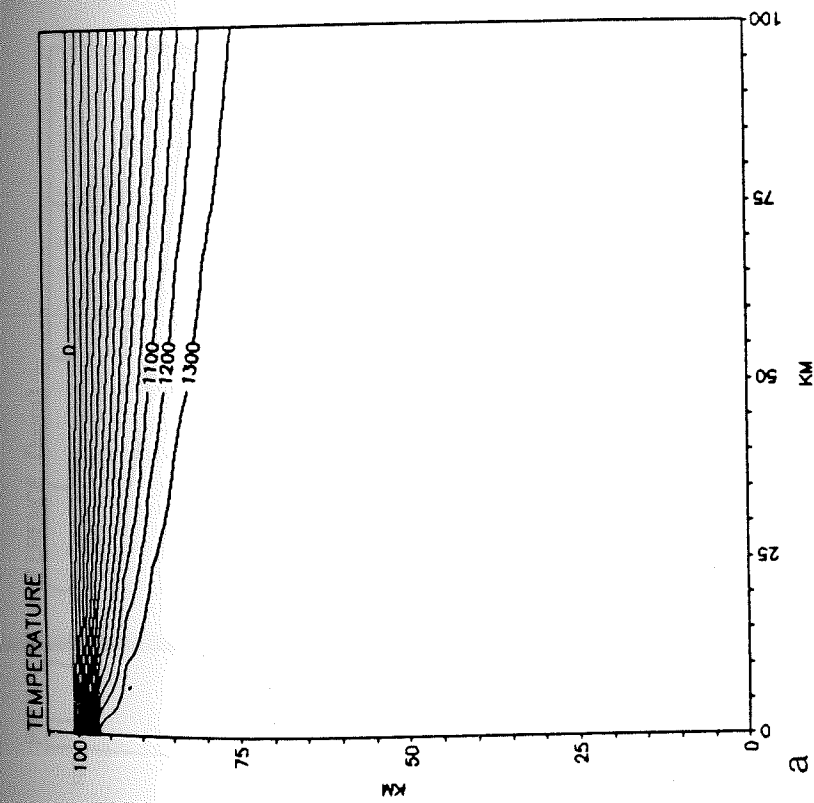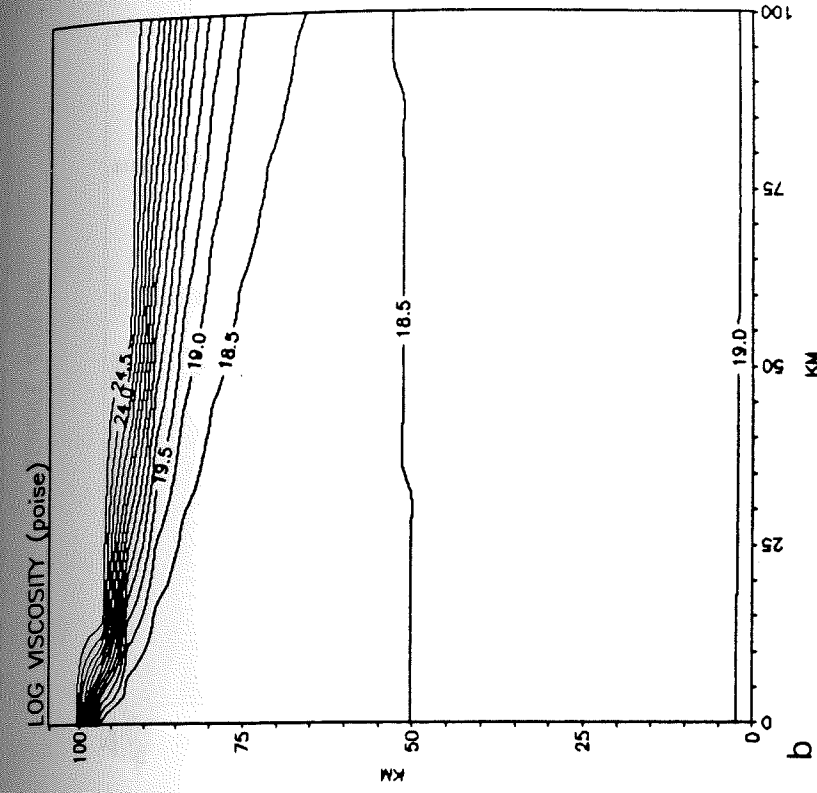
Figure 13. a) Temperature field (°C) for spreading velocity of 3 cm/yr and $T_m=1400°C$. b) Density field (g/cm³) with coefficient of thermal expansion $\alpha=0.00004$ and $\rho_m=3.3$ g/cm³.
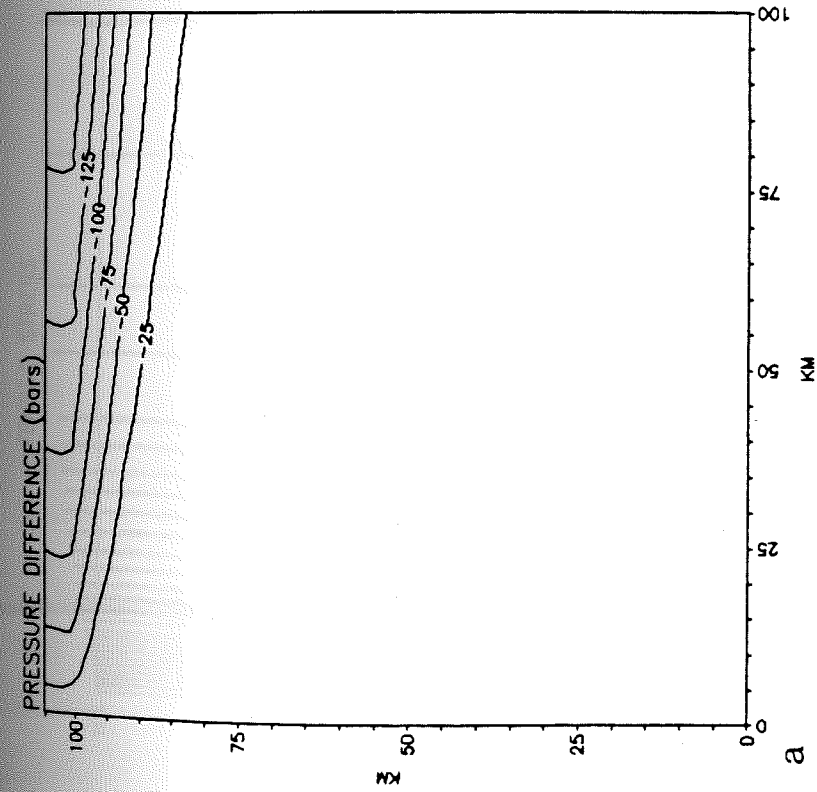
Figure 14. a) Horizontal pressure difference (bars) relative to lithostatic pressure at the ridge axis for $T_m=1400°C$. b) Log of Newtonian viscosity field (poise) with cutoff viscosity of 10^{25} poise.
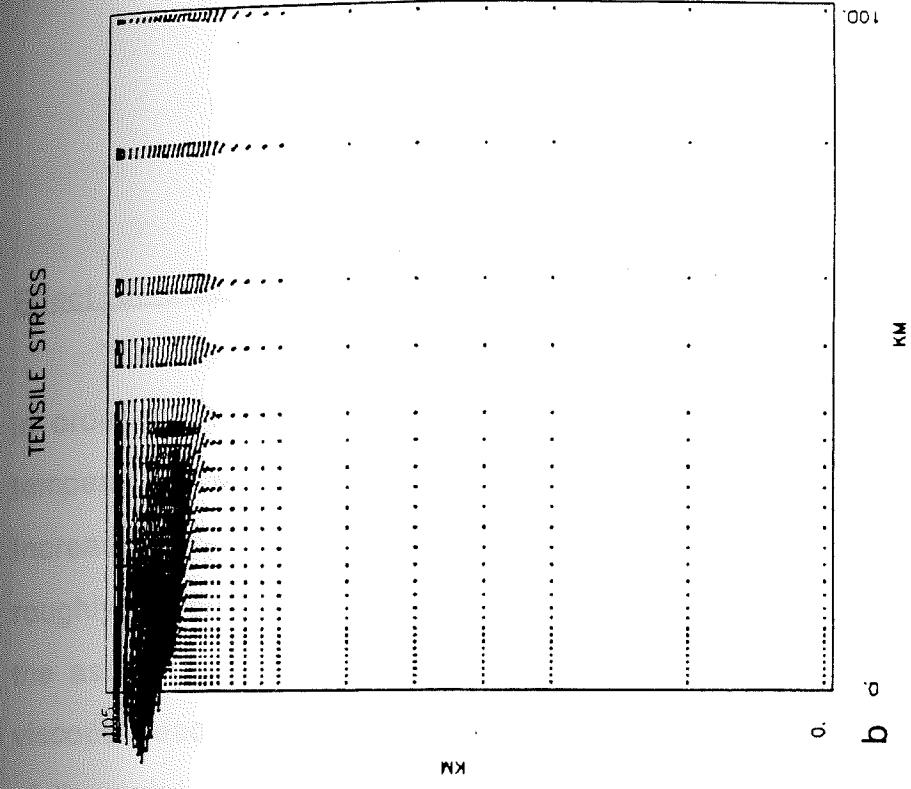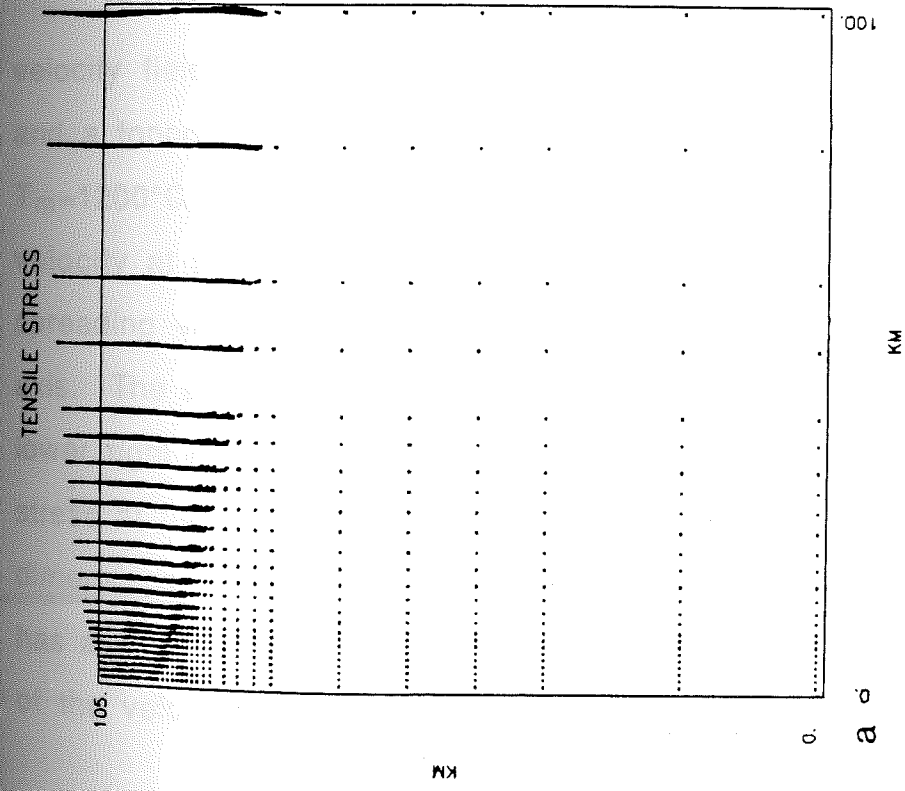
TENSILE STRESS

TENSILE STRESS

Figure 15. Tensile stress fields for $T_m = 1200°C$. a) Axial lithostatic pressure imposed at right boundary. b) Lithostatic pressure at right boundary.

Results of Numerical Modeling

Effect of Asthenospheric Viscosity

The first runs of the finite element program were carried out in order to investigate whether varying T_m, the bottom boundary temperature, could produce both axial peaks and axial valleys. Increasing T_m by 100°C lowers the viscosity of the asthenosphere by roughly an order of magnitude. This will reduce viscous forces in the asthenosphere by an order of magnitude. According to the viscous head loss theory (Sleep, 1969; Lachenbruch, 1973), the depth of the axial valley should be an order of magnitude smaller.

The results of the finite element modeling consist of a velocity field, a stress field, a strain rate field, a viscosity field, and a topographic profile. Figure 16a shows the velocity field for T_m=1200°C with a Newtonian viscosity. At the top, the horizontal velocity at the surface is plotted. The surface approaches the spreading velocity of 3 cm/yr at about 15 kilometers from the ridge axis. The appearance of what resembles a convection cell in the lower right corner is solely a consequence of imposing zero shear stress at the bottom and at the right side and the nearly square dimensions of the box. Since the viscosity is low in that corner it has a minuscule effect on the topography. Figure 16b is a close-up of the velocity field in the top left corner near the ridge axis.

Figure 17a shows the magnitudes and directions of the deviatoric tensile stress at all points. Deviatoric compressive stresses are perpendicular to the tensile stresses and have the same magnitudes. The lithosphere is clearly visible as a thickening surface layer with stress increasing with depth to a maximum at the brittle-ductile transition boundary. Below, in the asthenosphere, stress falls off rapidly to negligible values. The tensile stresses are horizontal all the way to the right boundary at 100 kilometers from the axis. Figure 17b is a close-up of the stress field in the top left corner.

Figure 18a is a contour plot of the logarithm of the strain rate invariant in the upper half of the box. This and the following contour plots have a vertical exaggeration to better display the lithosphere. -14.0 corresponds to a strain rate of 10^{-14} s^{-1}. Figure 18b is a contour plot of the logarithm of the viscosity in poise. Viscosities have been lowered in the lithosphere so the stresses will not exceed the yield stress. The lithosphere behaves as a perfectly plastic fluid rather than as a viscous fluid. The viscosities in the lithosphere have no physical significance since the lithosphere deforms by brittle faulting. Viscosities in the asthenosphere are unchanged.

Figure 19b is a contour plot of the logarithm of the stress invariant in bars. 1.0 corresponds to a stress of 10 bars; 2.0 corresponds to a stress of 100 bars. The band of highly stressed lithosphere is evident. Below, in the asthenosphere, stresses fall below 10 bars.

Figure 19a shows two topographic profiles. The solid line is the isostatic thermal topography derived solely from the temperature field and the assumption of isostasy at the bottom boundary. The triangles are the finite element dynamic topography obtained from

$$\tau_{zz}(x,L) - P(x,L) = - \rho_w g d - (\rho_m - \rho_w) g h(x)$$

using the normal stresses at the surface. The axial valley is 30 kilometers wide and 2 kilometers deep.

The grid used in the finite element calculation has a concentration of points near the surface at the axis. The points were concentrated where the viscosity and density fields vary greatly with position. However, if the grid is still too coarse, the results might be inaccurate. To test whether a finite element grid is fine enough, the number of points are doubled in both directions. If the results obtained with the fine grid are the same as the results from the coarse grid, the coarse grid is adequate to cover the variations of the parameters with position. The number of points of the grid in Figure 7 was doubled in both directions. The parameters for $T_m = 1200°C$ with Newtonian viscosity were used to calculate a solution. The topography from the fine grid (Figure 20a) is the same as the topography from the coarse grid (Figure 19a) so accurate solutions can be obtained with the grid in Figure 7.

The next four figures show the results for $T_m = 1300°C$ with Newtonian viscosity. The velocity field (Figure 21) is very similar

to the velocity field for $T_m=1200°C$. The tensile stresses (Figure 22) are also very similar although the lithosphere is slightly thinner at the right boundary. The contour plot (Figure 24b) shows that the region of highly stressed lithosphere is slightly smaller and thinner. Below, stresses in the asthenosphere fall below 1 bar, an order of magnitude less than for $T_m=1200°C$. The topographic profile (Figure 24a) shows a 30 kilometer wide, 1.8 kilometer deep axial valley. This is only 200 meters shallower than the axial valley for $T_m=1200°C$.

Figures 25-28 display the results for $T_m=1400°C$ with Newtonian viscosity. The velocity fields (Figure 25) are in contrast to those shown previously. The asthenosphere flows faster than the plate velocity. This is because the higher temperature and lower viscosity in the asthenosphere allows it to move in response to the small horizontal pressure gradient in the asthenosphere. However, the tensile stresses (Figure 26) in the lithosphere are quite similar to those for the previous two cases. The stress contour plot (Figure 28b) shows that the plate is slightly thinner at 100 kilometers and its bottom boundary is slightly flatter than before. The topographic profile (Figure 28a) shows a 30 kilometer wide, 1.5 kilometer deep axial valley which is only 300 meters shallower than for $T_m=1300°C$.

These results show that lowering the asthenospheric viscosity by an order of magnitude does not reduce the depth of the axial valley by a comparable factor. This contradicts the viscous head loss theory for ridge axis topography (Lachenbruch, 1973). By

looking at the tensile stress plots, it can be seen that the stresses in the upwelling asthenosphere are several orders of magnitude smaller than the stresses in the lithosphere. Viscous forces in the asthenosphere make a negligible contribution to ridge crest topography.

This conclusion is in agreement with Phipps Morgan et al. (1987) who derived temperature fields for realistic upwelling velocity fields. They found no thermal structure that resembled the narrow conduit postulated for the viscous head loss model. In fact, the temperature fields they derived were not substantially different from the temperature fields obtained using the simplifying assumption of uniform horizontal velocity (McKenzie, 1967; Parker and Oldenburg, 1973; Davis and Lister, 1974)

The tensile stress fields support the steady state necking theory for ridge crest topography (Tapponnier and Francheteau, 1978). The axial valley is produced by the horizontally tensile stresses in the brittle lithosphere. Isostasy imposed at the bottom boundary and zero shear stress imposed at both sides, require that the ridge be in overall isostatic equilibrium. The depth of the axial valley below the thermal topography is compensated by uplift of the shoulders on either side of the axis as seen in the topographic profiles (Figures 19a, 24a, and 28a).

Another result of Phipps Morgan et al. (1987) is useful in interpreting the topographic variation as a function of T_m. They calculated the shape of the upper surface of a perfectly plastic plate of constant thickness with an indentation of Gaussian shape on the

bottom. The amplitude of the indentation was small compared to the plate thickness. The strength of the plate was considered to be proportional to its thickness. The results show that the amplitude of the topography is proportional to both the strength of the plate and the amplitude of the Gaussian indentation on the bottom boundary.

Although the bottom boundary of the lithosphere does not have a Gaussian shape and its variation is not small compared to the plate thickness, the physical situation is analogous to the idealized solution of Phipps Morgan et al. (1987). The thickness of the lithosphere at the axis does not change significantly between $T_m=1200°C$ and $T_m=1400°C$. Therefore, the strength of the lithosphere is almost unchanged. However, the isotherms for $T_m=1400°C$ are flatter than the isotherms for $T_m=1200°C$. The lithosphere thickens less rapidly with distance for $T_m=1400°C$--i.e. the "indentation" is smaller. There is slightly less stress concentration at the axis and therefore the axial valley is slightly shallower. If the isotherms were completely flat there would be no stress concentration at the axis and there would be no axial valley.

Non-Newtonian Rheology

The next step is to investigate the effect of using non-Newtonian rather than Newtonian rheology. Figure 29 shows the non-Newtonian viscosity for $T_m=1200°C$ before the viscoplastic yield stresses are imposed. Since non-Newtonian viscosity for n=3 is inversely proportional to the square of the stress invariant, the

viscosities are lowered in regions of high stress. The effect is to slightly thin the lithosphere and to make the bottom boundary slightly flatter. The reason it doesn't have a greater effect is because of the dominance of the temperature term in the exponential. Figures 30-33 show the results for a non-Newtonian rheology with T_m=1200°C. The velocity fields are very similar to those shown before for Newtonian rheology. The tensile stresses (Figure 31) show that the lithosphere is slightly thinner and the bottom boundary doesn't deepen as rapidly with age as before. The topography has a 30 kilometer wide, 1.4 kilometer deep axial valley.

Figure 34 shows the non-Newtonian viscosity field for T_m=1300°C before the depth-dependent yield stresses were imposed. Figures 35-38 show the results. Once again they are very similar to the results for Newtonian rheology. The axial valley is 30 kilometers wide and 1.1 kilometers deep.

Figure 39 shows the non-Newtonian viscosity field for T_m=1400°C before the viscoplastic yield stresses were imposed. Notice that the viscosities in the asthenosphere are not as low as those for Newtonian rheology at T_m=1400°C. The velocity field (Figure 40) does not show the asthenosphere moving faster than the lithosphere as in Figure 25. The rest of the results (Figures 41-43) are very similar to the previous results. The axial valley is 30 kilometers wide and 1.0 kilometer deep.

Using non-Newtonian rheology results in axial valleys that are substantially shallower than those obtained using Newtonian rheology at the same T_m. Non-Newtonian viscosities for a given

pressure and temperature can be several orders of magnitude less than Newtonian viscosities because they are inversely proportional to the square of the stress. This makes the bottom of the lithosphere flatter and, consequently, the axial valley is shallower. However, the temperature term in the exponential limits the amount that the stress squared in the denominator can affect the shape of the bottom of the lithosphere. Therefore, the depth of the axial valley is still greater than a kilometer.

Thinning the Brittle Layer

Since the strength of the brittle layer is depth-dependent, thinning the layer might be expected to make the axial valley substantially shallower by reducing the total frictional force on normal faults at the axis. Halving the thickness of the layer would reduce the tensile stress integrated over depth to a fourth of its previous value. In all the subsequent models to be shown, the hydrothermally cooled layer is completely removed. A new grid with 725 points and 168 elements is introduced (Figure 44).

The temperature, density and horizontal pressure gradient fields used are the same as those shown previously (Figures 8, 9, and 11-14), but without the top five kilometers. The viscosity field is slightly different because the pressure term in the exponential is smaller without the 5 kilometer thick layer. However, this has very little effect on the viscosity fields, which are almost indistinguishable from those shown in Figures 9, 12, and 14. At the axis the temperature increases rapidly from 0°C to T_m. Therefore

the brittle-ductile transition is only 1.0-1.5 kilometers deep at the axis.

Figures 45-48 show the results for T_m=1300°C with Newtonian rheology. The horizontal surface velocity approaches 3 cm/yr at a distance of 5 kilometers from the axis. The tensile stress plot shows that the tensile stress is horizontal out to a distance of 80 kilometers from the axis. The brittle layer is extremely thin at the axis. The topography shows a 12 kilometer wide, 1.1 kilometer deep axial valley.

The number of points was doubled in both directions for the grid in Figure 44 to test whether it was fine enough to give accurate results. The solution was calculated for T_m=1300°C with Newtonian viscosity. The topography from the fine grid (Figure 20b) is very close to the topography from the coarse grid (Figure 48a). Therefore the grid in Figure 44 can be used to obtain accurate solutions.

The results for T_m=1400°C with Newtonian viscosity are shown in Figures 49-52. Again, viscosity is low enough in the asthenosphere to permit it to flow faster than the lithosphere. The tensile stresses are horizontal out to a distance of 40 kilometers from the axis where the deviatoric stress is small. Beyond 40 kilometers, the tensile stress becomes vertical and the compressional stress is horizontal. This is seen in Figure 52b where a region of low deviatoric stress in the lithosphere separates regions of horizontal tension towards the axis and horizontal compression away from the axis. The axial valley is 8 kilometers wide and 0.7 kilometers deep.

the brittle-ductile transition is only 1.0-1.5 kilometers deep at the axis.

Figures 45-48 show the results for T_m=1300°C with Newtonian rheology. The horizontal surface velocity approaches 3 cm/yr at a distance of 5 kilometers from the axis. The tensile stress plot shows that the tensile stress is horizontal out to a distance of 80 kilometers from the axis. The brittle layer is extremely thin at the axis. The topography shows a 12 kilometer wide, 1.1 kilometer deep axial valley.

The number of points was doubled in both directions for the grid in Figure 44 to test whether it was fine enough to give accurate results. The solution was calculated for T_m=1300°C with Newtonian viscosity. The topography from the fine grid (Figure 20b) is very close to the topography from the coarse grid (Figure 48a). Therefore the grid in Figure 44 can be used to obtain accurate solutions.

The results for T_m=1400°C with Newtonian viscosity are shown in Figures 49-52. Again, viscosity is low enough in the asthenosphere to permit it to flow faster than the lithosphere. The tensile stresses are horizontal out to a distance of 40 kilometers from the axis where the deviatoric stress is small. Beyond 40 kilometers, the tensile stress becomes vertical and the compressional stress is horizontal. This is seen in Figure 52b where a region of low deviatoric stress in the lithosphere separates regions of horizontal tension towards the axis and horizontal compression away from the axis. The axial valley is 8 kilometers wide and 0.7 kilometers deep.

Non-Newtonian rheology was also used for models without a cooled layer at the axis. Figure 53 shows the viscosity field for T_m=1300°C before the viscoplastic yield stresses were imposed. The results are shown in Figures 54-57. The velocity approaches 3 cm/yr at 4 kilometers from the axis. The axial valley is 12 kilometers wide and 0.8 kilometers deep.

Figure 58 shows the non-Newtonian viscosity field for T_m=1400°C before the yield stresses were imposed. The results are shown in Figures 59-62. The stresses are horizontally tensile out to 40 kilometers from the axis. Beyond 40 kilometers, they are horizontally compressive. The axial valley is 8 kilometers wide and 0.5 kilometers deep.

These results indicate that the depth and the width of the axial valley are significantly reduced when the hydrothermally cooled layer is removed. This is because the brittle layer at the axis is thinned from about 6 to 7 kilometers to 1 to 1.5 kilometers. Since the yield stress is depth-dependent, the strength of the brittle layer is much reduced. However, the axial valleys are still several hundred meters deep. The reason is that the lithosphere still thickens at the same rate as the plate moves away from the axis. Without the 5 kilometer thick cooled layer, the bottom boundary is much closer to the surface near the axis. This leads to a greater concentration of stress near the axis, which tends to narrow and deepen the axial valley. This effect partially offsets the effect of the strength reduction caused by the thinner brittle layer at the axis.
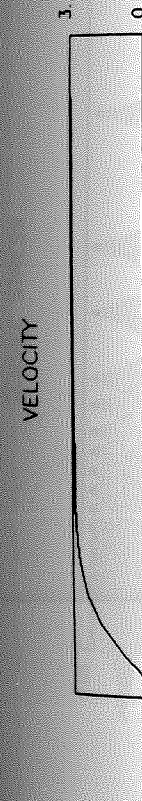
Non-Newtonian rheology was also used for models without a cooled layer at the axis. Figure 53 shows the viscosity field for $T_m = 1300°C$ before the viscoplastic yield stresses were imposed. The results are shown in Figures 54-57. The velocity approaches 3 cm/yr at 4 kilometers from the axis. The axial valley is 12 kilometers wide and 0.8 kilometers deep.

Figure 58 shows the non-Newtonian viscosity field for $T_m = 1400°C$ before the yield stresses were imposed. The results are shown in Figures 59-62. The stresses are horizontally tensile out to 40 kilometers from the axis. Beyond 40 kilometers, they are horizontally compressive. The axial valley is 8 kilometers wide and 0.5 kilometers deep.

These results indicate that the depth and the width of the axial valley are significantly reduced when the hydrothermally cooled layer is removed. This is because the brittle layer at the axis is thinned from about 6 to 7 kilometers to 1 to 1.5 kilometers. Since the yield stress is depth-dependent, the strength of the brittle layer is much reduced. However, the axial valleys are still several hundred meters deep. The reason is that the lithosphere still thickens at the same rate as the plate moves away from the axis. Without the 5 kilometer thick cooled layer, the bottom boundary is much closer to the surface near the axis. This leads to a greater concentration of stress near the axis, which tends to narrow and deepen the axial valley. This effect partially offsets the effect of the strength reduction caused by the thinner brittle layer at the axis.

VELOCITY

VELOCITY

KM

KM

KM

KM

b

a

69
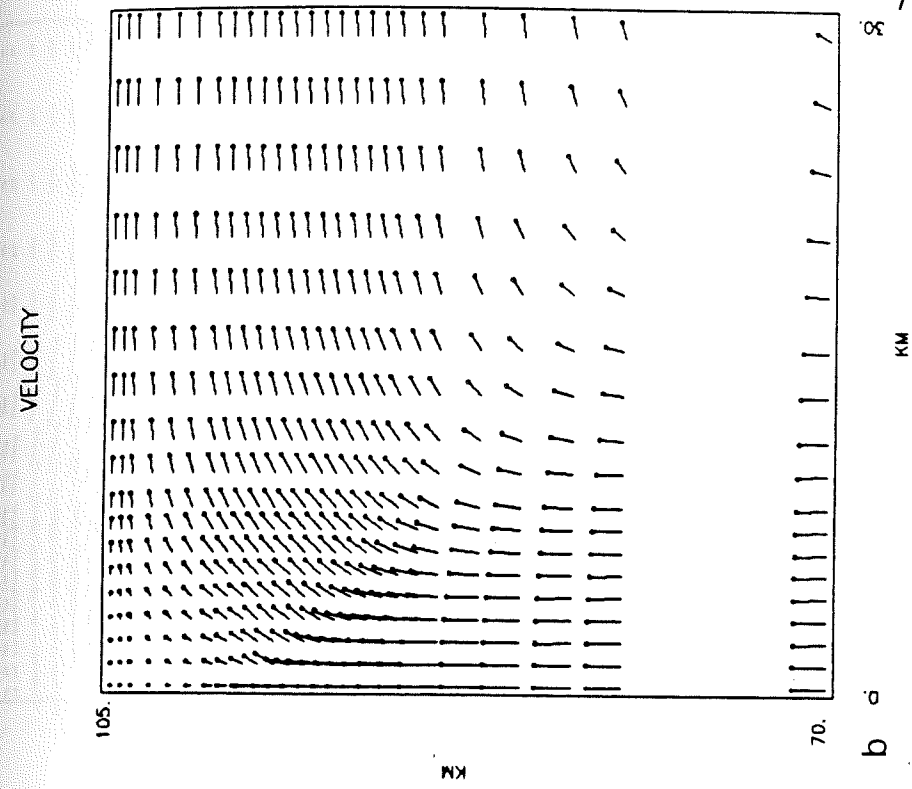
Figure 16.   Velocity field for $T_m=1200°C$ with Newtonian rheology
and a cooled crustal layer.
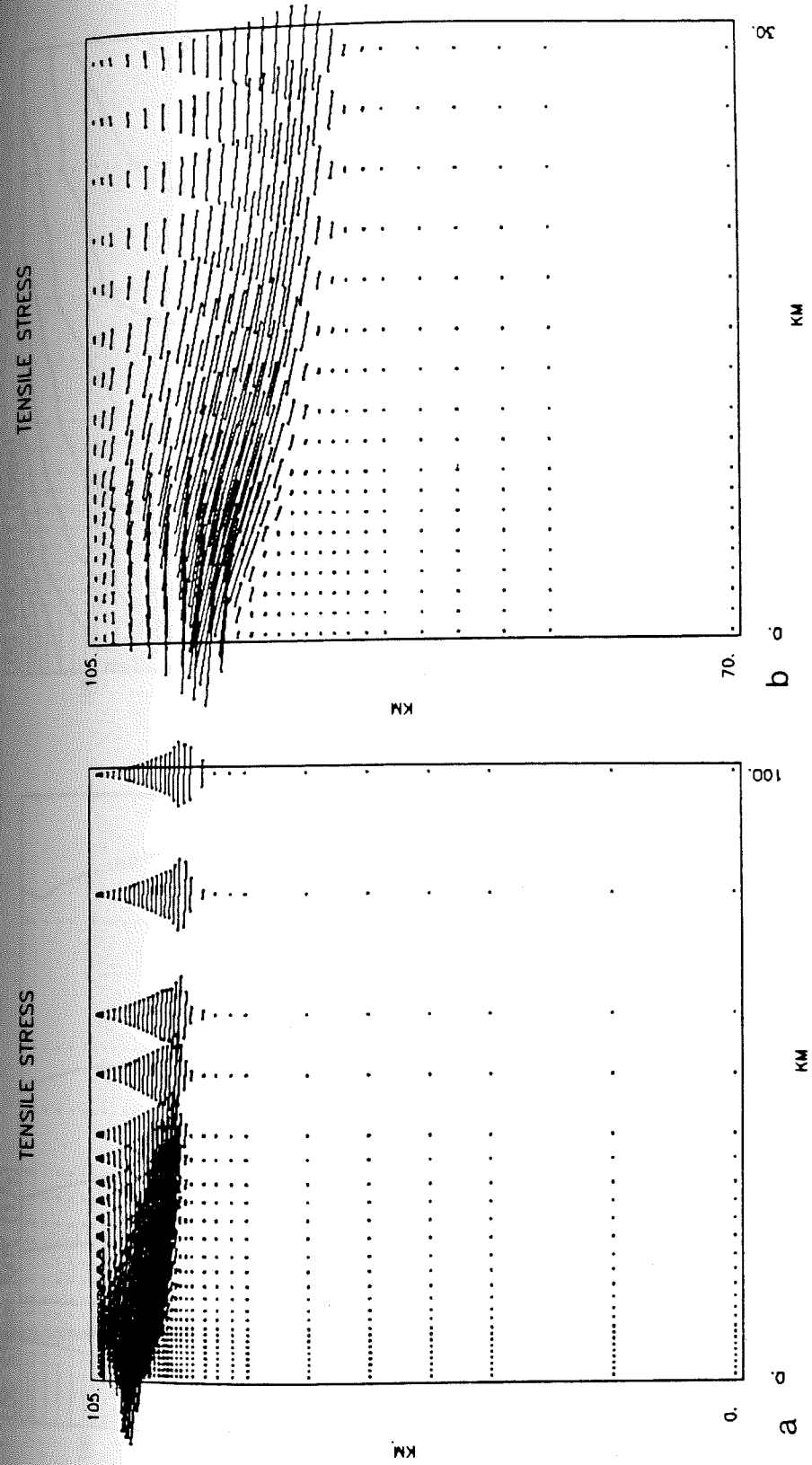
TENSILE STRESS

TENSILE STRESS

KM

KM

KM

KM

a

b
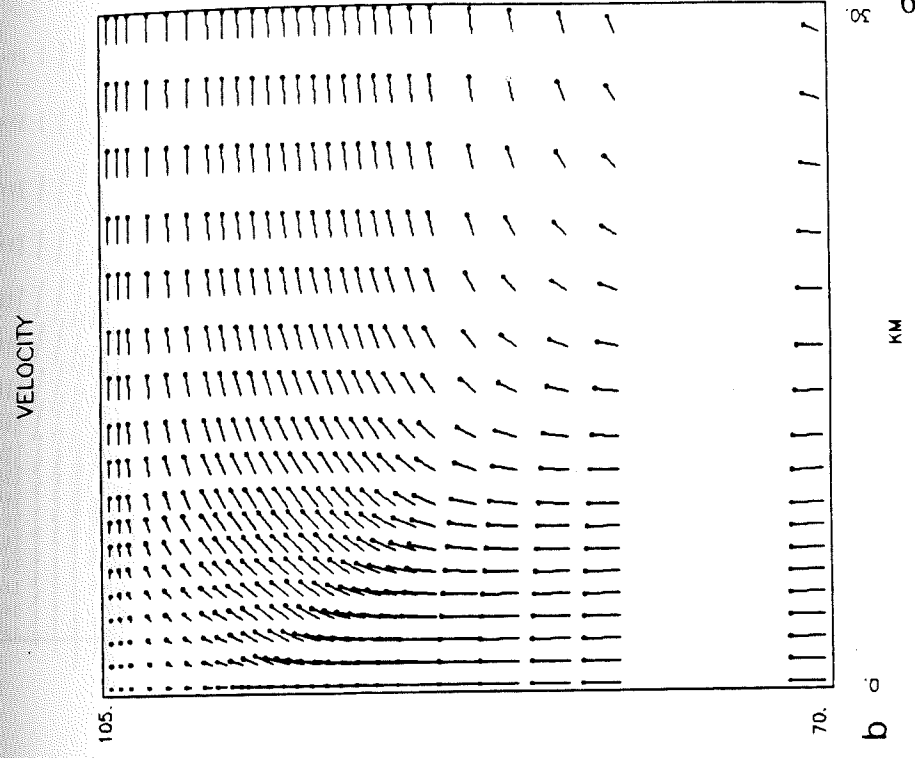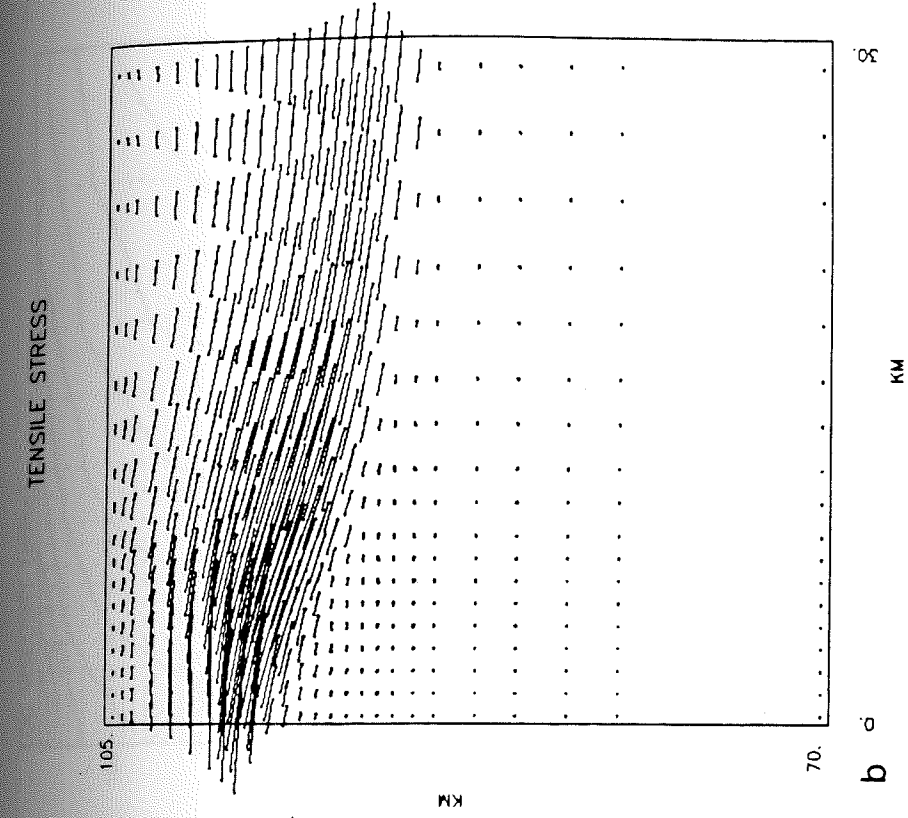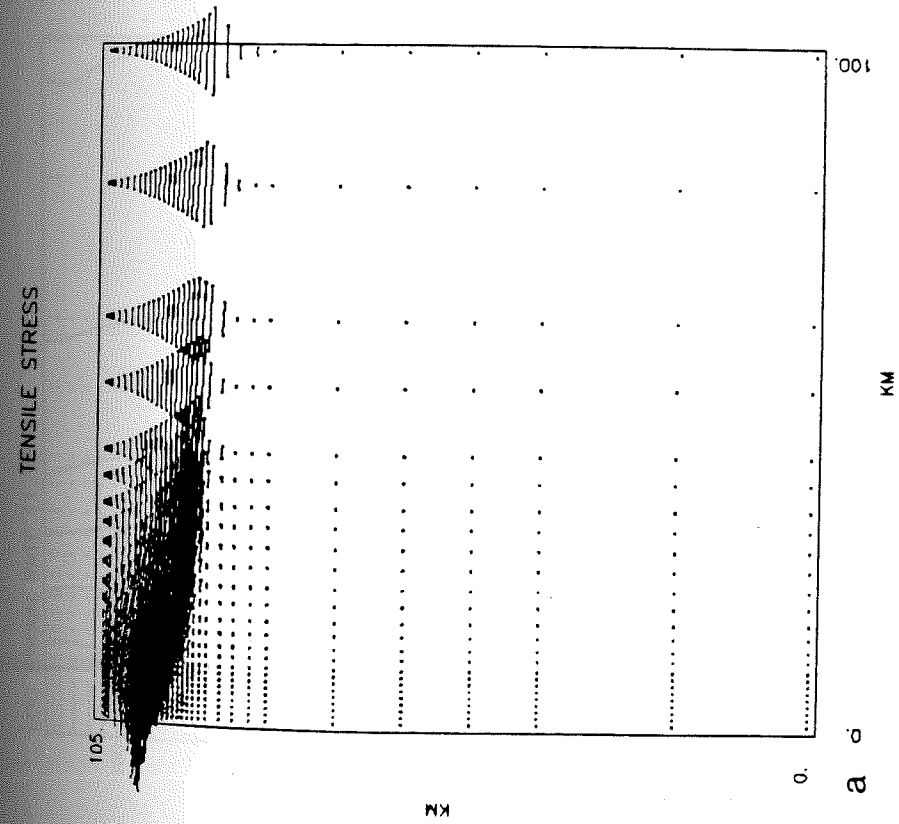
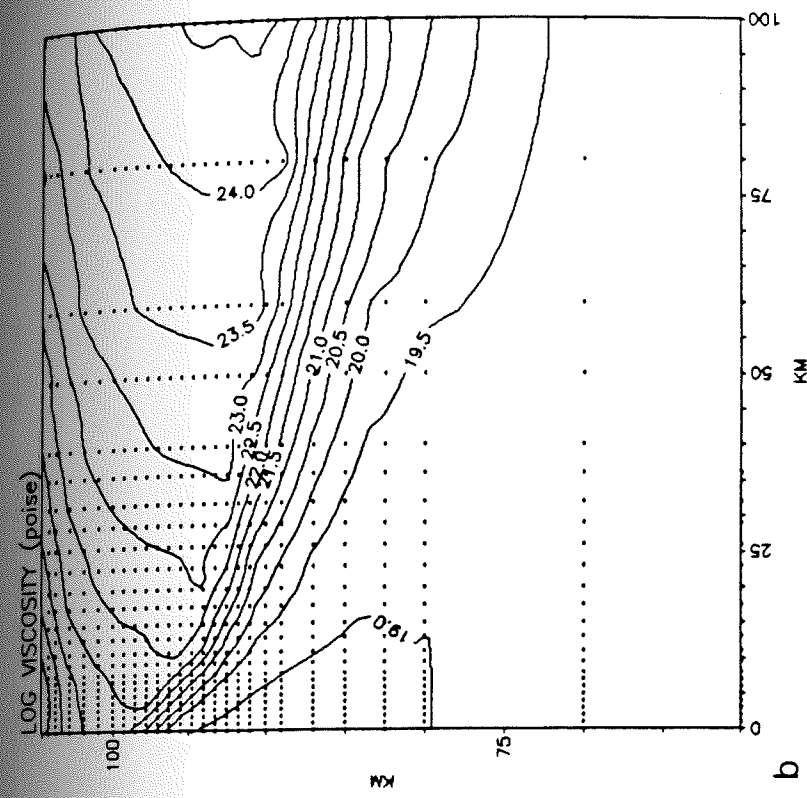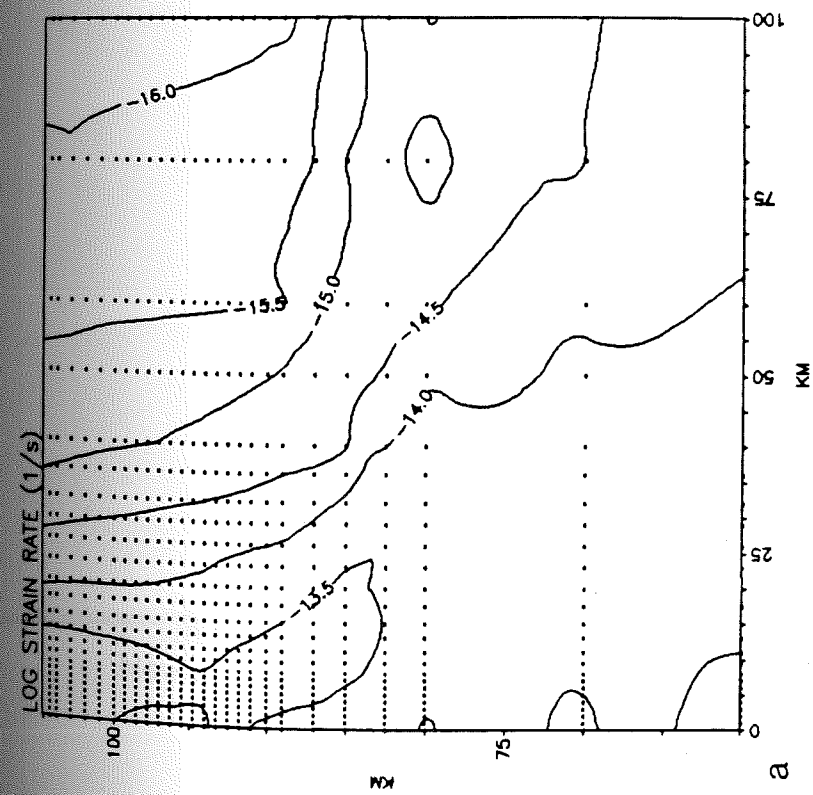Figure 17. Tensile stress field for $T_m = 1200°C$ with Newtonian rheology and a cooled crustal layer.
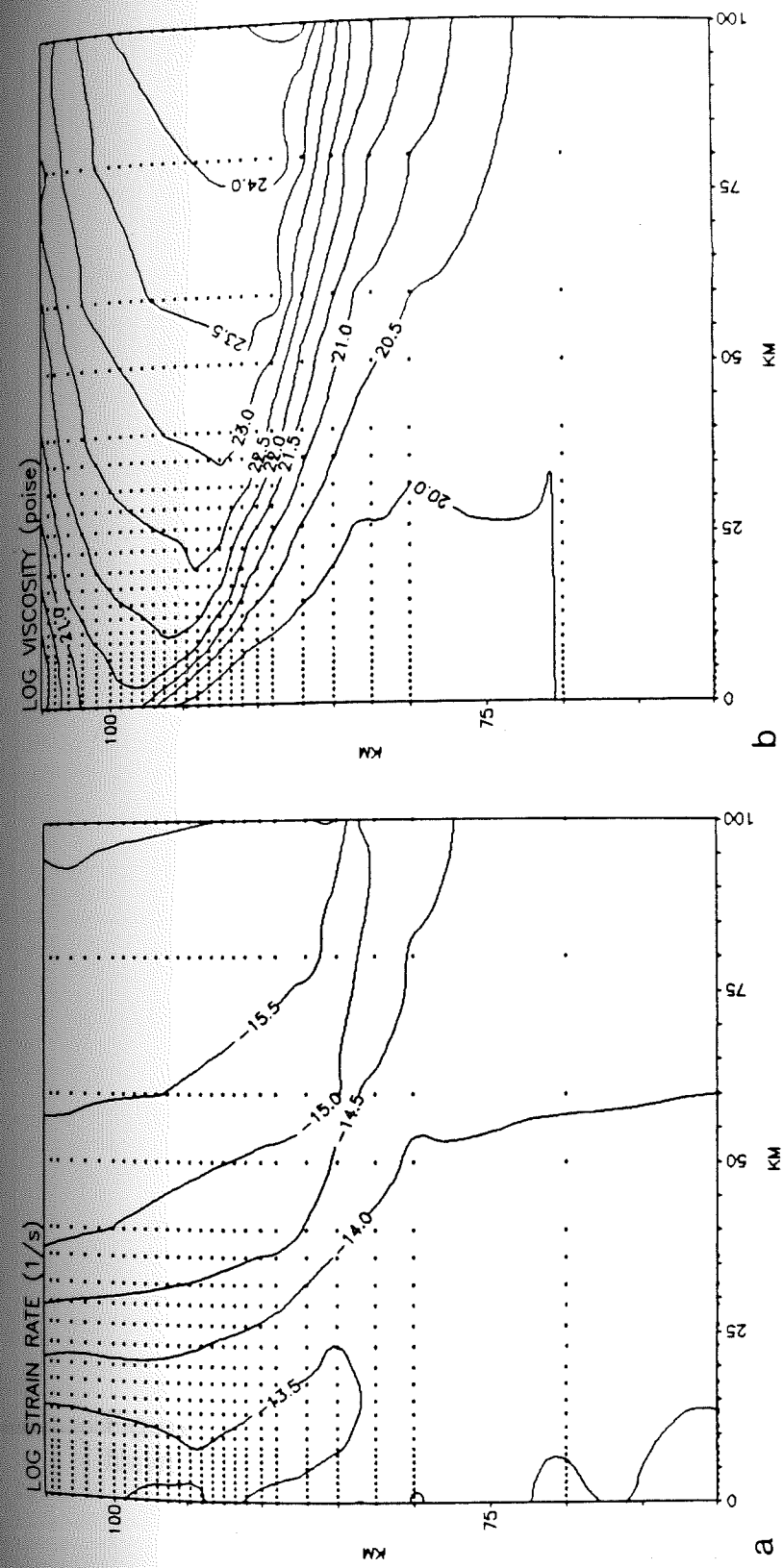
Figure 18. Strain rate and viscosity fields for $T_m = 1200°C$ with Newtonian rheology and a cooled crustal layer.
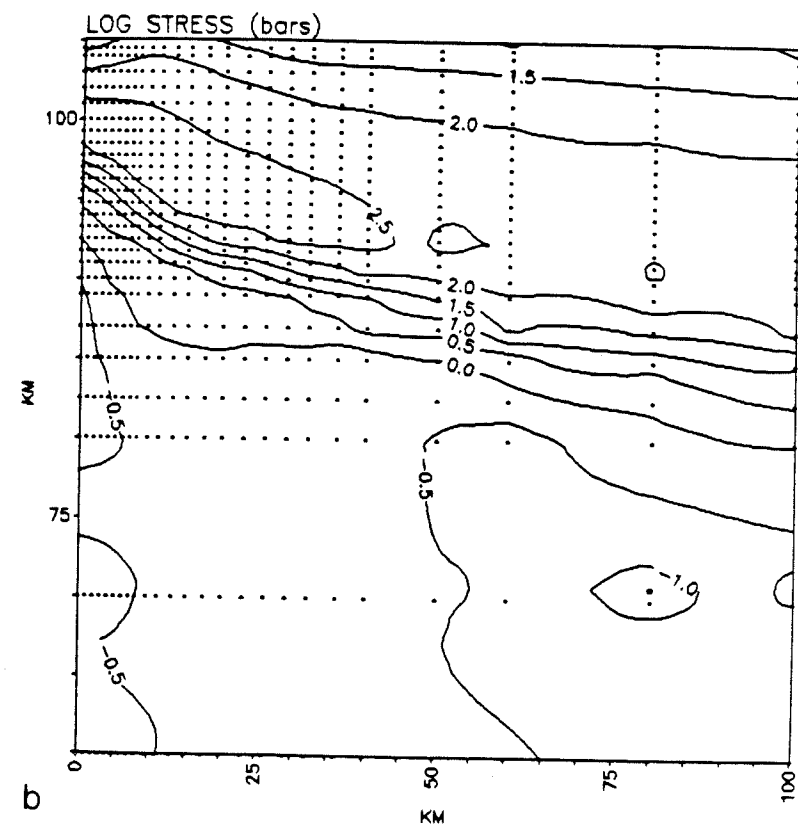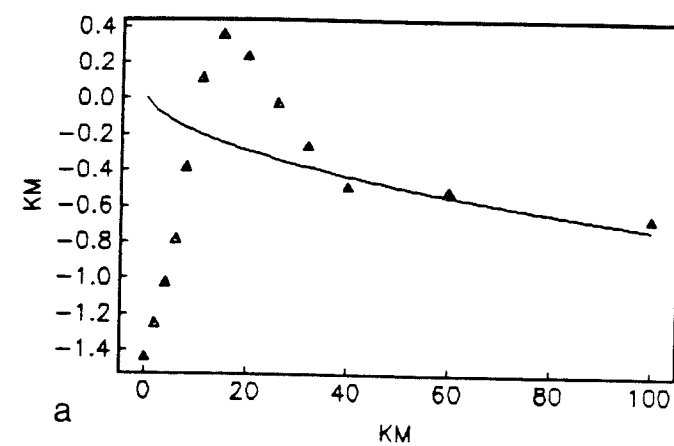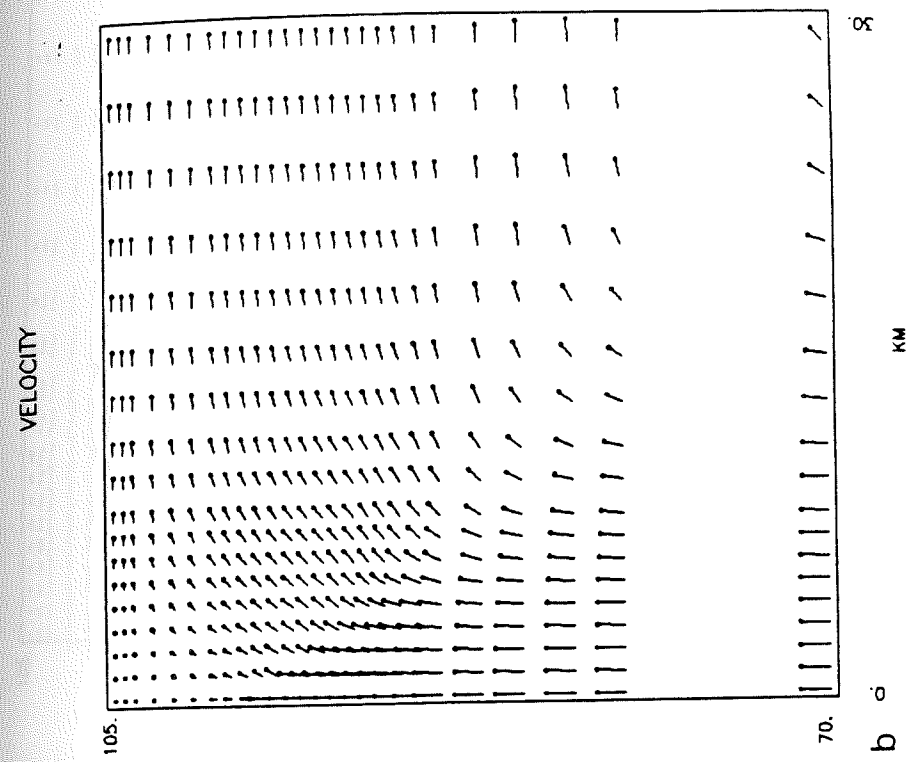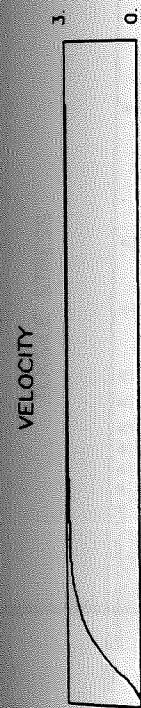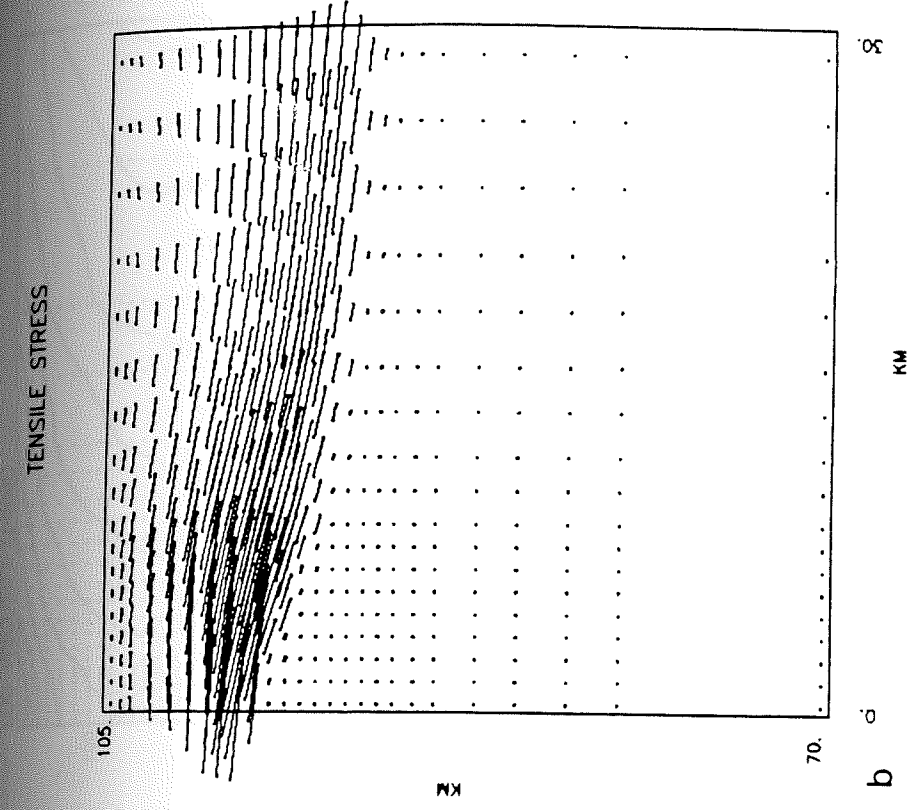
TOPOGRAPHY

a

LOG STRESS (bars)

b
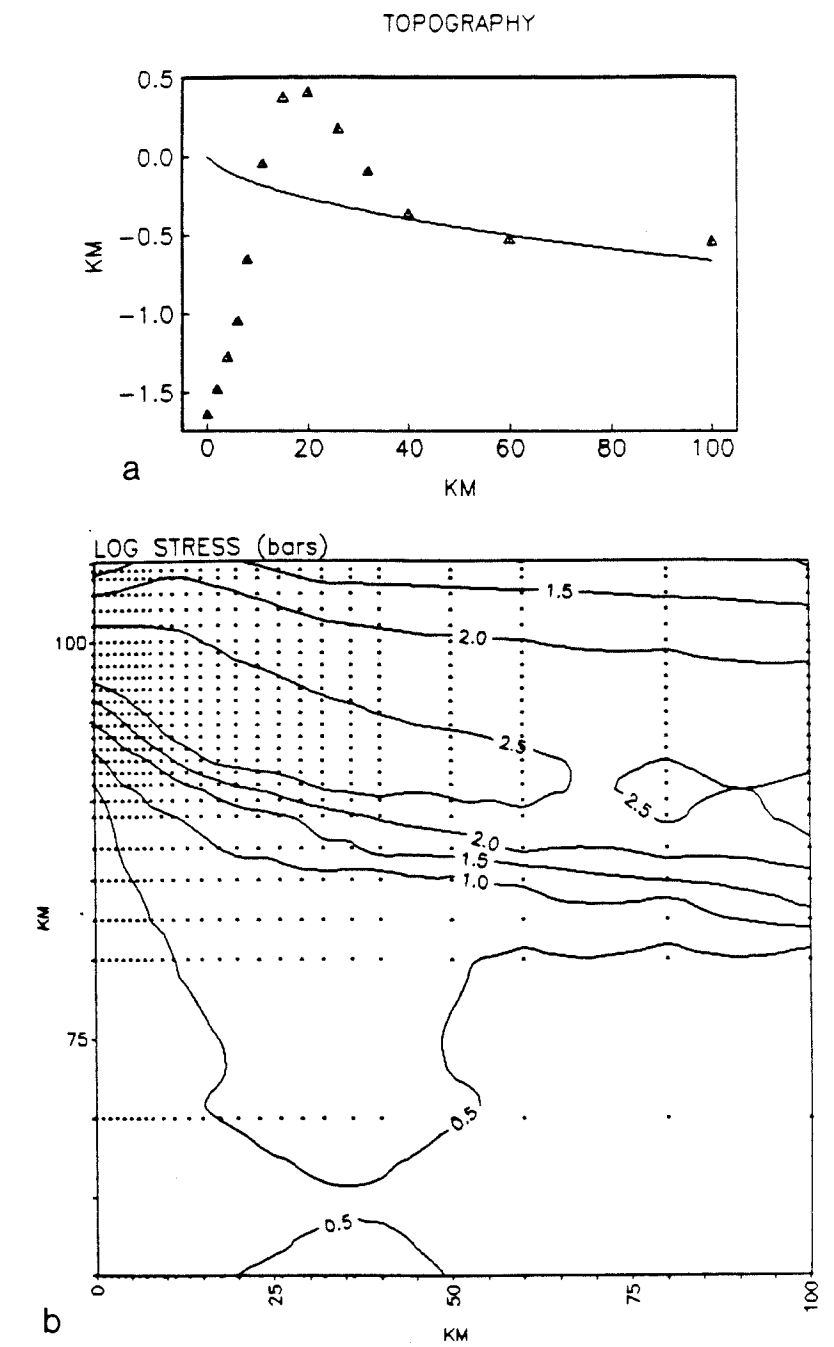
Figure 19. Stress field and topography for T_m=1200°C with Newtonian rheology and a cooled crustal layer.
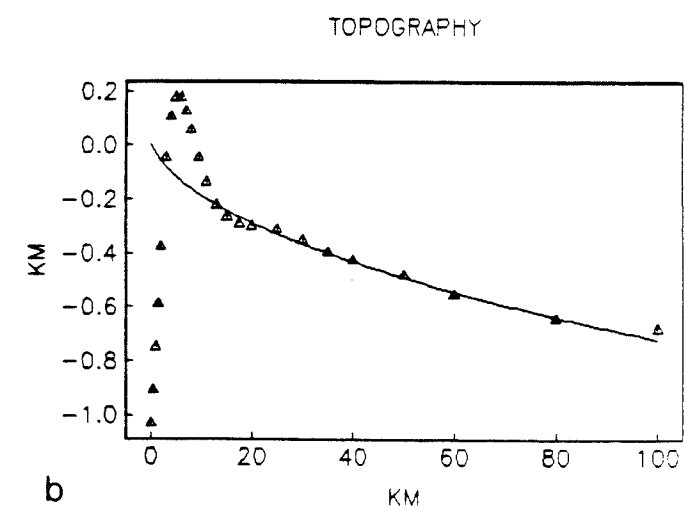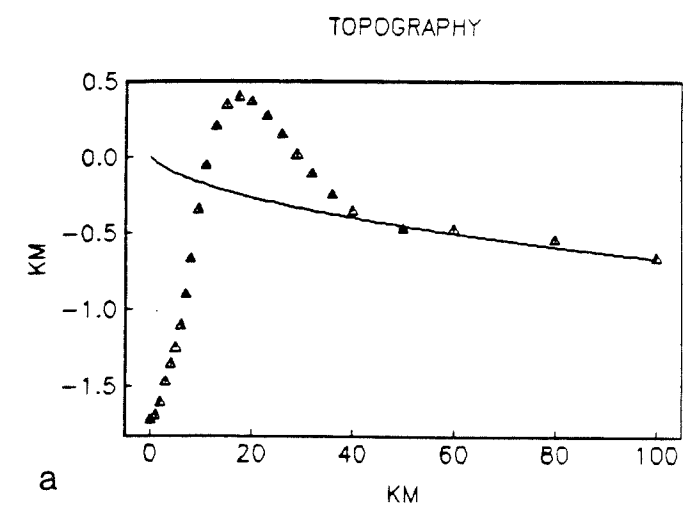
Figure 20. a) Topography for doubled grid with $T_m=1200°C$ and cooled crustal layer. b) Topography for doubled grid with $T_m=1300°C$ and without cooled crustal layer.
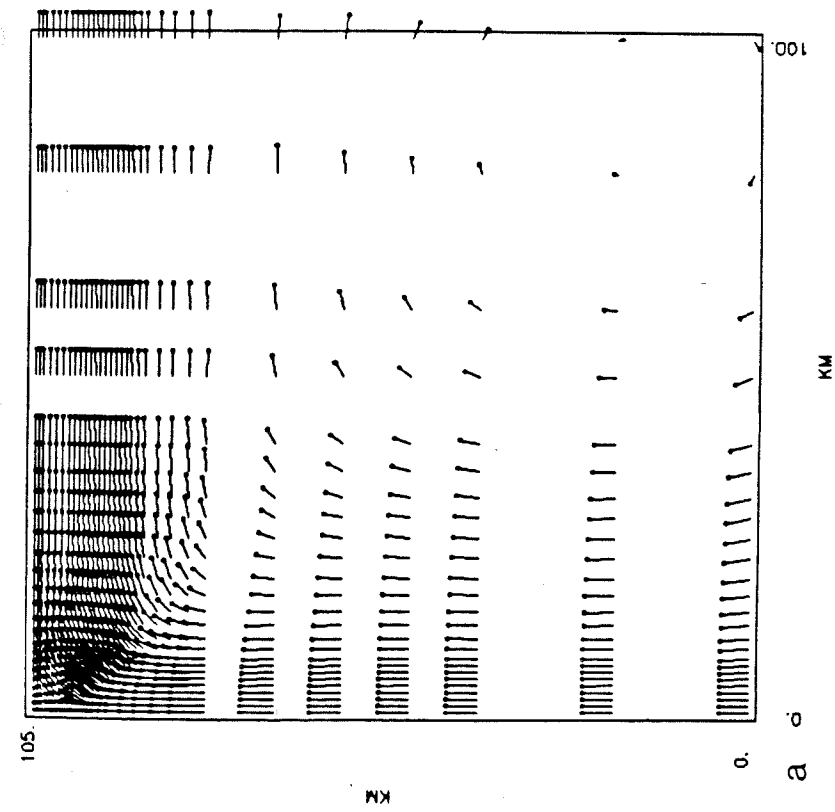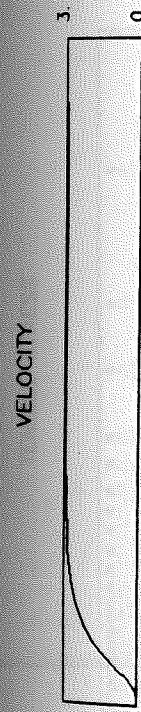
VELOCITY

VELOCITY

Figure 21. Velocity field for T_m=1300°C with Newtonian rheology and a cooled crustal layer.
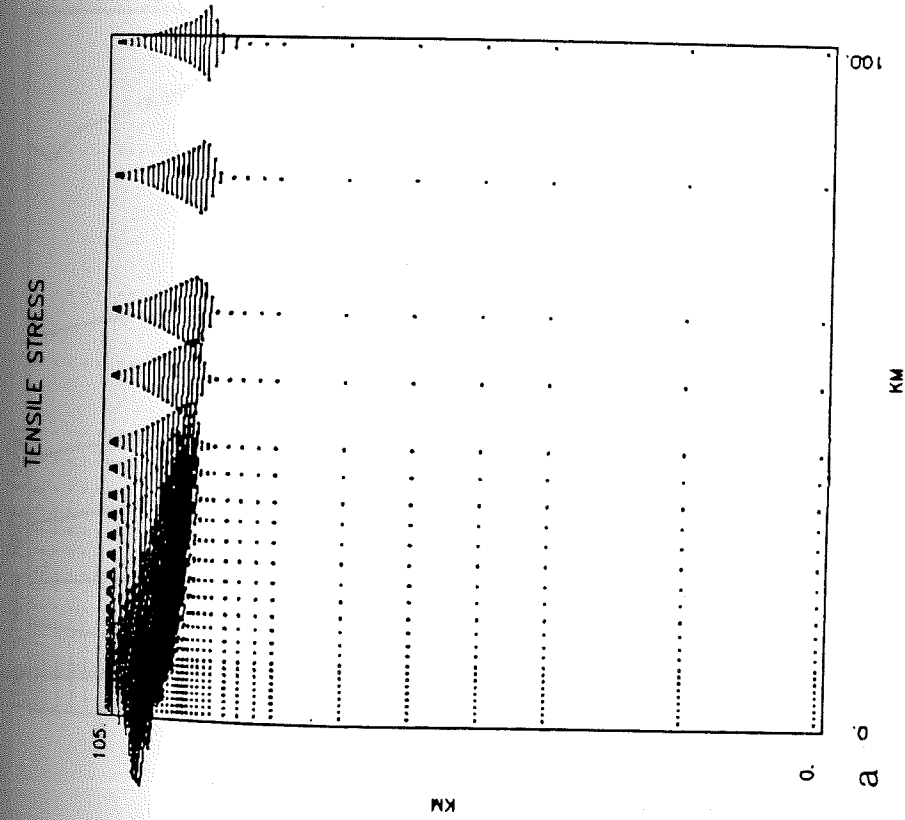
Figure 22. Tensile stress field for T_m=1300°C with Newtonian rheology and a cooled crustal layer.

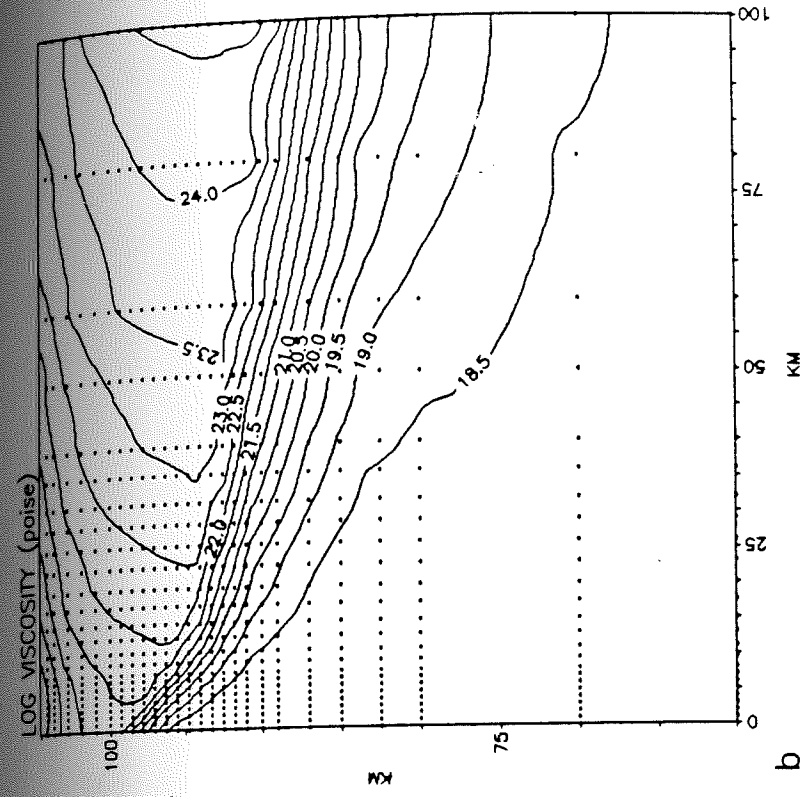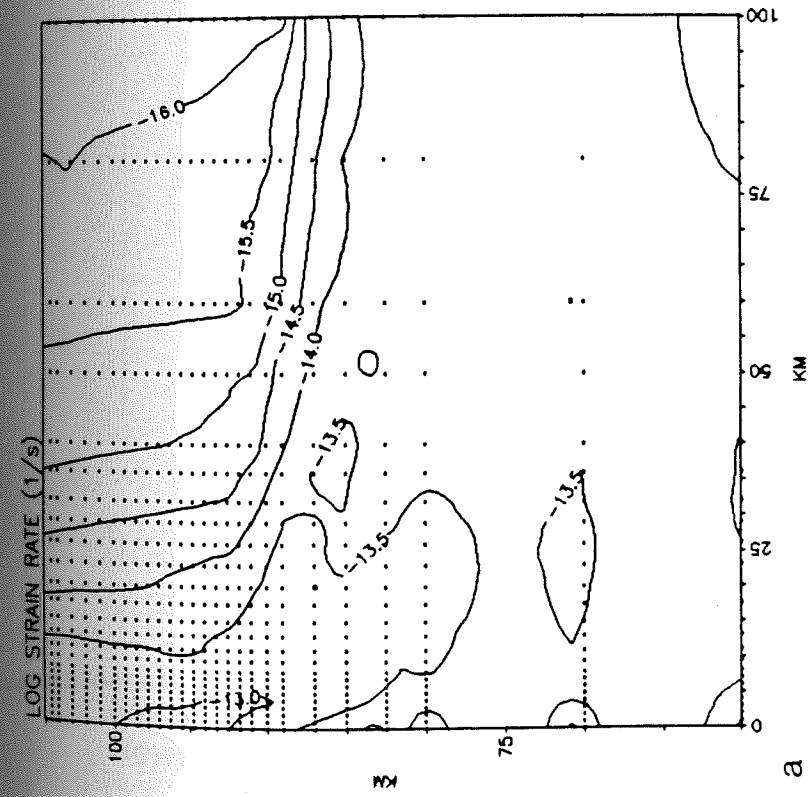Figure 23. Strain rate and viscosity fields for T_m=1300°C with Newtonian rheology and a cooled crustal layer.

Figure 24. Stress field and topography for $T_m=1300°C$ with Newtonian rheology and a cooled crustal layer.

VELOCITY

VELOCITY

b

KM

KM

KM

KM

a
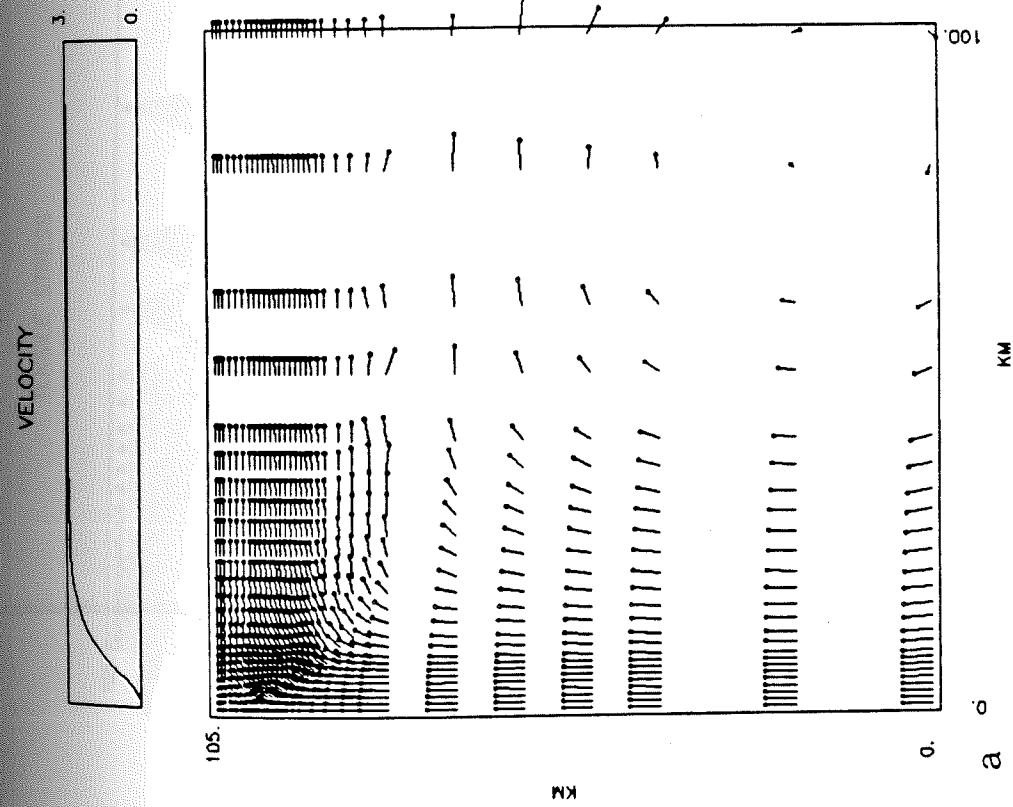
Figure 25. Velocity field for $T_m = 1400°C$ with Newtonian rheology
and a cooled crustal layer.

TENSILE STRESS

TENSILE STRESS

Figure 26. Tensile stress field for $T_m = 1400°C$ with Newtonian rheology and a cooled crustal layer.

Figure 27. Strain rate and viscosity fields for $T_m = 1400°C$ with Newtonian rheology and a cooled crustal layer.

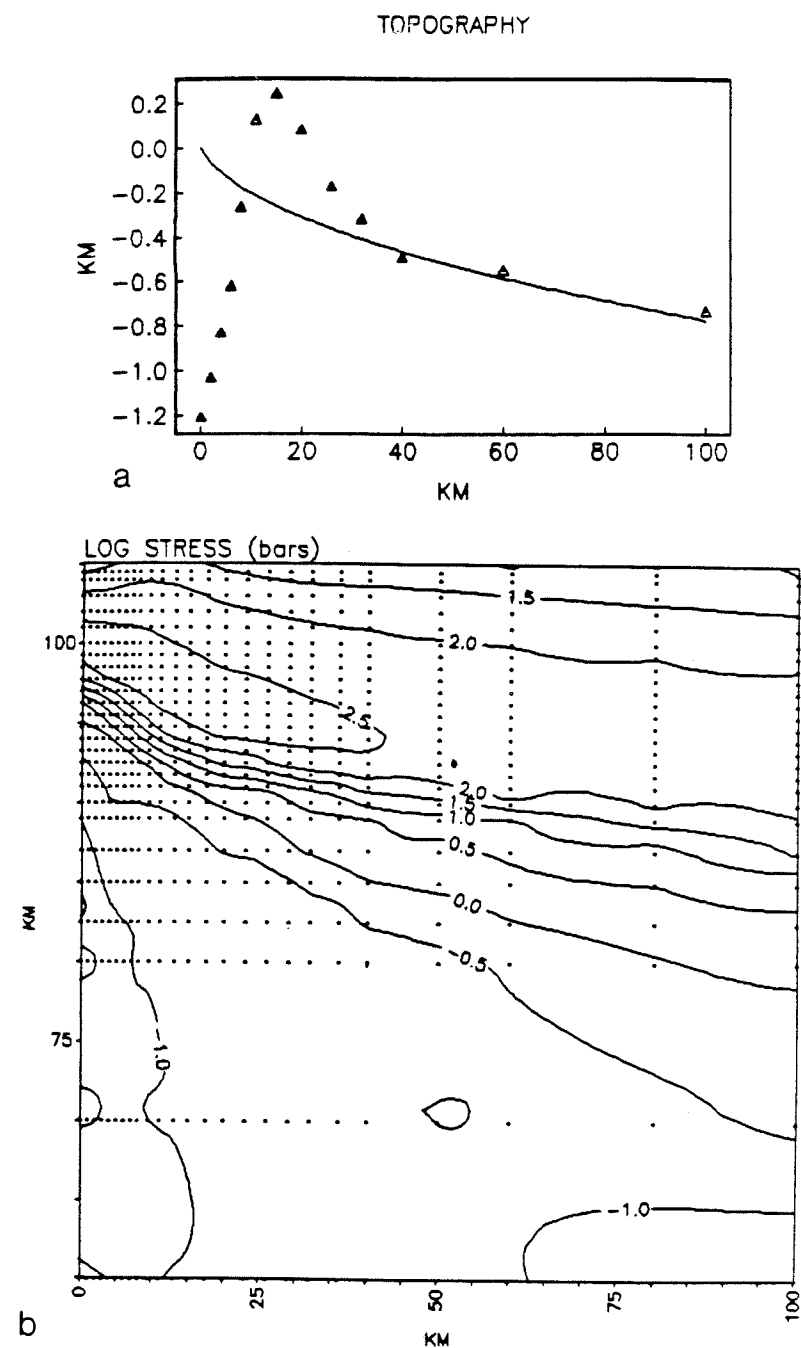Figure 28. Stress field and topography for T_m=1400°C with Newtonian rheology and a cooled crustal layer.

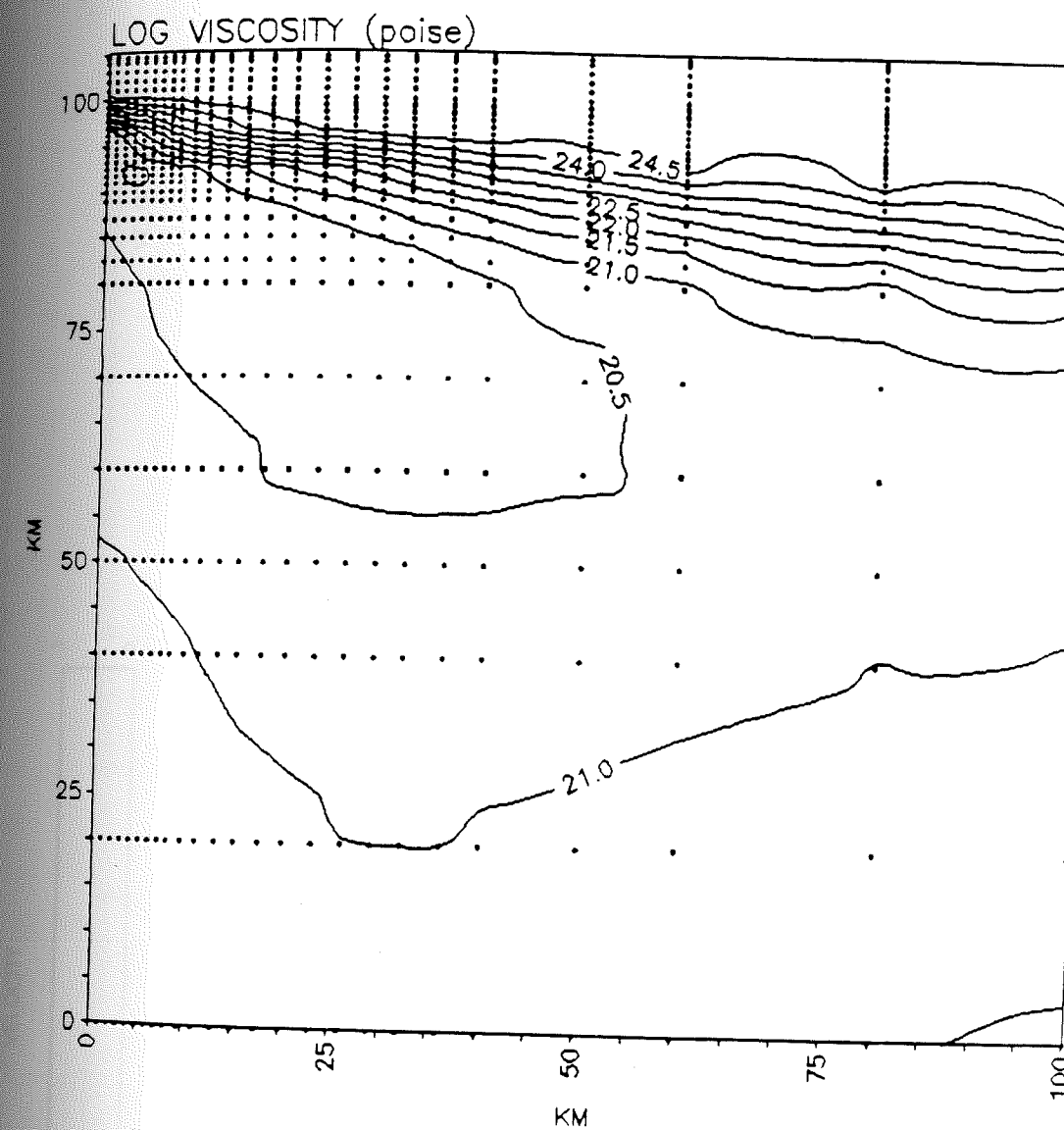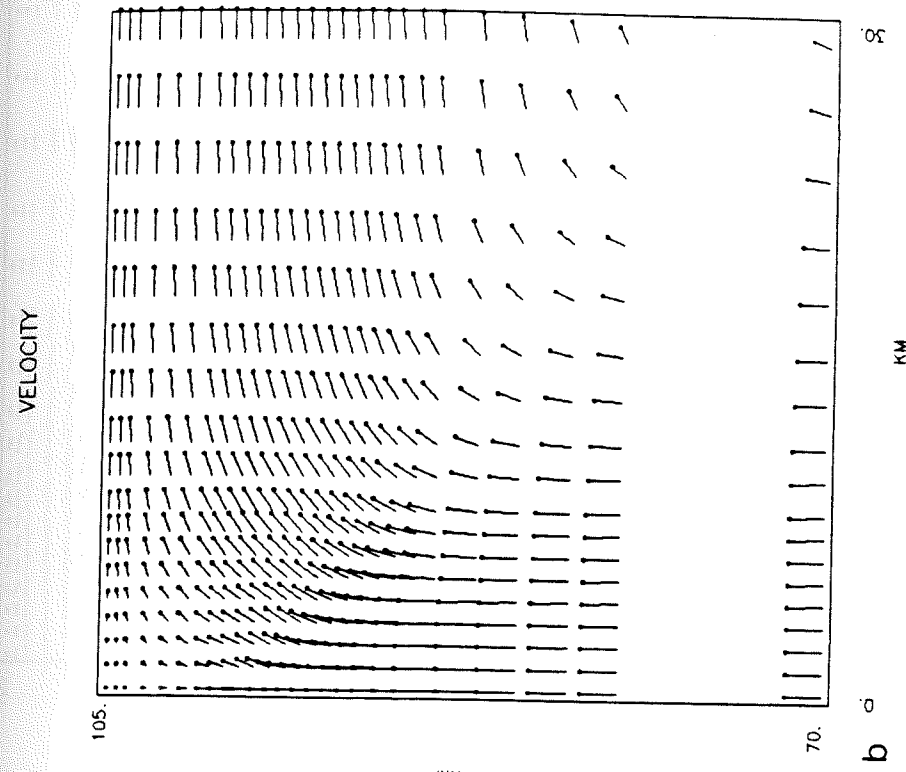Figure 29. Non-Newtonian viscosity field for $T_m=1200°C$ with 5 km thick cooled crustal layer.

VELOCITY

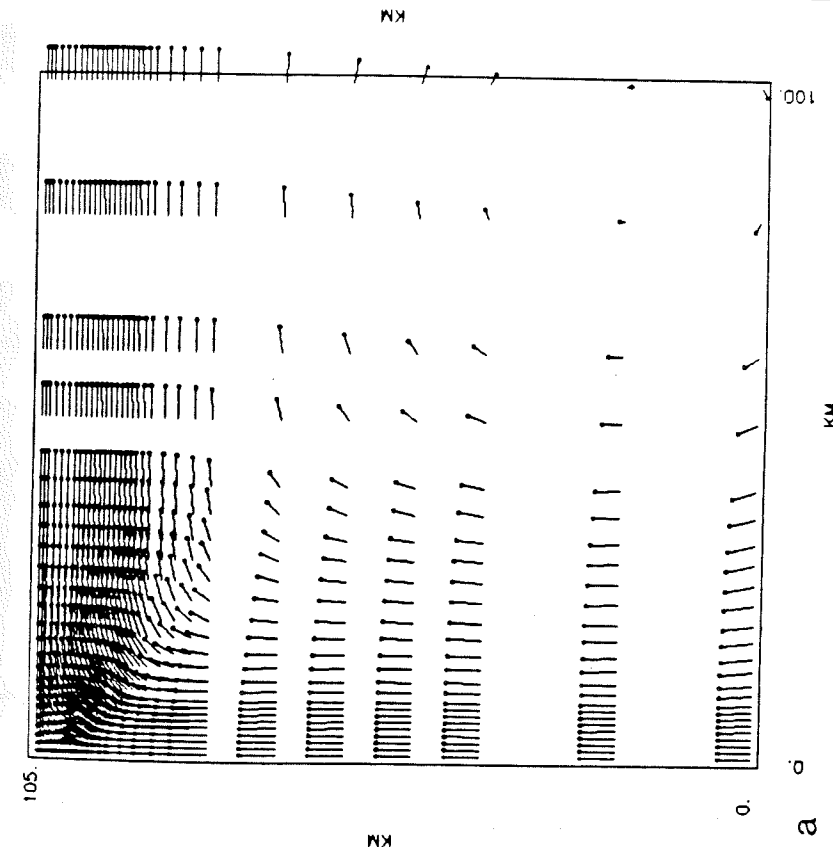VELOCITY

VELOCITY

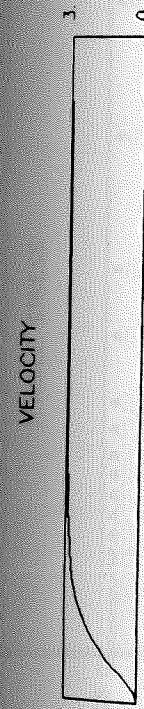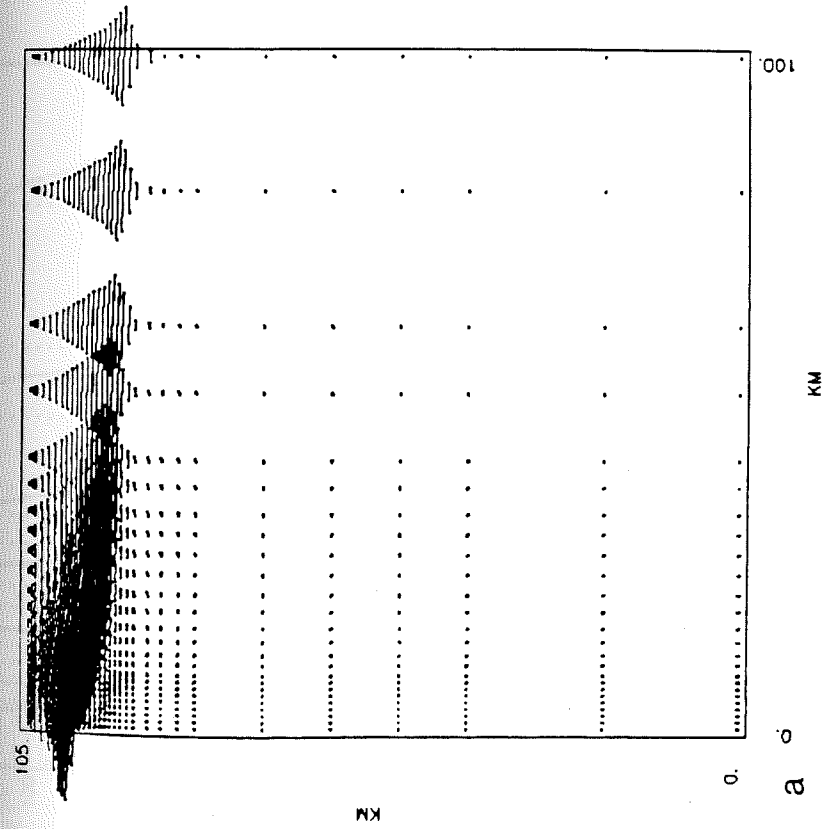Figure 30. Velocity field for T_m=1200°C with non-Newtonian rheology and a cooled crustal layer.

TENSILE STRESS

TENSILE STRESS

Figure 31. Tensile stress field for $T_m = 1200°C$ with non-Newtonian rheology and a cooled crustal layer.

Figure 32. Strain rate and viscosity fields for $T_m = 1200°C$ with non-Newtonian rheology and a cooled crustal layer.

TOPOGRAPHY

a

LOG STRESS (bars)

b

Figure 33.   Stress field and topography for T_m=1200°C with non-Newtonian rheology and a cooled crustal layer.

Figure 34. Non-Newtonian viscosity field for $T_m=1300°C$ with 5 km thick cooled crustal layer.
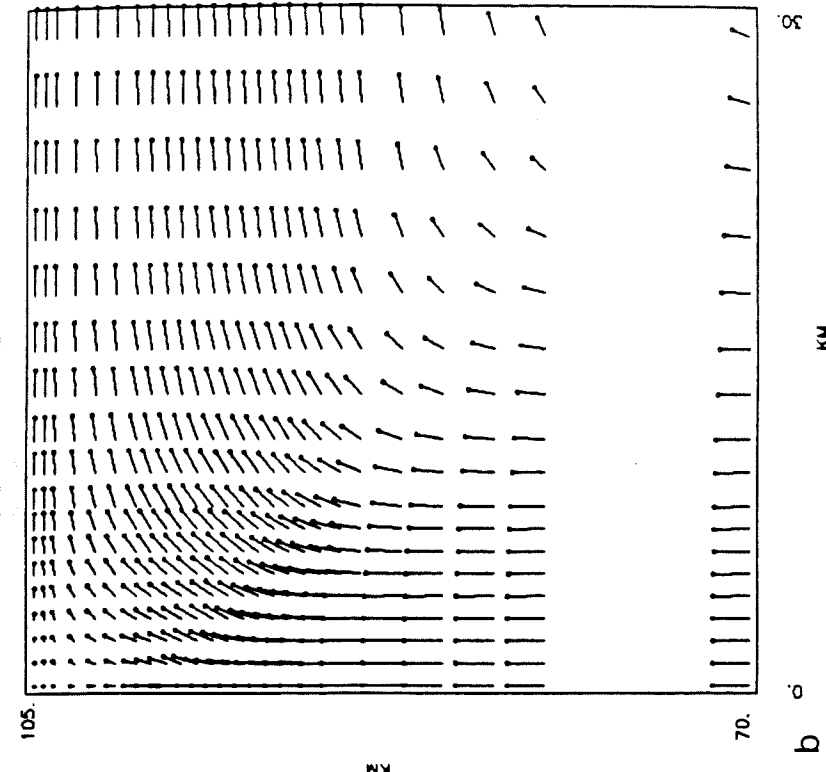
Figure 35. Velocity field for $T_m = 1300°C$ with non-Newtonian rheology and a cooled crustal layer.

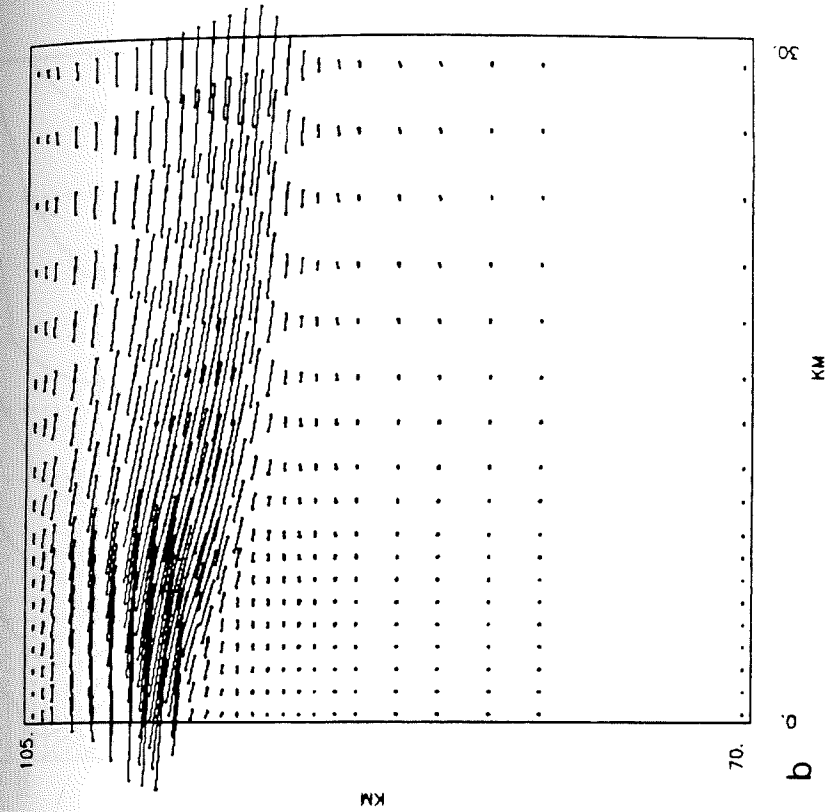Figure 36. Tensile stress field for $T_m=1300°C$ with non-Newtonian rheology and a cooled crustal layer.
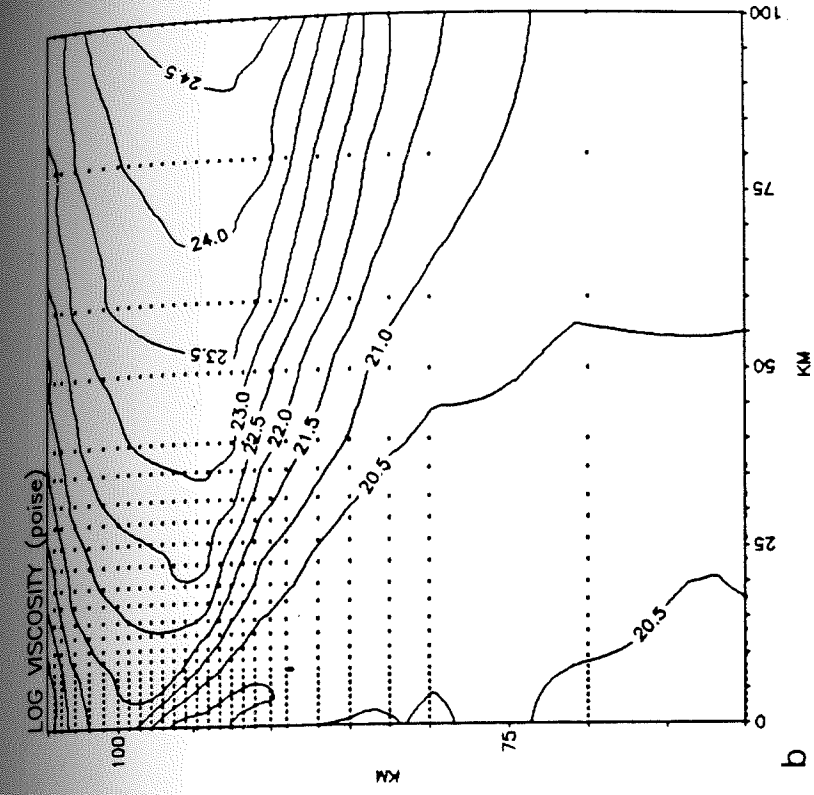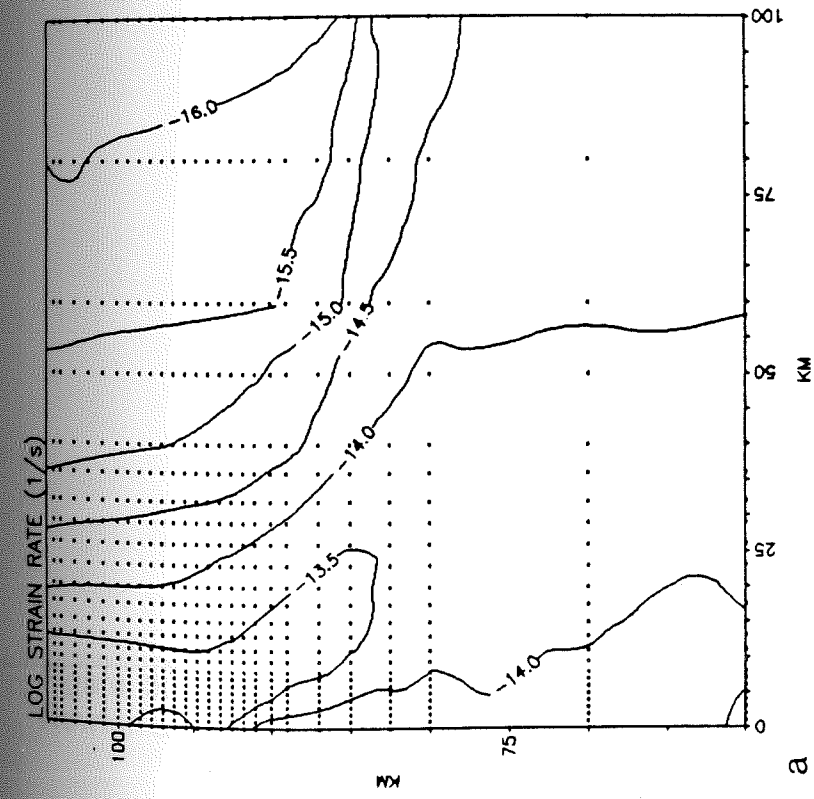
Figure 37. Strain rate and viscosity fields for $T_m=1300°C$ with non-Newtonian rheology and a cooled crustal layer.

Figure 38. Stress field and topography for T_m=1300°C with non-Newtonian rheology and a cooled crustal layer.

Figure 39. Non-Newtonian viscosity field for T_m=1400°C with 5 km thick cooled crustal layer.

VELOCITY

KM

b

VELOCITY

KM

a

Figure 40. Velocity field for $T_m = 1400°C$ with non-Newtonian rheology and a cooled crustal layer.

TENSILE STRESS

TENSILE STRESS

Figure 41. Tensile stress field for $T_m=1400°C$ with non-Newtonian
rheology and a cooled crustal layer.

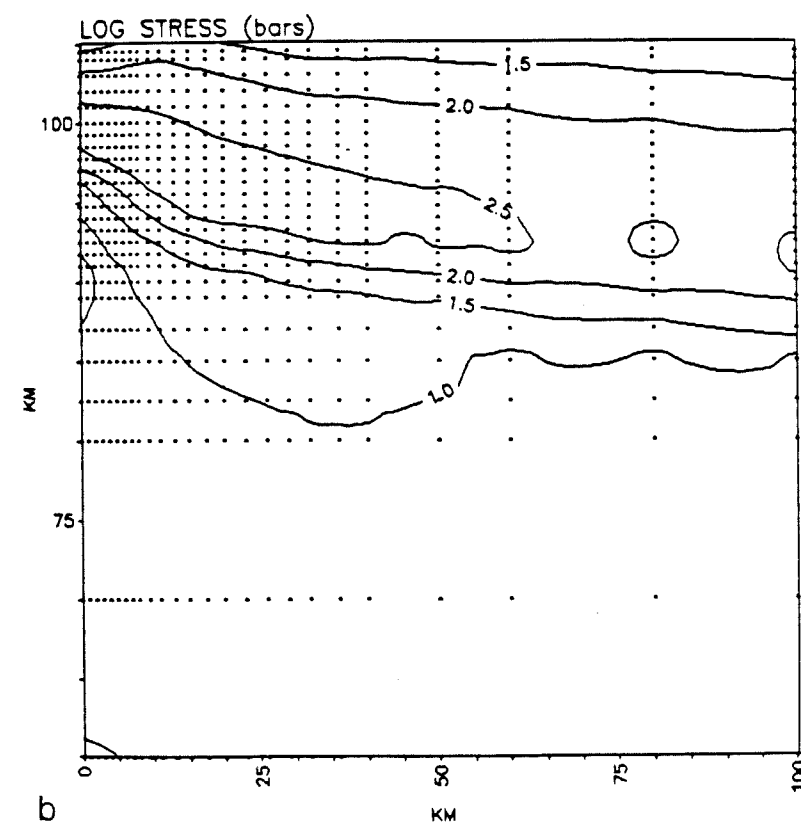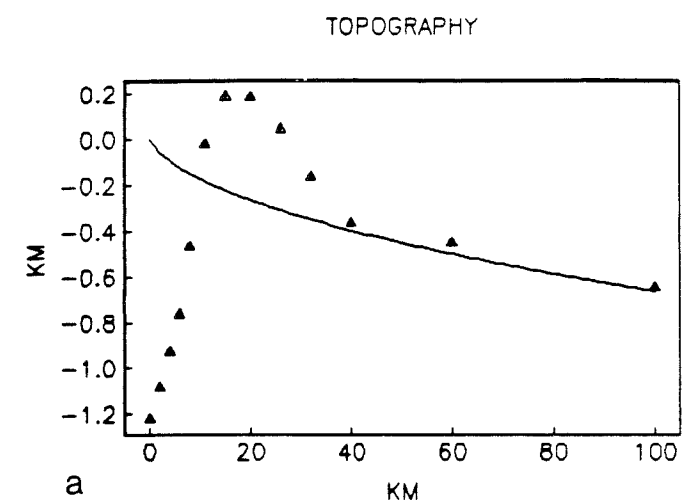Figure 42. Strain rate and viscosity fields for $T_m=1400°C$ with non-Newtonian rheology and a cooled crustal layer.
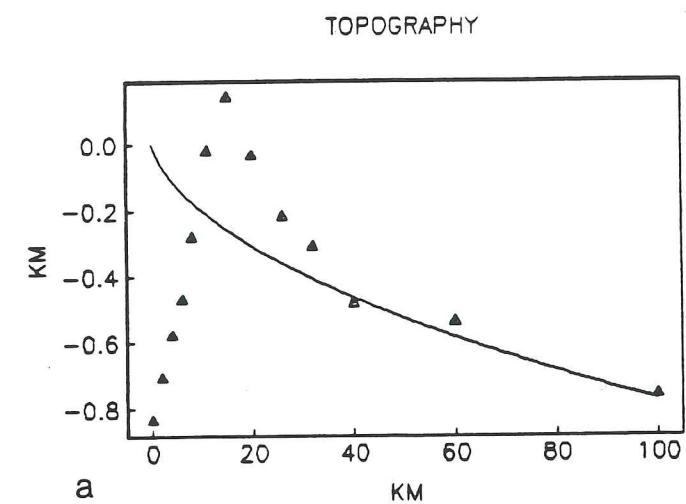
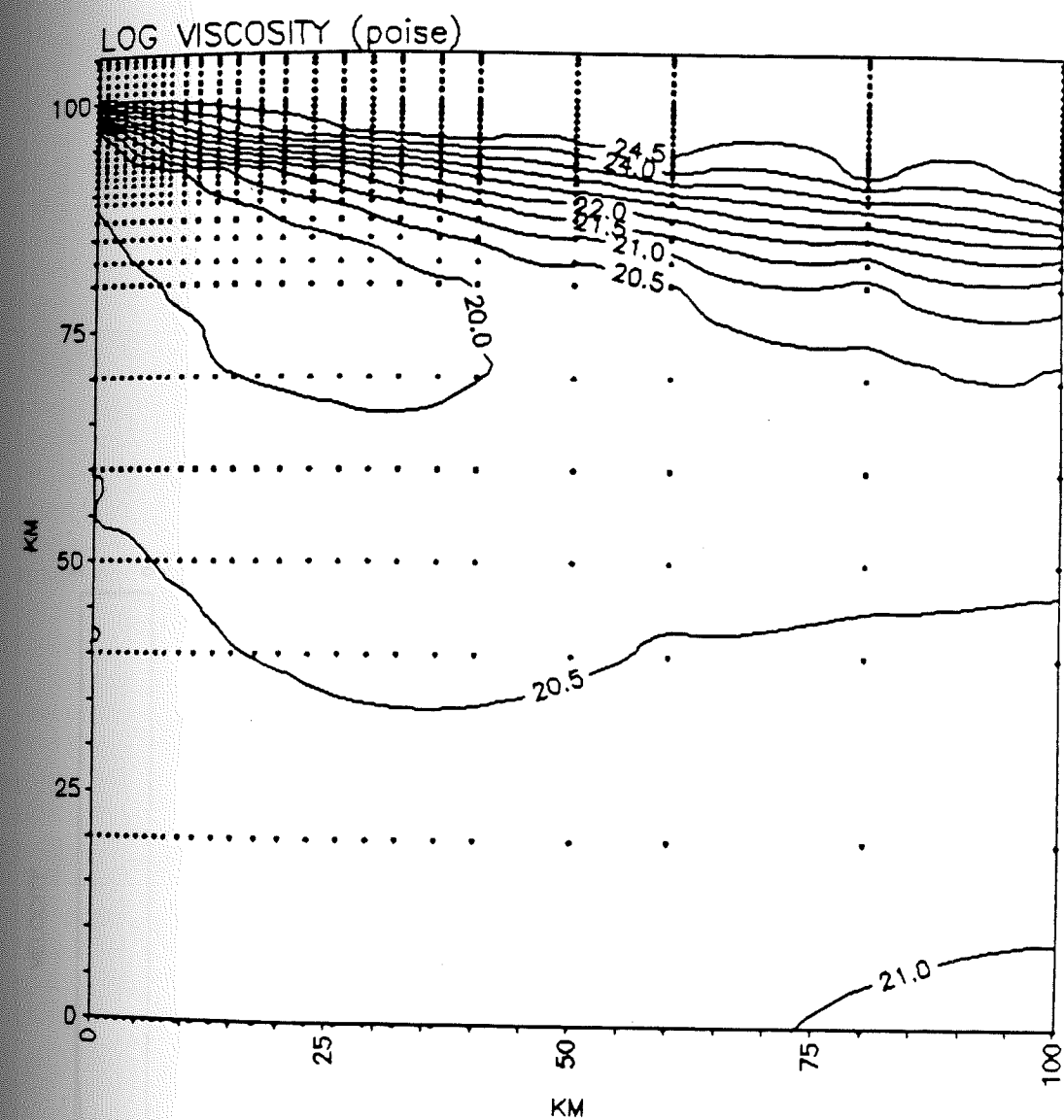Figure 43. Stress field and topography for T_m=1400°C with non-Newtonian rheology and a cooled crustal layer.
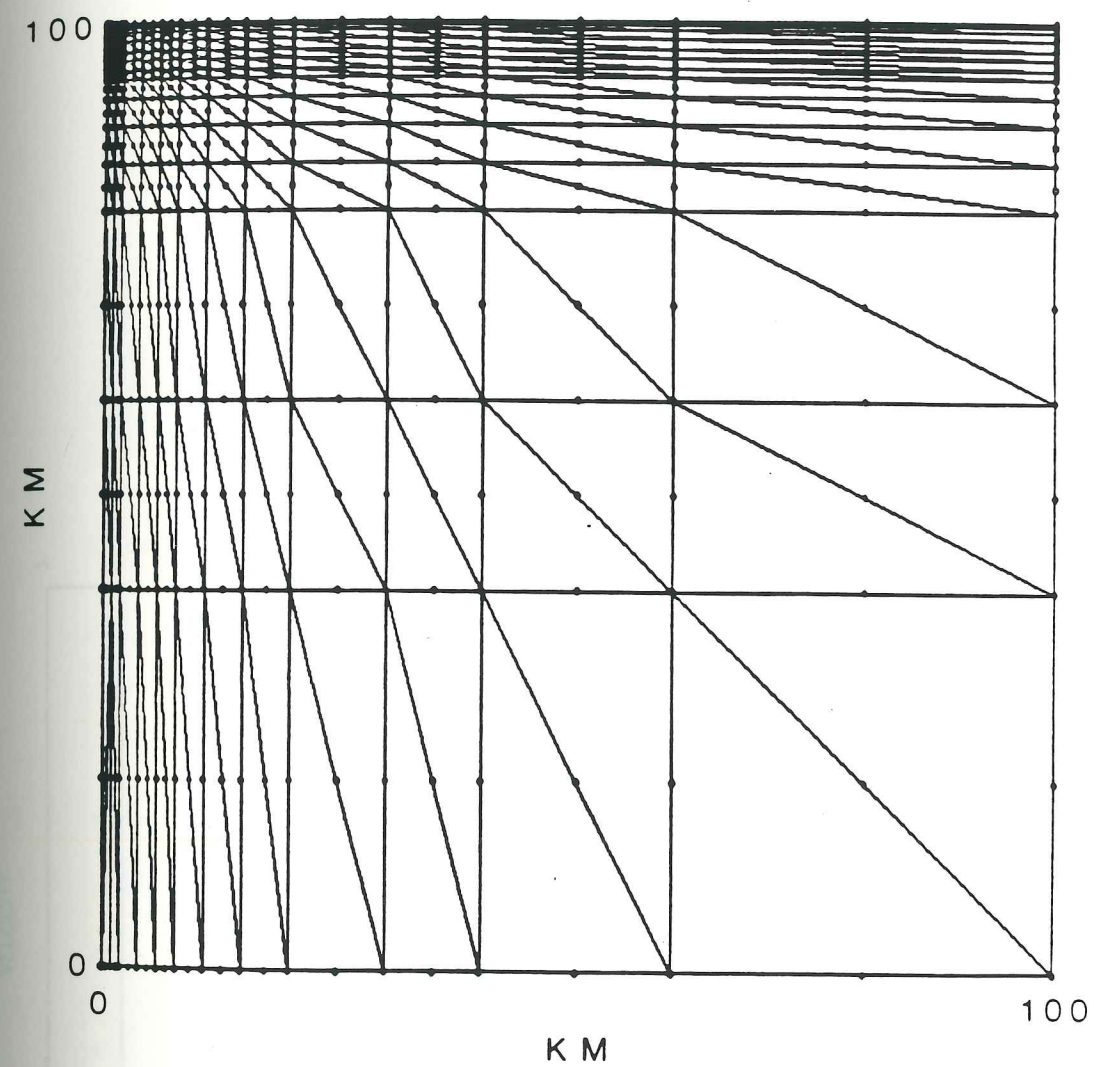
Figure 44. Finite element grid composed of 725 points and 168 elements without a cooled crustal layer.

VELOCITY
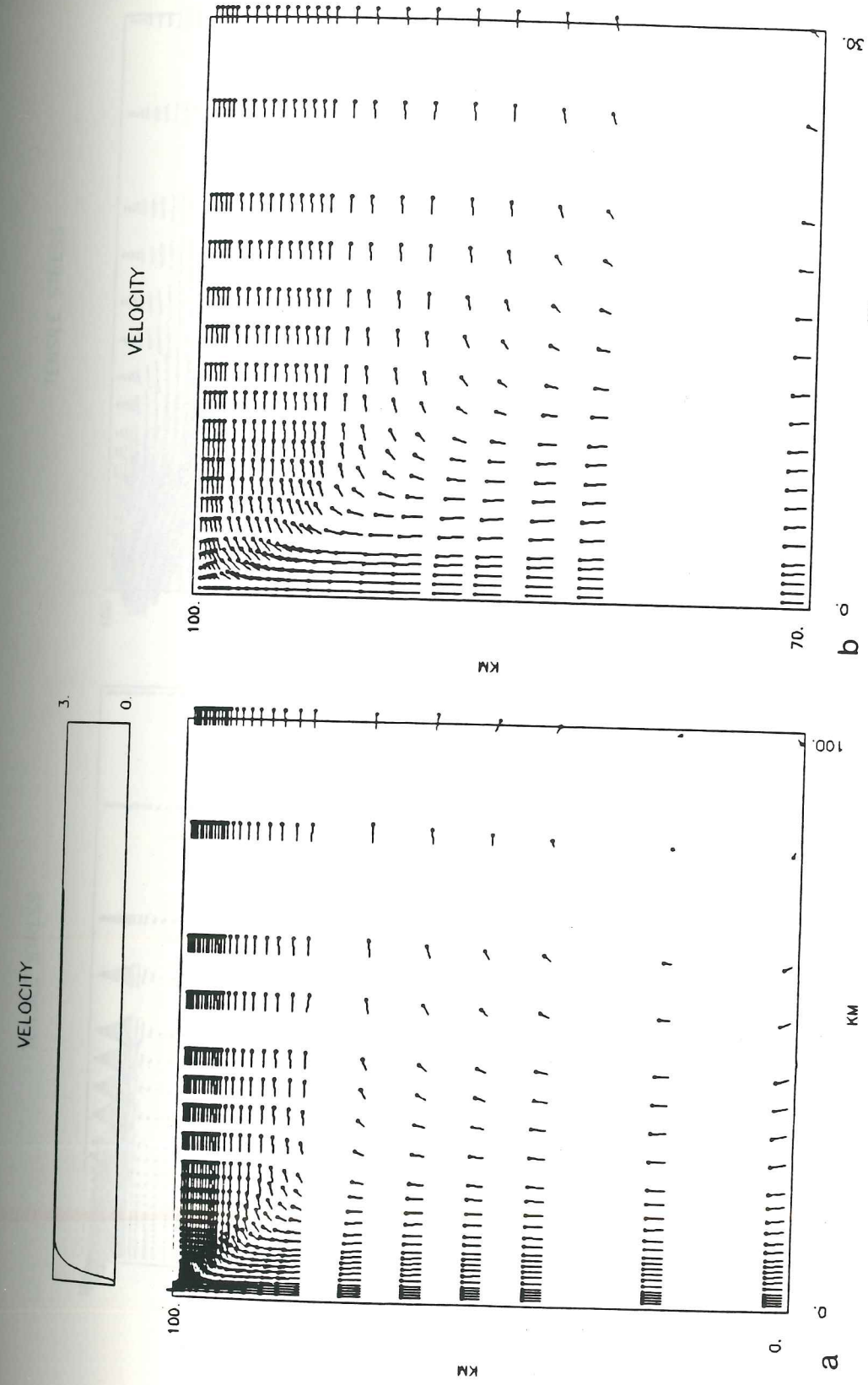
VELOCITY

VELOCITY
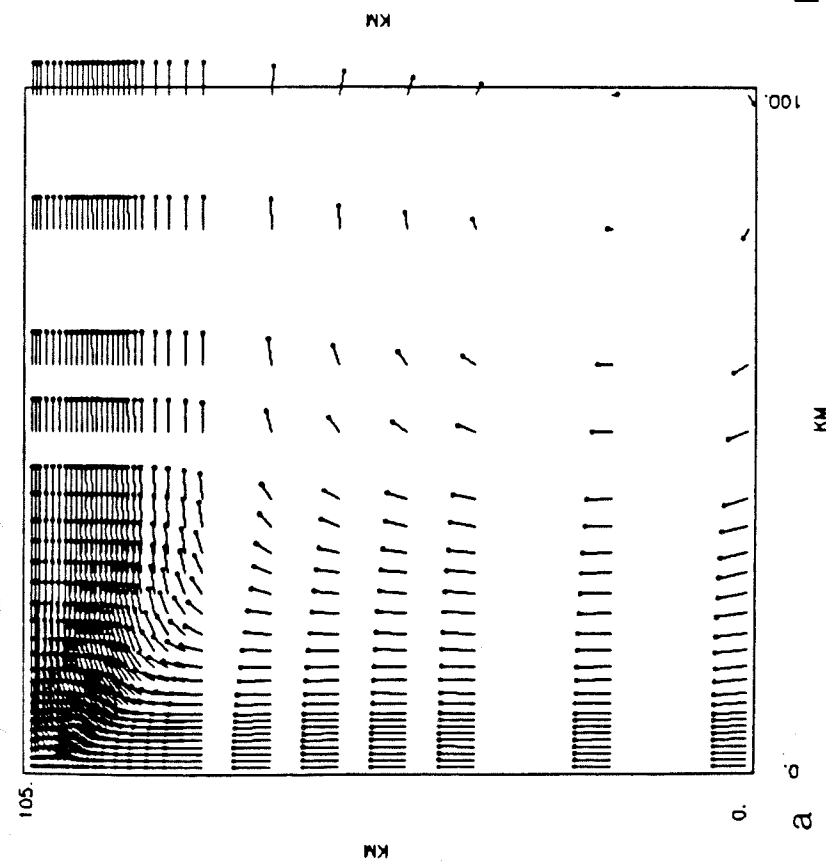
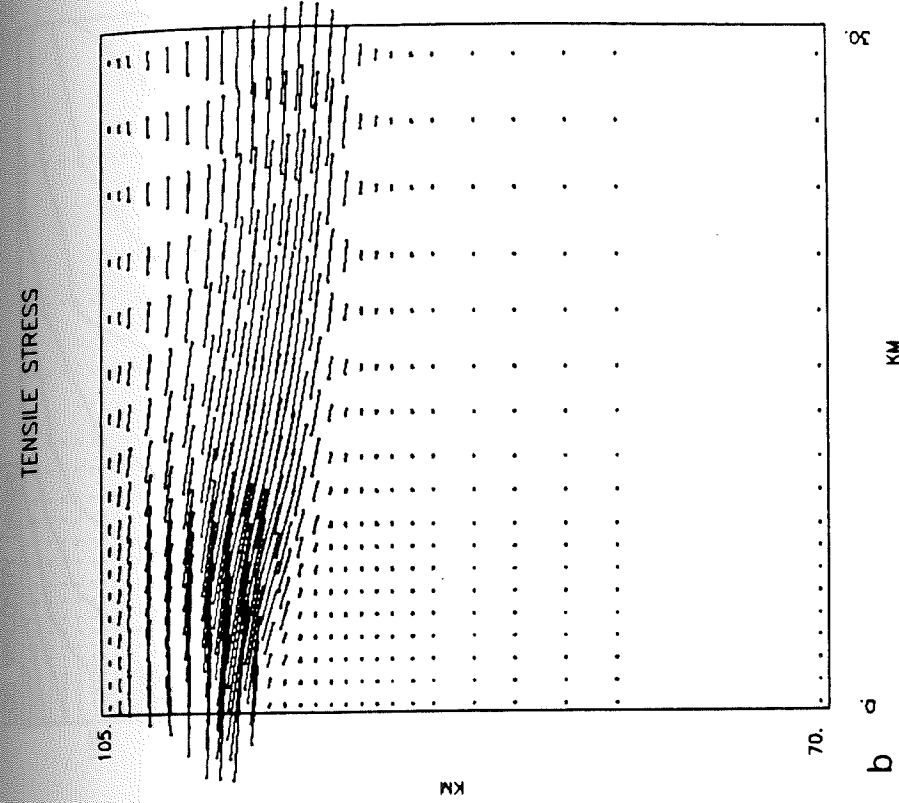Figure 45. Velocity field for $T_m = 1300°C$ with Newtonian rheology and without a cooled crustal layer.
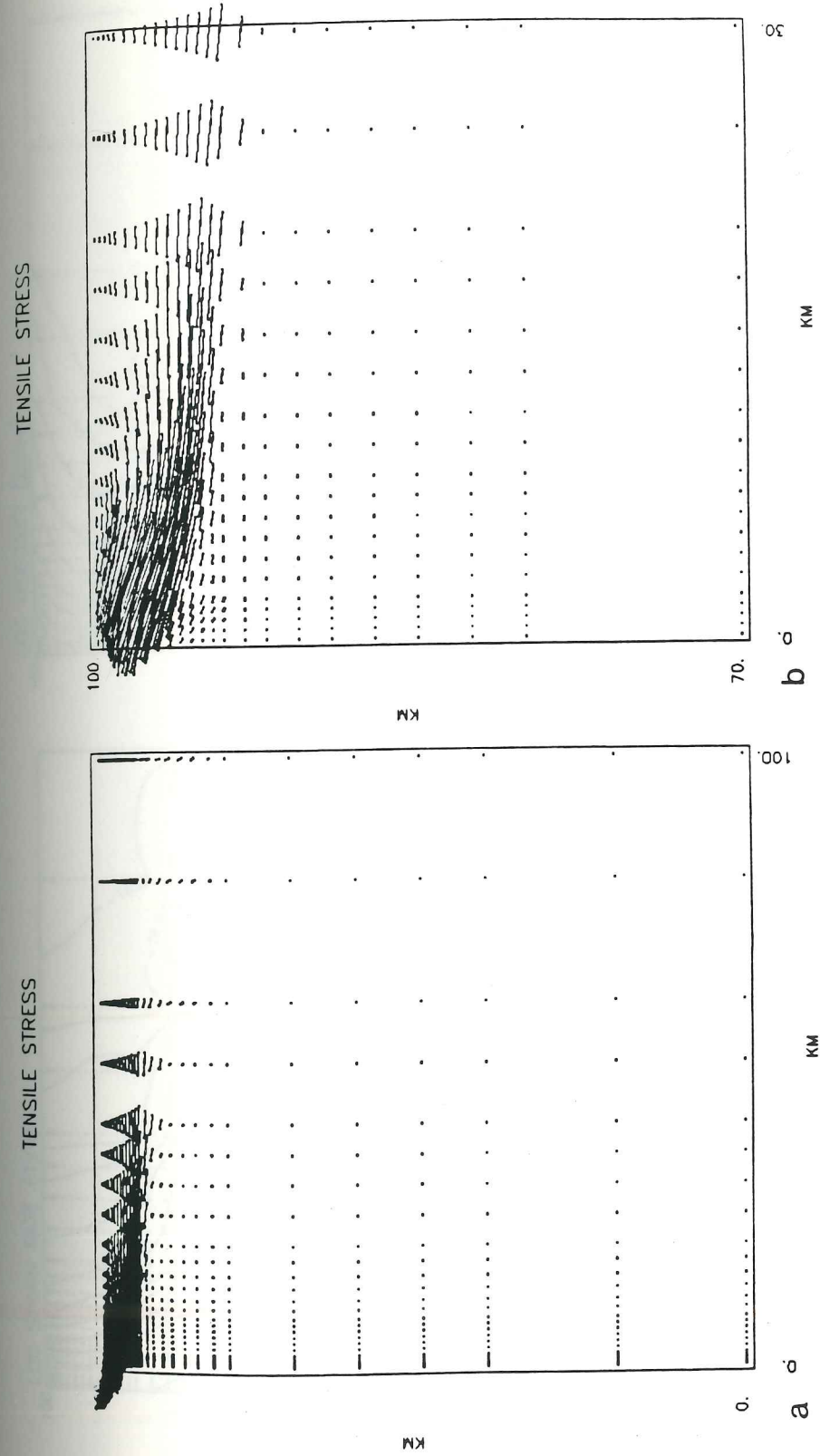
Figure 46. Tensile stress field for $T_m=1300°C$ with Newtonian rheology and without a cooled crustal layer.
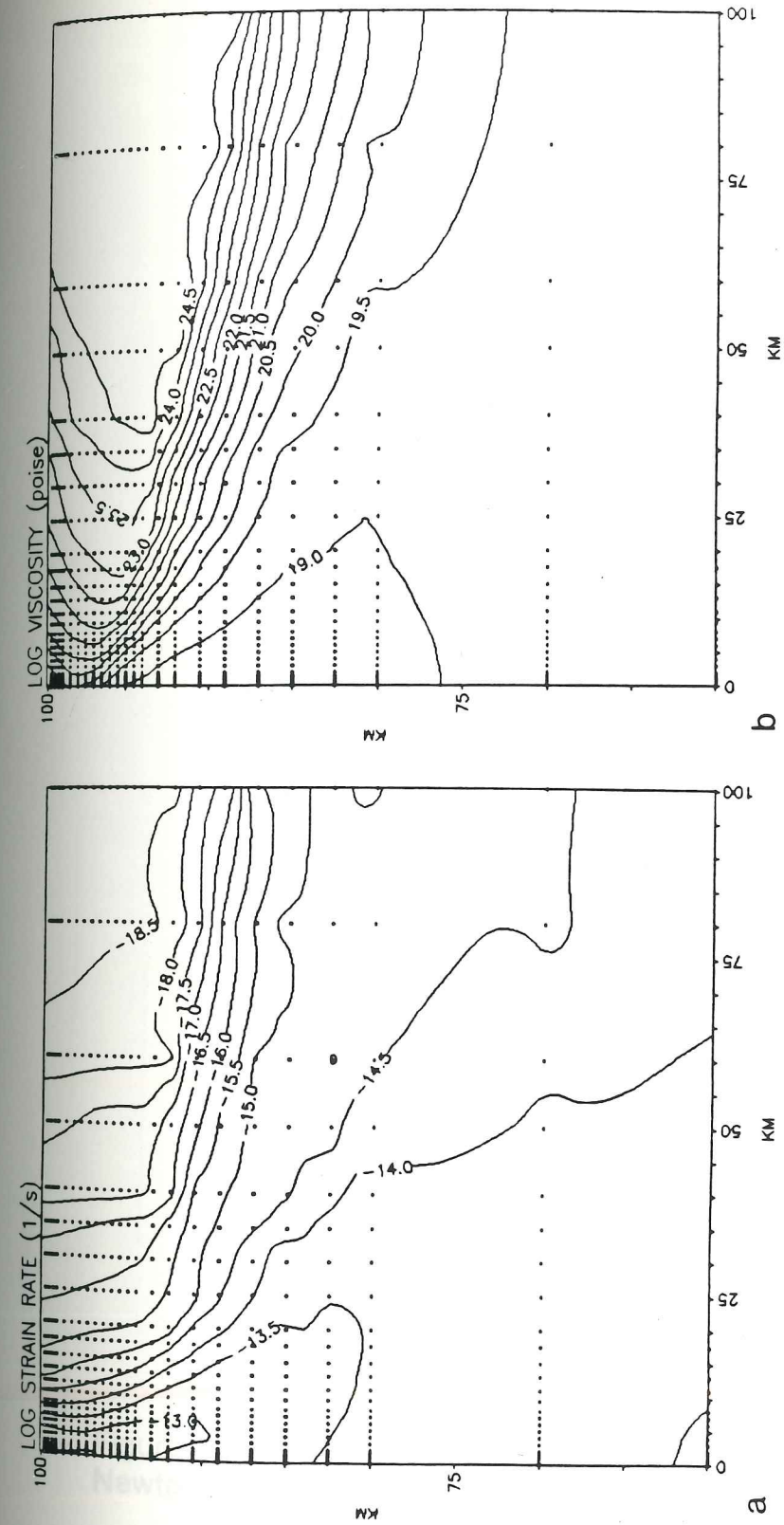
Figure 47. Strain rate and viscosity fields for $T_m = 1300°C$ with Newtonian rheology and without a cooled crustal layer.
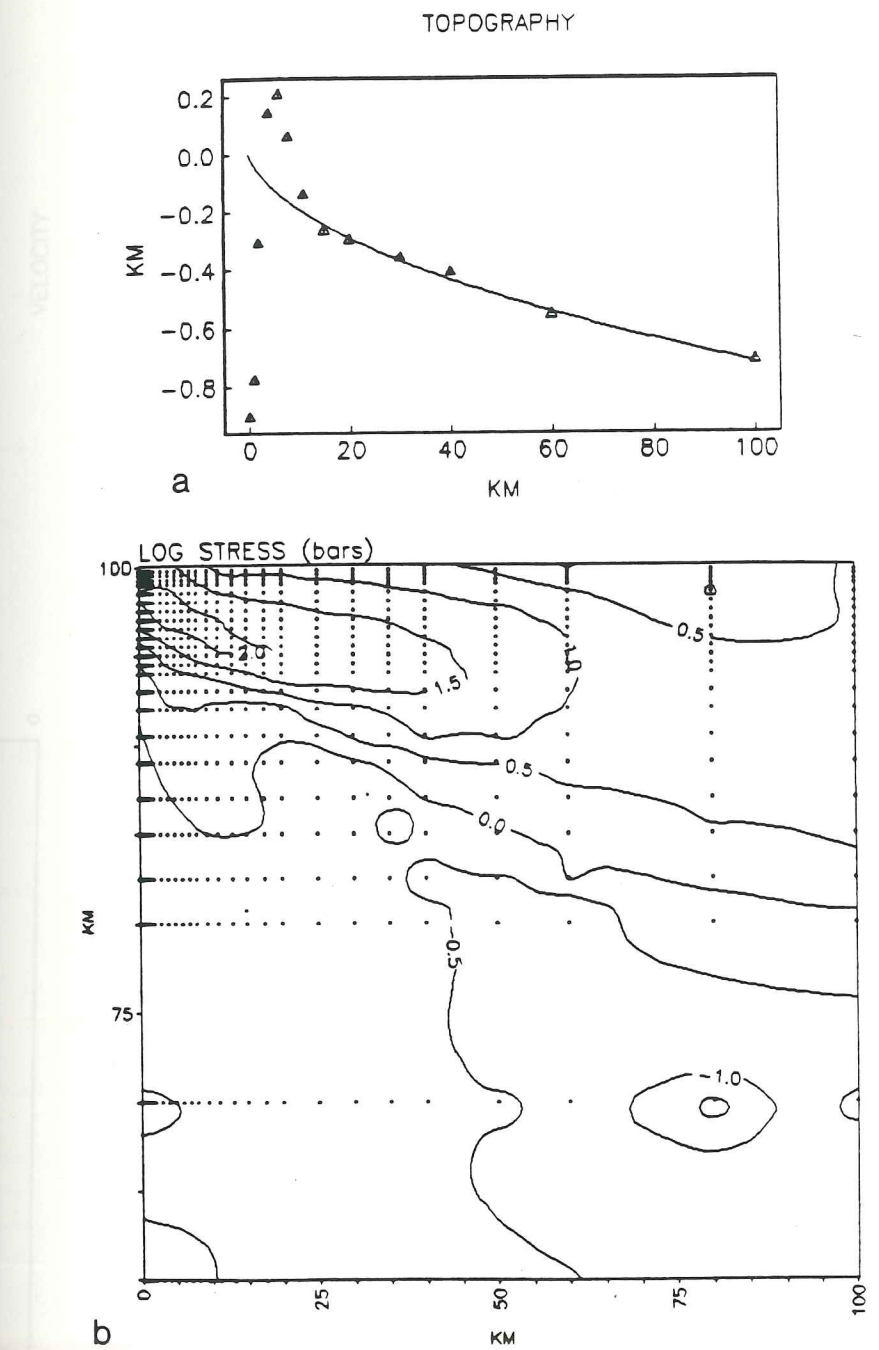
Figure 48. Stress field and topography for $T_m=1300°C$ with Newtonian rheology and without a cooled crustal layer.
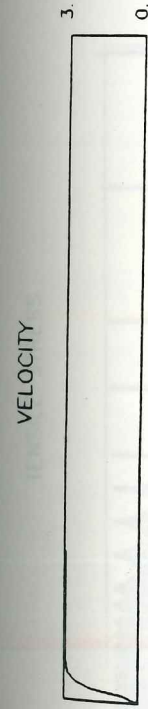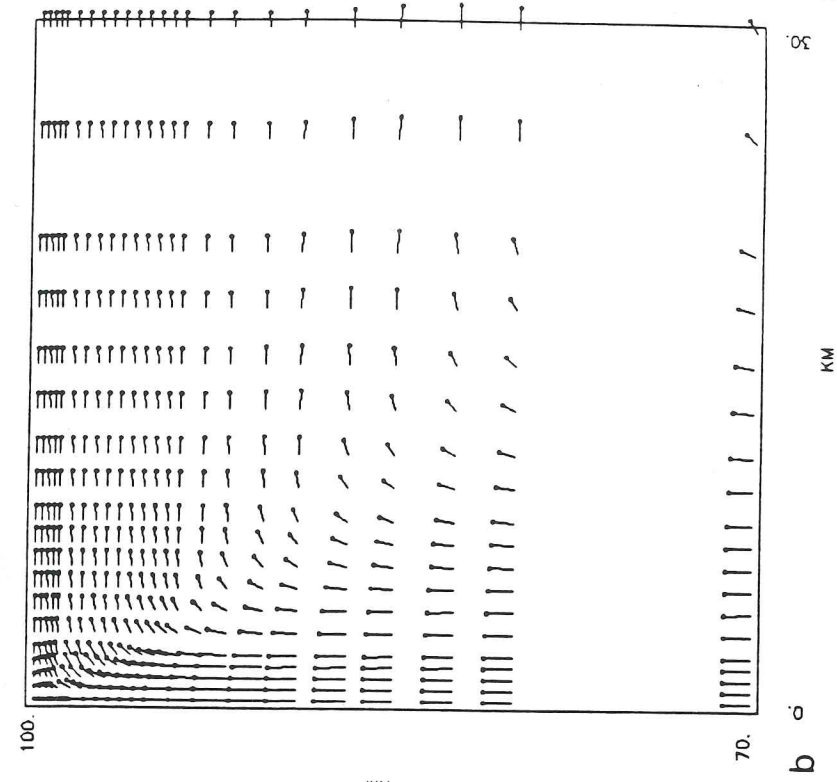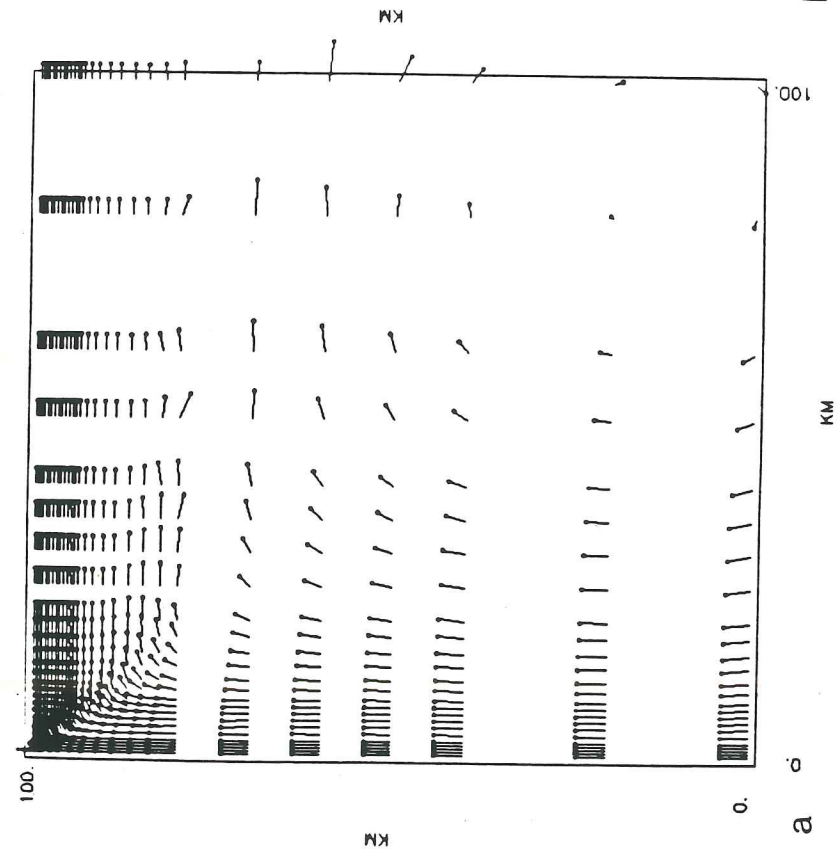
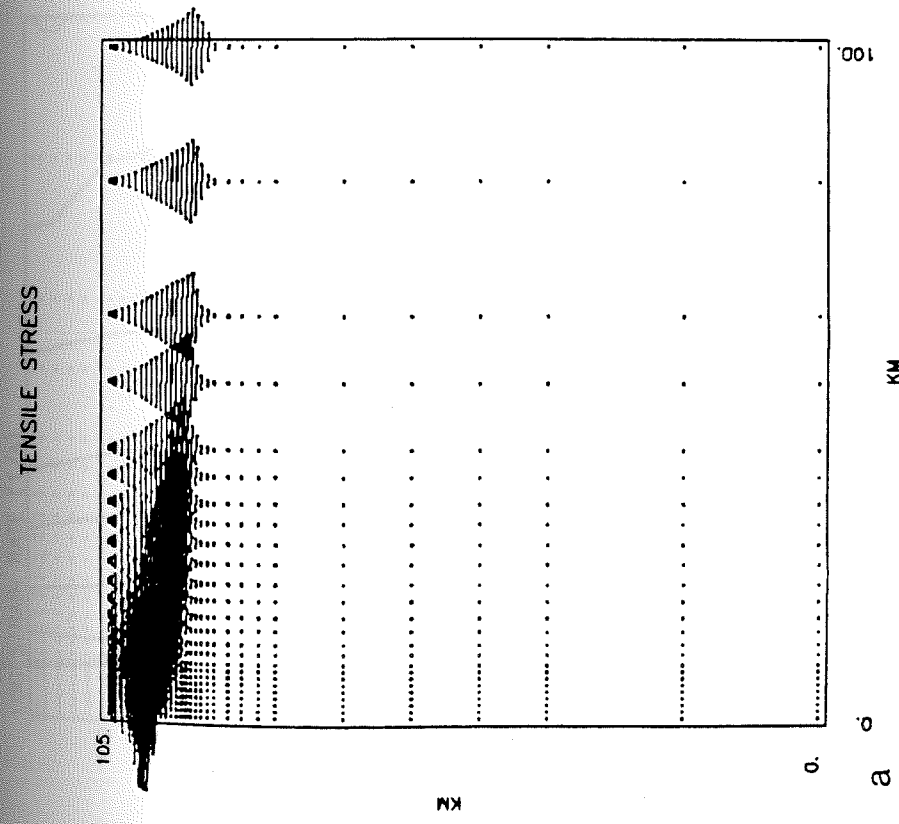Figure 49. Velocity field for $T_m = 1400°C$ with Newtonian rheology and without a cooled crustal layer.
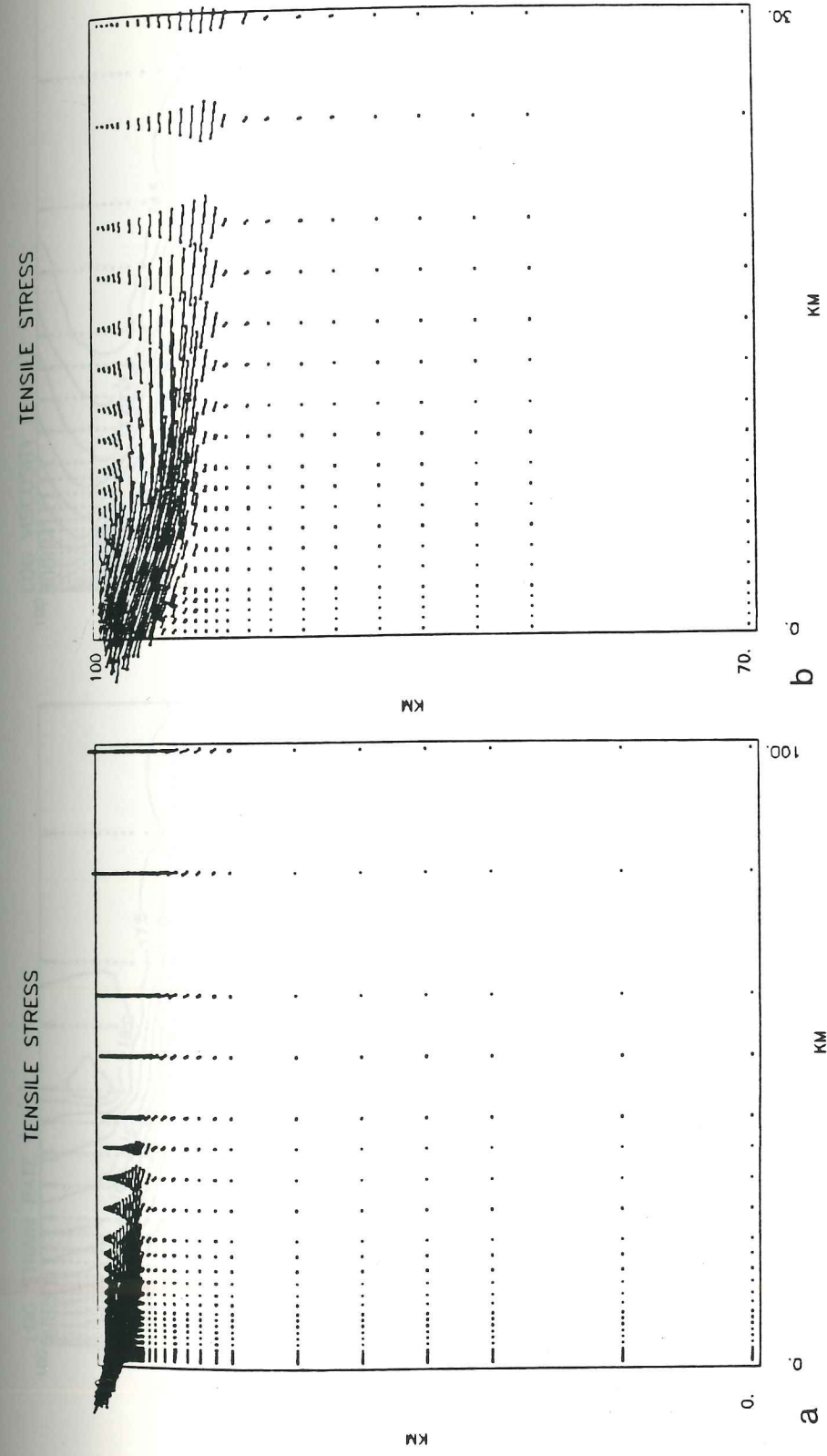
Figure 50. Tensile stress field for T_m=1400°C with Newtonian rheology and without a cooled crustal layer.
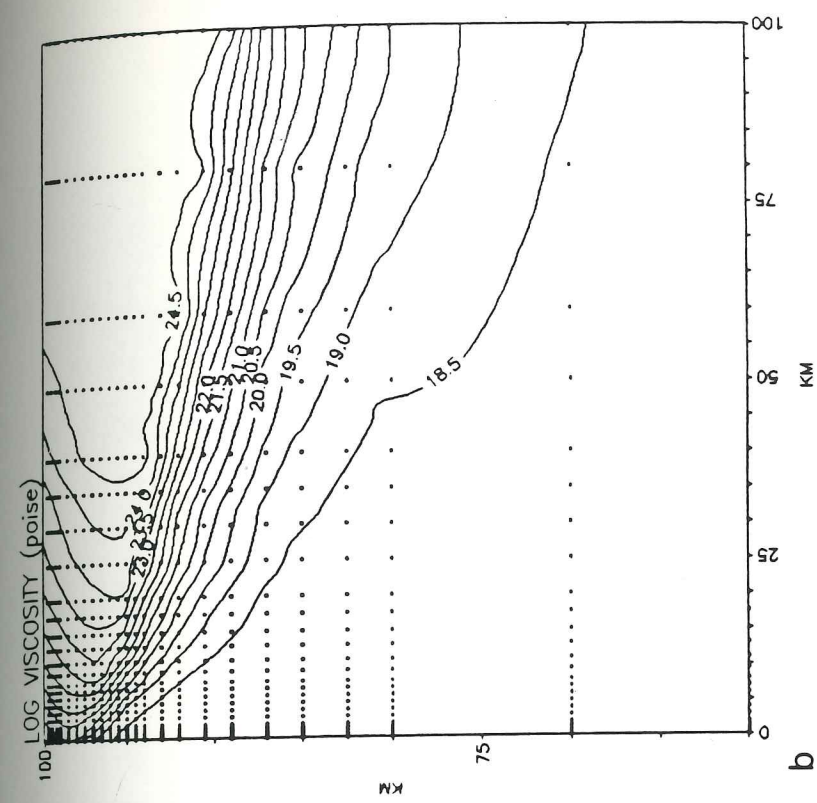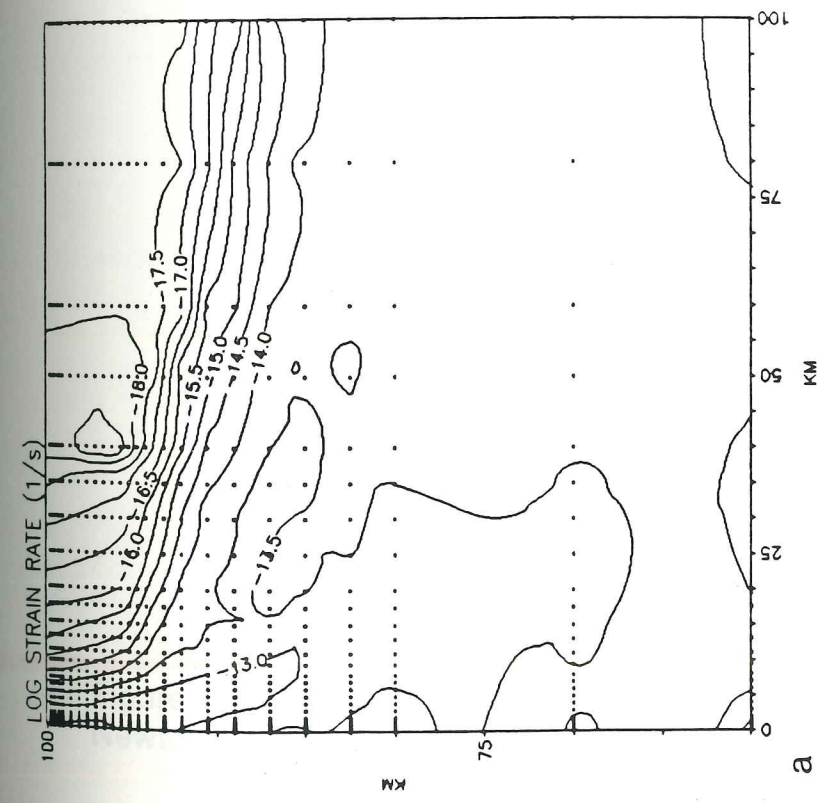
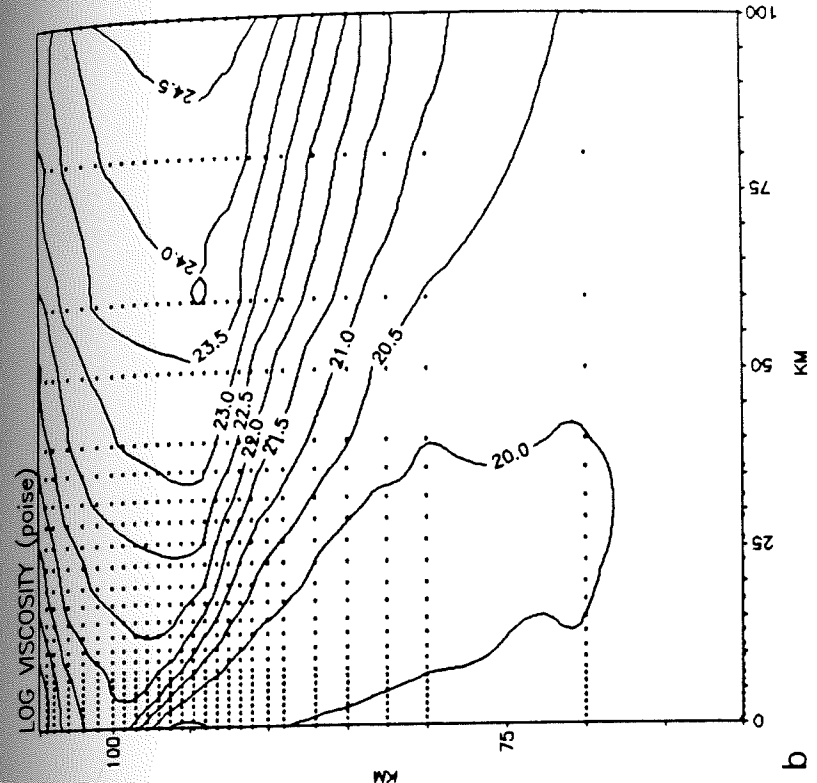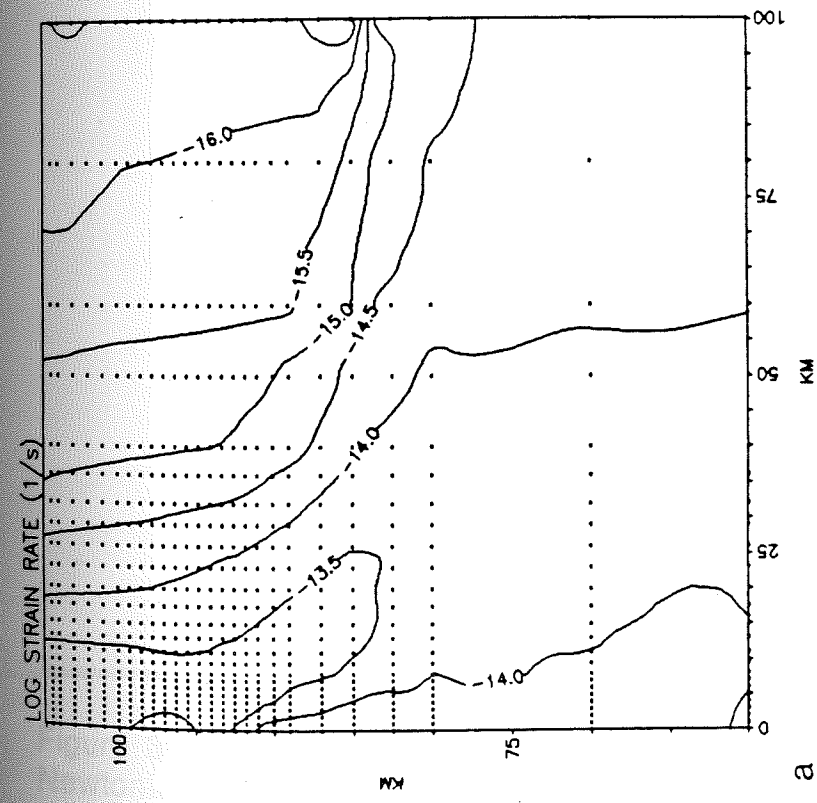Figure 51. Strain rate and viscosity fields for $T_m = 1400°C$ with Newtonian rheology and without a cooled crustal layer.
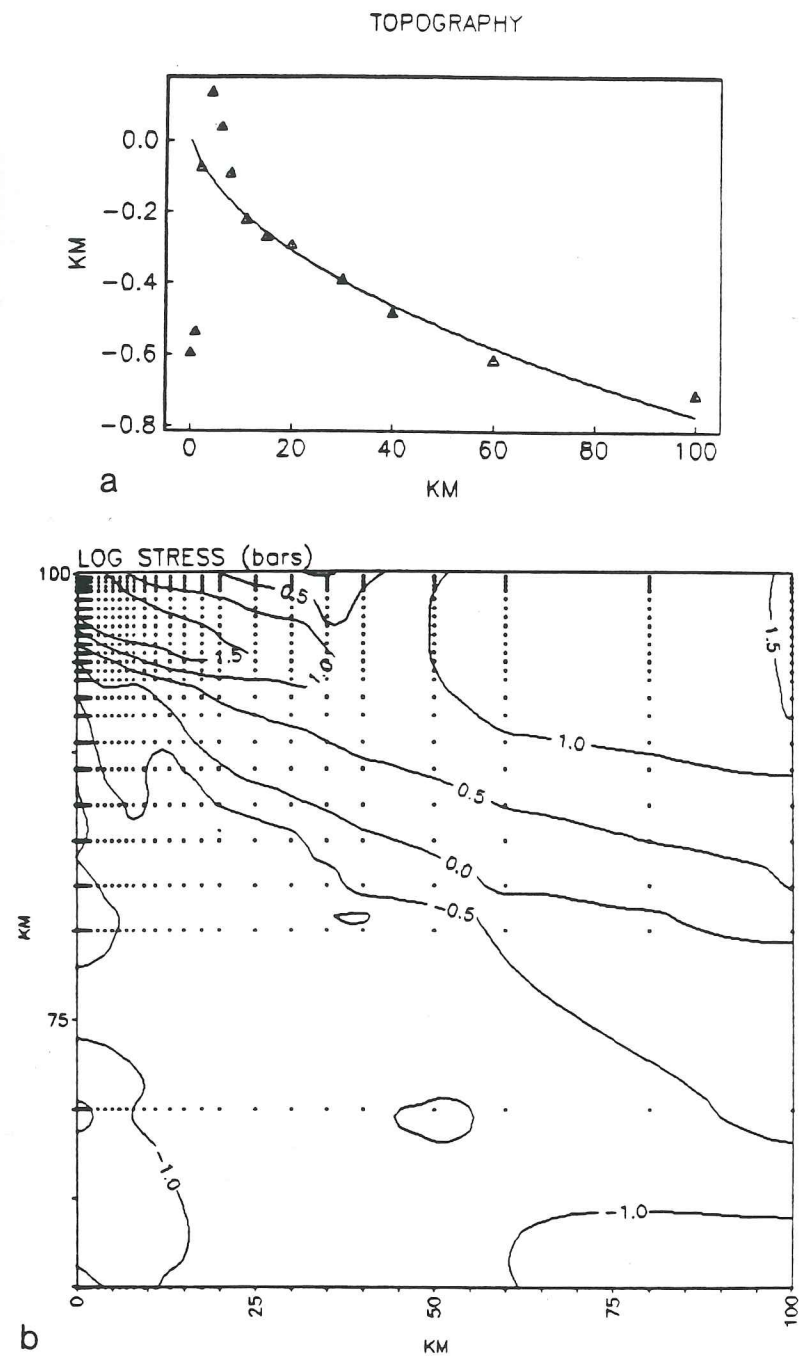
Figure 52. Stress field and topography for T_m=1400°C with Newtonian rheology and without a cooled crustal layer.
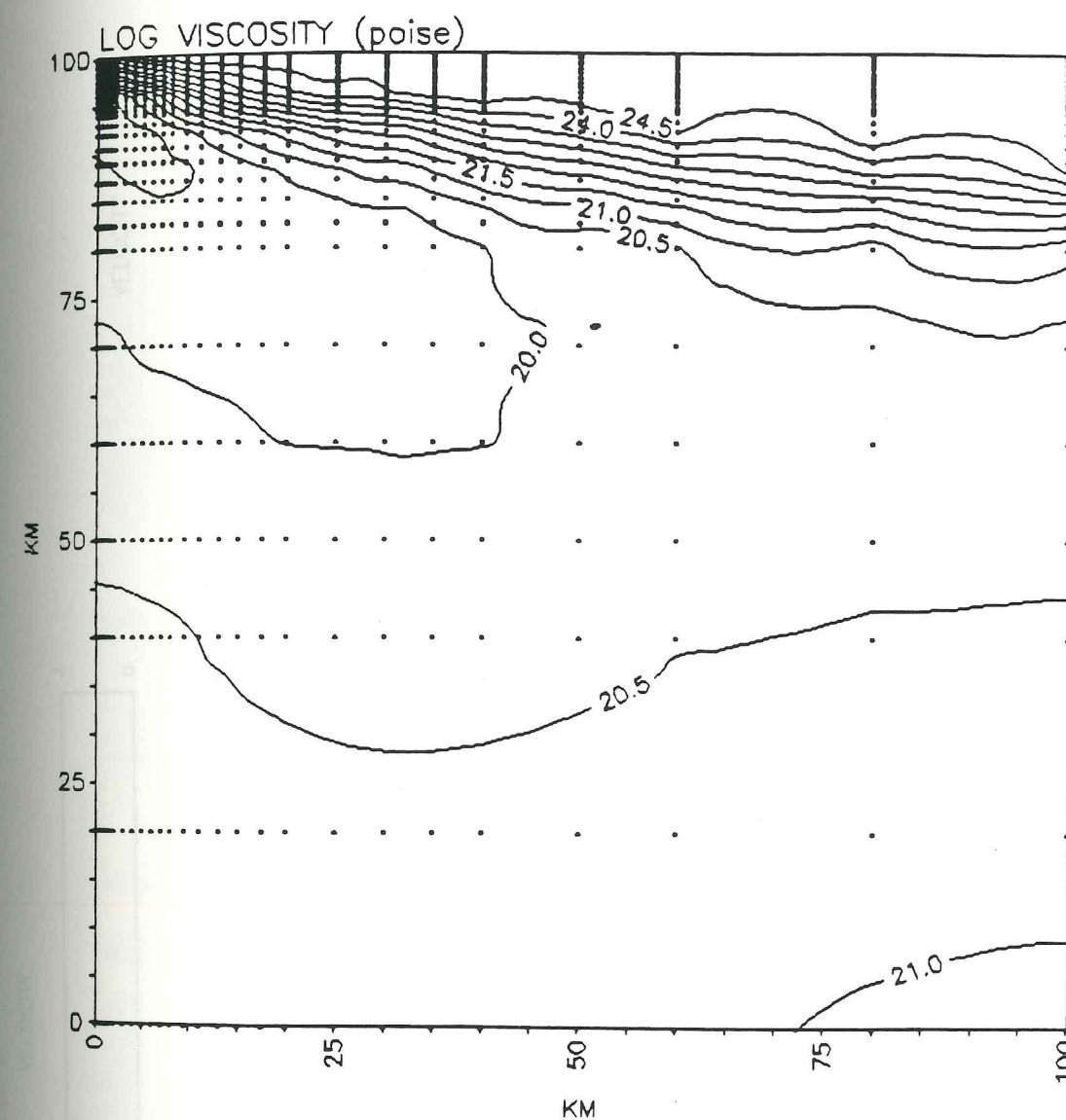
Figure 53. Non-Newtonian viscosity field for T_m=1300°C without cooled crustal layer.
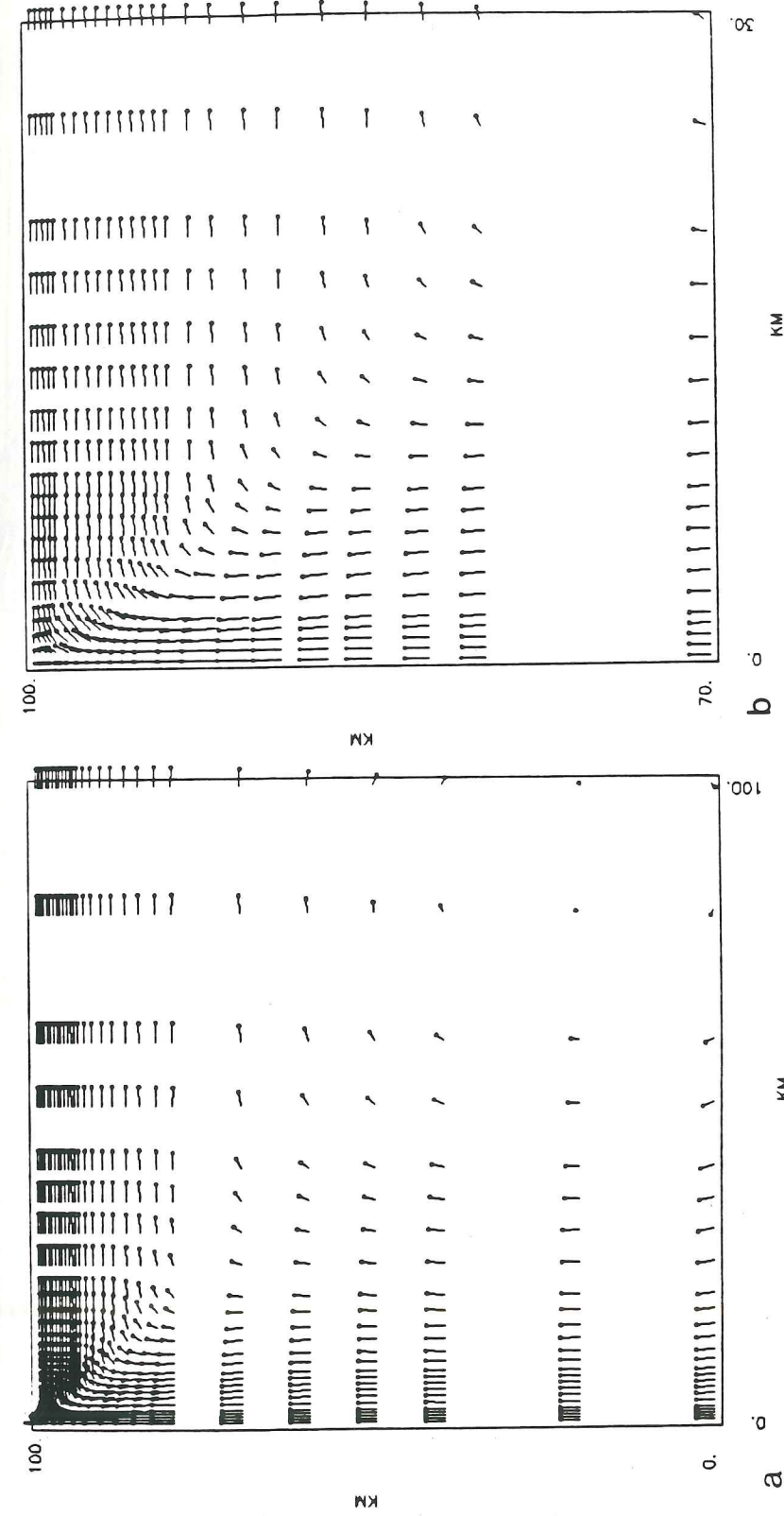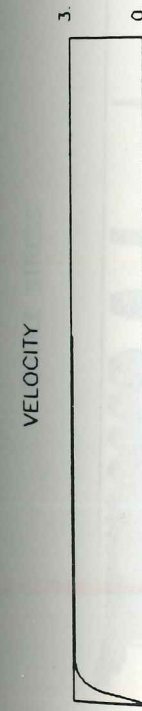
Figure 54. Velocity field for $T_m=1300°C$ with non-Newtonian rheology and without a cooled crustal layer.
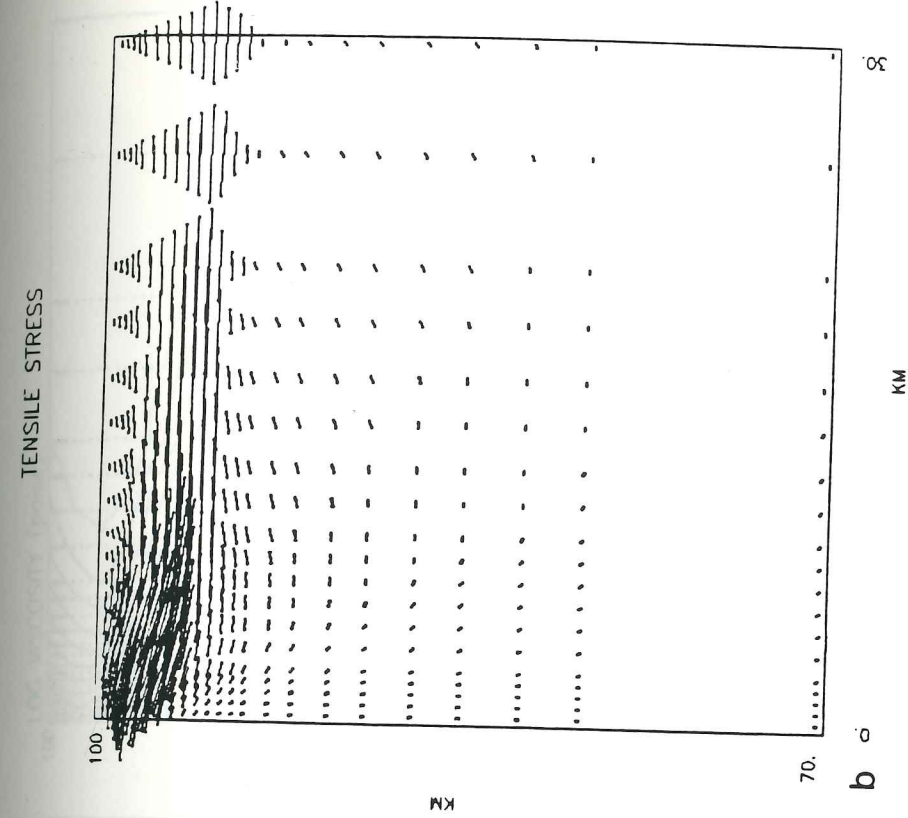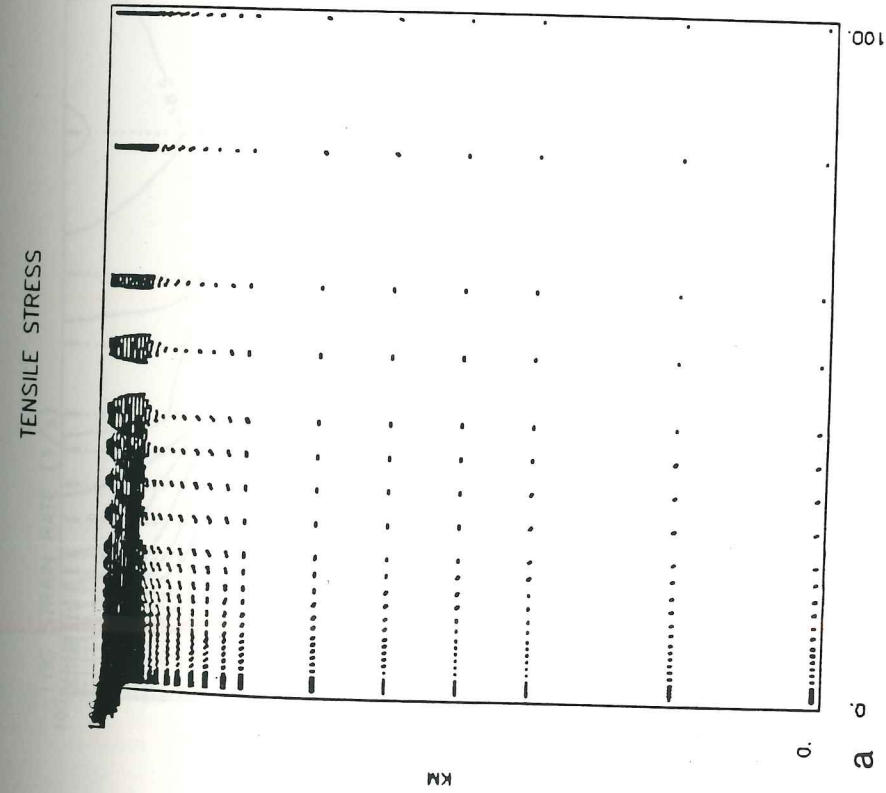
Figure 55. Tensile stress field for $T_m=1300°C$ with non-Newtonian rheology and without a cooled crustal layer.

109
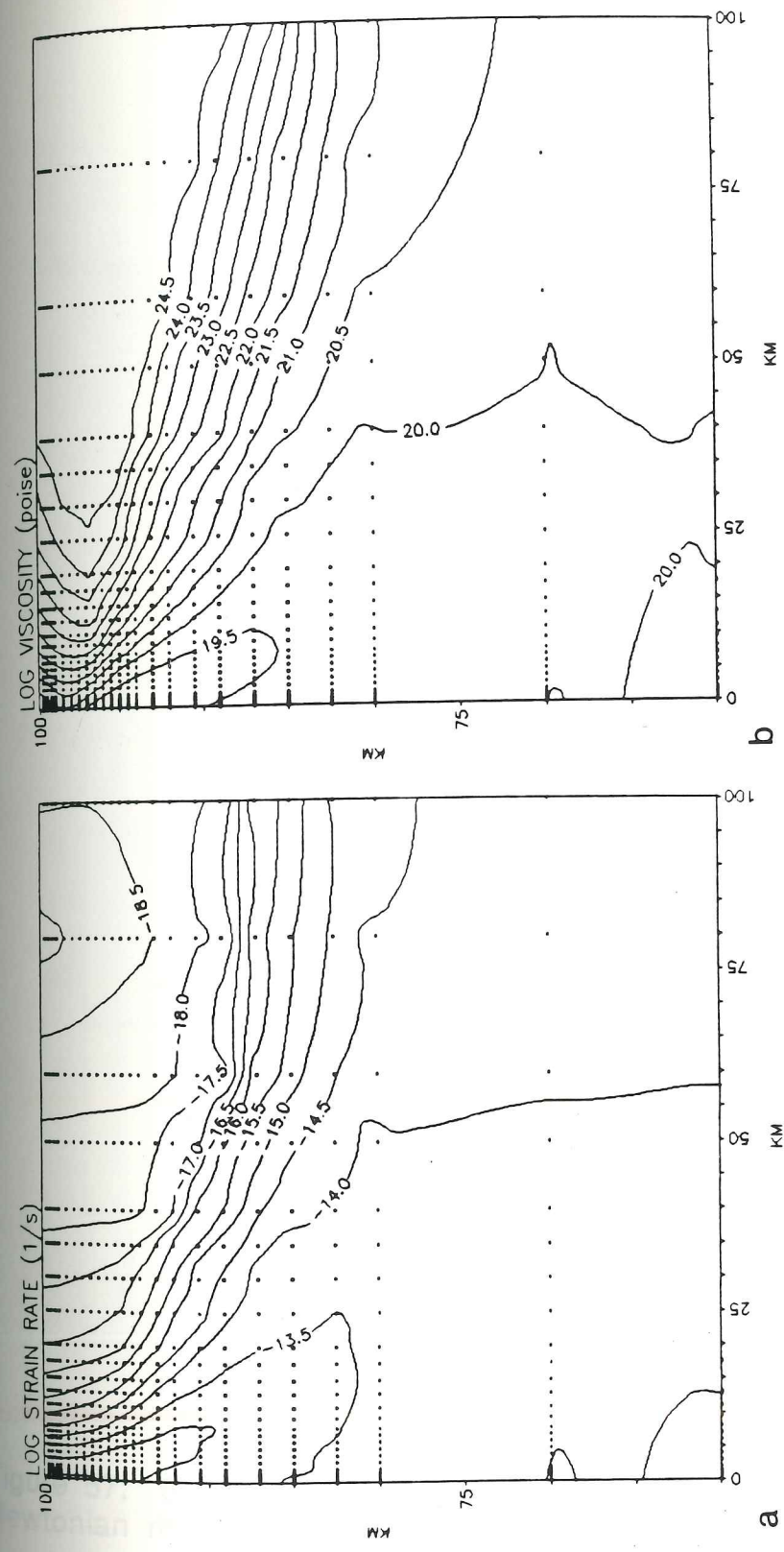
Figure 56. Strain rate and viscosity fields for $T_m = 1300°C$ with non-Newtonian rheology and without a cooled crustal layer.
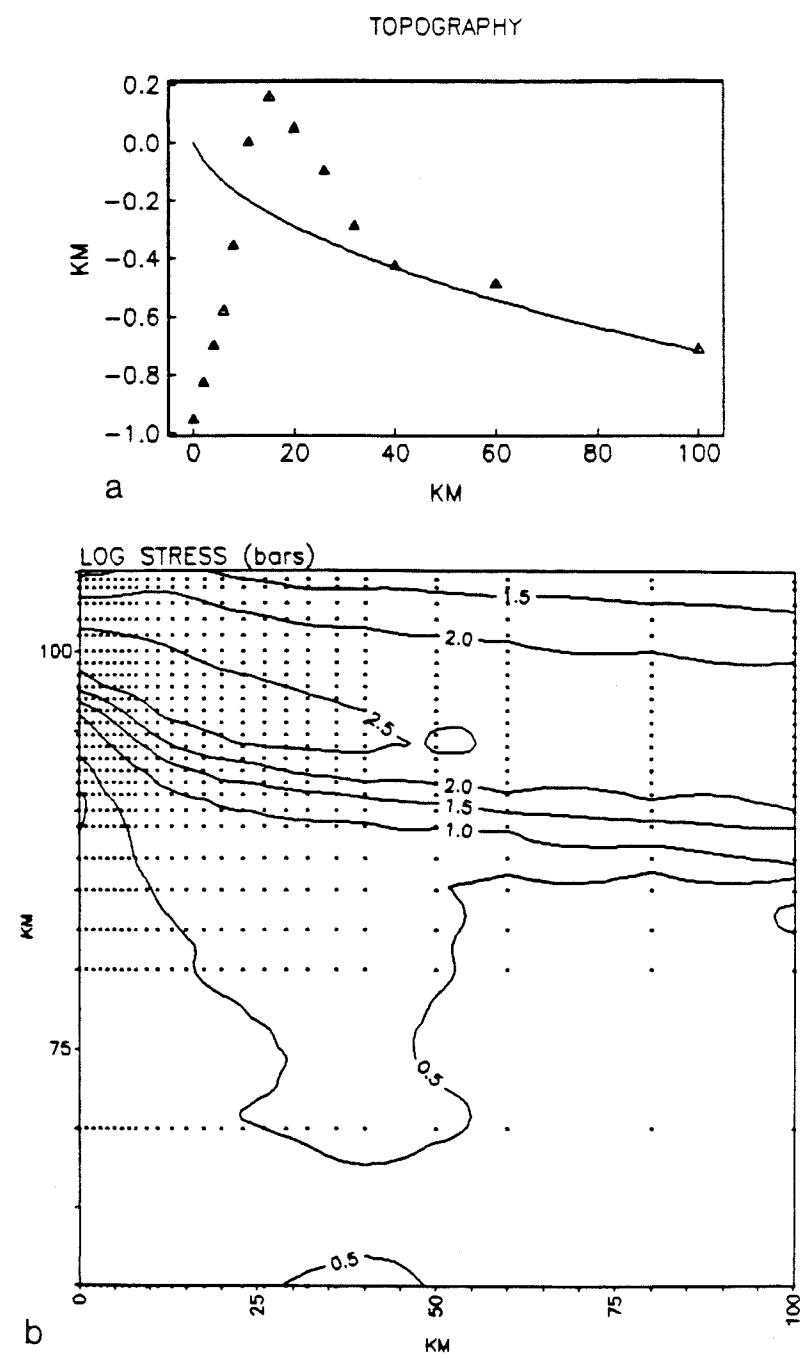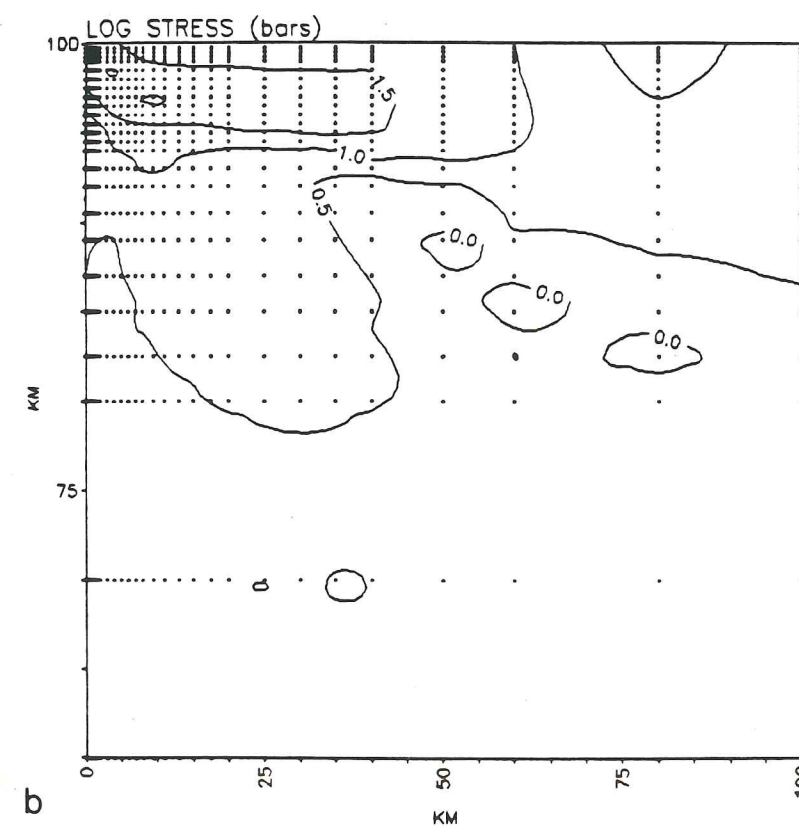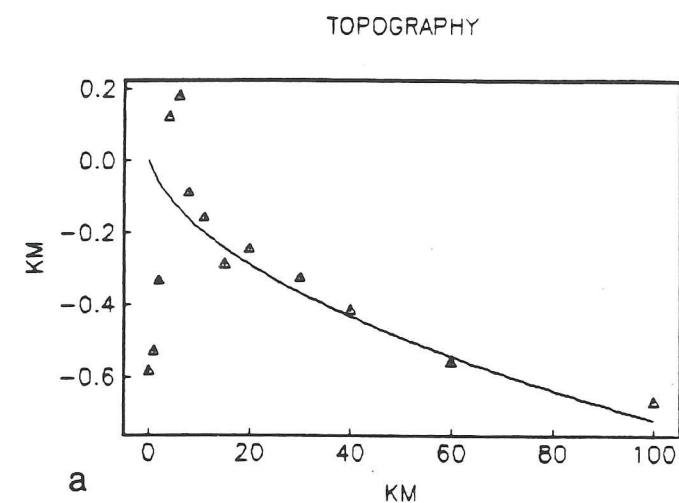
Figure 57. Stress field and topography for $T_m=1300°C$ with non-Newtonian rheology and without a cooled crustal layer.
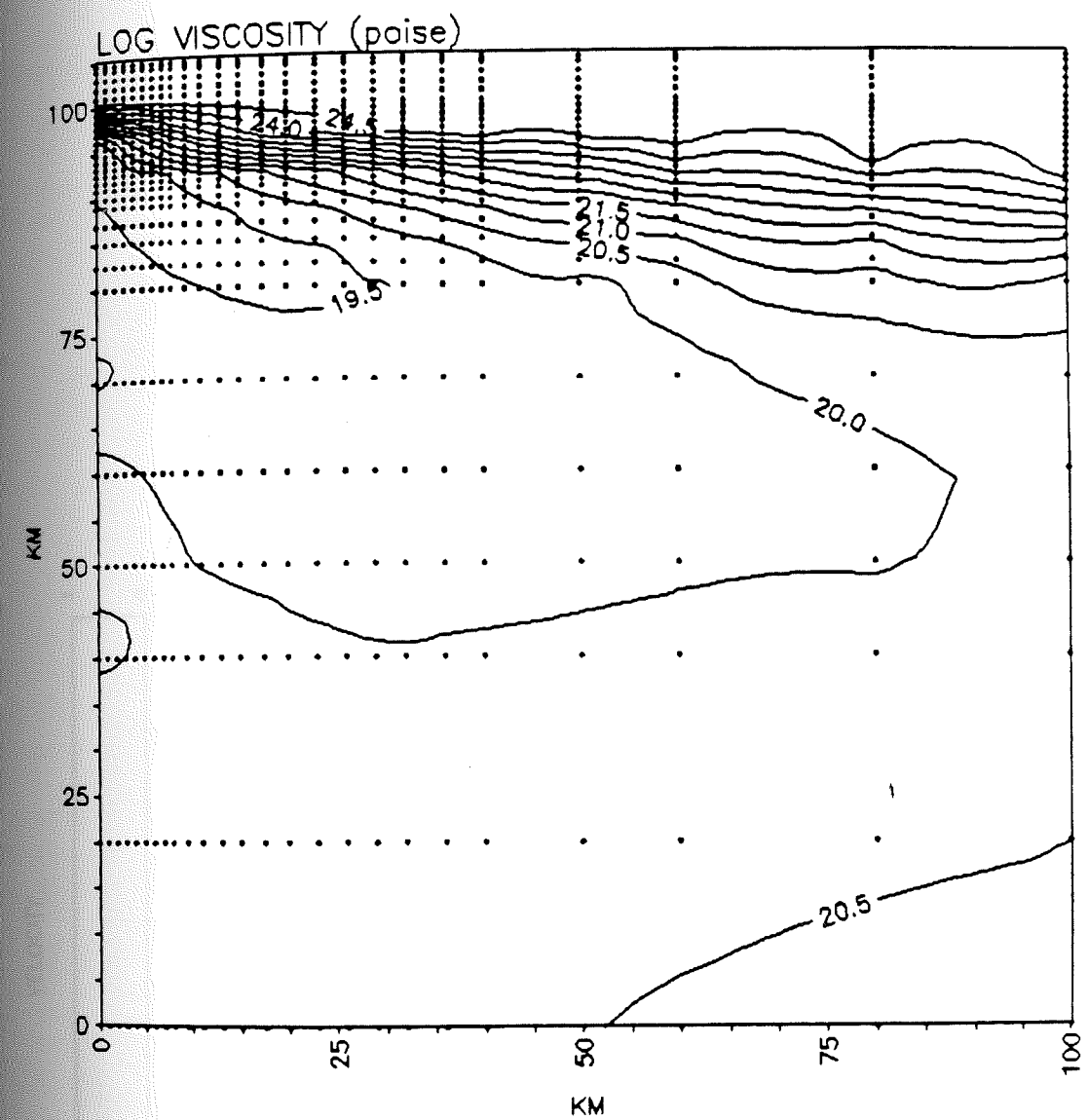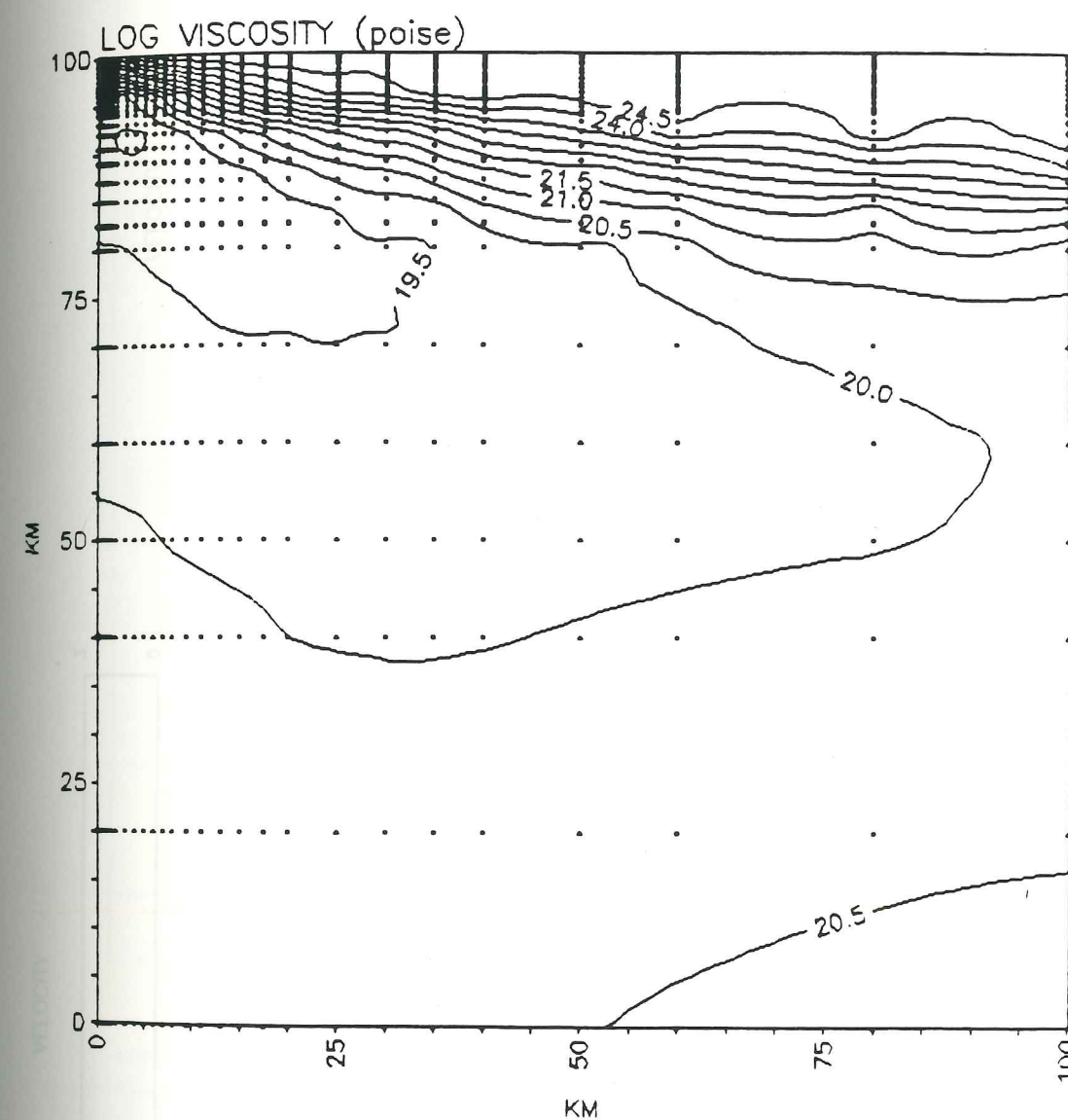
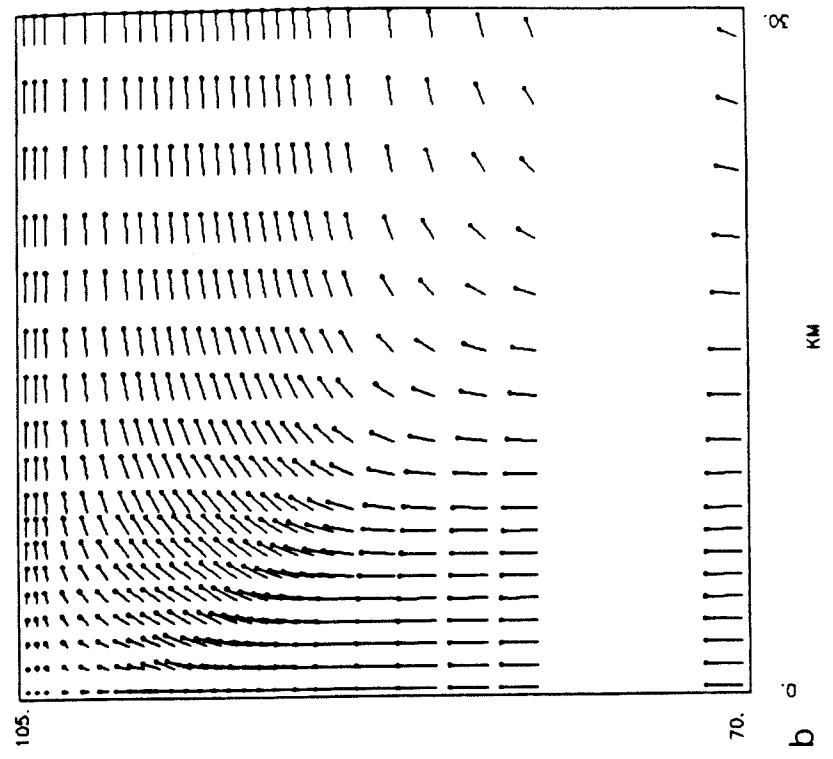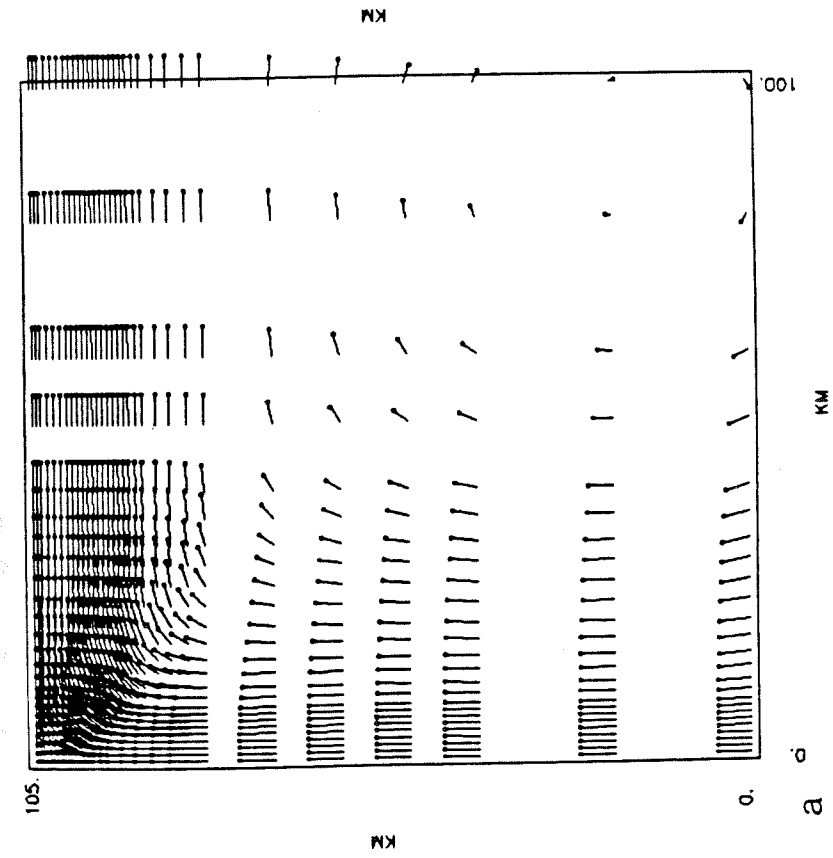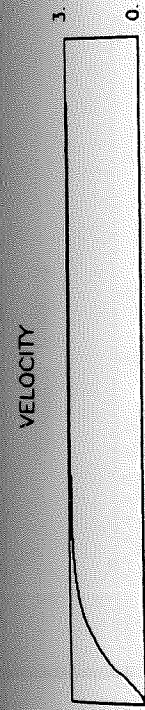Figure 58. Non-Newtonian viscosity field for T_m=1400°C without cooled crustal layer.
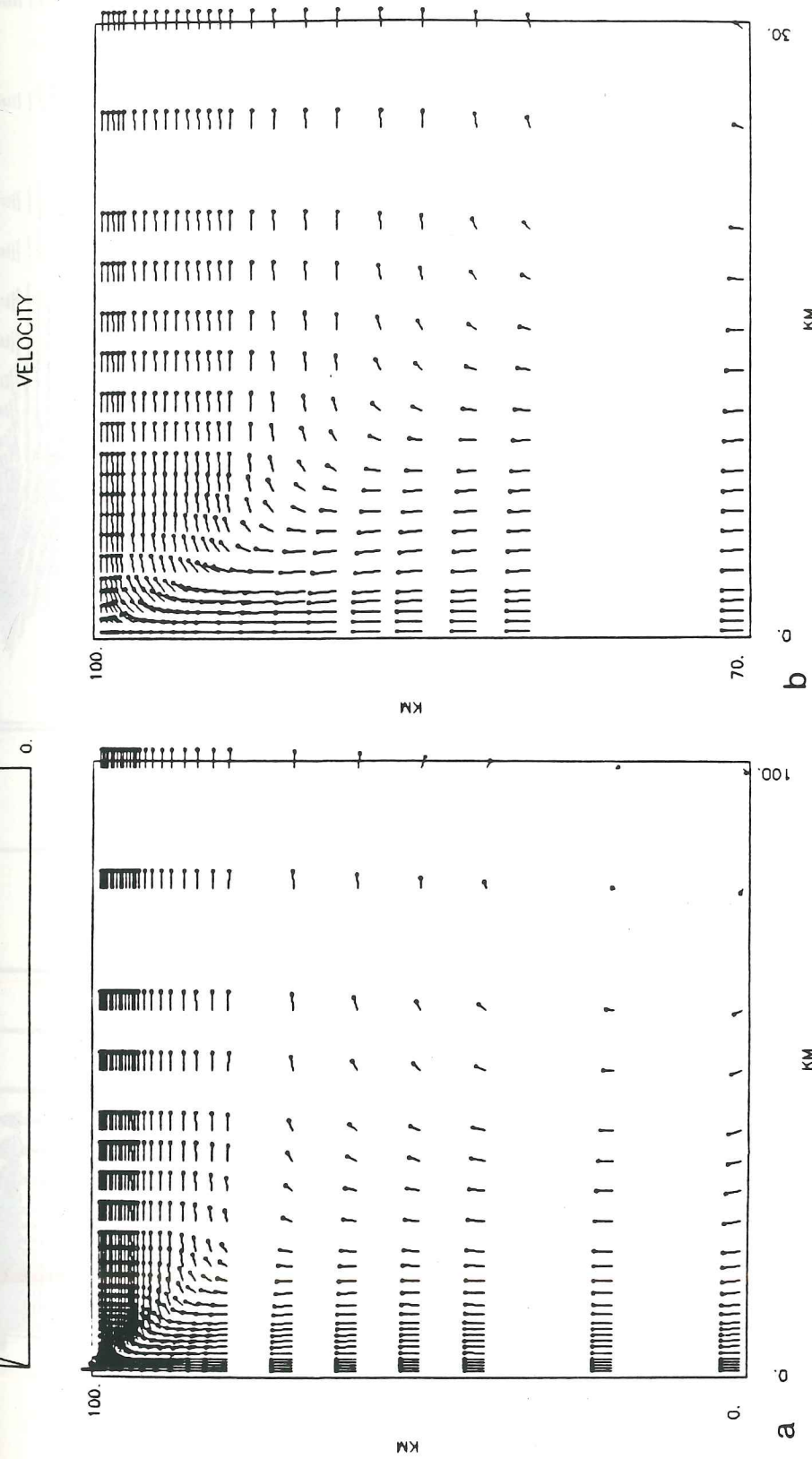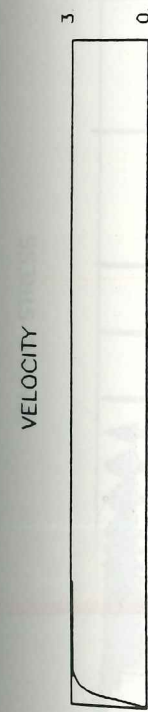
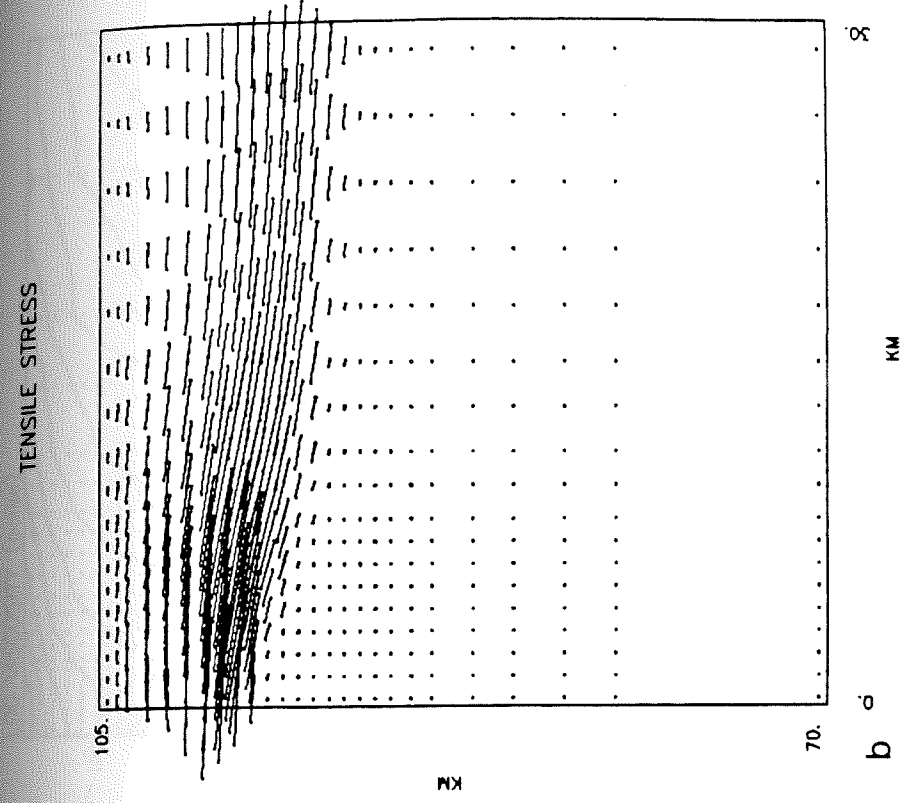Figure 59. Velocity field for $T_m=1400°C$ with non-Newtonian rheology and without a cooled crustal layer.
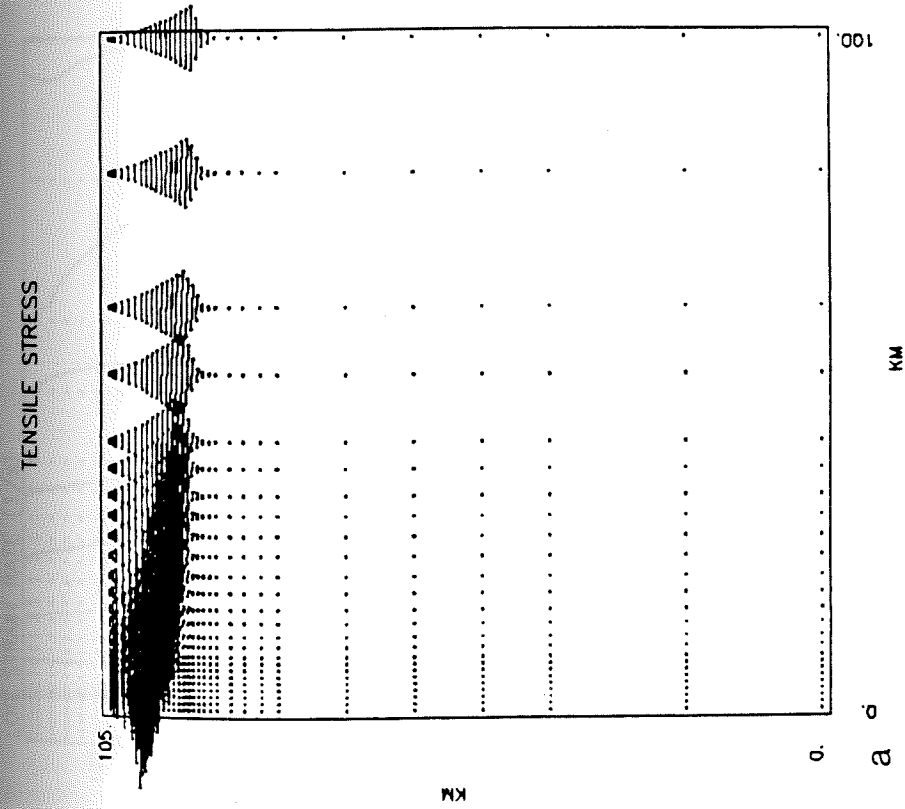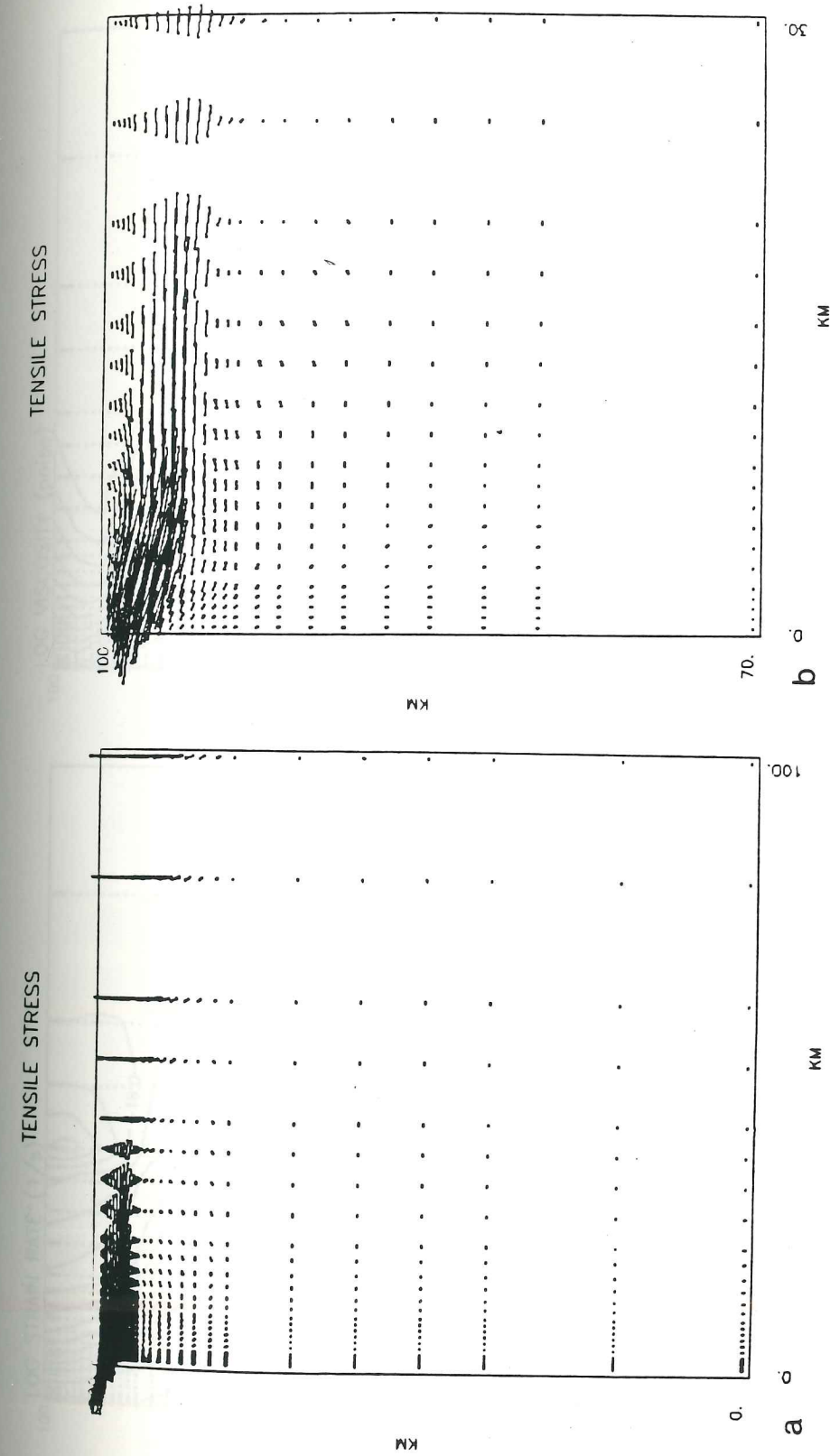
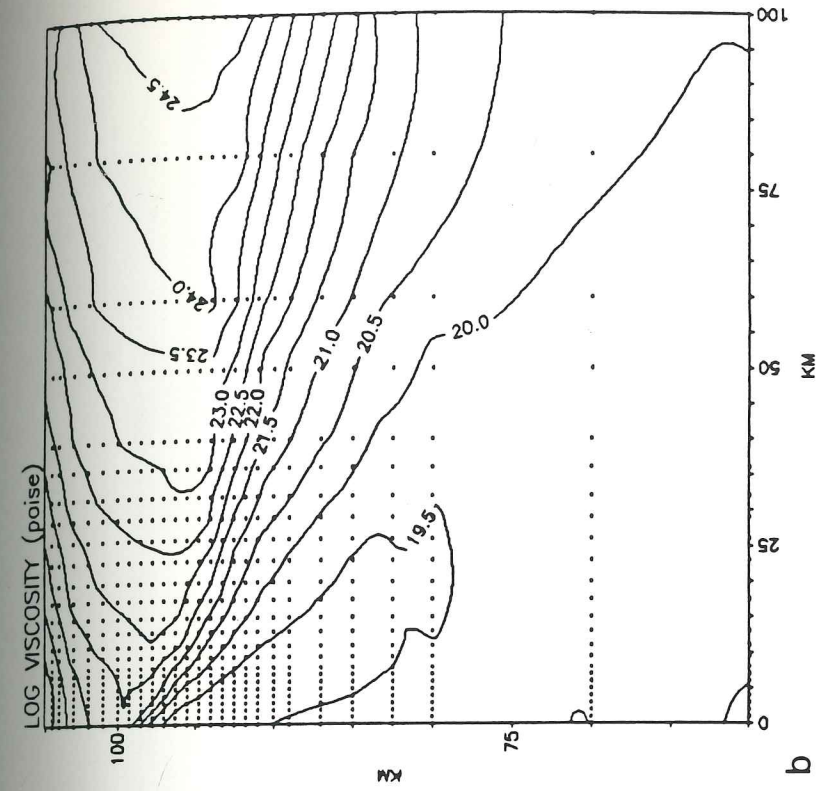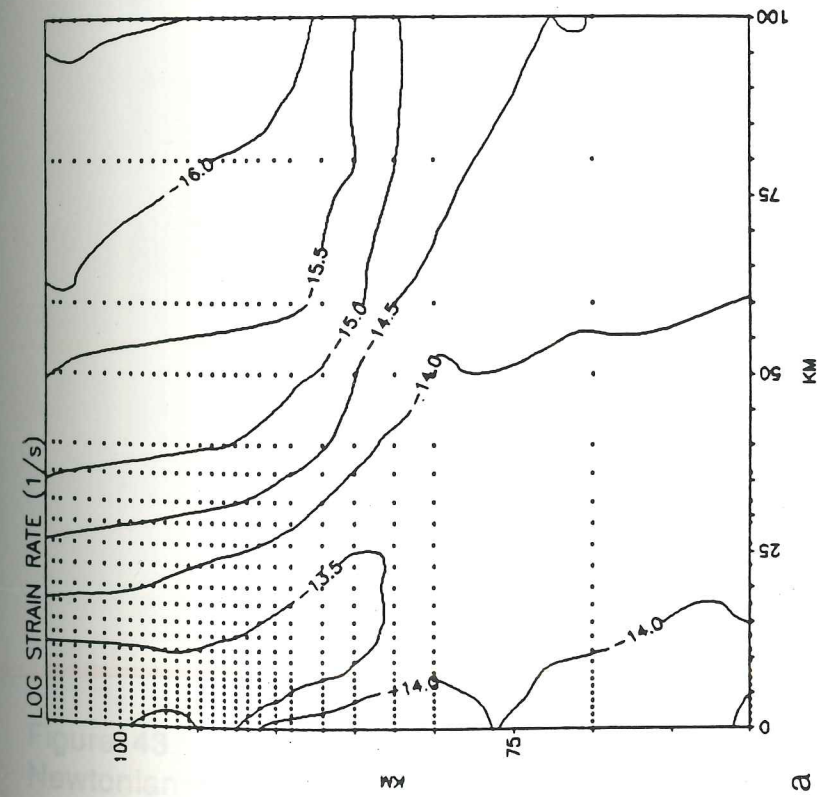Figure 60. Tensile stress field for $T_m = 1400°C$ with non-Newtonian rheology and without a cooled crustal layer.
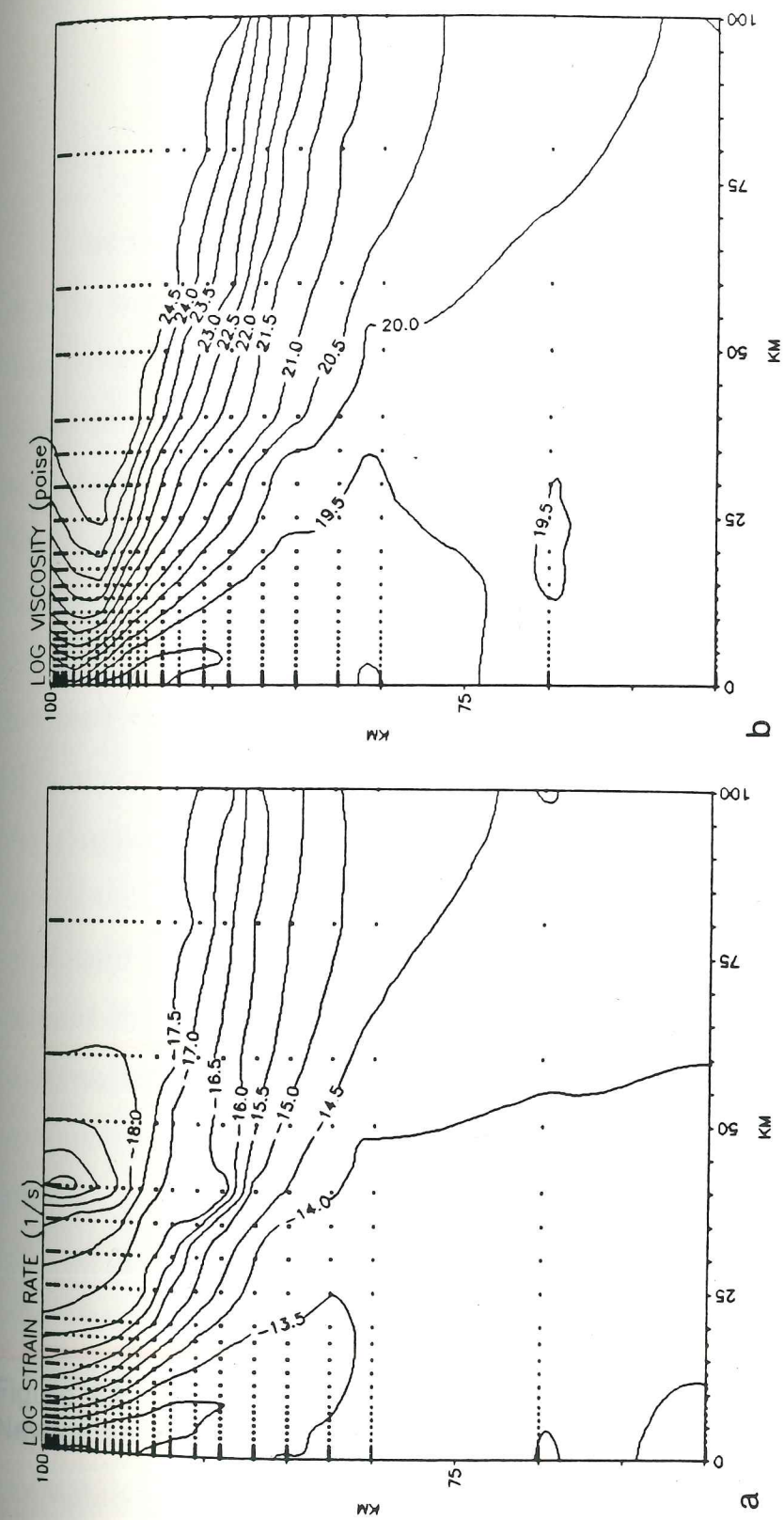
Figure 61. Strain rate and viscosity fields for T_m=1400°C with non-Newtonian rheology and without a cooled crustal layer.
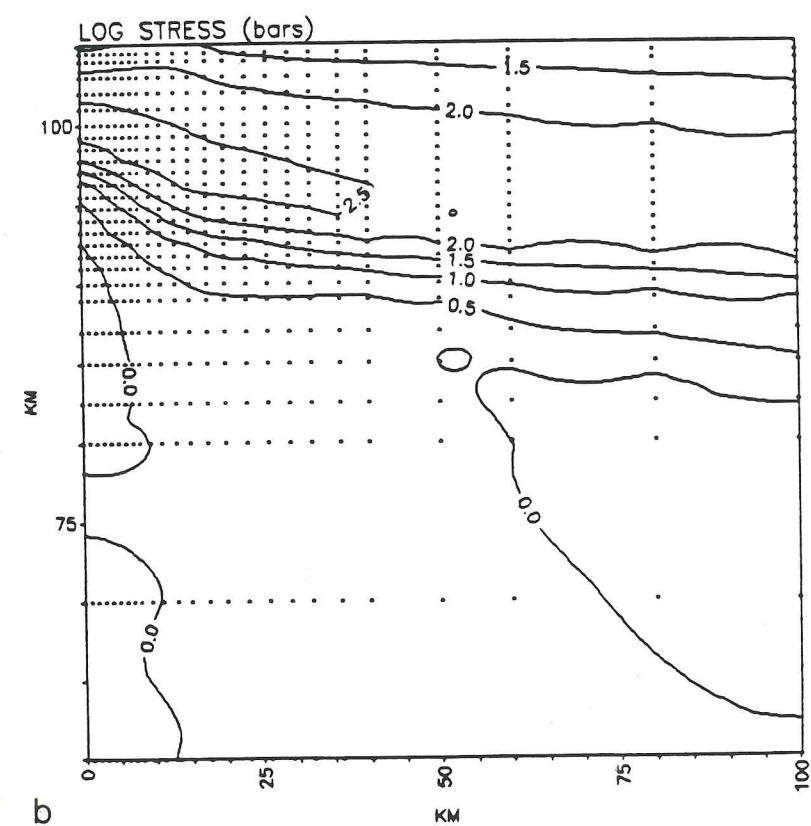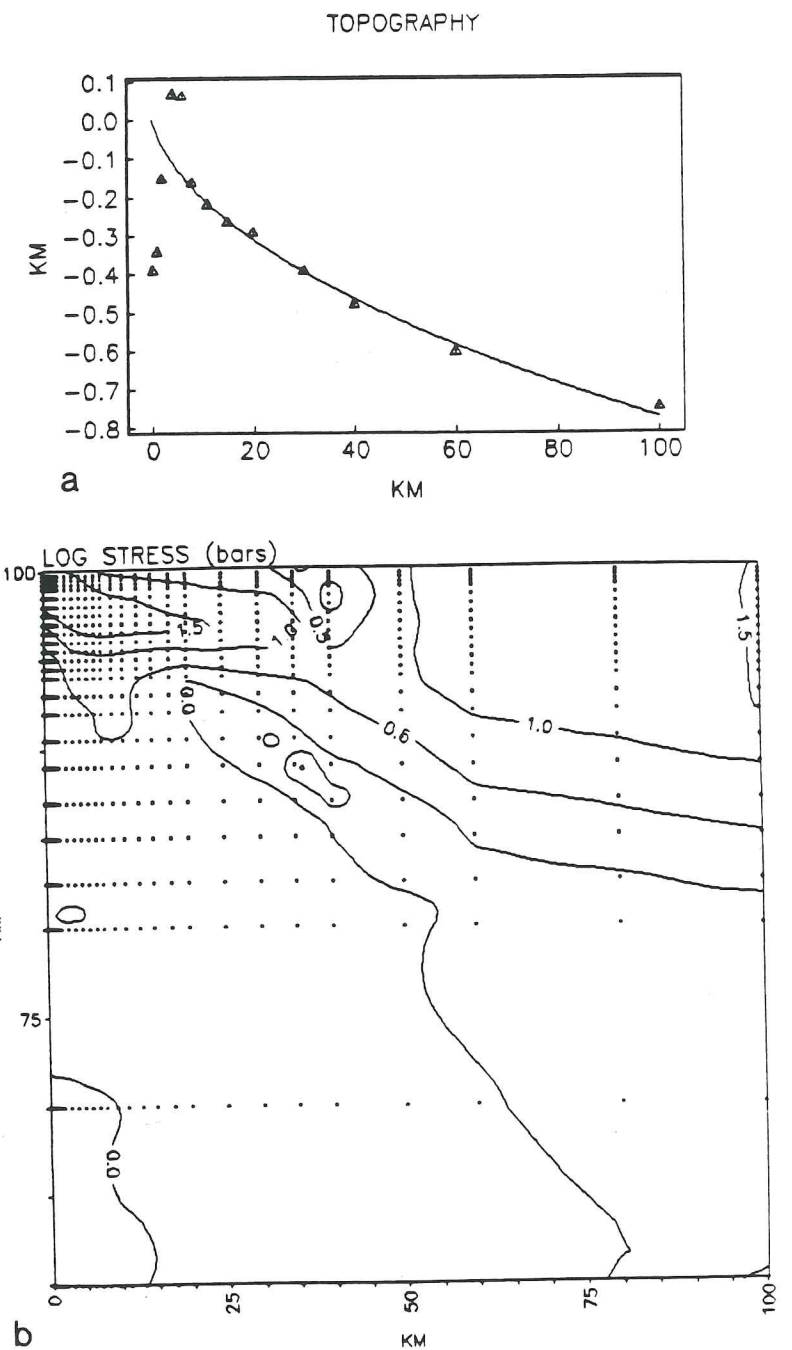
Figure 62. Stress field and topography for T_m=1400°C with non-Newtonian rheology and without a cooled crustal layer.

The Effects of Partial Melting

In the previous chapter, the viscous flow of solid rock in the mantle was considered. However, pressure release of the upwelling mantle will cause some components of the rock to undergo a solid to liquid phase change. A melted fraction of mantle rock will accumulate in the interstitial spaces between crystals (Waff, 1986). This melted fraction must be transported to the crust where it solidifies to form either basalts or gabbros depending on cooling rates. The transport mechanism is not known. Several hypotheses for melt transport have been put forward (Shaw, 1980; Spera, 1980). One mechanism is the porous flow of melt through the solid matrix. As mantle rock melts through pressure release, the melt in the interstitial spaces becomes interconnected. The buoyancy of the melt and pressure gradients in the mantle will drive the melt toward the surface at the axis where melt may accumulate in a magma chamber. A second hypothesis is that a fracturing mechanism could transport concentrations of melt through the solid matrix. The melt is driven by the same forces that would drive porous flow. A third hypothesis is that the presence of melt reduces the density and viscosity of the surrounding matrix and a partially melted region rises as a diapir. As it rises, more of the mantle rock will melt and fractionate and eventually the diapir may become completely liquid.

It is likely that all three transport mechanisms take place at some point in the process of transferring melt from its melting level to the crust. However, it is not known which process dominates at any level or in what order they may take place. The width of the melt transport zone and the velocity of melt transport are also unknown. Furthermore, very little is known about the physical properties of partially molten rock.

Simulating Partial Melting in the Mantle

Since there are so many unknown facts about the presence and movement of partial melt in the mantle it would be impossible to accurately model the effect of partial melt on viscous flow. Instead I wish to investigate whether partial melt in the mantle can have any effect on ridge crest topography. The viscous head loss theory for ridge crest topography is based on the assumption that all the vertical motion of the mantle takes place in a narrow conduit. The velocity fields shown in the previous chapter all have wide regions of upwelling beneath the ridge. If the buoyancy of melt was the only force driving melt to the surface, magma would be expected to extrude in a wide zone on both sides of the axis. However, volcanic extrusion is limited to a very narrow zone (less than 2 kilometers wide at the East Pacific Rise) at the axis (Macdonald, 1982). Pressure gradients driving porous flow in the mantle have been postulated as one way to concentrate melt at the axis (Phipps Morgan and Forsyth, in press). The alternative is that the width of the upwelling zone is much narrower than in the previous models.

The narrowing of the upwelling zone is to be simulated in a rather arbitrary way.

The percentage of melt present at a point will be a function of a number of factors. First, the temperature must be greater than the solidus of the mantle. The solidus is dependent on the pressure and, consequently, the depth at the point. The percentage of melt will be proportional to the amount by which the temperature exceeds the solidus temperature. Furthermore, a volume of rock that has undergone a larger vertical motion and therefore a greater pressure release will have a larger fraction of melt than a volume which hasn't undergone as much vertical motion.

These effects will be simulated in the following manner. First, a velocity field is calculated using the parameters obtained from the Davis and Lister temperature model. The solidus T_s is approximated by a linear depth dependence,

$$T_s(z) = 1100°C + 3.33\ z$$

where z is the depth in kilometers (Phipps Morgan and Forsyth, 1988). The temperature at every point will be increased by the amount by which the temperature exceeds the solidus multiplied by the ratio of the vertical velocity at that point to the maximum vertical velocity. The purpose is not to imply that the temperature is greater in these regions but to obtain lowered viscosity in regions of partial melting. The viscosity of basaltic melt at 1200°C is 100 to 1000 poise (Delaney and Pollard, 1982). Even a small amount of

partial melting will yield orders of magnitude reductions in viscosity. The new viscosity field is calculated using

$$\mu = \frac{T}{2B_1} \exp\left(\frac{E^* + PV^*}{RT}\right)$$

with $B_1 = 0.0024$ cm s °K/g, $E^* = 95$ kcal/mole, and $V^* = 10$ cm^3/mole, from which a new velocity field is derived. This process can be repeated several times to get low viscosities under the axis where the upwelling is fastest.

Lowering Viscosity

In the following examples, the starting temperature field was the Davis and Lister field for $T_m = 1300°C$. There is no hydrothermally cooled crust and Newtonian viscosity fields are used in all the subsequent solutions. Figure 63a shows the temperature field after three iterations and Figure 63b shows the corresponding viscosity field. The density field used was the density field for $T_m = 1300°C$ without partial melt (Figure 11b). The viscosity falls below 10^{16} poise, 5 to 10 kilometers beneath the axis.

The results from using this viscosity field in the finite element program are shown in Figures 64-67. These figures should be compared to Figures 45-48 where $T_m = 1300°C$ but viscosities are not lowered. The horizontal velocity at the surface reaches the spreading rate of 3 cm/yr at a distance of 4 kilometers from the axis similar to the surface velocity in Figure 45a. There is now a

narrow region of rapid upwelling under the axis. This narrowing is best seen in Figure 64b. The maximum vertical velocity is 37.5 cm/yr. The tensile stress plots (Figures 65 and 67b) show horizontal tension out to 40 kilometers from the axis. Beyond 40 kilometers, there is horizontal compression. The highly stressed layer is noticably thinner at the axis. The strain rate under the axis exceeds 10^{-12} sec^{-1}.(Figure 66a). The axial valley is 8 kilometers wide and 1.0 kilometers deep. This is only 100 meters shallower than the axial valley in Figure 48a.

Although partial melting of the upwelling mantle may have a significant effect on the viscosity under the axis and may cause the upwelling to form a narrow, fast-moving jet, it has little effect on the topography. Viscosities, and therefore stresses, are already low in the mantle and lowering them further has no effect on stresses in the overlying brittle layer.

Lowering Viscosity and Density

Another effect of partial melting in the mantle is a reduction in density. The density of basaltic melt at 1200°C is 2.6-2.7 g/cm^3. Even a small percentage of partial melt can make a significant difference in density. An increased buoyancy force beneath the axis due to an accumulation of low density material may offset the forces responsible for the axial valley. If the buoyancy force is large enough, it may cancel the other forces and result in an axial peak since the isostatic thermal topography will be more elevated at

the axis than for the case without partial melt. The densities are calculated using

$$\rho(x,z) = \rho_m(1+\alpha(T_m-T(x,z)))$$

There was no attempt to correlate a specific viscosity to a specific density or percentage of melt. The same iterative procedure described before was used to raise temperatures in rapidly upwelling regions except that now both the viscosities and the densities are lowered on each iteration.

Figure 68a shows the temperature field after two iterations and Figure 68b shows the density field. The 3.275 g/cm^3 contour in the density field would correspond to 4% melt if the density of melt is 2.7 g/cm^3. Lower densities below the ridge axis result in a stronger ridge push force as seen in Figure 69a. The horizontal pressure gradient is about twice as large as for the case without partial melt (Figure 12a). The viscosity (Figure 69b) falls below 10^{17} poise from 5 to 15 kilometers beneath the axis.

The results obtained using the density and viscosity fields in Figures 68b and 69b are shown in Figures 70-73. The surface velocity approaches the spreading rate at 4 kilometers from the axis. The upwelling narrows down to a fast-moving jet. The maximum vertical velocity is 1.37 m/yr. The tensile stress plots show horizontal tension changing to horizontal compression at 15 kilometers from the axis. The strain rate is highest in the fastest part of the jet. However, the topographic profile again has an 8

kilometer wide, 1.0 kilometer deep axial valley. Notice that the isostatic thermal topography has a much sharper peak than before due to the partial melt concentrated below the axis.

The buoyancy of the low density partial melt beneath the axis does not reduce the depth of the axial valley. The effect of the buoyancy force is not limited to the axial valley but is diffused over a wider region by the strength of the brittle layer. Therefore, both the axial valley and the shoulders are uplifted by partial melting.

Lowering Yield Stress

Thus far, a number of different factors have been tested to determine if they can produce both axial peaks and axial valleys. All the results have produced axial valleys of more than 400 meters depth. The strong brittle layer at the axis is under enough tensile stress to cause deep axial valleys. To produce an axial peak, the tensile stress at the axis must be much lower than the depth dependent shear failure criterion. Figures 74-77 show the results obtained when a yield stress of 40 bars is imposed at all depths. The density and viscosity fields in Figures 68b and 69b are used. The velocity field is indistinguishable from those in Figure 70. The tensile stress plots show that horizontal tension changes to horizontal compression at 8 kilometers from the axis. The axial valley has been reduced to a width of 4 kilometers and a depth of 250 meters. The results when the yield stress is reduced to 20 bars at all depths are displayed in Figures 78-81. Horizontal tension changes to horizontal compression at 5 kilometers from the axis.

The axial valley is now only 4 kilometers wide and 100 meters deep. Figures 82-85 show the results when the yield stress is only 10 bars at all depths. The region of horizontal tension is limited to 3 kilometers on either side of the axis. The axial valley is almost completely gone and the topographic profile resembles an axial peak. Therefore, the absence of an axial valley more than 100 meters deep suggests that there is a 10-20 bar limit for tensile stresses in the lithosphere at that axis.

124
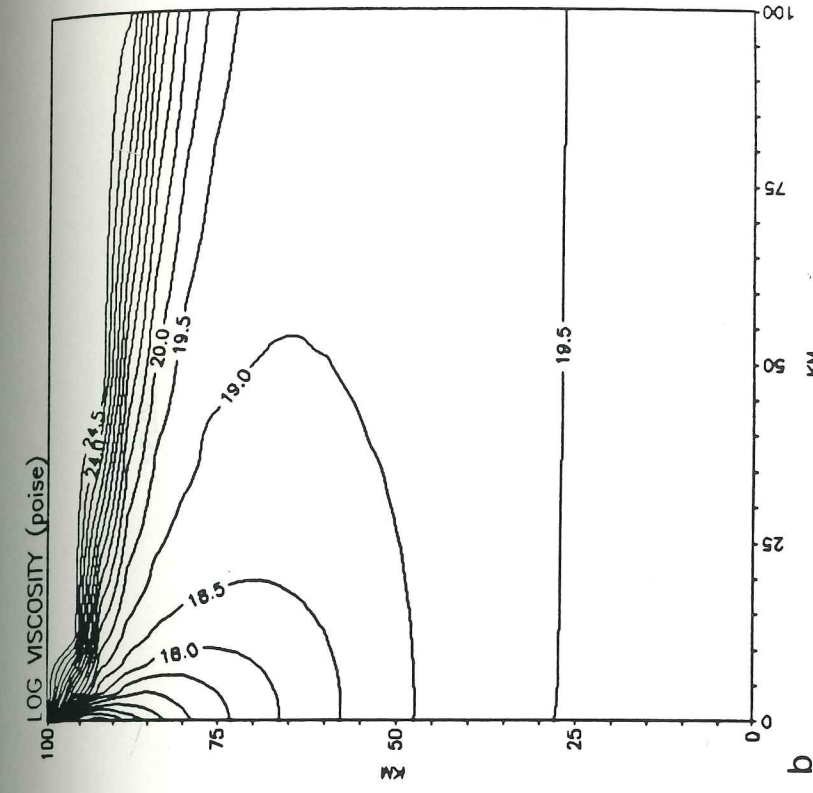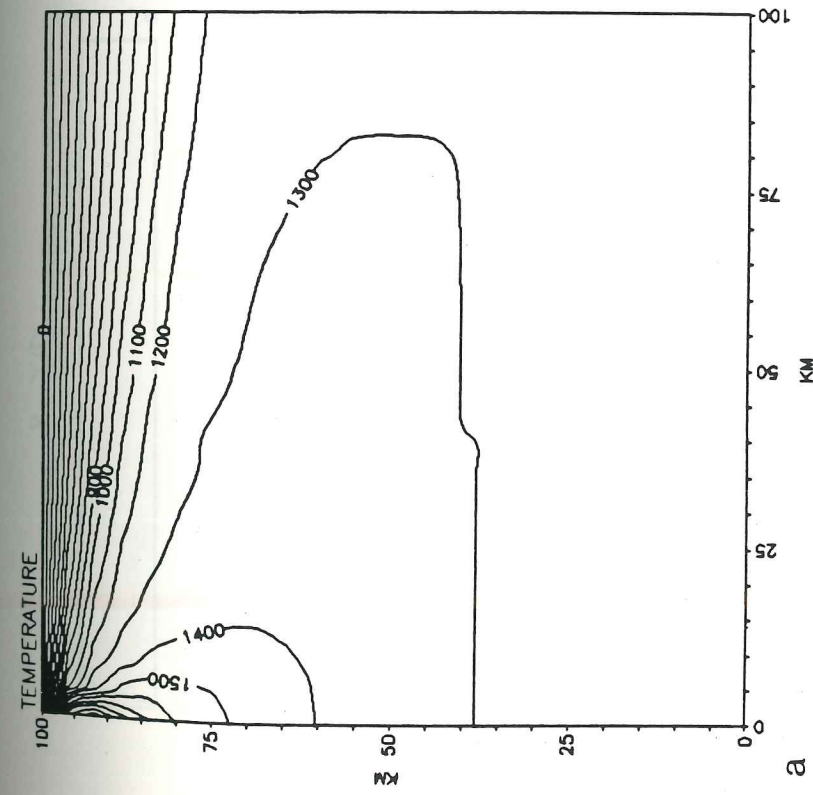
Figure 63. a) Temperature field (T_m=1300°C, no cooled crustal layer) after three iterations during which viscosity was lowered in order to simulate partial melting. b) Log of Newtonian viscosity field (poise).
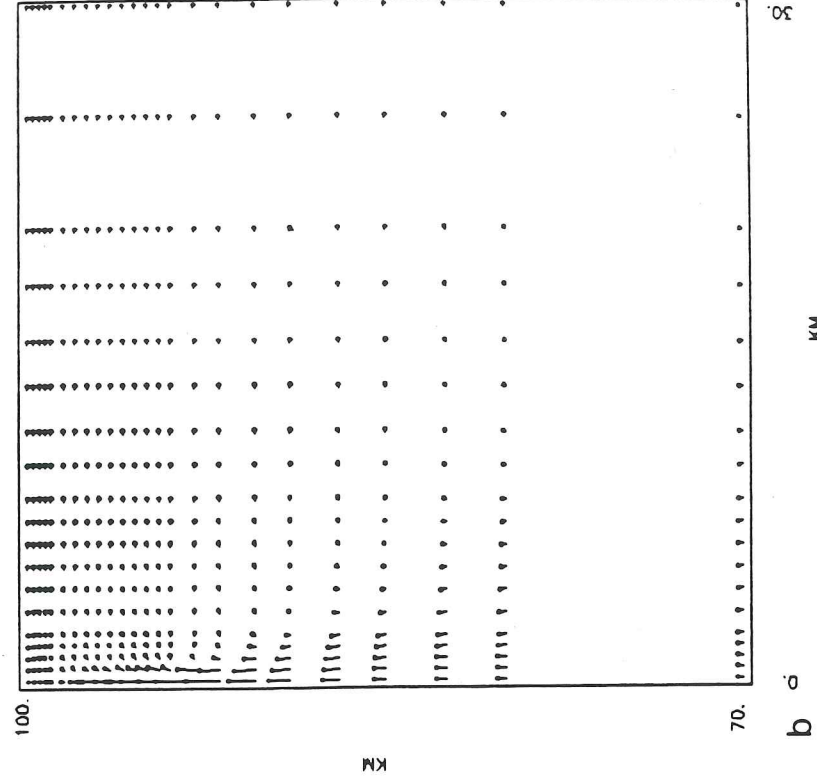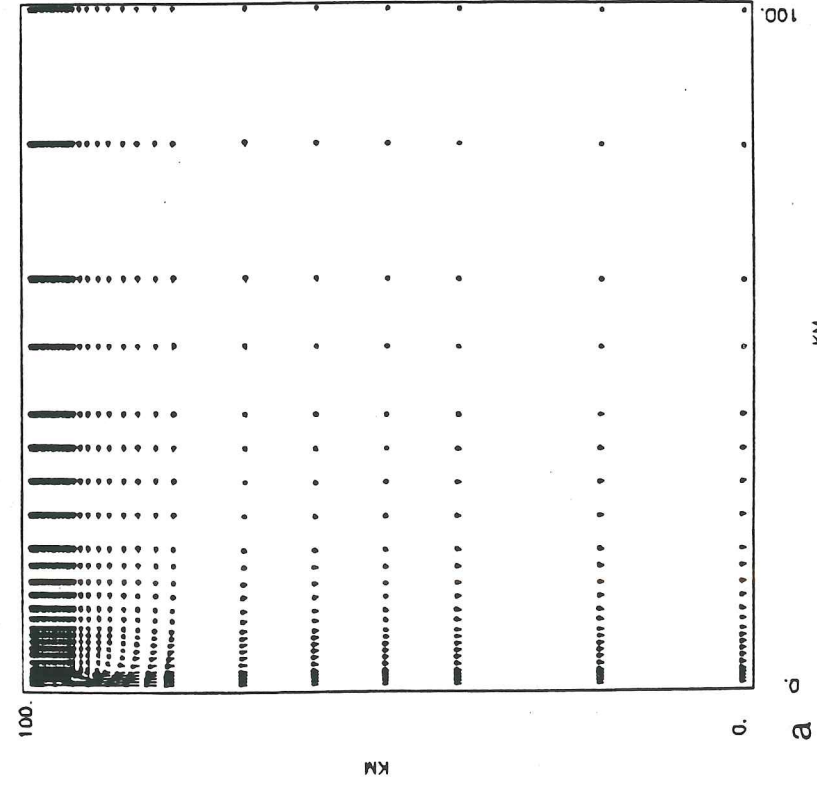
Figure 64. Velocity field for T_m=1300°C with Newtonian rheology, lowered viscosities, and without a cooled crustal layer.

126
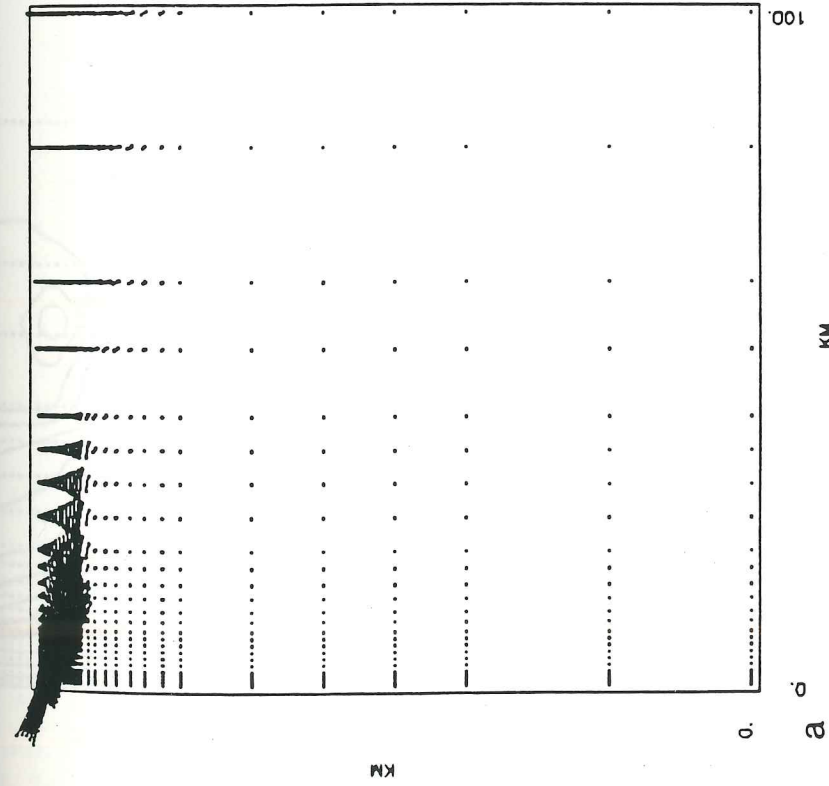
TENSILE STRESS
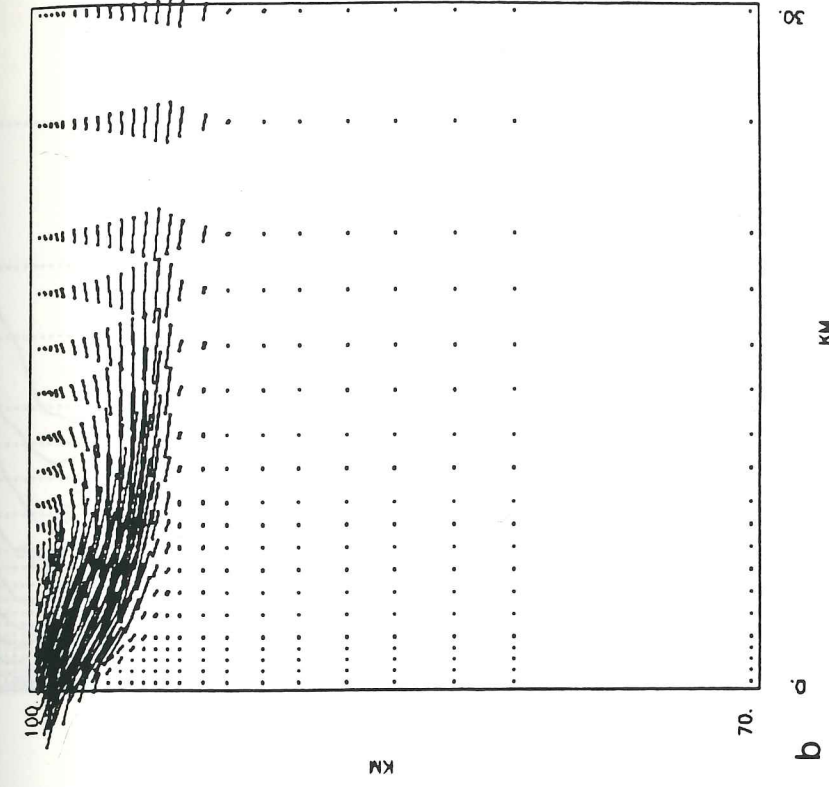
TENSILE STRESS

Figure 65. Tensile stress field for $T_m = 1300°C$ with Newtonian rheology, lowered viscosities, and without a cooled crustal layer.
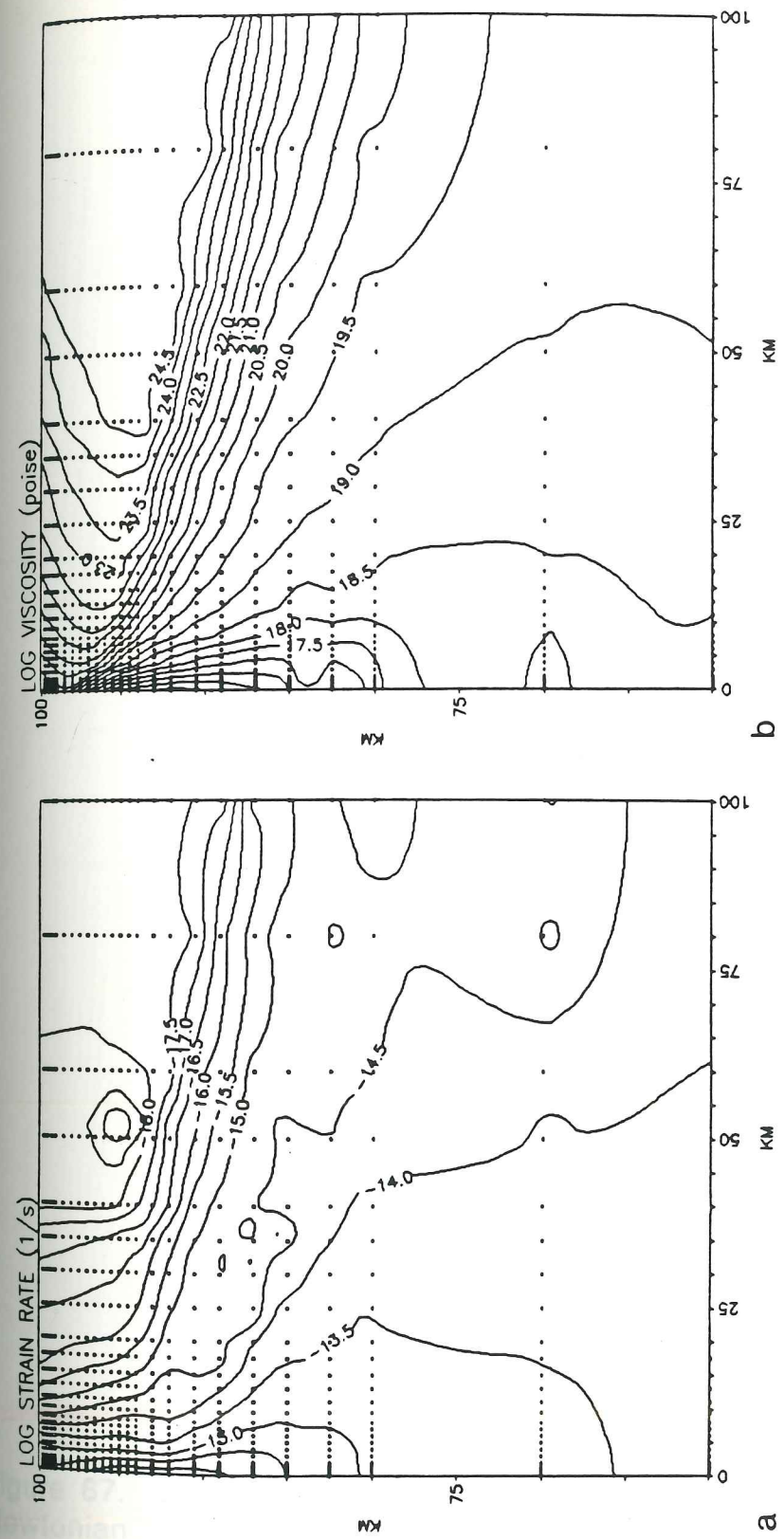
Figure 66.   Strain rate and viscosity fields for $T_m = 1300°C$ with Newtonian rheology, lowered viscosities, and without a cooled crustal layer.
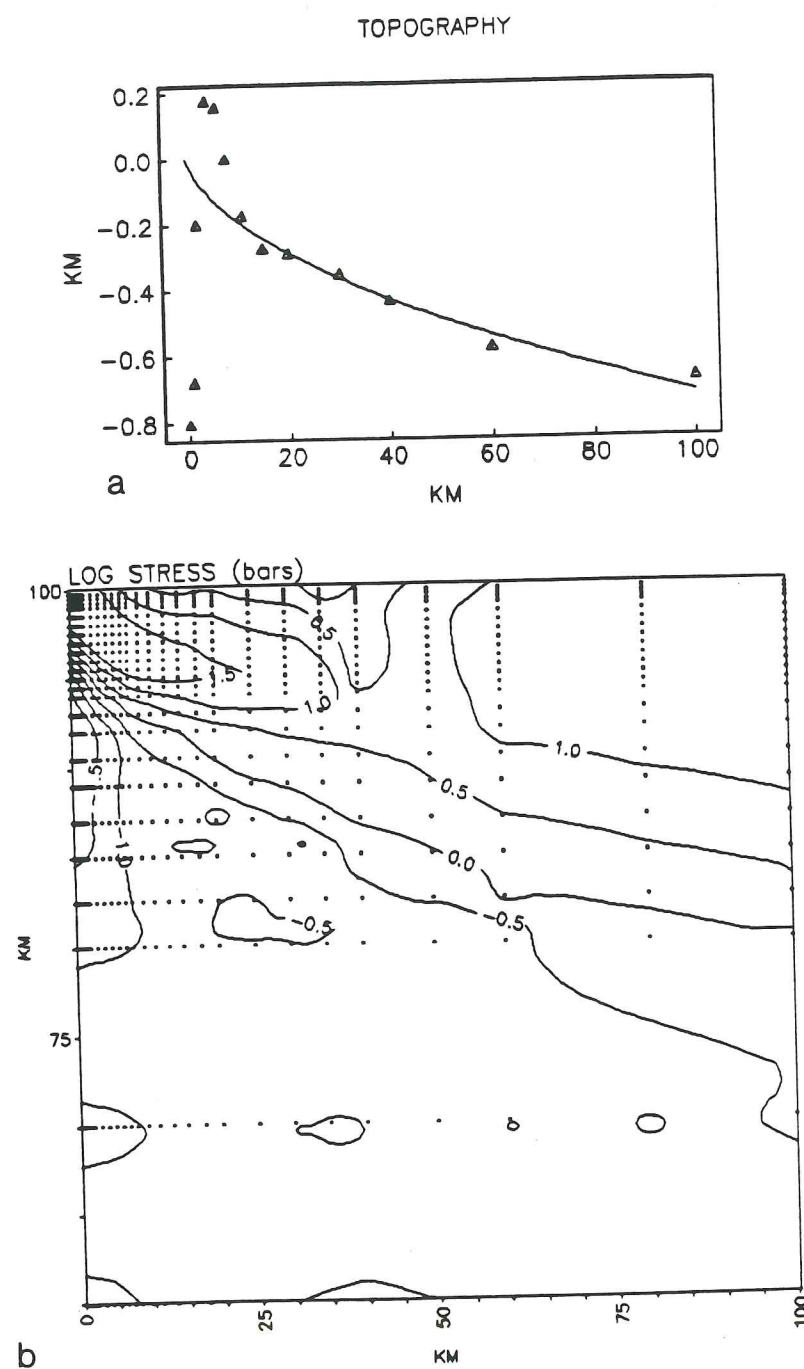
Figure 67. Stress field and topography for $T_m=1300°C$ with Newtonian rheology, lowered viscosities, and without a cooled crustal layer.
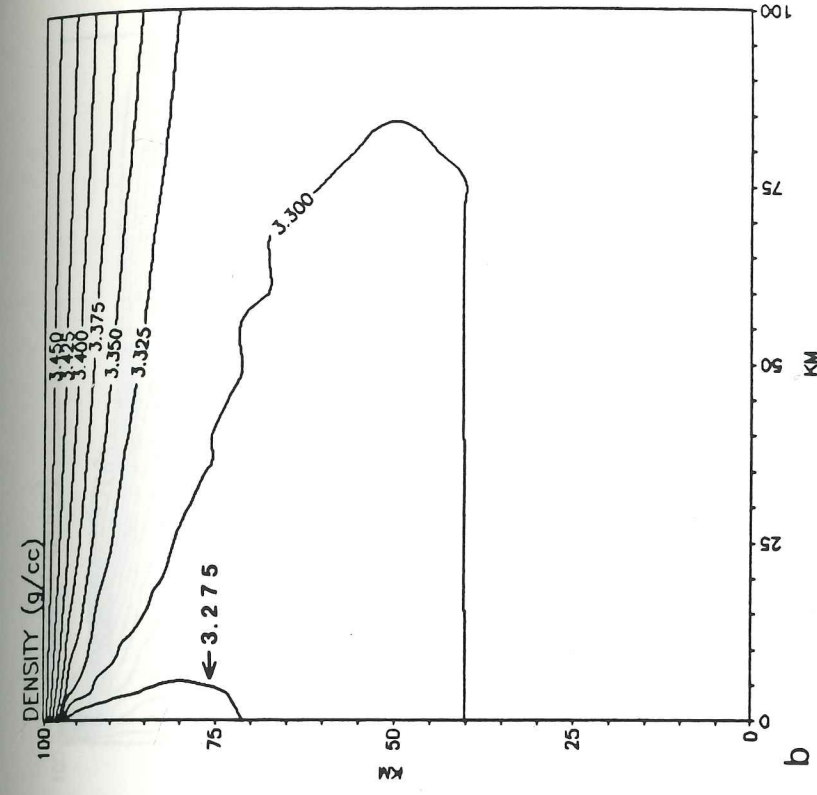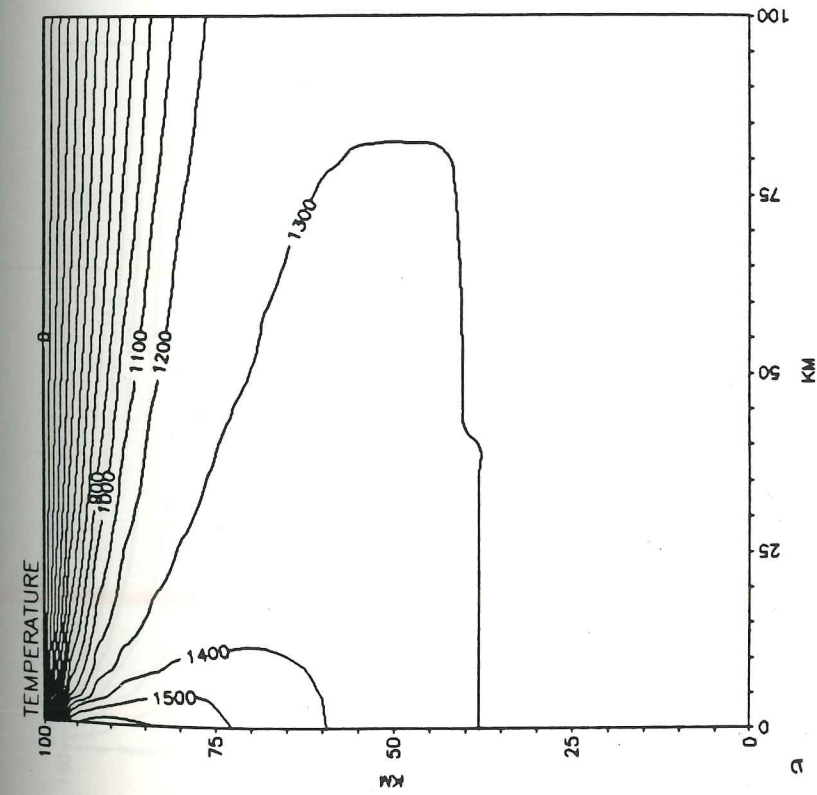
Figure 68. a) Temperature field (T_m=1300°C, no cooled crustal layer) after two iterations during which both density and viscosity were lowered in order to simulate partial melting. b) Density field (g/cm³) with ρ_m=3.3 g/cm³.
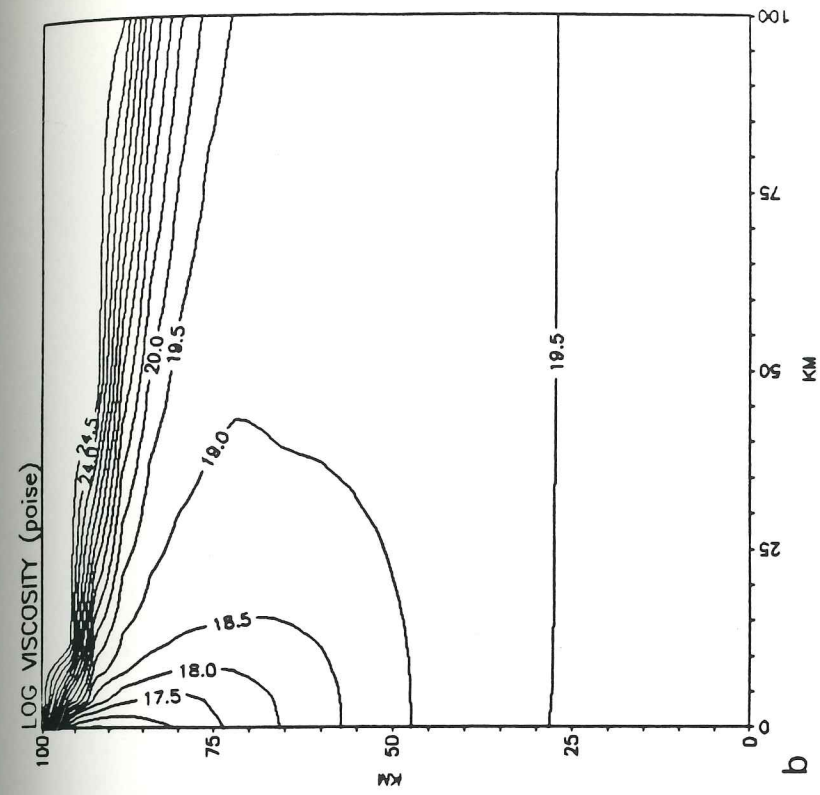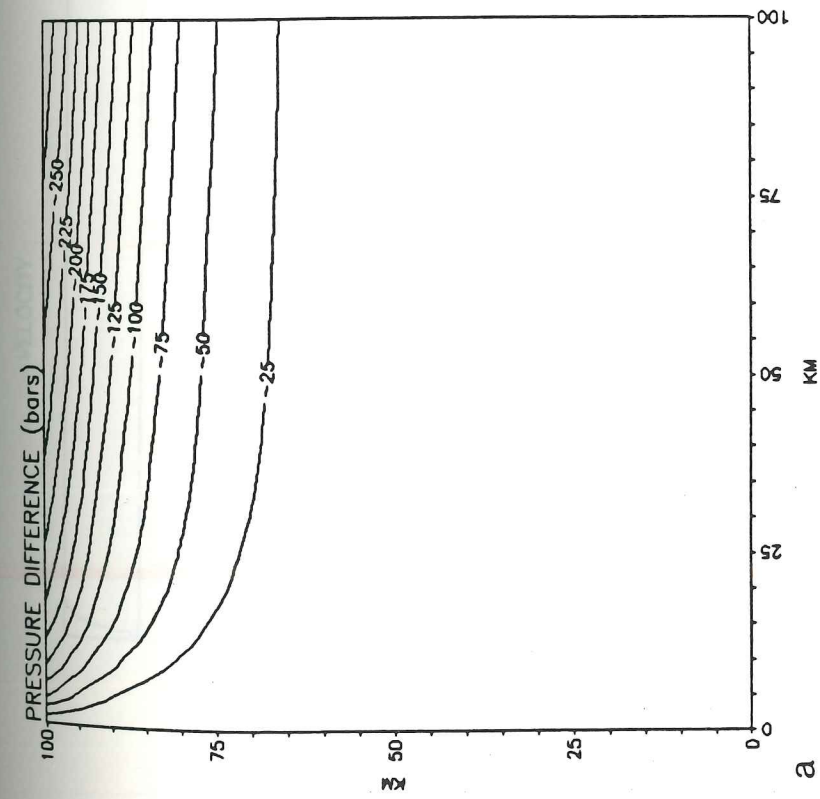
Figure 69. a) Horizontal pressure difference (bars) relative to lithostatic pressure at the ridge axis for the density field in Figure 68. b) Log of Newtonian viscosity field (poise).

131
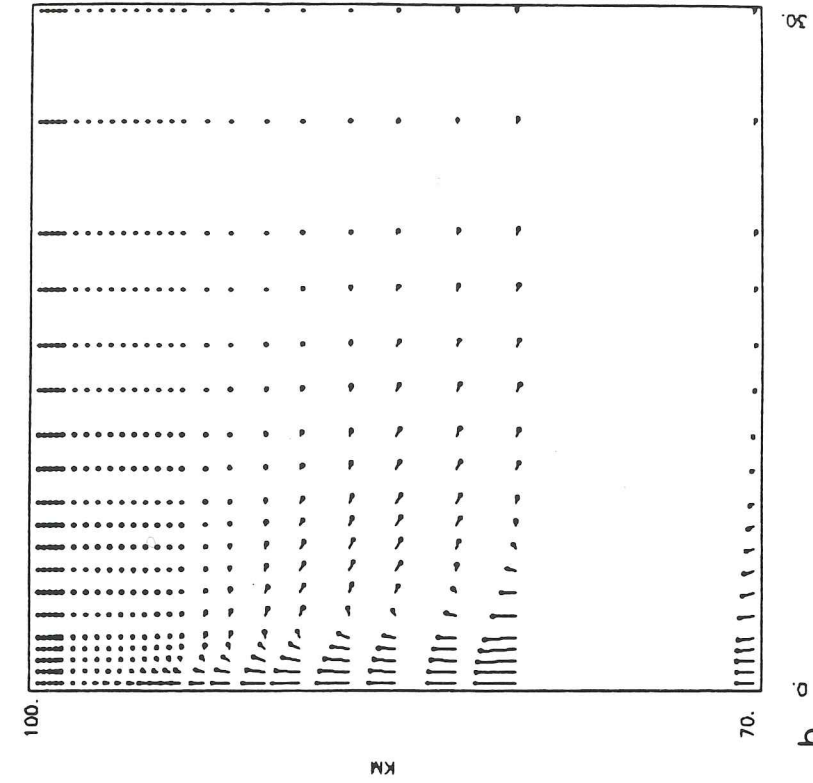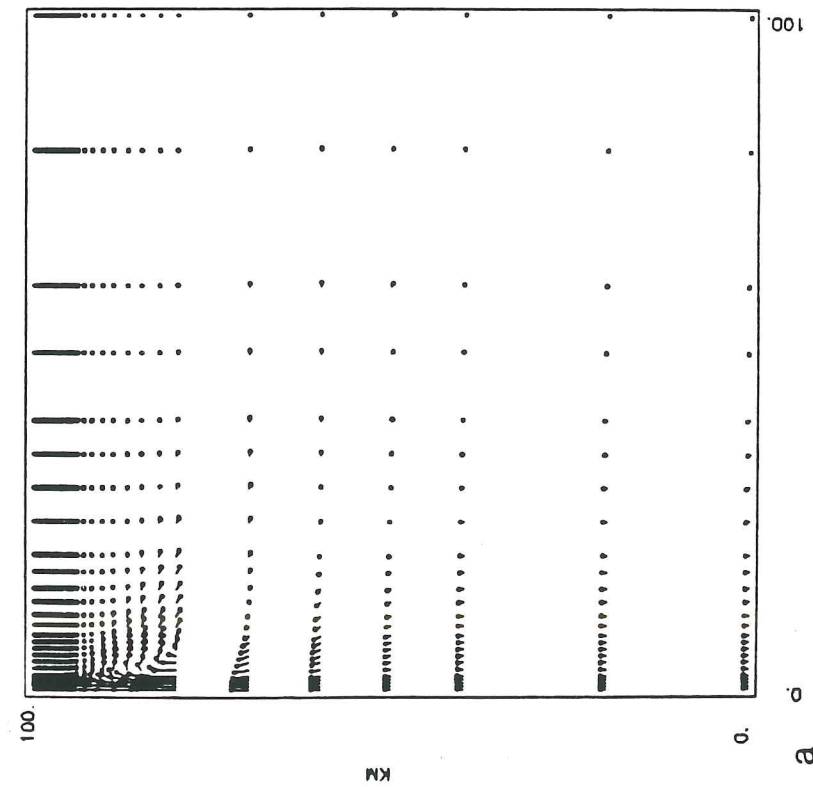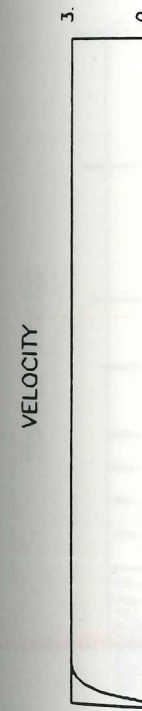
Figure 70. Velocity field for T_m=1300°C with Newtonian rheology, lowered viscosities and densities, and without a cooled crustal layer.
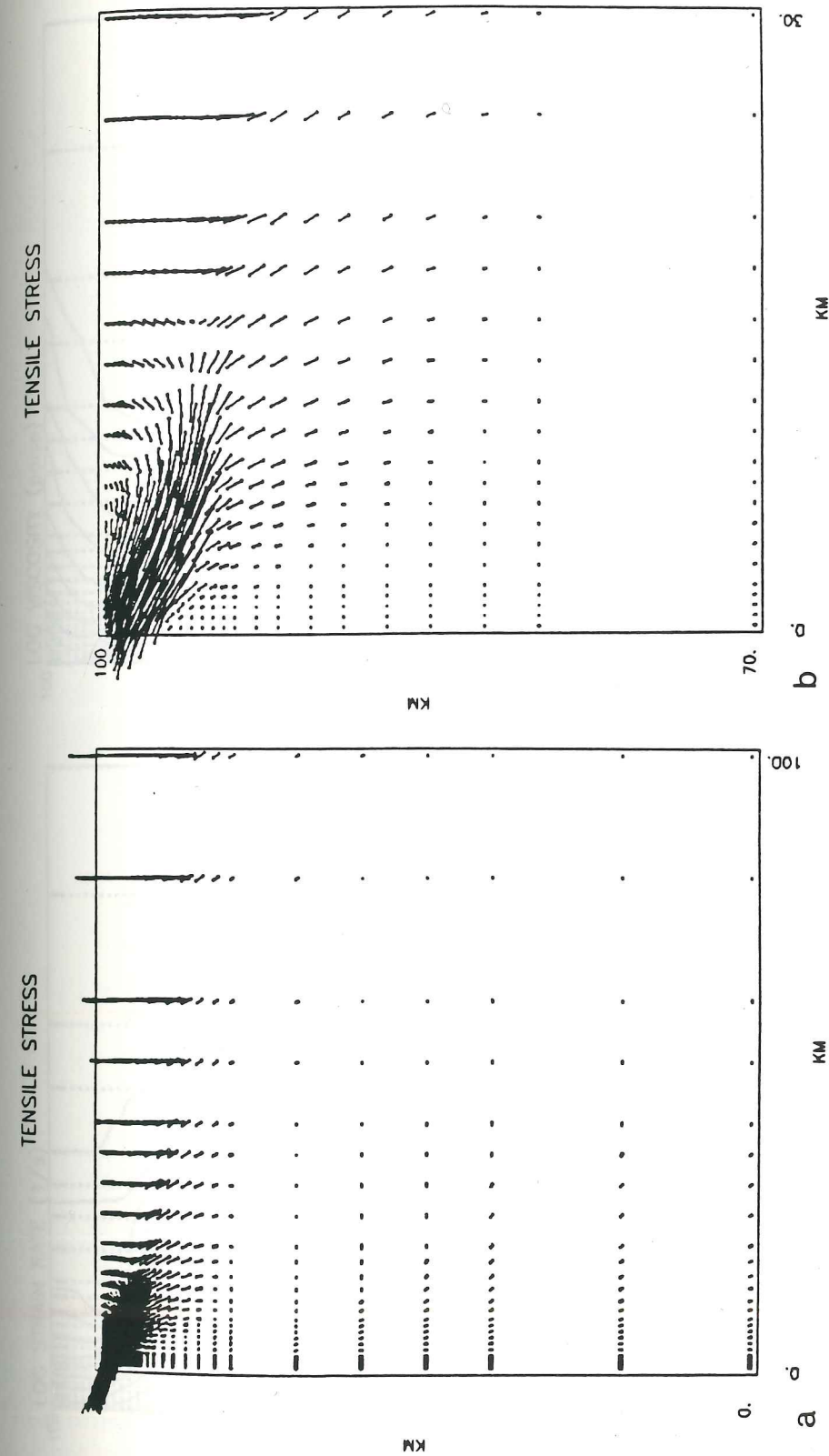
Figure 71. Tensile stress field for $T_m=1300°C$ with Newtonian rheology, lowered viscosities and densities, and without a cooled crustal layer.
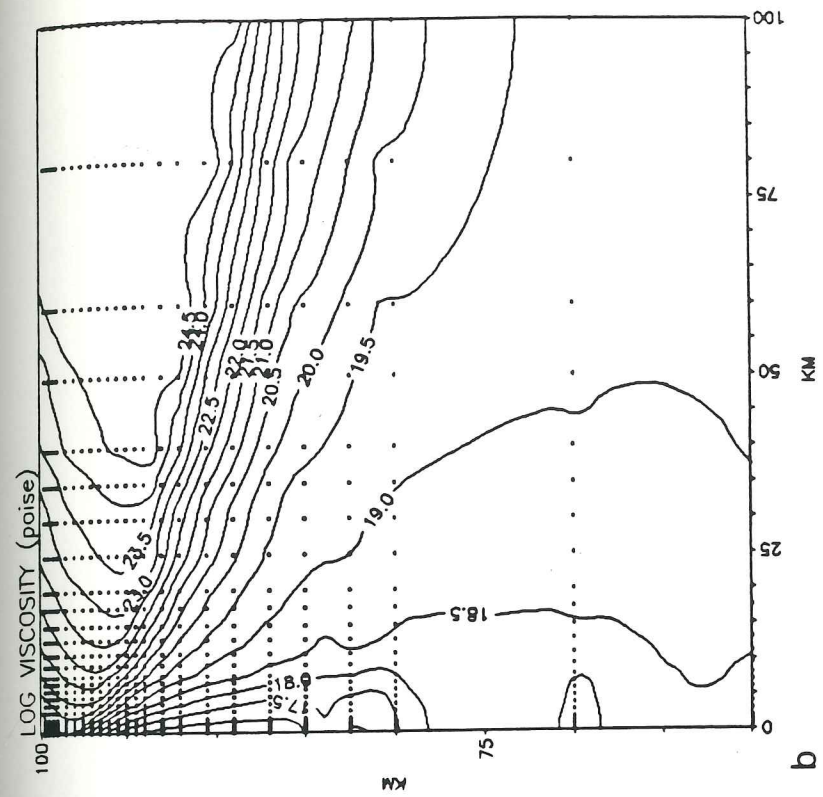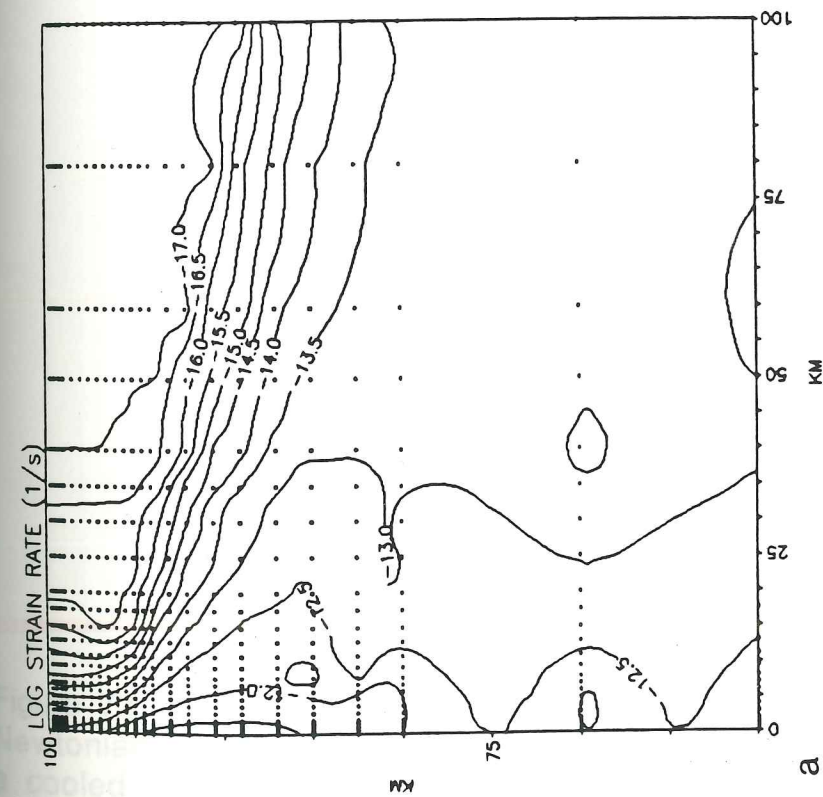
Figure 72. Strain rate and viscosity fields for $T_m = 1300°C$ with
Newtonian rheology, lowered viscosities and densities, and without
a cooled crustal layer.

133
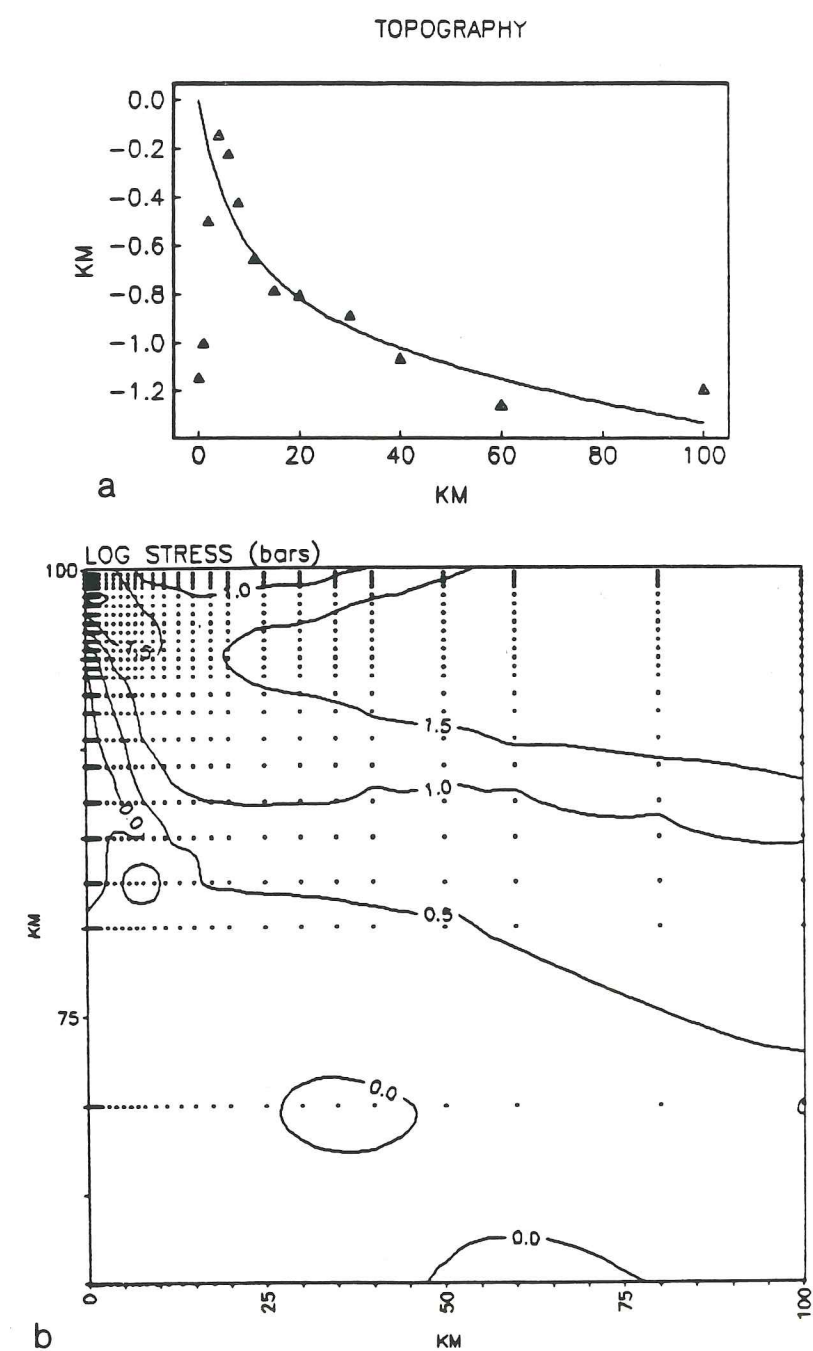
Figure 73.   Stress field and topography for T_m=1300°C with Newtonian rheology, lowered viscosities and densities, and without a cooled crustal layer.

135
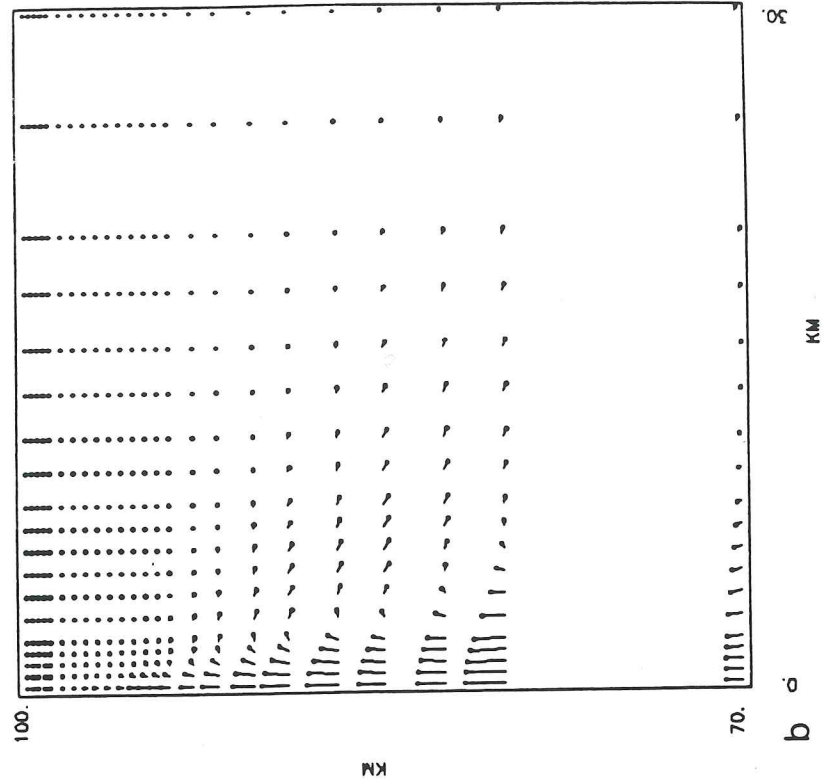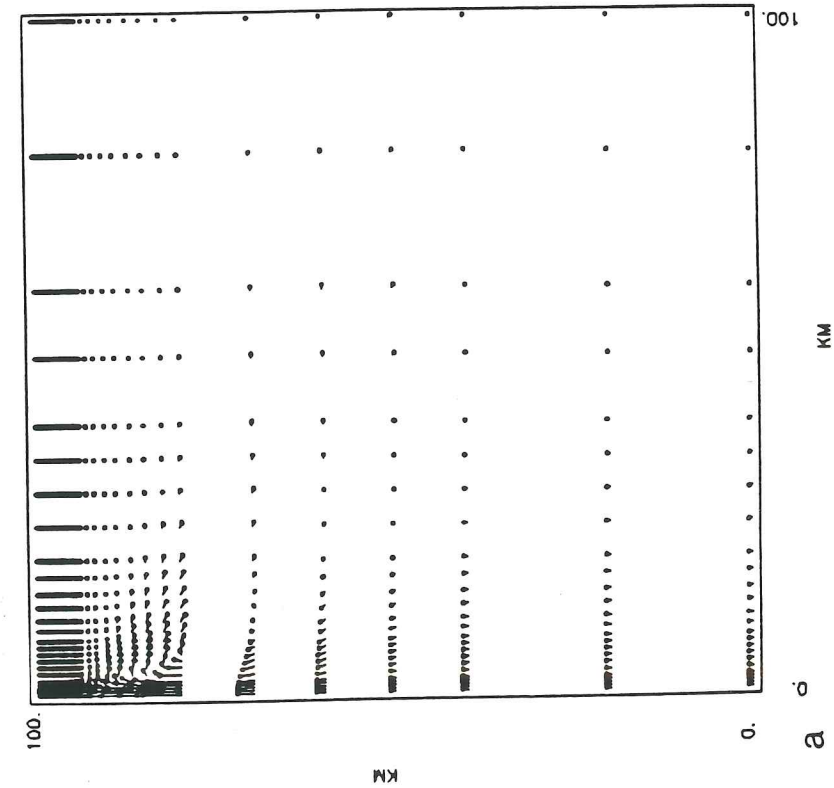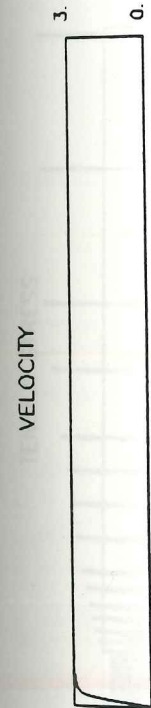
Figure 74. Velocity field for T_m=1300°C with Newtonian rheology, lowered viscosities and densities, and without a cooled crustal layer. Yield stress is 40 bars.
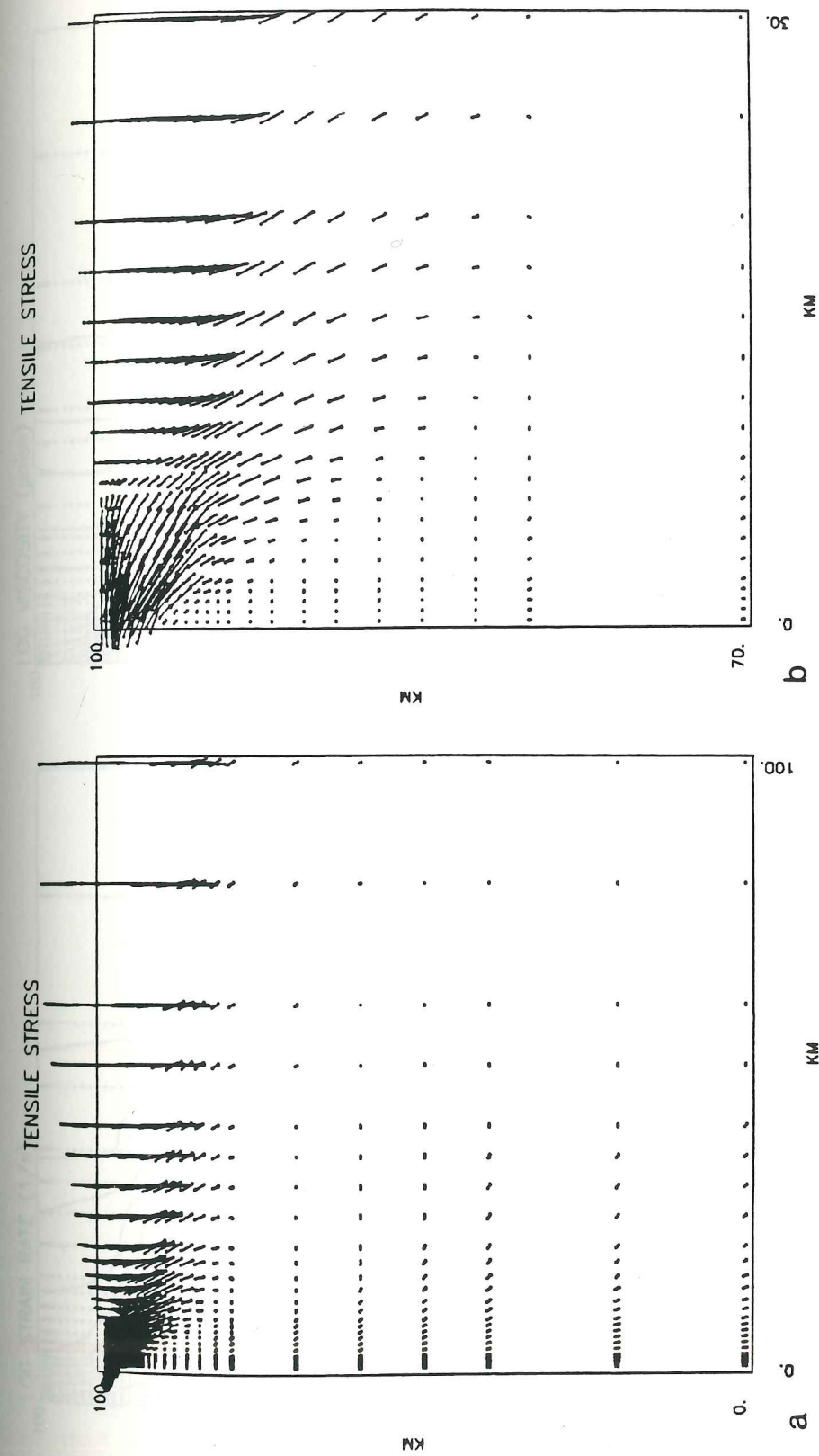
Figure 75. Tensile stress field for $T_m=1300°C$ with Newtonian rheology, lowered viscosities and densities, and without a cooled crustal layer. Yield stress is 40 bars.
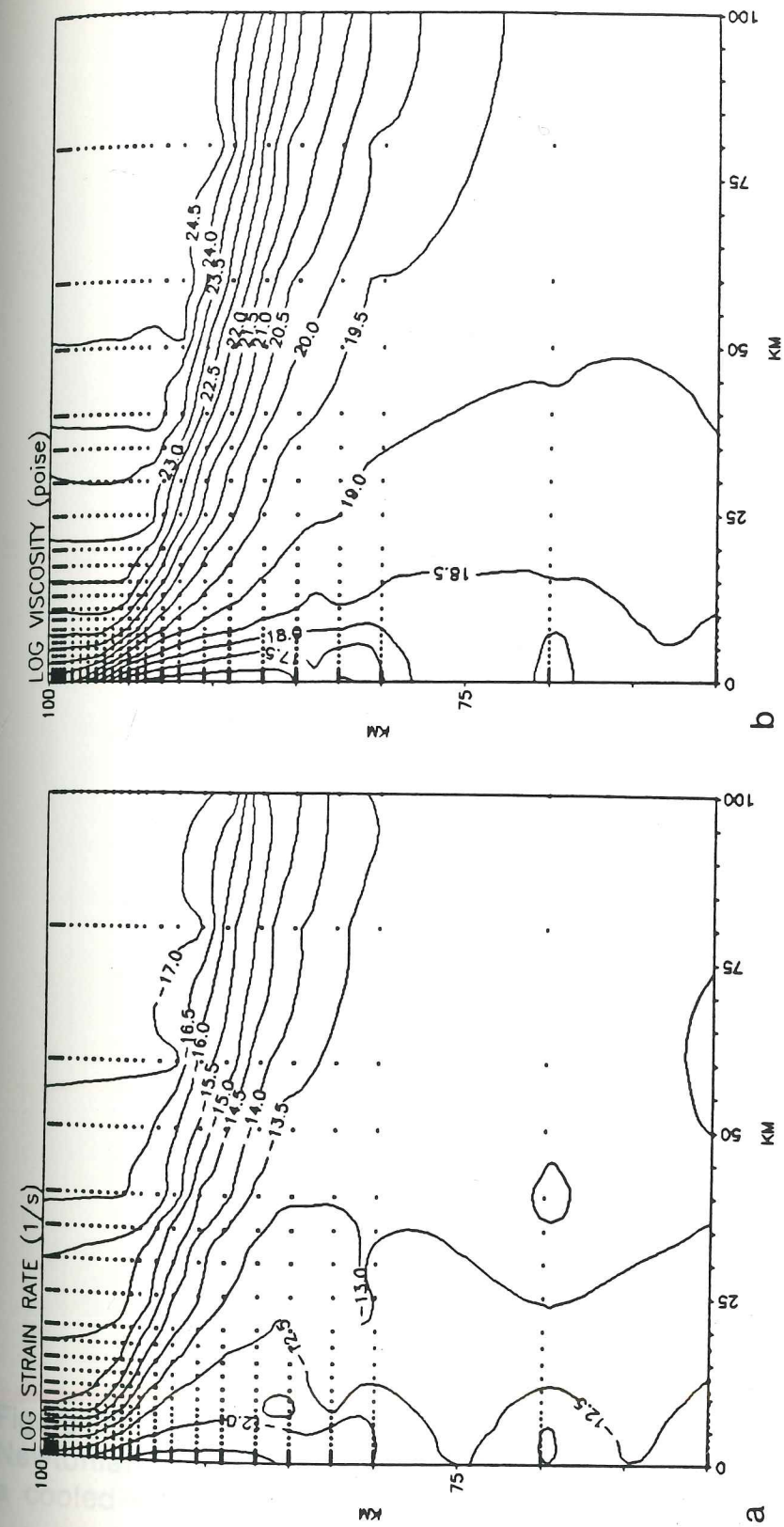
Figure 76. Strain rate and viscosity fields for T_m=1300°C with Newtonian rheology, lowered viscosities and densities, and without a cooled crustal layer. Yield stress is 40 bars.
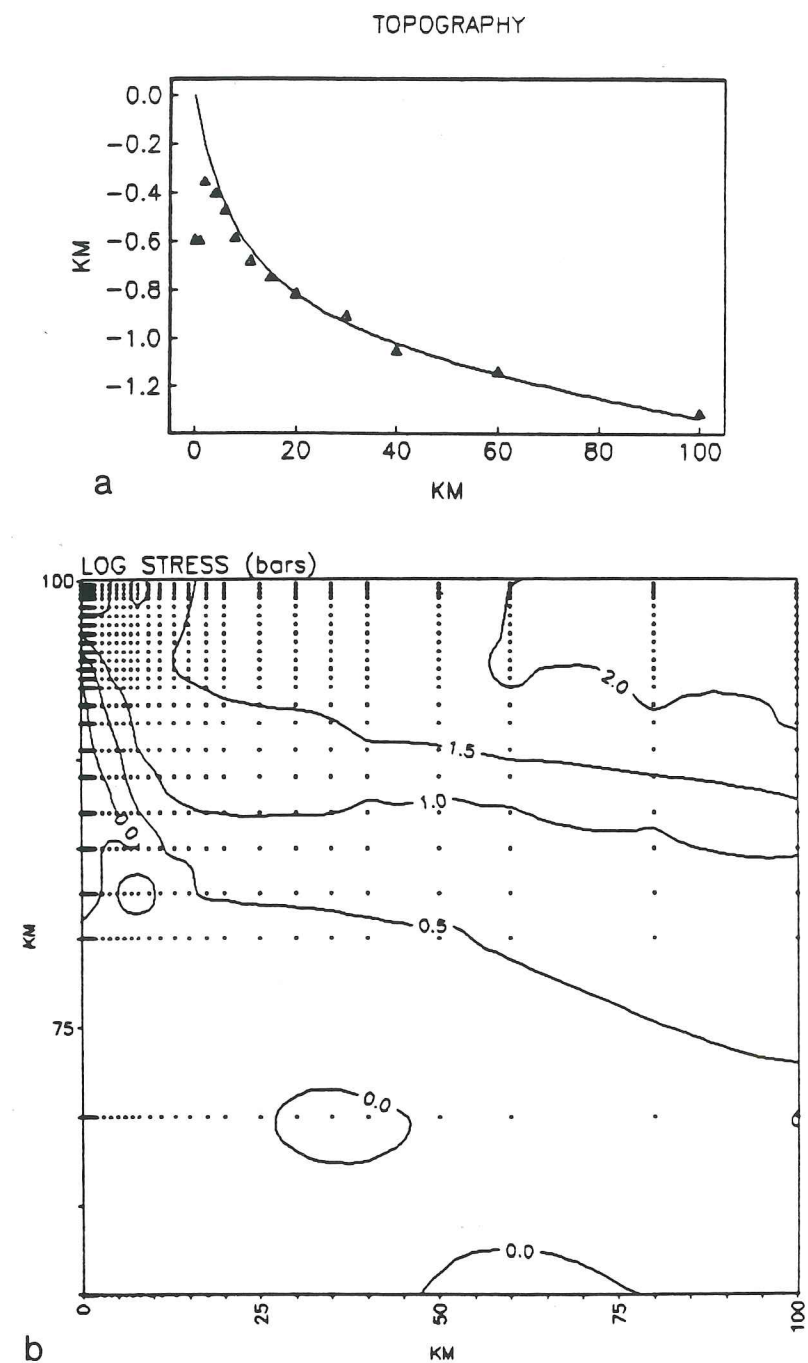
Figure 77. Stress field and topography for T_m=1300°C with Newtonian rheology, lowered viscosities and densities, and without a cooled crustal layer. Yield stress is 40 bars.
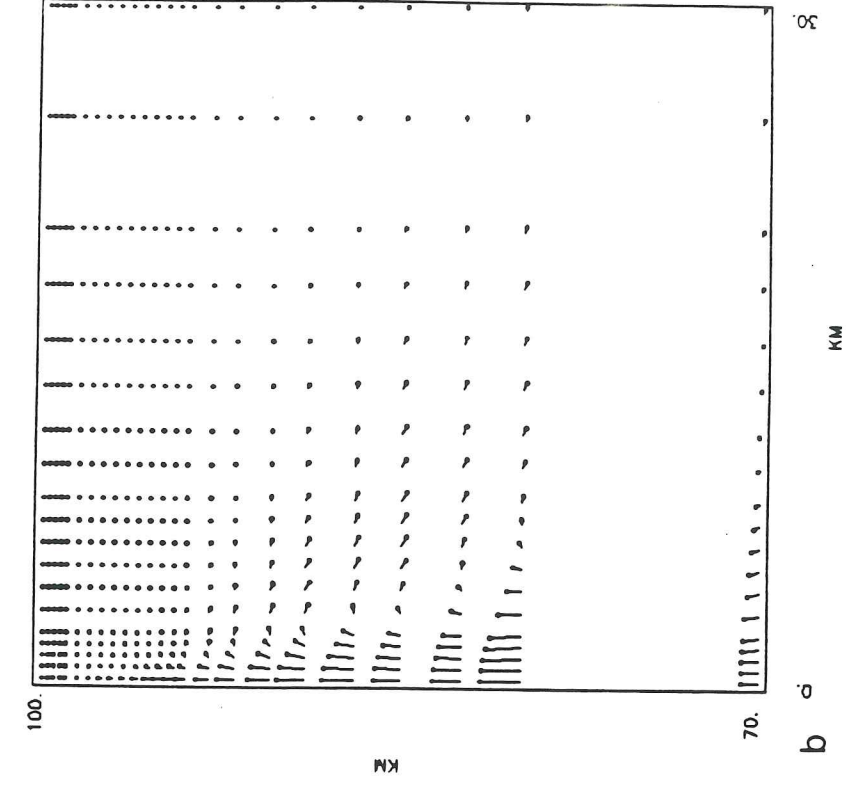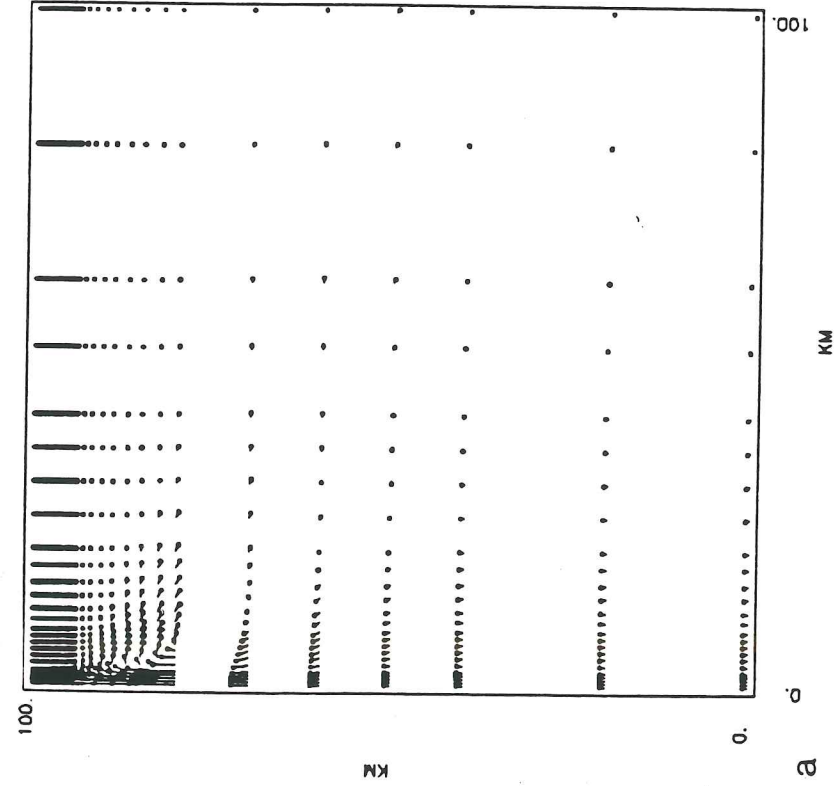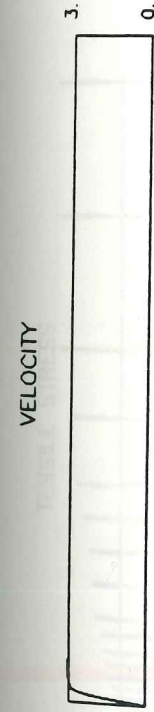
VELOCITY

VELOCITY

Figure 78. Velocity field for T_m=1300°C with Newtonian rheology, lowered viscosities and densities, and without a cooled crustal layer. Yield stress is 20 bars.
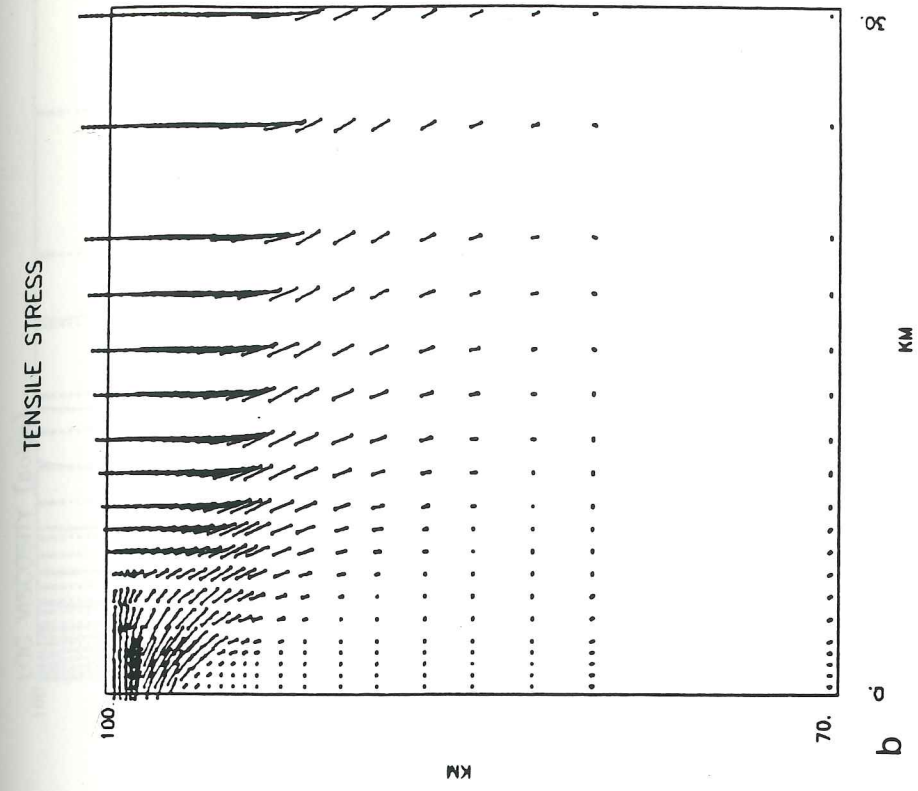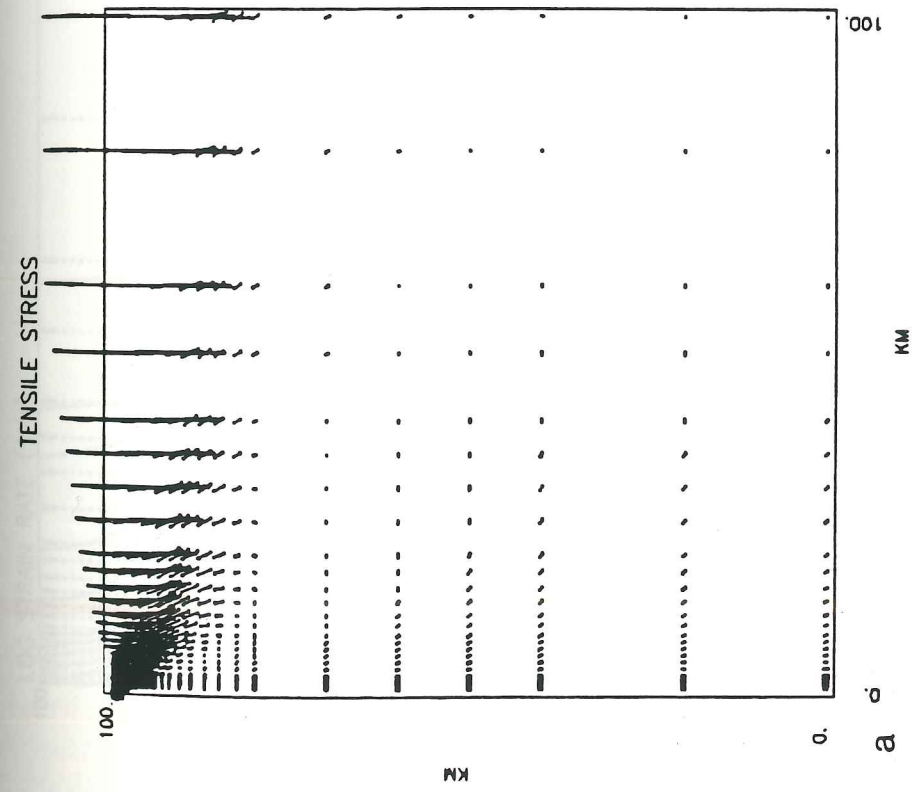
Figure 79. Tensile stress field for $T_m=1300°C$ with Newtonian rheology, lowered viscosities and densities, and without a cooled crustal layer. Yield stress is 20 bars.
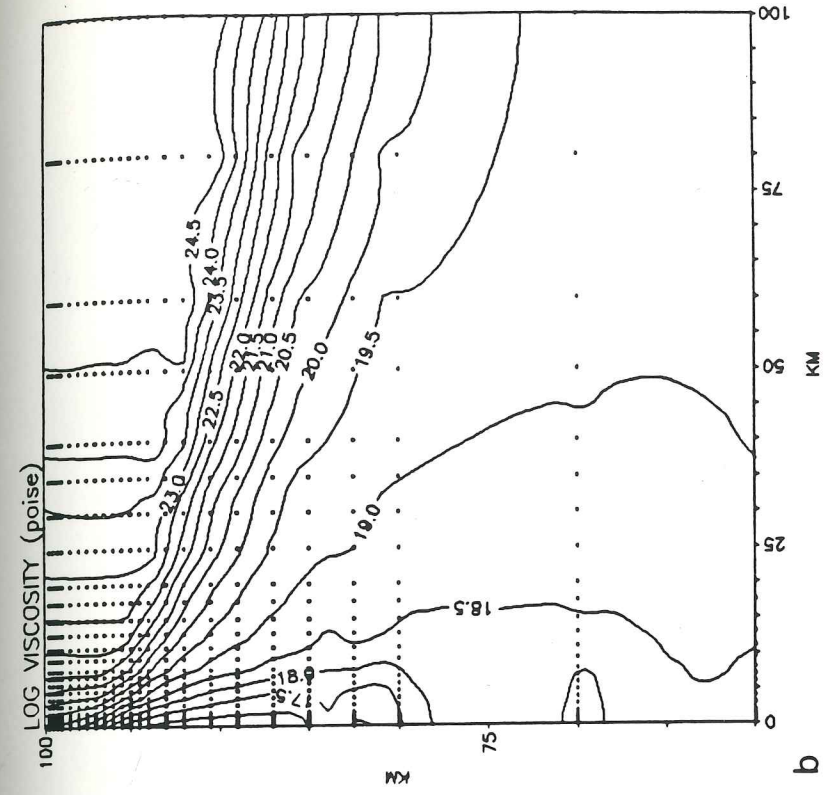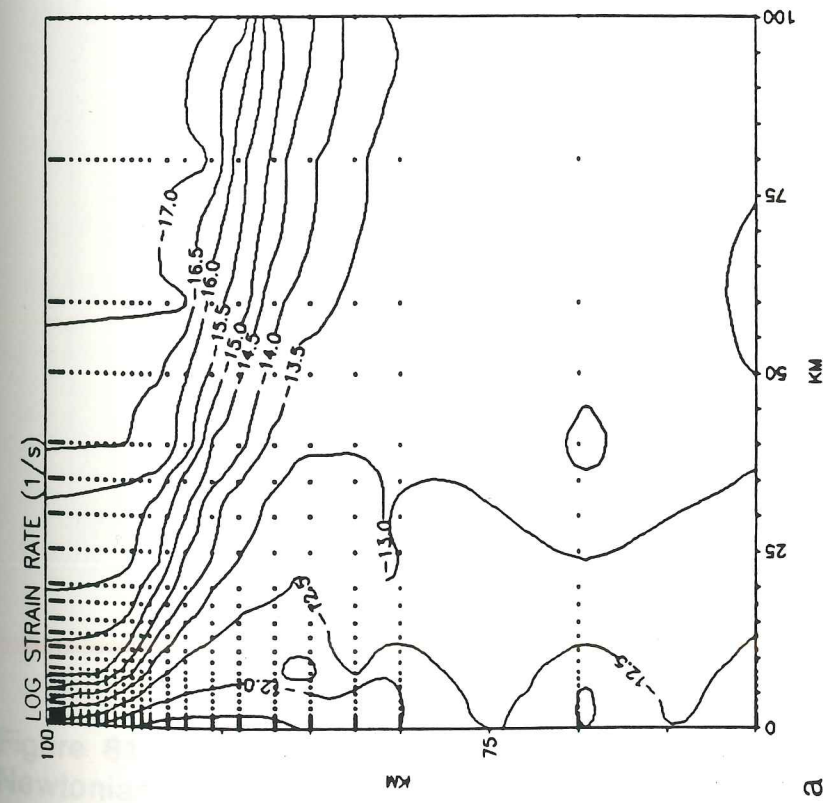
Figure 80. Strain rate and viscosity fields for $T_m=1300°C$ with Newtonian rheology, lowered viscosities and densities, and without a cooled crustal layer. Yield stress is 20 bars.
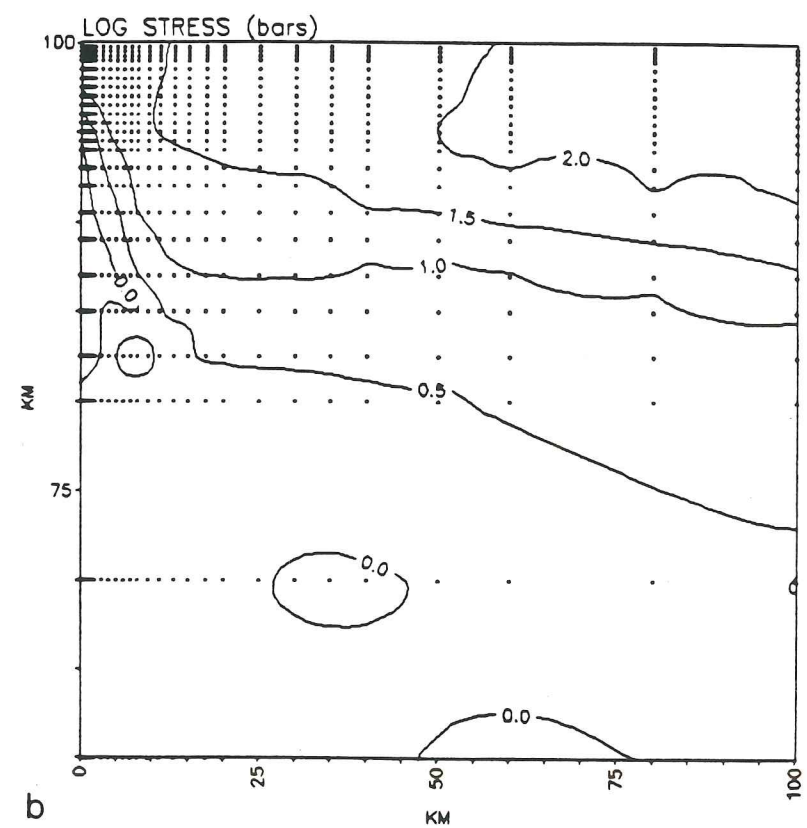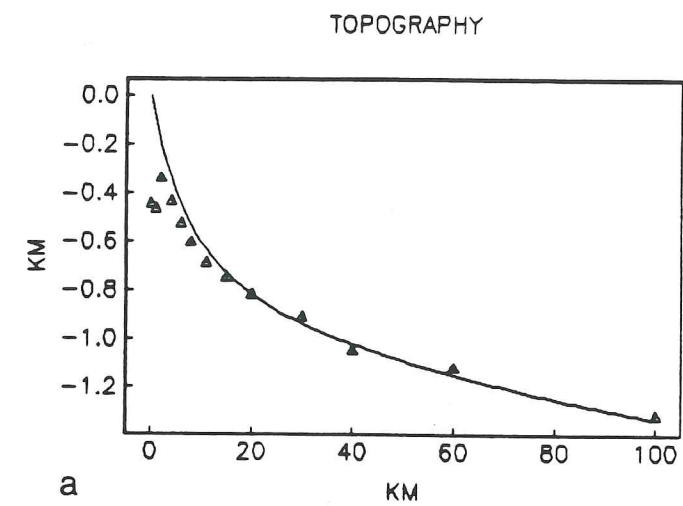
Figure 81. Stress field and topography for T_m=1300°C with Newtonian rheology, lowered viscosities and densities, and without a cooled crustal layer. Yield stress is 20 bars.

143
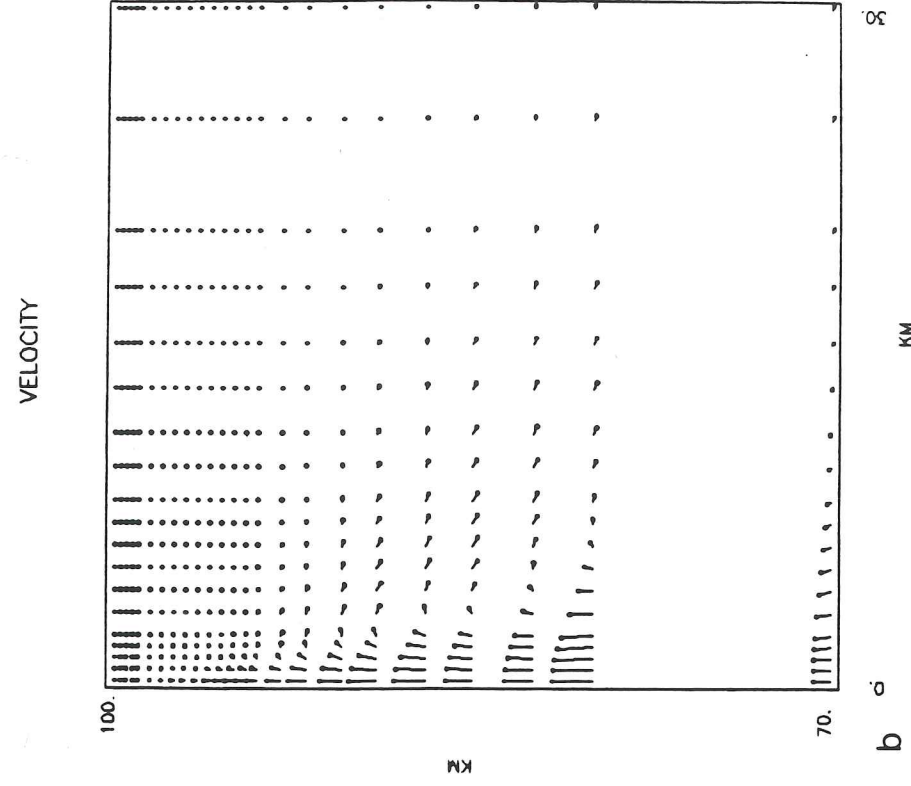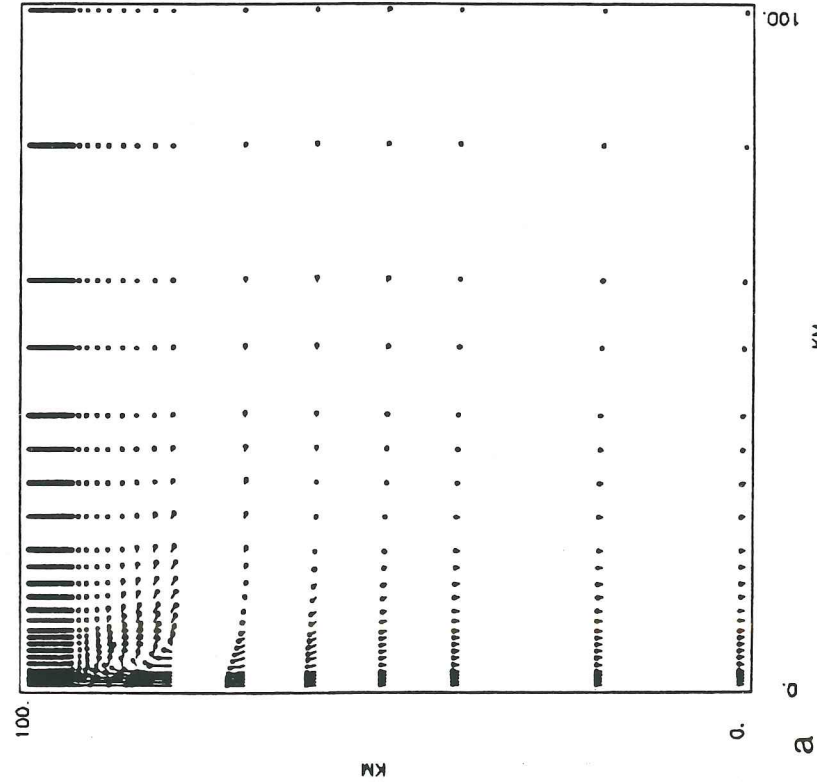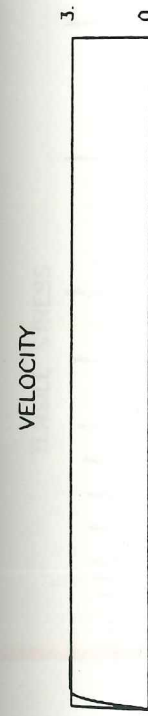
VELOCITY

VELOCITY

Figure 82. Velocity field for $T_m=1300°C$ with Newtonian rheology, lowered viscosities and densities, and without a cooled crustal layer. Yield stress is 10 bars.
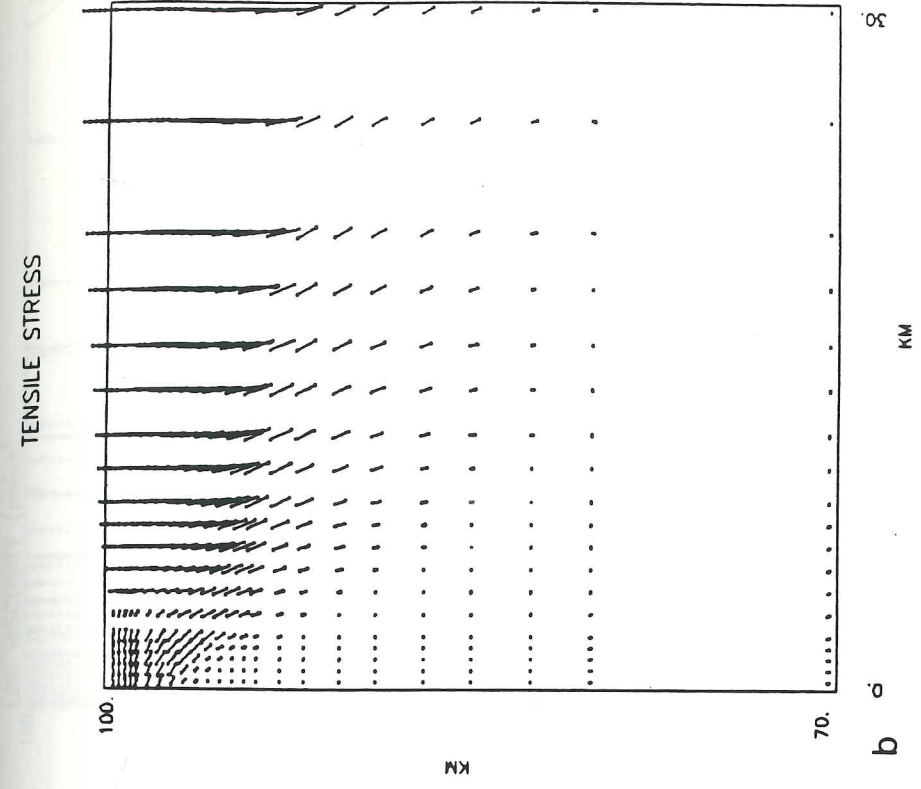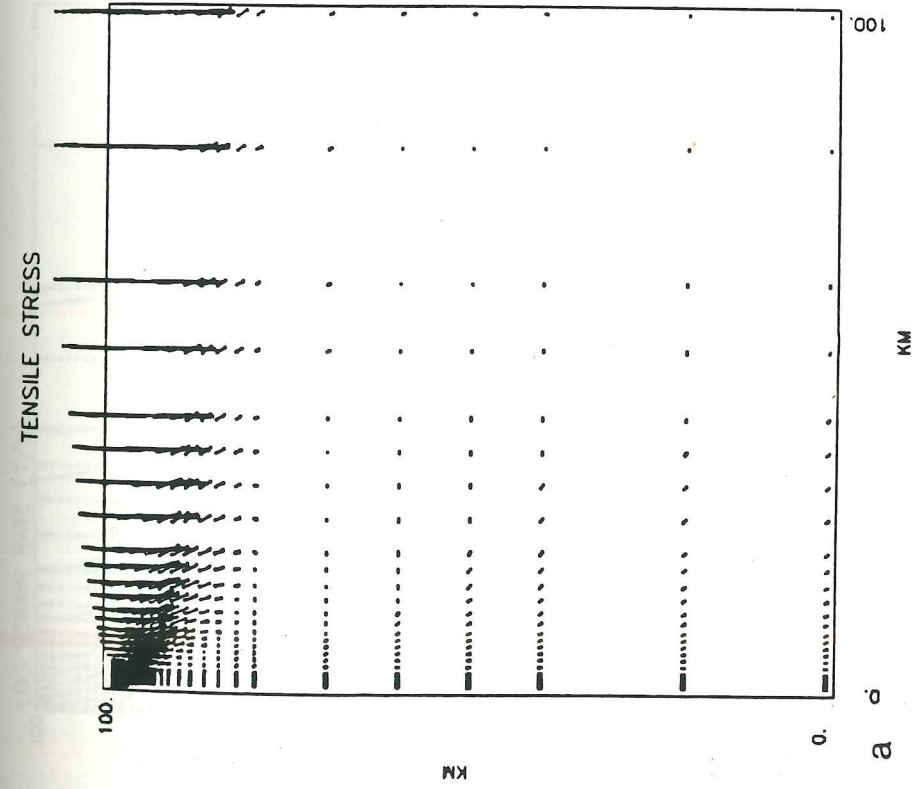
Figure 83. Tensile stress field for $T_m = 1300°C$ with Newtonian rheology, lowered viscosities and densities, and without a cooled crustal layer. Yield stress is 10 bars.
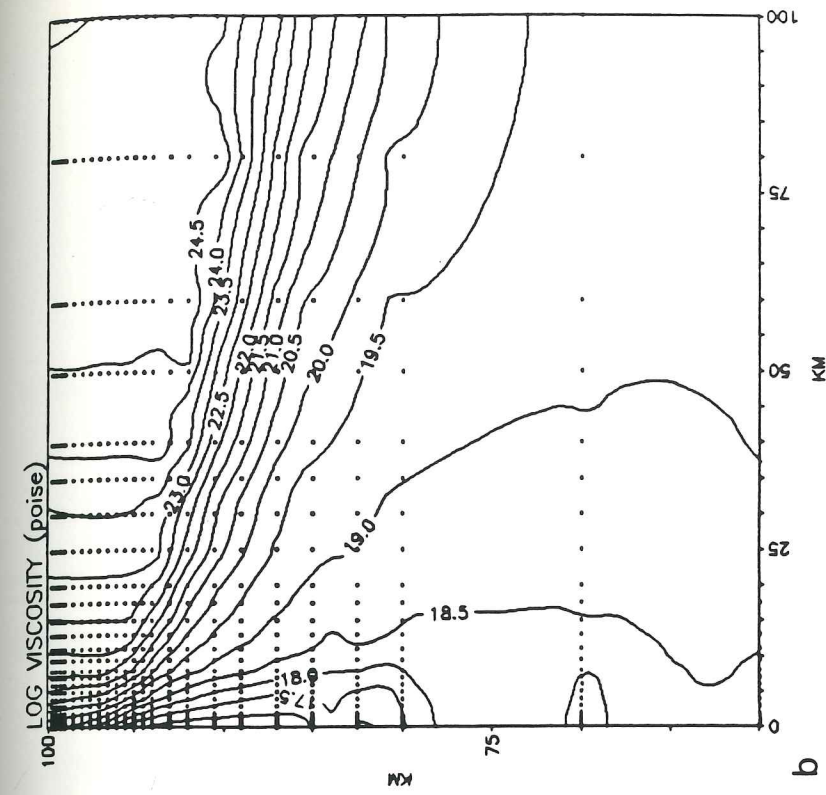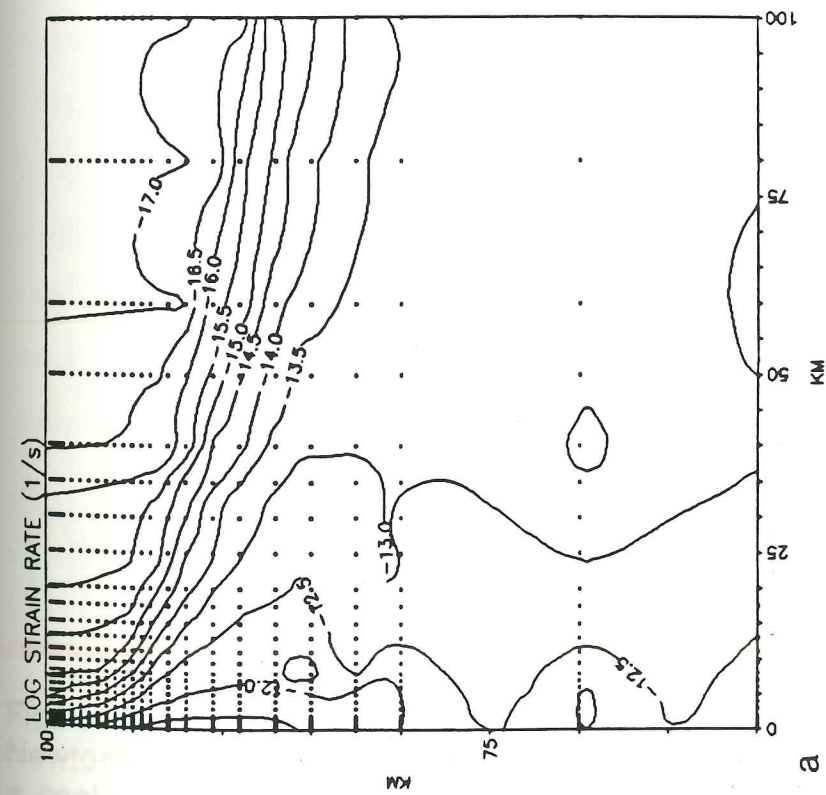
Figure 84.   Strain rate and viscosity fields for $T_m = 1300°C$ with
Newtonian rheology, lowered viscosities and densities, and without
a cooled crustal layer.   Yield stress is 10 bars.
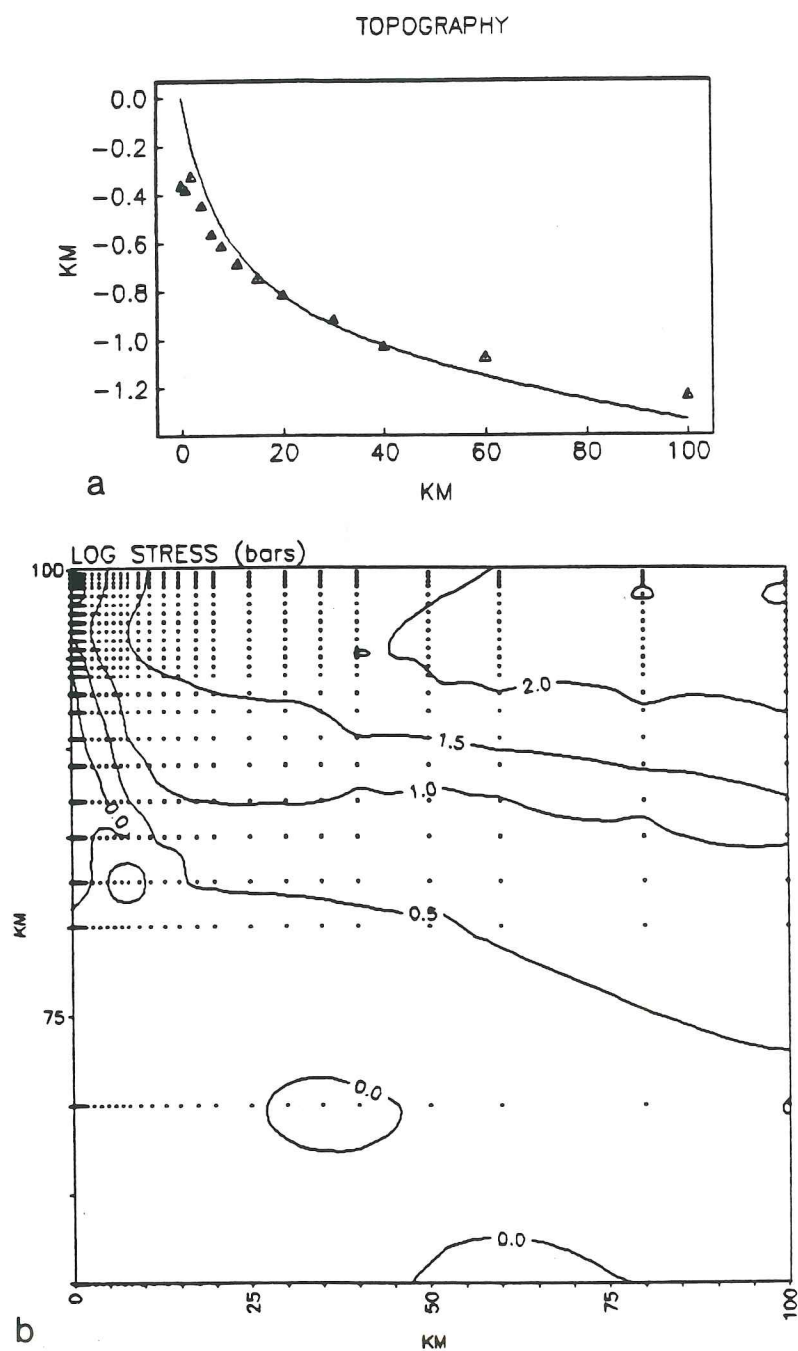
Figure 85.   Stress field and topography for T_m=1300°C with Newtonian rheology, lowered viscosities and densities, and without a cooled crustal layer.   Yield stress is 10 bars.

Discussion

The results obtained from finite element numerical modeling show that deep axial valleys are produced when the brittle lithosphere at the ridge axis is at the yield criterion for shear failure on pre-existing faults. A number of parameters were varied in an attempt to obtain an axial peak at the ridge axis. The temperature of the asthenosphere was raised. Non-Newtonian rheology was used. The thickness of the brittle layer was substantially reduced. The effect of partial melting of the mantle was simulated by lowering viscosities and lowering densities beneath the axis. In all models, the axial valley was deeper than 400 meters. Since the yield stress for shear failure is 80 bars per kilometer depth, even a 1 kilometer thick brittle layer is strong enough to produce an axial valley. To produce an axial peak, the horizontally tensile stress in the lithosphere at the axis cannot exceed 10 to 20 bars. The numerical modeling results are summarized in Table 2.

State of Stress

It must be concluded therefore, that stresses at the axis of the Juan de Fuca ridge are much lower than the shear failure criterion for brittle rock. This conclusion is strongly supported by the absence of seismicity at the Juan de Fuca ridge as seen in Figure 4.

In contrast, the abundant seismicity at the Gorda ridge confirms that the lithosphere at its axis is near the shear failure yield stress.

The state of stress at the Juan de Fuca and Gorda ridges is depicted in Figure 86. Topographic profiles are shown at the top of each figure. On the lower right, the deepening of the brittle-ductile transition away from the axis is shown, assuming a hydrothermally cooled crust at each ridge axis. Horizontal stresses are shown for various distances from the axis. On the lower left, the horizontal tensile stresses at the axis (x=0) are plotted versus depth.

At the Gorda ridge (Figure 86a), the tensile stress at the axis increases linearly with depth in the lithosphere (80 bars/km) and falls off rapidly in the asthenosphere. There are large horizontally tensile stresses at the axis. Stresses become horizontally compressive far from the axis. At the Juan de Fuca ridge (Figure 86b), horizontal tensile stresses are very weak at the axis (less than 10 bars). Stresses become compressive a short distance from the axis.

The transition from tensile to compressional stress due to different yield stresses at the axis is not expected to explain intraplate seismicity. The tensile stresses are near the shear failure criterion only at the ridge axis. Tensile stresses will drop below shear failure levels away from the axis as the plate gets thicker. Shear failure will not occur until compressive stresses become large enough to cause slip on a thrust fault. This would occur a long way from the axis since the compressive strength of

rock (400 bars/km of depth assuming hydrostatic pore pressure) is much greater than the tensile strength.

Studies of oceanic intraplate seismicity (Bergman and Solomon, 1984; Wiens and Stein, 1984) show a mixture of normal, strike slip, and thrust faulting in young oceanic lithosphere. Older oceanic lithosphere tends to show predominantly thrust faulting. There is no evidence for a transition from normal to thrust earthquake mechanisms at any specific age. The compression axes or tension axes in focal mechanism solutions do not line up with the spreading direction. Normal faulting tends to occur near the bottom of the plate. Thrust faulting occurs near the surface with strike slip faulting at intermediate levels. Seismicity in young oceanic crust is probably caused by differential thermoelastic cooling, a phenomenon not considered in this investigation.

Yield Stresses

The Byerlee frictional strength laws were obtained from laboratory experiments on already fractured rock over a range of normal stresses from 30 bars to 17 kilobars (Brace and Kohlstedt, 1980). These laws can be depicted on a graph of shear stress τ versus normal stress σ as shown in Figure 87. The line is known as the Coulomb failure envelope. Because the rock is already fractured, the line passes through the origin. Any circle centered on the σ axis is known as a Mohr circle and represents the stresses in the solid on any plane. The two intersections with the σ axis are at the maximum and minimum principal stresses σ_1 and σ_3. If the circle is

tangent to the Coulomb failure envelope, the point of tangency represents the normal stress σ and shear stress τ on the failure plane. The angle 2α is twice the angle α between the maximum principal stress and the normal to the failure plane.

If the rock is unfractured, the Coulomb failure envelope will have the form

$$\tau = \tau_o + \sigma \tan \phi$$

where ϕ is called the angle of internal friction (Shaw, 1980). As shown in Figure 88a, the line does not pass through the origin. τ_o is called the cohesive strength and is the shear stress required to fracture the rock on a plane with zero normal stress. $K=\tau_o/\tan \phi$ is known as the tensile strength and is the point at which the Coulomb failure envelope crosses the σ axis.

According to the Griffith theory of fracture (Shaw, 1980), the failure envelope near $\sigma=0$ departs from a straight line. The Griffith failure envelope is a parabola

$$\tau^2 - 4K\sigma - 4K^2 = 0$$

near the origin (Figure 88b). The cohesive strength is equal to 2K and the tensile strength is equal to K. The Griffith failure envelope can be divided into four sections by the points A, B, and C in Figure 88b. If the point of tangency of a Mohr circle is to the right of C, shear failure occurs and both principal stresses σ_1 and σ_3 are

compressive. If the tangent point is between B and C, shear failure occurs but the minimum principal stress σ_3 is tensile. If the tangent point is between A and B, extensional shear fracture occurs in which the displacement has both a shear and an extensional component. If A is the tangent point, then pure extensional fracture occurs on a plane perpendicular to $\sigma_3=-K$, the minimum principal stress. All Mohr circles with radii less than 2K will be tangent to the Griffith failure envelope at A.

Consider a small pocket of melt in a solid matrix. The fluid pressure in the melt will be the average of the principal stresses $(\sigma_1 + \sigma_3)/2$. The normal stresses in the Mohr circle diagrams are the effective stresses--pore pressure has been subtracted. Therefore, there is a limit to the stresses in the matrix imposed by the presence of melt at lithostatic pressures. At that limit $\sigma_1=K$, $\sigma_3=-K$, and extensional fracture occurs.

Figure 89 from Shaw (1980) shows the tensile stress K as a function of the volume fraction composed of crystals. The figure is based on both data and theoretical considerations. Although the uncertainty is large, even with a small amount of melt the tensile strength or yield strength is quite small. Therefore partially melted regions, with the melt under lithostatic pressures, cannot sustain large deviatoric stresses.

Magma Injection into Dikes

One of the characteristic features of the oceanic crust, the sheeted dike complex, must have been formed by pure extensional

fracture. A dike begins at the roof of a magma reservoir and propagates vertically towards the surface. The plane in which a dike propagates will be normal to the minimum principal stress (Pollard, 1973) which is horizontal at the ridge axis. However, the dike is not propagating through a partially melted region but through the cold, brittle lithosphere. From Figure 89, the yield stress could be between 1 and 100 bars.

The amount of tensile stress that can build up in brittle rock above a magma reservoir, before crack propagation occurs, is dependent on the fracture toughness or critical stress intensity factor for the rock. The critical stress intensity factor K_c quantifies the concentration of stress at the tip of a crack at which the crack becomes unstable and propagates. For a fluid-filled edge crack in a half plane (Paris and Sih, 1964)

$$p - \sigma_3 = \frac{K}{1.12\sqrt{\pi L}}$$

where p is the pressure in the crack, σ_3 is the regional normal stress on the crack, and L is the crack length. The pressure in the magma at the crack entrance will be equal to the overburden pressure σ_1 (Figure 90). Therefore, near the entrance

$$\sigma_1 - \sigma_3 = 2\tau = \frac{K}{1.12\sqrt{\pi L}}$$

where τ is the maximum shear stress. From experiments on rocks, the critical stress intensity factor is between 0.5 and 5.0 MNm$^{-3/2}$ (Spence and Turcotte, 1985). For K_c=1 MNm$^{-3/2}$ and a deviatoric stress of 10 bars, any crack with a length greater than 6.3 centimeters is unstable and will propagate. For larger deviatoric stresses, even smaller cracks are unstable. Therefore the fracture toughness of rock is very low and if a small crack can be supplied with magma it will propagate.

Suppose an inviscid magma is entering a vertical crack in a gravitational field. As the crack lengthens, the overpressure at the tip of the crack increases due to the lower density of the magma relative to the rock. At a distance h from the entrance of the dike, the overpressure will be $\sigma_1 - \sigma_3 + (\rho - \rho_m)gh$ where ρ is the rock density and ρ_m is the magma density (Figure 90). If $\rho - \rho_m$=0.4 gm/cm^3, the overpressure at the tip of a magma filled dike will increase by 40 bars/km. This increasing overpressure will accelerate crack propagation. Therefore, resistance to propagation by the solid rock is negligible. To quote Pollard (1973):

The important point is that sheet intrusions have a tremendous mechanical advantage over the host rock by virtue of their own geometry and that of the ubiquitous microscopic flaws in the host rock, and therefore they will propagate at very small values of $(\rho - \sigma_3)$. For a brittle host rock the problem is not the initiation of propagation, but why sheet intrusions ever stop

propagating. A drop in magma pressure due to a deficient supply, crystallization, and/or changing rheological properties is apparently the parameter which inhibits propagation.

Therefore, the probability of dike emplacement is dependent on the viscosity of the magma entering the crack and on the magma overpressure which drives the flow.

The average velocity of two-dimensional Poiseuille flow in a channel of half width a is

$$V = \frac{a^2}{3\mu} \frac{dp}{dz}$$

where μ is the viscosity of the fluid and $\frac{dp}{dz}$ is the pressure gradient driving the flow. If a conduit is opened up between a magma reservoir and the ocean floor, the driving pressure gradient would be $(\rho - \rho_m)g = 40$ bars/km. For a 1 meter wide conduit, magma with a viscosity of 1000 poise would have a velocity of 3.3 m/sec. This is slightly higher than the propagation rate of sheet intrusions determined from seismicity studies in Hawaii and Iceland (Delaney and Pollard, 1982).

When the dike propagates into cold rock, it is in danger of slowing down and freezing through the loss of heat to the walls. The dike must propagate fast enough to keep this from happening. A

solidified boundary layer grows inward from both walls while the magma is flowing and eventually chokes off magma flow.

Delaney and Pollard (1982) have developed a model for the solidification of flowing magma in a conduit of thickness T. The magma is an incompressible Newtonian fluid with density ρ, viscosity μ, conductivity k, heat capacity C_v, and thermal diffusivity $\kappa = k/\rho C_v$. The Reynolds number and the Prandtl number of the magma are

$$Re = V\frac{\rho}{\mu}\frac{T}{2} \qquad Pr = \frac{\mu C_v}{k}$$

where V is the initial fluid velocity. A non-dimensionalized solution is obtained for the velocities in the dike and the temperatures in both the dike and wall rock. Laminar flow is assumed.

The dike is divided into three regions: 1) an isothermal flowing core, 2) a thermal boundary layer across which the temperature falls from the isothermal core temperature to half that value, and 3) a solidified magma layer frozen to the wall. A solidification temperature θ_s is defined in the thermal boundary layer to separate flowing magma from stagnant magma. Its location is a function of the temperature dependent magma viscosity and the initial temperature difference between the core of the dike and the wall rock $\theta_i - \theta_w$. A solution is obtained using the non-dimensionalized variables

$$\frac{y}{T/2}, \quad \frac{z}{RePr(T/2)}, \quad \frac{\kappa t}{(T/2)^2}, \quad \text{and} \quad \frac{\theta - \theta_w}{\theta_i - \theta_w}$$

where y is the distance from the wall, z is the downstream position, t is time, θ is temperature, θ_i is the initial magma temperature, and θ_w is the wall rock temperature. Figure 91 shows the position of the solidification surface with time and the volumetric flow rate Q for different downstream positions.

To redimensionalize the solution, the magma density is $\rho = 2.6$ g/cm^3, the thermal diffusivity is $\kappa = 0.0085$ cm^2/s, and the thickness is T=1 m. The initial velocity is estimated to be 1 m/s based on observations of fissure eruptions in Hawaii and Iceland (Delaney and Pollard, 1982). If $\mu = 1000$ poise, the Prandtl number is 4.5 x 10^4 and the Reynolds number is 13. If $\mu = 100$ poise, the Prandtl number is 4.5 x 10^5 and the Reynolds number is 130. The flow is laminar if Re<1000. If the magma temperature is 1200°C and the wall rock is initially at 0°C, the non-dimensional solidification temperature θ_s is estimated to be 0.95 (Delaney and Pollard, 1982).

The times and distances obtained using the above parameters are shown in Figure 91. It can be seen that after nine hours, the solidification surface at 300 meters from the entrance is 75% of the way to the center of the dike. As the solidification surface moves inward, the flow is constricted. Since the velocity in a channel is proportional to the square of the half thickness and the volumetric flow rate is proportional to the cube of the half thickness, both V and Q will drop quickly. Figure 91b shows that the flow at 3

kilometers from the entrance is almost completely choked off after only 5 hours. This is much less than the time it takes to freeze solid a 1 meter wide static dike. Since magma solidification can choke off flow in a dike in only 5 hours, the dike must have been formed in a fraction of that time.

Observations of fissure eruptions in Hawaii and Iceland (Delaney and Pollard, 1982) support the conclusion that the freezing magma quickly chokes off flow in a dike. As an example, for the Kilauea Iki eruption in 1959, six en echelon fissures opened in 30 minutes. After 1.5 hours, the fissures reached their maximum length with a "curtain of fire" at each fissure. After 2 hours, the curtain of fire broke up into 1 or 2 vents along each fissure. At 8 hours, only 1 or 2 vents were erupting along the whole system and at 24 hours, only a single vent was still active.

Magma Supply

If dike injection is the mechanism that keeps horizontally tensile stresses from building up at the axis, magma supply is the most important factor controlling ridge axis topography. The magma must have a viscosity low enough to be able to flow up the dike and make it propagate fast enough to keep from freezing. There must a large enough reservoir of low viscosity magma available to be able to emplace a dike whenever the tensile stresses build up. Every time a dike is injected into the crust, the tensile stresses are partially relaxed.

The axial valley at the Gorda ridge implies that a steady-state magma chamber does not exist there. The large tensile stresses required for the axial valley would be quickly relaxed by dike injection. Magma must be delivered to the Gorda ridge axis intermittently.

The axial peak at the Juan de Fuca ridge suggests one of three possibilities: 1) there is a steady-state magma chamber present in the mantle; 2) there are small, discontinuous, steady-state magma chambers in the crust supplying long segments of the ridge; or 3) magma is supplied often enough to keep tensile stresses from building up but without forming a steady-state magma chamber. If there is a steady-state magma chamber, tensile stresses will build up gradually due to tectonic forces or suddenly whenever there is a fresh infusion of magma into the magma chamber. Stresses in the brittle crust could even become slightly compressive in between spreading episodes. This may happen due to the cooling and contraction of the magma chamber in between spreading episodes. Stresses may not become tensile again until there is a fresh infusion of magma. There is no evidence of reverse faulting at ridge axes, but it would take a huge buildup of compressive stresses (400 bars/km of depth) for such an earthquake to occur.

If there is a long enough period without replenishment of the magma chamber, it will freeze. Then, due to tectonic forces, compressive stress at the axis will be gradually reduced to zero before becoming tensile. At this point, a new magma chamber must

be emplaced and extrusion must occur to prevent the formation of an axial valley.

The difference in magma supply to the Gorda and Juan de Fuca ridges need not be large. In fact, since the crust has roughly the same thickness at both ridges, there cannot be a large difference in magma supply. A small magma undersupply to the Gorda ridge, over a long period of time, would allow tensile stresses in the crust to build up, forming an axial valley. Alternatively, a small magma oversupply to the Juan de Fuca ridge, over a long period of time, would relax tensile stresses in the crust and build an axial peak. An analogy can be made to two identical funnels which allow the same amount of fluid to flow out the bottom. Fluid is intermittently added to one funnel at a rate slightly higher than the outflow rate and to the other at a rate slightly lower than the outflow rate. One funnel will gradually fill with the fluid while the other remains empty.

If there is a difference (albeit small) in the magma supply rates to the Gorda and Juan de Fuca ridges, there must be some difference in the upper mantle beneath the ridges. The upper mantle beneath the Juan de Fuca ridge could be slightly warmer than the upper mantle beneath the Gorda ridge, thus producing more magma. Or, the basaltic melt component may be slightly higher beneath the Juan de Fuca ridge. The proximity of the hot spot at the mid-point of the ridge may also increase the magma supply at the Juan de Fuca ridge. Hot spot upwelling is believed to originate from deep in the mantle (Burke and Wilson, 1976). The pressure release effect would

be greater and a larger proportion of melt could be produced. The absence of an axial valley on the Reykjanes ridge, which is adjacent to the Icelandic hot spot, may be an analogous situation (Vogt and Johnson, 1975).

Another possibility is suggested by the fact that spreading centers are not stationary with time, but migrate with respect to the lower mantle (i.e. the hot spot frame of reference). The Pacific plate is moving to the northwest at 5.5 cm/yr and the Juan de Fuca plate is moving to the northeast at 2.5 cm/yr (Figure 92) (Davis and Karsten, 1986). Therefore, the Juan de Fuca ridge is moving to the north-northwest at 3.0 cm/yr relative to the lower mantle. The component of motion normal to the ridge axis is 2.0 cm/yr.

Davis and Karsten (1986) suggested that the abundance of seamounts on the Pacific plate west of the Juan de Fuca ridge and the near absence of seamounts on the Juan de Fuca plate, can be explained by ridge migration. They postulate that the mantle has small heterogeneities with solidus temperatures 20-50°C lower than the normal peridotite solidus. As the mantle upwells, the heterogeneities can melt at a higher pressure and deeper depth than the surrounding mantle. The lowered density of the heterogeneity will result in a stronger buoyancy force driving it toward the surface earlier than the still solid peridotite.

The lower mantle moves horizontally at a rate an order of magnitude less than the velocities of the plates, as indicated by relative motions of the hot spots. If the lower mantle is assumed to be horizontally stationary, the vertical velocity required to supply a

migrating spreading center can be calculated. Davis and Karsten (1986) calculated this ascent velocity for the Juan de Fuca ridge versus the distance to the ridge or, equivalently, time before or after the crossing of the ridge over a certain point (Figure 93). It is obvious that the ascent velocity is much greater in advance of the ridge axis under the Pacific plate. If a partially melted heterogeneity segregates from the peridotite matrix, and rises to the surface faster than the ascent velocity it will reach the surface before the ridge axis on the Pacific plate. If the seamounts are the result of the heterogeneities reaching the surface, almost all the seamounts are emplaced on the Pacific plate. After the ridge axis passes over, the ascent velocity drops substantially and most of the heterogeneities have been swept from the mantle. Therefore, seamounts are rare on the Juan de Fuca plate.

Schouten et al. (1987) have defined the mantle consumption ratio to be the ratio of the full spreading rate to the ridge normal component of the migration velocity. This ratio gives an estimate of the thickness of mantle material which is removed when a migrating ridge passes over a point. If the mantle consumption ratio is 2, the trailing plate is stationary and the ridge normal migration velocity is half the full spreading rate. As the ridge axis passes over a point, the thickness of mantle material removed to form both lithospheres of thickness L would be 2L. If the mantle consumption ratio is very large, the migration velocity is very small relative to the full spreading rate and a very thick layer of the mantle is dredged up to form both lithospheres.

Figure 94 shows streamlines in the ridge axis frame of reference for mantle consumption ratios of 3, 6, and 16. When the mantle consumption ratio is low, the asymmetry in the ascent rates is more pronounced. The mantle consumption ratio of the Juan de Fuca and the northern Gorda ridges is (2 x 3 cm/yr)/2 cm/yr = 3.

When a layer of the mantle is being removed, deeper mantle upwells to take its place. Some melting may take place, segregate from the matrix and be transported to the surface. A depleted residual would be left behind which is not incorporated into either plate. If another spreading center happened to migrate over the same spot, it would be entraining mantle material which had already been partially depleted of both heterogeneities and normal mid-ocean ridge basalts. There would be a small magma deficiency at the axis.

If the migration velocity of the Juan de Fuca ridge (3 cm/yr to the north-northwest) has been constant in the past, then 15 to 20 million years ago, the Juan de Fuca was spreading over the same region of the mantle where the Gorda ridge is today. To check this, the poles of rotation calculated by Riddihough (1984) for the Juan de Fuca plate relative to the hot spot frame of reference were used to retrace the track of the Juan de Fuca ridge. The magnetic record preserved on the Juan de Fuca plate limits the accurate determination of the poles of rotation to the past 7 million years. The spreading rate and direction, migration rate and direction, mantle consumption ratio and angle between spreading and migration directions were calculated for two points on the Juan de Fuca ridge

(Table 3). The positions of the points for the past 7 million years are plotted in Figure 95. According to Riddihough (1984), the Explorer plate was detached from the Juan de Fuca plate and the Sovanco fracture zone was formed about 4 million years ago. Before that the Juan de Fuca ridge extended further to the north. It seems very likely that in the past the Juan de Fuca ridge was located at the present position of the Gorda ridge. The Juan de Fuca ridge has migrated about 500 kilometers since then. If the deep mantle moves an order of magnitude slower than the plates, it cannot have traveled more than 50 kilometers in that time. Therefore, the Juan de Fuca ridge could have partially depleted the mantle under the present day Gorda ridge.

Table 2

Results of Numerical Modeling

T_m(°C)	n	Cooled Crust	Lowered Viscosity	Lowered Density	Yield Stress	Axial Width	Axial Depth
1200	1	Yes	No	No	80b/km	30	2.0
1300	1	Yes	No	No	80b/km	30	1.8
1400	1	Yes	No	No	80b/km	30	1.5
1200	3	Yes	No	No	80b/km	30	1.4
1300	3	Yes	No	No	80b/km	30	1.1
1400	3	Yes	No	No	80b/km	30	1.0
1300	1	No	No	No	80b/km	12	1.1
1400	1	No	No	No	80b/km	8	0.7
1300	3	No	No	No	80b/km	12	0.8
1400	3	No	No	No	80b/km	8	0.5
1300	1	No	Yes	No	80b/km	8	1.0
1300	1	No	Yes	Yes	80b/km	8	1.0
1300	1	No	Yes	Yes	40b	4	0.25
1300	1	No	Yes	Yes	20b	4	0.10
1300	1	No	Yes	Yes	10b	-	0.0
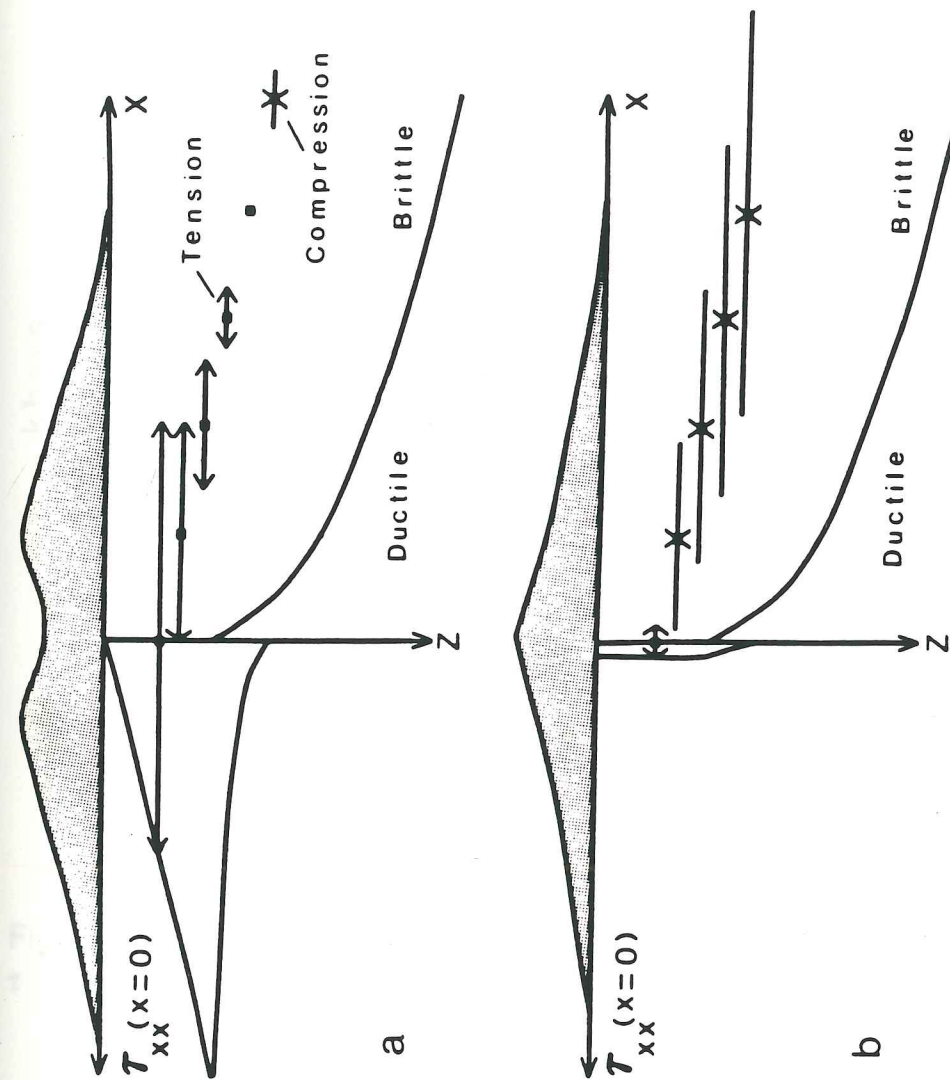
Figure 86. State of stress at (a) the Gorda ridge and (b) the Juan de Fuca ridge. A topographic profile is at the top of each figure. Horizontal tensile stresses at the axis (x=0) are plotted versus depth at the lower left. Horizontal stresses in the lithosphere at various distances from the axis are shown at the lower right.
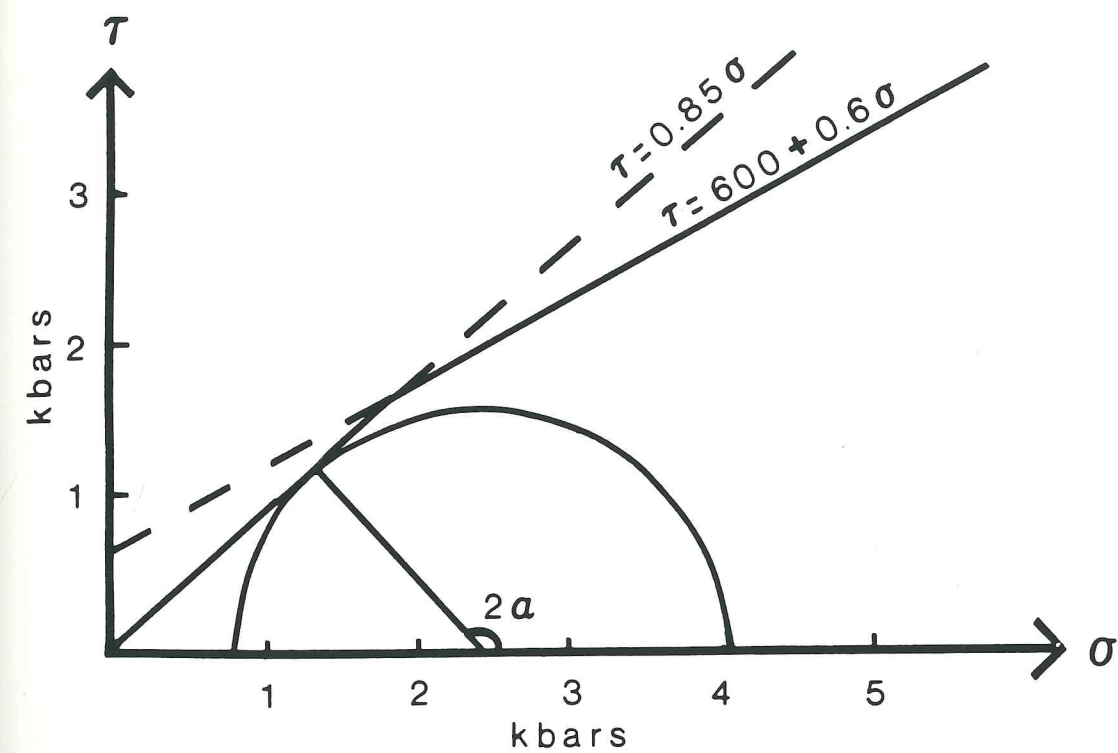
Figure 87. Byerlee's frictional strength law. Maximum shear stress τ (bars) as a function of normal stress σ (bars) on a fault.
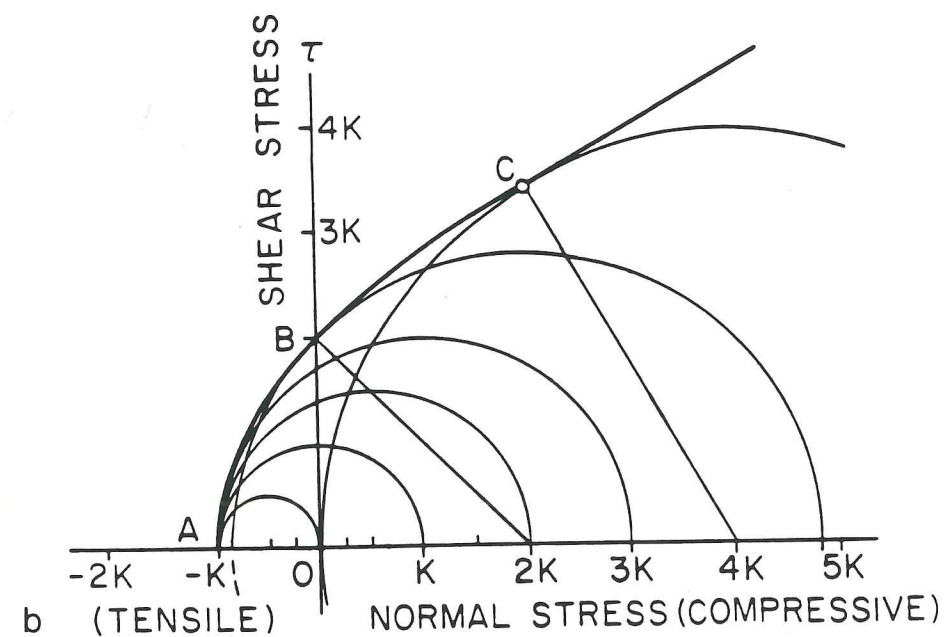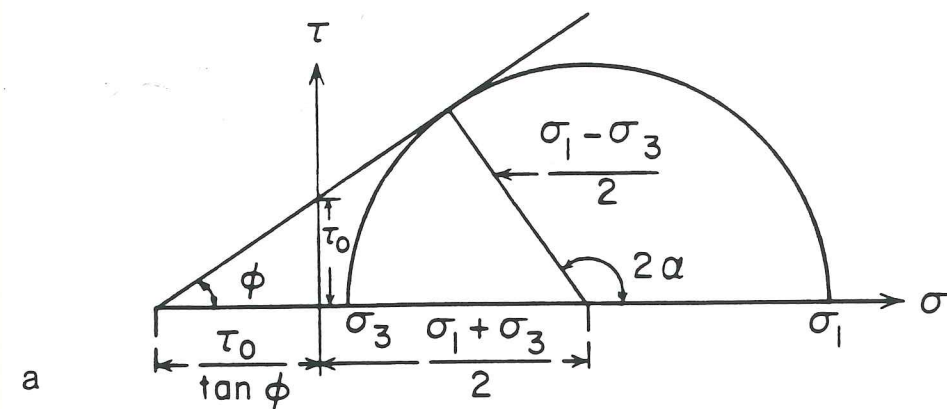
Figure 88. a) Coulomb failure envelope and Mohr circle. b) Griffith failure envelope and a range of Mohr circles. (Shaw, 1980)
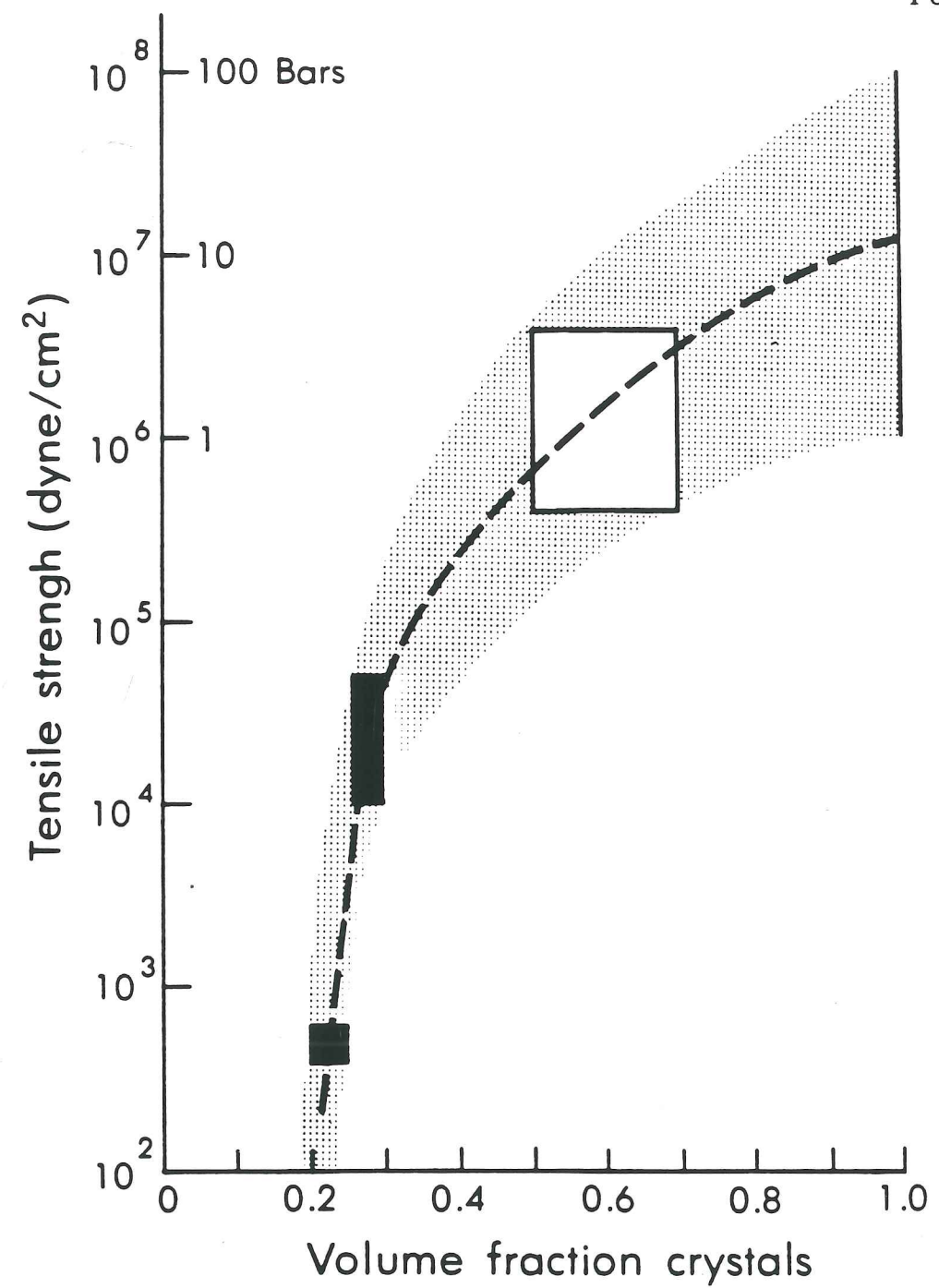
Figure 89. Tensile strength of rock as a function of volume fraction of crystals (Shaw, 1980).
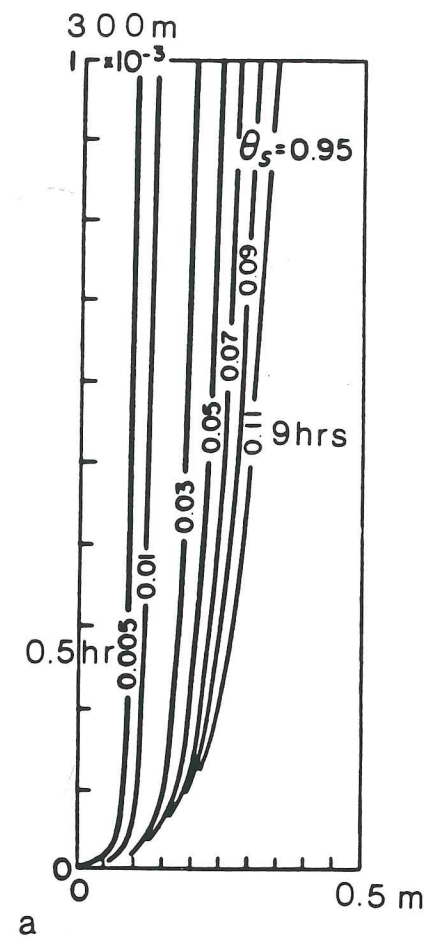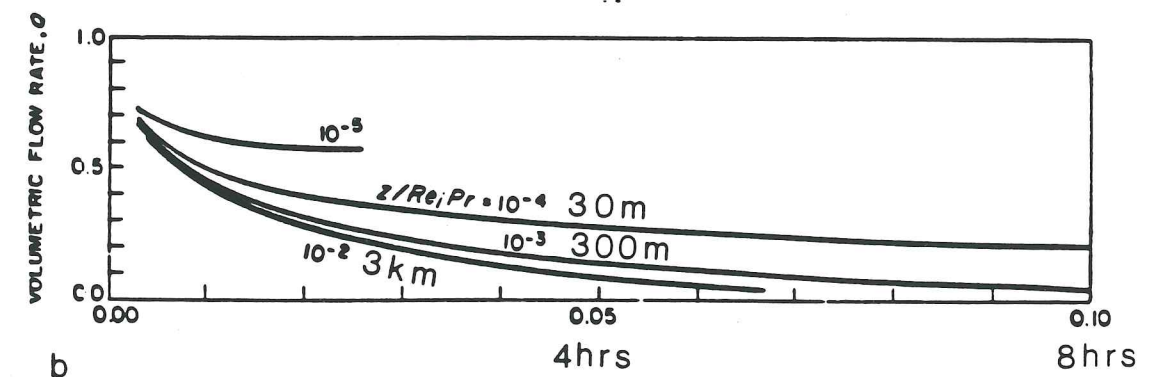
Figure 91. a) Position of solidification surface for θ_s=0.95 versus downstream position at various times. b)Volumetric flow rate versus time for several downstream positions (Delaney & Pollard, 1982). Redimensionalized with indicated parameters to obtain times and distances.
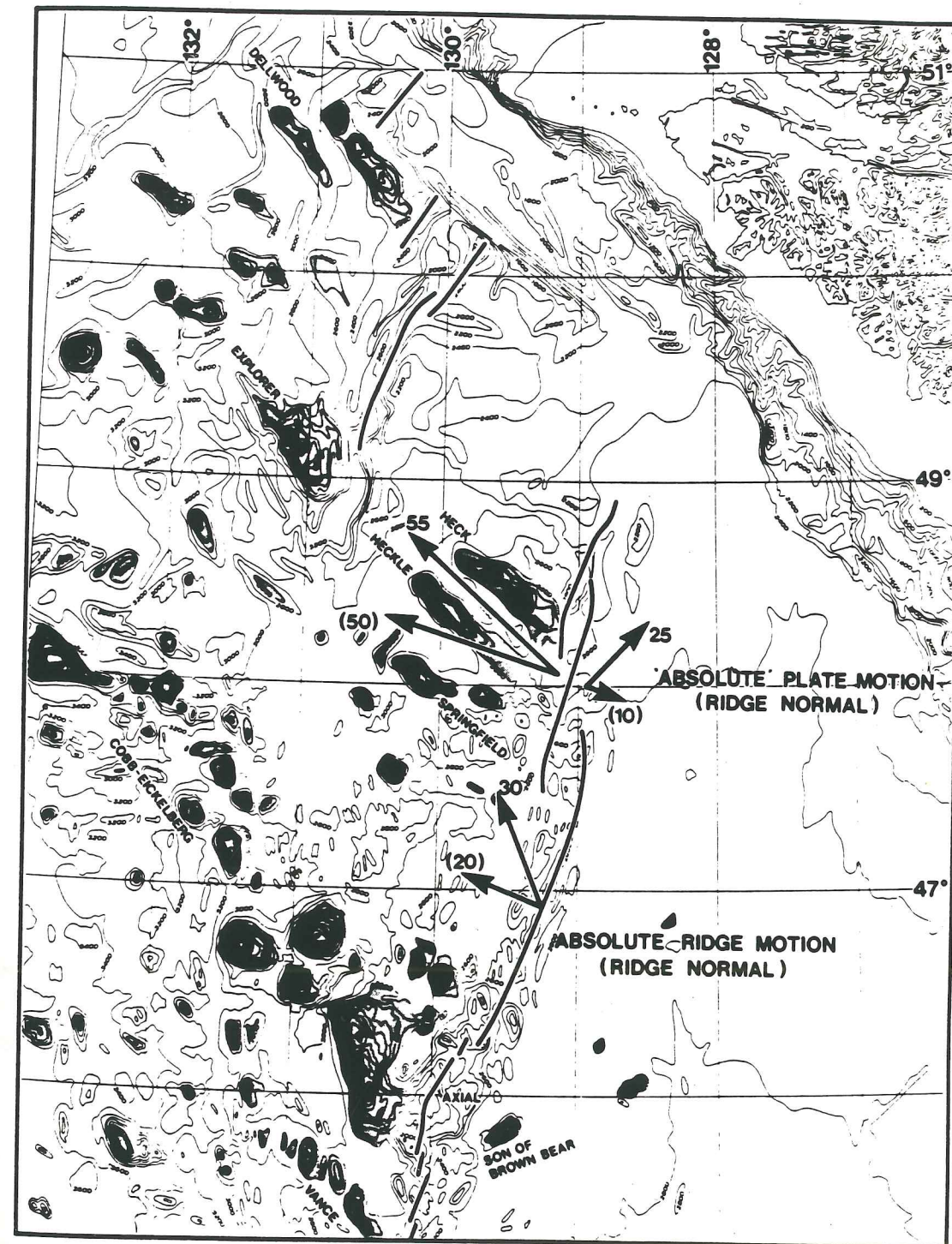
Figure 92. Motion (mm/yr) of the Juan de Fuca and Pacific plates and of the Juan de Fuca ridge relative to the hot spot frame of reference (Davis and Karsten, 1986).
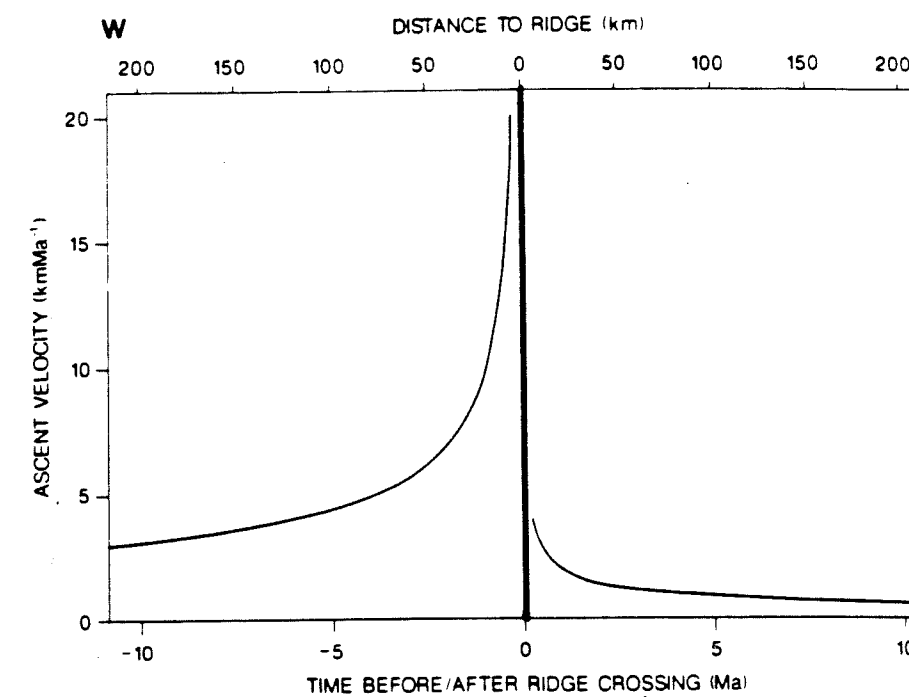
Figure 93. Ascent velocity for the Pacific plate (west) and the Juan de Fuca plate (east) versus distance to ridge and time before or after the ridge crosses a fixed point (Davis and Karsten, 1986).

Leading plate ← V/2   V/2 → Trailing plate

Ratio 3

L

0.75L   1.5L
2.25 L
3.0 L

V/3

Ratio 6

L

1.5L

3.0 L

4.5 L

6.0 L

V/6

Ratio 16

L

4L

8L

12L

16L

V/16
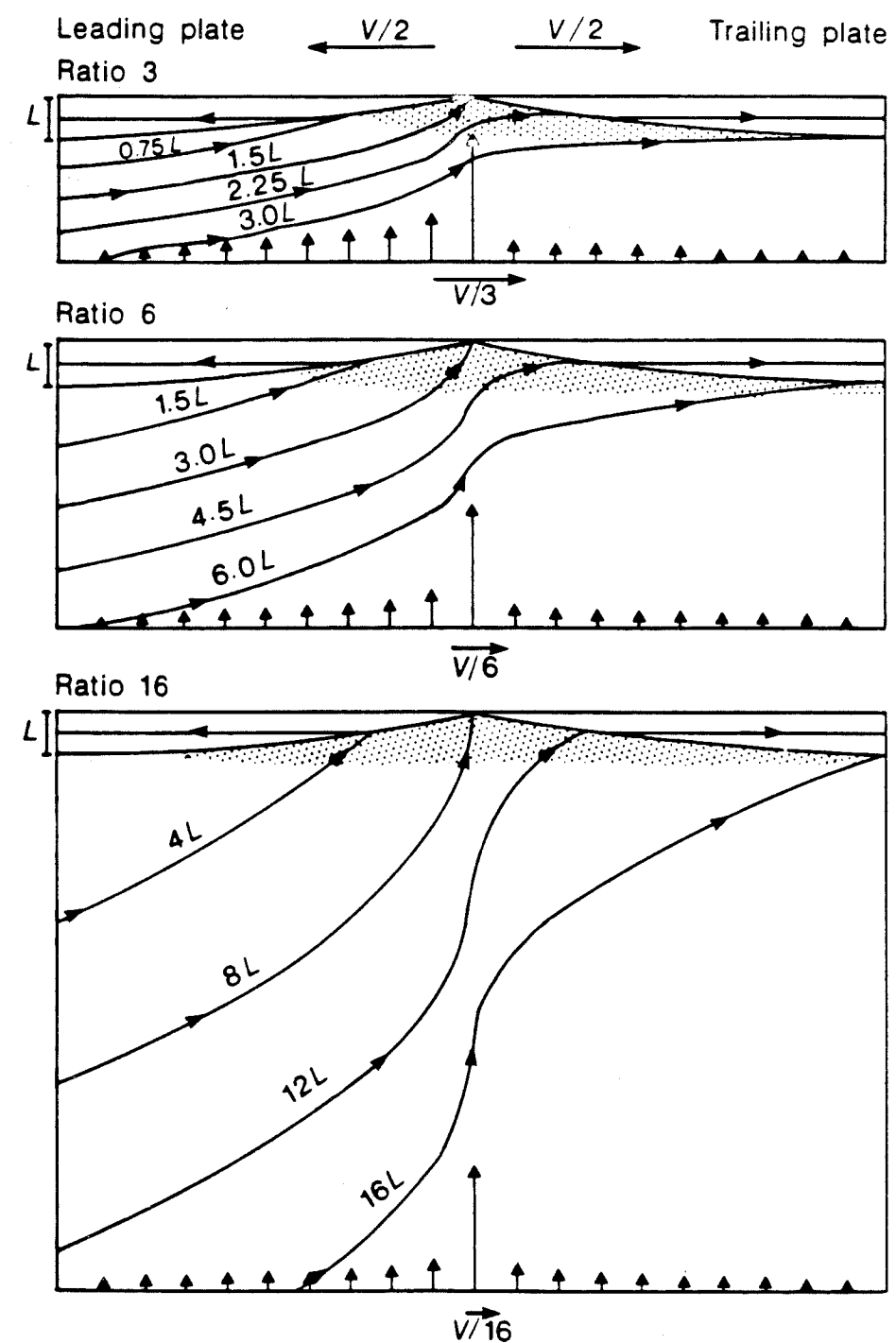
Figure 94.   Streamlines in the frame of reference of a migrating ridge for mantle consumption ratios of 3, 6, and 16.   Streamlines are labeled with starting depth below lithosphere of thickness L on left side.   Vertical (ascent) velocities in asthenospheric frame of reference are also shown.   Arrow on bottom shows velocity of asthenosphere relative to ridge axis.   (Schouten et al., 1987).

Table 3

Motion of the Juan de Fuca ridge over the past 7 million years

Latitude	Longitude	Spreading Rate	Direction	Migration Rate	Direction	MCR	Angle
48.00	-129.00						
47.76	-128.88	2.98	-70.48	2.84	-18.55	3.40	51.93
47.51	-128.76	2.96	-73.15	2.96	-17.79	3.53	55.36
47.26	-128.64	3.05	-72.94	2.91	-17.24	3.73	55.70
47.02	-128.51	2.95	-70.13	2.86	-21.33	3.14	48.80
46.76	-128.42	3.28	-76.17	2.95	-13.01	4.93	63.16
46.45	-128.31	3.09	-85.65	3.51	-13.24	5.83	72.41
46.14	-128.24	3.36	-86.71	3.50	-9.39	8.77	77.32
45.00	-130.00						
44.75	-129.81	2.88	-71.00	3.19	-28.40	2.45	42.60
44.48	-129.62	2.87	-73.67	3.29	-27.34	2.53	46.33
44.23	-129.46	3.18	-73.79	3.10	-23.85	3.19	49.94
43.99	-129.29	3.18	-71.37	3.00	-26.14	3.01	45.23
43.73	-129.21	3.80	-77.18	2.93	-13.04	5.94	64.13
43.42	-129.10	3.51	-85.45	3.54	-14.86	5.97	70.58
43.11	-129.01	3.74	-86.52	3.54	-11.70	8.08	74.82

MCR = Mantle Consumption Ratio

Angle = Migration Direction - Spreading Direction
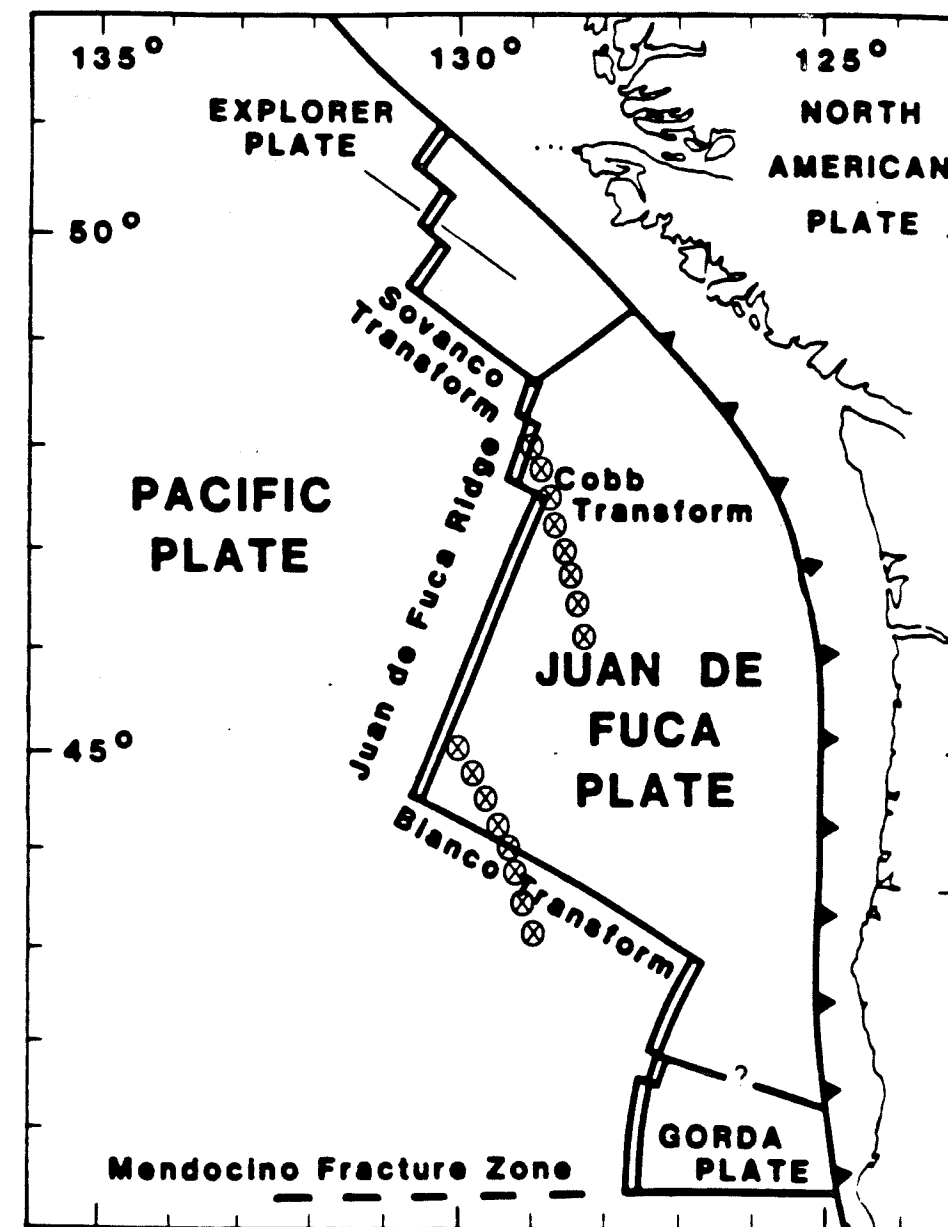
Figure 95. Track of two points on the Juan de Fuca ridge for the past 7 million years.

Conclusion

The purpose of this investigation was to determine the cause
of the topographic difference between the Juan de Fuca and the
Gorda ridges. The similarity in crustal structure at both ridge axes
suggested that the variation in topography is caused by some
difference in the upper mantle. The viscous head loss theory of
ridge axis topography (Sleep, 1969; Lachenbruch, 1973) is often used
to explain topographic variation at spreading centers. Parmentier
and Forsyth (1985) used viscous head loss in a narrow conduit to
explain the deepening of axial valleys toward fracture zones. It
seemed plausible that spreading rate independent topographic
variation could be caused by a difference in upper mantle viscosity
below the Juan de Fuca and Gorda ridges. An order of magnitude
difference in viscosity would change the viscous drag forces in the
mantle and, consequently, the depth of an axial valley by an order of
magnitude. The thermally activated creep laws for olivine indicate
that a 100°C temperature difference would result in an order of
magnitude difference in viscosity.

A finite element program for two-dimensional, steady state,
viscous flow was used to calculate the dynamic topography at the
spreading center in order to test which parameters, when varied,
could reproduce both topographic profiles. A specified temperature
field was used to obtain the density and viscosity fields. The cold,

brittle lithosphere at the axis deforms by faulting rather than by viscous flow. A viscoplastic rheology was used to represent this type of behavior. Wherever high strain rates would make the stresses exceed a specified yield stress, the viscosity was lowered. The yield stress was the limit imposed on tectonic stresses by shear failure on normal faults. This limit was determined to be 80 bars/km of depth.

In the first models, the temperature of the asthenosphere was varied by several hundred degrees. All models produced deep axial valleys despite the order of magnitude changes in the viscosity of the asthenosphere. The stresses in the asthenosphere due to the upwelling of the mantle were too weak to have any effect on the dynamic topography. The stress fields indicated that the largest stresses were horizontal tensile stresses in the brittle lithosphere. These results support the steady state necking theory of ridge axis topography (Tapponnier and Francheteau, 1978) over the viscous head loss model. The viscosity of the mantle is only important in determining the location of the bottom boundary of the lithosphere-- the brittle-ductile transition.

Next, non-Newtonian stress-dependent rheology was tested. The resulting stress fields were very similar to those produced using Newtonian viscosity since the exponential temperature dependence is more important than the stress dependence in the power law viscosity equation. Although axial valleys were shallower, an axial peak could not be produced. Then, the thickness of the hydrothermally cooled crust was reduced to test whether an

axial peak could be produced with a thinner, and therefore weaker, brittle lithosphere at the axis. When the hydrothermally cooled layer was completely removed, the lithosphere was only 1.0 to 1.5 kilometers thick at the axis. Although the axial valley was shallower, the lithosphere was still too strong to produce an axial peak.

The effect of partial melting in the mantle was investigated by lowering viscosities and densities beneath the axis. When only viscosities were lowered, the upwelling was concentrated into a narrow fast-moving jet resembling the narrow conduit postulated in the viscous head loss theory. However, this had no effect on the surface topography. Then, both viscosities and densities were simultaneously lowered under the axis. The lowered densities elevate the level of the isostatic thermal topography at the axis. This buoyancy force might be expected to offset the forces creating the axial valley. However, the results show that the buoyancy effect is distributed over a wider area by the strength of the brittle lithosphere. Both the axial valley and the shoulders are elevated by lowered densities in the mantle but the depth of the valley remains the same.

All the models tested using the brittle shear failure criterion as the yield stress had axial valleys greater than 400 meters in depth. To obtain an axial peak, the tensile stress in the brittle lithosphere must be much lower than the shear failure limit. This conclusion is supported by the contrast between the absence of seismic activity at the Juan de Fuca ridge and the abundant

seismicity at the Gorda ridge. To obtain an axial valley less than 100 meters deep, the tensile yield stress must be reduced to 10-20 bars for all depths.

The injection of magma into dikes was put forward as an explanation for the low yield stresses necessary for an axial peak. The sheeted dike complex in the ocean crust is formed by extensional failure caused by a propagating, magma-filled crack. The tensile stress in the lithosphere necessary to permit dike propagation was shown to be very small. The probability of dike emplacement is dependent on the availability of low viscosity magma.

Ridge crest topography is determined by the state of stress in the lithosphere, not by the viscous flow of the asthenosphere. The deepening of the brittle-ductile transition away from the axis and the thickness of the cooled brittle layer at the axis are the most important factors if the lithosphere at the axis is at the shear failure criterion. Magma chambers are emplaced intermittently and can only partially relax the tensile stress at the axis. The topography in this case will be an axial valley. However, the presence of a steady-state magma chamber or the frequent delivery of magma to the ridge axis can keep tensile stresses in the crust from approaching the shear failure criterion. Then, an axial peak can be sustained. Therefore, the amount of partial melting of the upwelling mantle has an important effect on ridge crest topography, not through its effect on the density or viscosity of the asthenosphere, but through its effect on the stress state in the

brittle crust. Any seismicity at an axial peak will have low magnitudes and be of volcanic rather than tectonic origin. Stresses could become compressive at the axis between spreading episodes.

The difference in topography at the Juan de Fuca and the Gorda ridges is due to a greater supply of magma to the Juan de Fuca ridge. The difference in magma supply cannot be large since the crustal thickness is about the same at both ridge crests. A small magma deficit at the Gorda ridge, over a long period, could form the axial valley or a small magma surplus at the Juan de Fuca ridge, over a long period, could build the axial peak.

There must be some reason for this difference in magma supply. Both ridges are migrating to the north-northwest with respect to the hot spot reference frame. The spreading center entrains material from below the leading (Pacific) plate. The Juan de Fuca ridge may have simply reached a warmer part of the lower mantle or a region with heterogeneities which melt at lower than normal temperatures. The Juan de Fuca ridge has also just reached the position of the Axial Seamount hot spot. This may increase the availability of melt at the Juan de Fuca ridge.

Another possibility is that the upper mantle under the Gorda ridge is cooler than normal due to its proximity to the thick, cool, North American continental crust. The subducting Juan de Fuca plate could add to the effect by further cooling the upper mantle in its vicinity. However, this hypothesis is less likely since the Gorda ridge also is moving to the west and entrains material from under

the Pacific plate. This material should not be affected by the cooler temperatures beneath North America.

A more likely explanation is that the Gorda ridge is spreading over the same section of the lower mantle that the Juan de Fuca ridge passed over 15 to 20 million years ago. The Juan de Fuca ridge could have partially depleted the area of some early melting heterogeneities or normal mid-ocean ridge basalt. Since the lower mantle moves an order of magnitude slower than the plates, the Gorda ridge is now spreading over this same region.

Although the results of this investigation lead to the conclusion that the Juan de Fuca ridge has a magma supply available whenever tensile stresses at the axis build up to 10 to 20 bars, there is little evidence for a shallow, wide, crustal magma chamber. However, seismic reflection and refraction methods do not probe deeply into the lower crust or upper mantle. The magma chamber reflector found on the Valu Fa Ridge in the Lau back-arc basin was 3.5 kilometers deep. There could be a steady-state magma chamber even deeper under the Juan de Fuca ridge. Alternatively, there may be small, discontinuous crustal magma chambers along the Juan de Fuca axis that supply magma to long segments of the ridge. Another possibility is that magma chambers are rarely present but magma is supplied to the ridge often enough to prevent tensile stresses from forming an axial valley. The period between eruptive episodes may be long if the stresses at the axis become compressive after a spreading episode.

In many discussions of plate tectonic driving forces, the ridge push force is represented as a boundary force acting on a plate along the ridge crest. The ridge push force is actually a body force caused by the thickening of the lithosphere and deepening of the ocean floor with age. In fact, the force at a ridge crest boundary is more likely to resist plate motion. The frictional forces on normal faults in a tensional environment opposes the ridge push body force. If there is an axial peak at the ridge crest, this interplate resistance force will be negligible. However, when there is an axial valley at the ridge crest, the interplate resistance force should be considered in any discussion of lithospheric stress. Although smaller than the major plate driving forces, it can put the plate in horizontal tension for several hundred kilometers from the spreading center.

LIST OF REFERENCES

Andrews, D. J., Numerical simulation of sea-floor spreading, *J. Geophys. Res.*, **77**, 6470-6481, 1972.

Atwater, T., Implications of plate tectonics for Cenozoic tectonic evolution of western North America, *Geol. Soc. Am. Bull.*, **81**, 3513-3536, 1970.

Bergman, E. A., and S. C. Solomon, Source mechanisms of earthquakes near mid-ocean ridges from body waveform inversion: Implications for early evolution of oceanic lithosphere, *J. Geophys. Res.*, **89**, 11415-11441, 1984.

Brace, W. F., and D. L. Kohlstedt, Limits on lithospheric stress imposed by laboratory experiments, *J. Geophys. Res.*, **85**, 6248-6252, 1980.

Bratt, S. R., and S. C. Solomon, Compressional and shear wave structure of the East Pacific Rise at 11° 20'N. Constraints from three-component ocean bottom seismometer data, *J. Geophys. Res.*, **89**, 6095-6110, 1984.

Burke, K. C., and J. T. Wilson, Hot spots on the earth's surface, *Scientific American*, **235**, 46-57, 1976.

Davis, E. E., and J. L. Karsten, On the causes of the asymmetric distribution of seamounts about the Juan de Fuca ridge: Ridge-crest migration over a heterogeneous asthenosphere, *Earth Planet. Sci. Lett.*, **79**,385-396, 1986.

Davis, E. E., and C. R. B. Lister, Fundamentals of ridge crest topography, *Earth Planet. Sci. Lett.*, **21**, 405-413, 1974.

De Bremaecker, J. C., Convection in the earth's mantle, *Tectonophysics*, **41**, 195-208, 1977.

Delaney, P. T., and D. D. Pollard, Solidification of basaltic magma during flow in a dike, *Am. J. Sci.*, **282**, 856-885, 1982.

Denny, S. E., Crustal structure of the Juan de Fuca ridge as determined from deep towed seismic reflection profiles, MS thesis, University of Washington, 1988.

Detrick, R. S., P. Buhl, E. Vera, J. Mutter, J. Orcutt, J. Madsen, and T. Brocher, Multi-channel seismic imaging of a crustal magma chamber at the East Pacific Rise, *Nature*, **326**, 35-41, 1987.

Gass, I. G., Ophiolites, *Scientific American*, **247**, 122-131, 1982.

Hale, L. D., C. J. Morton, and N. H. Sleep, Reinterpretation of seismic reflection data over the East Pacific Rise, *J. Geophys. Res.*, **87**, 7707-7717, 1982.

Herron, T. J., Lava flow layer--East Pacific Rise, *Geophys. Res. Lett.*, **9**, 17-20, 1982.

Herron, T. J., P. L. Stoffa, and P. Buhl, Magma chamber and mantle reflections--East Pacific Rise, *Geophys. Res. Lett.*, **7**, 989-992, 1980.

Houseman, G., and P. England, A dynamic model for lithosphere extension and sedimentary basin formation, *J. Geophys. Res.*, **91**, 719-729, 1986.

Houston, M. H., and J. C. De Bremaecker, Numerical models of convection in the upper mantle, *J. Geophys. Res.*, **80**, 742-751, 1975.

Huang, P. Y., and S. C. Solomon, Centroid depths and mechanisms of mid-ocean ridge earthquakes in the Indian Ocean, Gulf of Aden, and Red Sea, *J. Geophys. Res.*, **92**, 1361-1382, 1987.

Huang, P. Y., S. C. Solomon, E. A. Bergman, and J. L. Nabelek, Focal depths and mechanisms of Mid-Atlantic ridge earthquakes from body wave inversion, *J. Geophys. Res.*, **91**, 579-598, 1986.

Johnson, D. A. L., Crustal structure and seismicity of the northern Gorda ridge, MS thesis, University of Washington, 1987.

Juhlin, H. C., Mantle convection near a spreading center, MS thesis, University of Washington, 1983.

Jung, H., Velocity and attenuation in young ocean crust, PhD dissertation, University of Washington, 1988.

Kopitzke, U., Finite element convection models: Comparison of shallow and deep mantle convection, and temperatures in the mantle, *J. Geophys. Res.*, **46**, 97-121, 1979.

Lachenbruch, A. H., A simple mechanical model for ocean spreading centers, *J. Geophys. Res.*, **78**, 3395-3417, 1973.

Lachenbruch, A. H., and J. H. Sass, Heat flow and energetics of the San Andreas fault zone, *J. Geophys. Res.*, **85**, 6185-6222, 1980.

Lewis, B. T. R., The process of formation of ocean crust, *Science*, **220**, 151-157, 1983.

Lewis, B. T. R., and J. D. Garmany, Constraints on the structure of the East Pacific Rise from seismic refraction data, *J. Geophys. Res.*, **87**,8417-8425, 1982.

Lister, C. R. B., On the penetration of water into hot rock, *Geophys. J. R. astr. Soc.*, **39**, 465-509, 1974.

Lister, C. R. B., Gravitational drive on oceanic plates caused by thermal contraction, *Nature*, **257**, 663-665, 1975.

Lister, C. R. B., On the intermittency and crystallization mechanisms of sub-seafloor magma chambers, *Geophys. J. R. astr. Soc.*, **73**, 351-366, 1983.

Macdonald, K. C., Mid-ocean ridges: Fine scale tectonic, volcanic and hydrothermal processes within the plate boundary zone, *Ann. Rev. Earth Planet. Sci.*, **10**, 155-190, 1982.

Macdonald, K. C., Crustal processes at spreading centers, *Rev. Geophys. Space Phys.*, **21**, 1441-1454, 1983.

McClain, J. S., and B. T. R. Lewis, A seismic experiment at the axis of the East Pacific Rise, *Marine Geol.*, **35**, 147-169, 1980.

McClain, K. J., and B. T. R. Lewis, Geophysical evidence for the absence of a crustal magma chamber under the northern Juan de Fuca ridge: A contrast with ROSE results, *J. Geophys. Res.*, **87**, 8477-8490, 1982.

McClain, J. S., J. A. Orcutt, and M. Burnett, The East Pacific Rise in cross section: A seismic model, *J. Geophys. Res.*, **90**, 8627-8640, 1985.

McKenzie, D. P., Some remarks on heat flow and gravity anomalies, *J. Geophys. Res.*, **72**, 6261-6273, 1967.

McKenzie, D., J. Roberts, and N. Weiss, Convection in the earth's mantle: Towards a numerical simulation, *J. Fluid. Mech.*, **62**, 465-538, 1974.

Morton, J. L., and N. H. Sleep, Seismic reflections from a Lau Basin magma chamber, in *Geology and Offshore Resources of Pacific Island Arcs--Tonga Region, Circum-Pacific Council for Energy and Mineral Resources Earth Science Series*, ed. by D. W. Sholl and T. L. Vallier, Houston, V. 2, 441-453, 1985.

Morton, J. L., N. H. Sleep, W. R. Normark, and D. H. Tompkins, Structure of the southern Juan de Fuca ridge from seismic reflection records, *J. Geophys. Res.*, **92**, 11315-11326, 1987.

Oldenburg, D. W., A physical model for the creation of the lithosphere, *Geophys. J. R. astr. Soc.*, **43**, 425-451, 1975.

Orcutt, J. A., Structure of the earth: Oceanic crust and uppermost mantle, *Rev. Geophys.*, **25**, 1177-1196, 1987.

Orcutt, J. A., B. L. N. Kennett, and L. M. Dorman, Structure of the East Pacific Rise from an ocean bottom seismometer array, *Geophys. J. R. astr. Soc.*, **45**, 305-320, 1976.

Orcutt, J. A., J. S. McClain, and M. Burnett, Evolution of the oceanic crust: Results from recent seismic experiments, in *Ophiolites and Oceanic Lithosphere*, ed. by I. G. Gass, S. J. Lippard, and A. W. Shelton, pp. 7-15, Blackwell, London, 1984.

Paris, P. C., and G. C. Sih, Stress analysis of cracks, Fracture Toughness Testing and its Applications, *ASTM Spec. Tech. Publ.*, **381**, 30-83, Philadelphia, 1964.

Parker, R. L., and D. W. Oldenburg, Thermal model of ocean ridges, *Nature Phys. Sci.*, **242**, 137-139, 1973.

Parmentier, E. M., and D. W. Forsyth, Three-dimensional flow beneath a slow spreading ridge axis: A dynamic contribution to the deepening of the median valley toward fracture zones, *J. Geophys. Res.*, **90**, 678-684, 1985.

Parmentier, E. M., and D. L. Turcotte, Two-dimensional mantle flow beneath a rigid accreting lithosphere, *Phys. Earth Planet. Interiors*, **17**, 281-289, 1978.

Parmentier, E. M., D. L. Turcotte, and K. E. Torrance, Studies of finite amplitude non-Newtonian thermal convection with application to convection in the earth's mantle, *J. Geophys. Res.*, **81**, 1839-1846, 1976.

Parsons, B. and J. G. Sclater, An analysis of the variation of ocean floor bathymetry and heat flow with age, *J. Geophys. Res.*, **82**, 803-827, 1977.

Pearson, W. C., and C. R. B. Lister, The gravity signatures of isostatic, thermally-expanded ridge crests, *Phys. Earth Planet. Interiors*, **19**, 73-84, 1979.

Phipps Morgan, J., and D. W, Forsyth, 3-D flow and temperature perturbations due to a transform offset: Effects on oceanic crustal and upper mantle structure, *J. Geol. Soc. London*, in press.

Phipps Morgan, J., E. M. Parmentier, and J. Lin, Mechanisms for the origin of mid-ocean ridge axial topography: Implications for the thermal and mechanical structure of accreting plate boundaries, *J. Geophys. Res.*, **92**, 12823-12836, 1987.

Pollard, D. D., Derivation and evaluation of a mechanical model for sheet intrusions, *Tectonophysics*, **19**, 233-269, 1973.

Purdy, G. M., and R. S. Detrick, Crustal structure of the Mid-Atlantic ridge at 23°N from seismic refraction studies, *J. Geophys. Res.*, **91**, 3739-3762, 1986.

Reid, I. D., J. A. Orcutt, and W. A. Prothero, Seismic evidence for a narrow zone of partial melting underlying the East Pacific Rise at 21°N, *Geol. Soc. Amer. Bull.*, **88**, 678-682, 1977.

Riddihough, R., Recent movements of the Juan de Fuca plate system, *J. Geophys. Res.*, **89**, 6980-6994, 1984.

Riedesel, M., J. A. Orcutt, K. C. Macdonald, and J. S. McClain, Microearthquakes in the black smoker hydrothermal field, East Pacific Rise at 21°N, *J. Geophys. Res.*, **87**, 10613-10623, 1982.

Sawyer, D. S., Brittle failure in the upper mantle during extension of continental lithosphere, *J. Geophys. Res.*, **90**, 3021-3025, 1985.

Schmeling, H., and W. R. Jacoby, On modeling the lithosphere in mantle convection with non-linear rheology, *J. Geophys.*, **50**, 89-100, 1981.

Schouten, H., H. J. B. Dick, and K. D. Klitgord, Migration of mid-ocean ridge volcanic segments, *Nature*, **326**, 835-839, 1987.

Schubert, G. C. Froidevaux, and D. A. Yuen, Oceanic lithosphere and asthenosphere: Thermal and mechanical structure, *J. Geophys. Res.*, **81**, 3525-3540, 1976.

Schubert, G., D. A. Yuen, C. Froidevaux, L. Fleitout, and M. Souriau, Mantle circulation with partial shallow return flow: Effects on stresses in oceanic plates and topography of the sea floor, *J. Geophys. Res.*, **83**, 745-758, 1978.

Sempere, J. C., and K. C. Macdonald, Marine tectonics: Processes at mid-ocean ridges, *Rev. Geophys.*, **25**, 1313-1347, 1987.

Shaw, H. R., The fracture mechanisms of magma transport from the mantle to the surface, in *Physics of Magmatic Processes*, ed. by R. B. Hargraves, pp. 201-264, Princeton, N. J., 1980.

Sleep, N. H., Sensitivity of heat flow and gravity to the mechanism of sea-floor spreading, *J. Geophys. Res.*, **74**, 542-549, 1969.

Sleep, N. H., Formation of ocean crust: Some thermal constraints, *J. Geophys. Res.*, **80**, 4037-4042, 1975.

Sleep, N. H., and B. R. Rosendahl, Topography and tectonics of mid-oceanic ridge axes, *J. Geophys. Res.*, **84**, 6831-6839, 1979.

Smith, R. B., and R. L. Bruhn, Intraplate extensional tectonics of the eastern Basin-Range, *J. Geophys. Res.*, **89**, 5733-5762, 1984.

Spence, D. A., and D. L. Turcotte, Magma-driven propagation of cracks, *J. Geophys. Res.*, **90**, 575-580, 1985.

Spera, F. J., Aspects of magma transport, in *Physics of Magmatic Processes*, ed. by R. B. Hargraves, pp. 263-323, Princeton, N. J., 1980.

Solano-Borrego, A. E., Microseismicity on the Gorda ridge, MS thesis, Oregon State University, 1982.

Sverdrup, K. A., K. C. Macdonald, and W. A. Prothero, Ocean bottom seismometer detection of earthquakes on the Gorda rise near 41.5°N, *Mar. Geophys. Res.*, **7**, 439-453, 1985.

Sykes, L. R., and M. L. Sbar, Intraplate earthquakes, lithospheric stresses, and the driving mechanism of plate tectonics, *Nature*, **245**, 298-302, 1973.

Tapponnier, P., and J. Francheteau, Necking of the lithosphere and the mechanics of slowly accreting plate boundaries, *J. Geophys. Res.*, **83**, 3955-3970, 1978.

Toomey, D. R., S. C. Solomon, G. M. Purdy, and M. H. Murray, Microearthquakes beneath the median valley of the Mid-Atlantic ridge near 23°N: Hypocenters and focal mechanisms, *J. Geophys. Res.*, **90**, 5443-5458, 1985.

Torrance, K. E., Numerical approaches to solid-state convection in planetary bodies, *Phys. Earth Planet. Interiors*, **19**, 158-167, 1979.

Torrance, K. E., and D. L. Turcotte, Structure of convection cells in the mantle, *J. Geophys. Res.*, **76**, 1154-1161, 1971.

Turcotte, D. L., and G. Schubert, *Geodynamics*, John Wiley, New York, 1982.

Vogt, P. R., and G. L. Johnson, Transform faults and longitudinal flow below the midoceanic ridge, *J. Geophys. Res.*, **80**, 1399-1428, 1975.

Waff, H. S., Introduction to special section on partial melting phenomena in earth and planetary evolution, *J. Geophys. Res.*, **91**, 9217-9221, 1986.

Wiens, D. A., and S. Stein, Intraplate seismicity and stresses in young oceanic lithosphere, *J. Geophys. Res.*, **89**, 11442-11464, 1984.

VITA

Chris E. Zervas was born in Evanston, Illinois on October 3, 1957. He graduated from high school at the American International School of Kabul, Afghanistan in June, 1975. He was an undergraduate at Johns Hopkins University, where he received a Bachelor of Arts degree with a major in physics in May, 1979. He entered the geophysics program at the University of Washington in September, 1982, where he obtained a Master of Science degree in July, 1984. His thesis was entitled "A Time Term Analysis of Pn Velocities in Washington". In 1986, he published a paper in the Bulletin of the Seismological Society of America entitled "Pn Observations and Interpretations in Washington".